Technische Universität München
TUM School of Engineering and Design

Aerodynamic Shape Optimization and Analysis of a Compound-Helicopter Full-Fairing Rotor Head

Patrick Martin Pölzlbauer

Vollständiger Abdruck der von der TUM School of Engineering and Design der Technischen Universität München zur Erlangung eines

Doktors der Ingenieurwissenschaften (Dr.-Ing.)

genehmigten Dissertation.

Vorsitz: Prof. Dr.-Ing. Volker Gümmer

Prüfende der Dissertation:

1. apl. Prof. Dr.-Ing. Christian W.M. Breitsamter
2. Prof. Dr.-Ing. Manfred Hajek

Die Dissertation wurde am 11.10.2024 bei der Technischen Universität München eingereicht und durch die TUM School of Engineering and Design am 05.12.2024 angenommen.

Typesetting: LaTeX

Vorwort

Die vorliegende Arbeit ist während und nach meiner Tätigkeit als wissenschaftlicher Mitarbeiter am Lehrstuhl für Aerodynamik und Strömungsmechanik der Technischen Universität München entstanden. Die Veröffentlichung dieser Arbeit möchte ich zum Anlass nehmen, mich bei all jenen zu bedanken, die mich während meines Promotionsvorhabens begleitet und unterstützt haben.

An erster Stelle möchte ich meinem Doktorvater, Herrn apl. Prof. Dr.-Ing. Christian Breitsamter, ein großes Dankeschön aussprechen. Seine Unterstützung im Rahmen des Forschungsprojektes und seine wertvollen Ratschläge haben maßgeblich zum Gelingen dieser Arbeit beigetragen. Ich bin ihm besonders dankbar für die Freiheiten, die er mir gewährt hat, und das Vertrauen, das er in meine Arbeit gesetzt hat.

Des Weiteren möchte ich mich bei Herrn Prof. Dr.-Ing. Manfred Hajek für die Übernahme des Zweitprüfers bedanken. Ebenfalls bedanke ich mich bei Herrn Prof. Dr.-Ing. Volker Gümmer, der als Prüfungsvorsitzender für einen reibungslosen Ablauf der Promotionsprüfung gesorgt hat.

Ein herzliches Dankeschön geht an meine ehemaligen Lehrstuhlkollegen, die stets für eine angenehme und freundschaftliche Arbeitsatmosphäre gesorgt haben. An die gemeinsame Zeit am Lehrstuhl erinnere ich mich gerne zurück und die enstandenen Freundschaften bleiben hoffentlich lange bestehen. Insbesondere möchte ich mich bei meinen langjährigen Bürokollegen Marco Stuhlpfarrer, Andreas Kümmel, Florian Heckmeier und Jonathan Pflüger für ihre Unterstützung und die konstruktiven Diskussionen bedanken. Ein besonderer Dank geht außerdem an Andreas Hövelmann, Phillip Ohmer, Christopher Reinbold, Stefan Pfnür, Matteo Moioli, Maximilian Gruber und Fabian Sturm für ihr fachliches Feedback und das Korrekturlesen der Arbeit.

Meinen Freunden aus dem Studium möchte ich für die moralische Unterstützung und die vielen Zusprüche während der Promotion danken. Namentlich erwähnen möchte ich hier vor allem Benedikt und Sebastian, die mich bereits seit der Schulzeit begleiten.

Tiefste Dankbarkeit geht an meine Familie, die mich während der gesamten schulischen und universitären Laufbahn bedingungslos unterstützt hat. Meine Eltern Gertraud und Martin, sowie meine Schwester Tanja haben mir immer den Rücken gestärkt und sind stets hinter meinen Entscheidungen gestanden. Meiner Partnerin Angelika möchte ich besonders danken. Ihre Geduld, ihr Verständnis und ihre ständige Ermutigung haben mir die Kraft gegeben, diese Herausforderung zu meistern. Die Fröhlichkeit und das Lachen unseres Sohnes Christoph haben mir in der stressigen Endphase der Promotion geholfen, Energie zu tanken und auf den erfolgreichen Abschluss hinzuarbeiten.

München, Januar 2025 Patrick Pölzlbauer

Abstract

In the present thesis, a blade-sleeve fairing is aerodynamically optimized for the full-fairing rotor head of the RACER compound helicopter. The design optimization is conducted for a steady, sea-level cruise flight with 220 knots. For this purpose, a CFD-based optimization tool chain is developed, which enables automated, aerodynamic design optimization. Steady-state and transient RANS simulations are conducted in the design optimization process. The expansion of the flight envelope towards higher cruising speeds is one of the main challenges the helicopter industry is facing nowadays. In order to tackle this challenge, the implementation of drag-reduction measures is an important topic. One of the main drag sources is given by the rotor head and previous investigations have shown that rotor-head fairings can significantly improve the cruise performance of a high-speed helicopter. However, the integration of a full-fairing rotor head is challenging from several perspectives including mechanical, kinematic and thermal aspects. Therefore, such rotor-head fairings have not been introduced yet on serial-production helicopters and the present work helps to prove the concept for future applications.

In order to keep the computational effort during the design optimization within a reasonable frame, a single, steady rotor blade is considered and a step-wise optimization strategy is employed. The evaluation of drag for a single rotor blade shows that the highest drag values are obtained at the advancing and the retreating blade position. Therefore, these two positions are considered for the aerodynamic design optimization. At first, a two-dimensional shape optimization of selected blade-sleeve sections is conducted, which serves as the basis for subsequent three-dimensional design optimization of the blade-sleeve fairing. Two competing objective functions are applied, which are given by the maximization of the lift-to-drag ratio for the advancing blade case and the minimization of drag for the retreating blade case. Therefore, a robust, multi-objective, genetic optimization algorithm is chosen. The genetic algorithm is computationally expensive, but it offers a robust alternative to conventional, gradient-based algorithms. Furthermore, Latin hypercube sampling is used to define the initial population of candidates. Additionally, design constraints regarding the permissible design space are applied.

Finally, the newly developed blade-sleeve fairing is put to test on the isolated rotor head as well as the full compound-helicopter configuration. The proper cyclic blade-pitch motion is realized by an overset-mesh approach and mesh motion. Moreover, two different full-fairing beanie shapes are analyzed in combination with the optimized blade-sleeve fairing to determine the most promising full-fairing concept in terms of drag reduction. Regarding the isolated rotor-head simulations, the baseline beanie with the optimized blade-sleeve fairing yields a drag reduction of 5 % and a lift increase of 22 % compared to the reference rotor head.

The evaluation of the aerodynamic forces for the full compound-helicopter configuration reveals a drag reduction of 1.4 % in combination with a lift increase of 1.3 %. Hence, an even higher drag-reduction potential can be expected considering an iso-lift condition. Furthermore, the larger full-fairing beanie together with the optimized blade-sleeve fairing provides a drag reduction of 4.1 % at comparable lift. The main achievements of the present work include a versatile, CFD-based optimization tool chain, guidelines for the aerodynamic design optimization of rotor-head fairings and an optimized blade-sleeve fairing, which can be used as a retrofit measure on the new compound-helicopter demonstrator RACER.

Zusammenfassung

Die vorliegende Arbeit beschäftigt sich mit der aerodynamischen Formoptimierung einer Blattanschlussverkleidung für den vollverkleideten Rotorkopf des RACER Compound-Hubschraubers. Die Formoptimierung erfolgt für den stationären Reiseflug in Meereshöhe mit 220 Knoten. Hierfür wird eine CFD-basierte Optimierungskette entwickelt, die eine automatisierte, aerodynamische Formoptimierung ermöglicht. Im Rahmen der Optimierung werden stationäre und instationäre RANS-Simulationen durchgeführt. Die Erweiterung des Flugbereichs zu höheren Geschwindigkeiten ist eine der größten Herausforderungen, denen sich die Hubschrauberindustrie heutzutage stellen muss. Ein wichtiges Thema ist hierbei die Einführung von Maßnahmen zur Widerstandsreduktion, um diese Herausforderung bewältigen zu können. Der Rotorkopf leistet einen großen Beitrag zum Gesamtwiderstand des Hubschraubers und vorherige Untersuchungen haben gezeigt, dass Rotorkopfverkleidungen die Reiseflugleistung eines Hubschraubers erheblich verbessern können. Die Integration eines vollverkleideten Rotorkopfs ist jedoch in vielerlei Hinsicht herausfordernd, da mechanische, kinematische und thermische Aspekte berücksichtigt werden müssen. Aufgrund der hohen Komplexität sind solche Rotorkopfverkleidungen bis heute noch nicht im Einsatz bei Serienhubschraubern. Die vorliegende Arbeit hilft bei der Überprüfung eines solchen Konzepts für zukünftige Anwendungen.

In der aerodynamischen Formoptimierung wird ein einzelnes, stationäres Rotorblatt betrachtet und eine stufenweise Optimierungsstrategie herangezogen. Hierdurch kann der numerische Aufwand in einem vernünftigen Rahmen gehalten werden. Die Auswertung des Widerstandes eines einzelnen Rotorblattes in Abhängigkeit der Rotorblattposition zeigt, dass der höchste Widerstand für das vor- und das rücklaufende Blatt erreicht wird. Aus diesem Grund erfolgt die aerodynamische Formoptimierung der Blattanschlussverkleidung für diese beiden Rotorblattpositionen. Im ersten Schritt wird eine zweidimensionale Formoptimierung ausgewählter Blattanschlusssektionen durchgeführt. Diese Profile dienen anschließend als Grundlage für die dreidimensionale Formoptimierung der Blattanschlussverkleidung. Es werden zwei unterschiedliche Zielfunktionen für das vor- und das rücklaufende Rotorblatt angewendet. Für das vorlaufende Rotorblatt wird das Verhältnis von Auftrieb zu Widerstand maximiert und für das rücklaufende Rotorblatt wird der Widerstand minimiert. Aus diesem Grund kommt ein robuster, genetischer Mehrziel-Optimierungsalgorithmus zum Einsatz. Der genetische Algorithmus ist zwar sehr rechenintensiv, er bietet jedoch eine robuste Alternative zu herkömmlichen, gradientenbasierten Algorithmen. Latin Hypercube Sampling wird verwendet, um die erste Generation an Kandidaten zu erzeugen. Zusätzlich berücksichtigt die Opimierung Randbedingungen hinsichtlich des zulässigen Bauraums.

Die neu entwickelte Blattanschlussverkleidung wird schließlich am isolierten Rotorkopf und auf dem Compound-Hubschrauber selbst getestet. Die zyklische Blattverstellung wird durch einen Overset-Mesh-Ansatz und Mesh-Motion realisiert.

Die optimierte Blattanschlussverkleidung wird mit zwei unterschiedlichen Rotorkopfhauben untersucht, um die vielversprechendste Rotorkopfverkleidung hinsichtlich Widerstandsreduktion zu ermitteln. Die Strömungssimulationen für den isolierten Rotorkopf mit der Basis-Rotorkopfhaube und der optimierten Blattanschlussverkleidung zeigen eine Widerstandsreduktion von 5 % und eine Auftriebserhöhung von 22 % im Vergleich zum Referenzrotorkopf. Die Auswertung der Kräfte des Compound-Hubschraubers liefert eine Widerstandsreduktion von 1.4 % zusammen mit einer Auftriebserhöhung von 1.3 %. Bei vergleichbarem Auftrieb kann somit noch eine weitere Reduktion des Widerstandes erwartet werden. Außerdem bietet die Rotorkopfverkleidung mit der größeren Rotorkopfhaube und der optimierten Blattanschlussverkleidung eine höhere Widerstandsreduktion von 4.1 % bei vergleichbarem Auftrieb. Die wichtigsten Ergebnisse der vorliegenden Arbeit beinhalten eine vielseitige, CFD-basierte Optimierungskette, Richtlinien für die aerodynamische Formoptimierung von Rotorkopfverkleidungen und eine optimierte Blattanschlussverkleidung, die auf dem neuen Compound-Hubschrauber RACER nachgerüstet werden kann.

Contents

List of Figures

List of Tables

Nomenclature

Latin Symbols

a	Speed of sound	m/s
A	Rotor-disk area	m^2
$\vec{A}$	Surface-area vector	m^2
$\vec{A}_f$	Area vector of a cell face	m^2
$b_{i,n}(t)$	Bernstein basis polynomial of the degree n	$-$
$B(t)$	Beziér curve	$-$
c	Chord length	m
c_i	Cell center of cell i	$-$
C_d	Drag coefficient (2D)	$-$
C_D	Drag coefficient (3D)	$-$
C_f	Skin-friction coefficient	$-$
C_{fx}	Axial skin-friction coefficient	$-$
C_l	Lift coefficient (2D)	$-$
C_L	Lift coefficient (3D)	$-$
C_p	Pressure coefficient	$-$
d	Diameter	m
d_{FFB}	Diameter of the full-fairing beanie	m
$d[i,j]$	Distance between the individuals i and j	m
$d\vec{S}$	Local normal vector of the control-volume boundary	m^2
d_{UP}	Euclidean distance to the utopia point	m
D	Diameter	m
D	Drag	N
D_ω	Cross-diffusion term	kg/m^3s^2
E	Specific internal energy	m^2/s^2
f	Vortex-shedding frequency or frequency	$1/s$
$f_i(\mathbf{x})$	Objective function	$-$
F_x, F_y, F_z	Force components in the respective coordinate system	N
F_{xj}	Target cumulative distribution function (LHS)	$-$
$g_i(\mathbf{x})$	Inequality constraint	$-$
G_k	Production of turbulent kinetic energy k	kg/ms^3
G_ω	Generation of specific dissipation rate	kg/m^3s^2
$h_i(\mathbf{x})$	Equality constraint	$-$
H	Specific enthalpy	m^2/s^2
k	Wave number	$-$
k	Turbulent kinetic energy	m^2/s^2
K	Number of input variables (LHS)	$-$
l	Characteristic length scale	m

L	Lift	N
L	Characteristic length scale	m
L_c	Chord length	m
$\dot{m}$	Mass flow	kg/s
m_i	Niche count	$-$
M	Mach number	$-$
M_{tip}	Mach number at the rotor-blade tip	$-$
$M^*_{90^\circ}$	Mach number at the blade tip of the advancing rotor blade	$-$
M_x, M_y, M_z	Moment components in the respective coordinate system	Nm
$\vec{n}$	Face-normal vector	$-$
n_D	Number of designs dominating the current design	$-$
n_{pop}	Size of the population	$-$
n_{rotor}	Rotor speed	$1/min$
N	Number of realizations (LHS)	$-$
N_{faces}	Number of cell faces	$-$
$\mathbf{P}$	Permutation matrix (LHS)	$-$
P_i	Coordinates of the control point i	m
Q	Q-criterion	$1/s^2$
r	Non-dimensional radial position on the rotor blade	$-$
$\vec{r}$	Distance vector	m
R	Rotor radius	m
$\mathbf{R}$	Matrix containing independent random numbers (LHS)	$-$
Re	Reynolds number	$-$
Re_m	Reynolds number per meter	$1/m$
S	Control-volume boundary	m^2
S	Strain-rate magnitude	$1/s$
$\mathbf{S}$	Matrix containing the basic sampling plan for LHS	$-$
$Sh(d)$	Sharing function	$-$
S_φ	Source of an arbitrary quantity φ per unit volume	$1/m^3$
$\mathbf{S_{ij}}$	Mean shear-rate tensor	$1/s$
S_k	User-defined source term for turbulent kinetic energy k	kg/ms^3
S_ω	User-defined source term for specific turbulence dissipation rate ω	kg/m^3s^2
St	Strouhal number	$-$
t	Time	s
t	Local coordinate of a curve segment	$-$
t_{ave}	Time-averaging interval used to derive mean quantities	s
t_{sim}	Total simulation time	s
t^*	Fictious pseudo time	$-$
Δt	Time-step size	s

T	Thrust	N
T	Temperature	K
Tu	Turbulence intensity	$-$
u, v, w	Velocity components	m/s
$\bar{u}, \bar{v}, \bar{w}$	Mean (time-averaged) velocity components	m/s
$u^{'}, v^{'}, w^{'}$	Velocity fluctuation components	m/s
U	Flow velocity	m/s
v_i	Induced flow velocity	m/s
$\vec{V}$	Velocity vector	m/s
V	Volume of a computational cell	m^3
V_t	Tangential velocity component	m/s
V_{tip}	Flow velocity at the blade tip	m/s
V_r	Radial velocity component	m/s
V_∞	Free-stream velocity	m/s
V_x, V_y, V_z	Velocity components	m/s
x, y, z	Component of the respective coordinate direction	m
$\mathbf{x}$	Vector of design variables	$-$
x_{TR}	Lever arm of the tail rotor	m
y	Wall distance	m
y^+	Dimensionless wall distance	$-$
Y_k	Dissipation of turbulent kinetic energy k due to turbulence	kg/ms^3
Y_ω	Dissipation of the spec. turbulence dissipation rate ω due to turbulence	kg/m^3s^2
$\mathbf{z}$	Vector of objective functions	$-$

Greek Symbols

α	Angle of attack	$^\circ$
α^*	Damping factor acting as a low-Reynolds number correction for the turbulent viscosity	$-$
β	Angle of sideslip	$^\circ$
γ	Ratio of specific heats	$-$
Γ_k	Effective diffusivity of the turbulent kinetic energy k	kg/ms
Γ_φ	Diffusion coefficient for the arbitrary quantity φ	$-$
Γ_ω	Effective diffusivity of the specific turb. dissipation rate ω	kg/ms
δ_{ij}	Kronecker-Delta	$-$
ε	Turbulence dissipation rate	m^2/s^3
ε	Characteristic surface roughness	m
θ	Pitch angle of the rotor blade	$^\circ$
$\dot{\theta}$	Pitch velocity of the rotor blade	$^\circ/s$

θ_0	Collective pitch input	$^\circ$
θ_{1c}	Lateral cyclic blade-pitch input	$^\circ$
θ_{1s}	Longitudinal cyclic blade-pitch input	$^\circ$
θ_{nc}	Higher harmonics of the lateral cyclic blade-pitch input	$^\circ$
θ_{ns}	Higher harmonics of the longitudinal cyclic blade-pitch input	$^\circ$
θ_{tw}	Twist of the rotor blade due to elastic deformation	$^\circ$
θ_{total}	Total pitch angle of the rotor blade	$^\circ$
κ_l	Laminar thermal conductivity	kgm/Ks^3
μ	Advance ratio	$-$
μ	Dynamic viscosity	kg/ms
ν	Kinematic viscosity	m^2/s
ν_t	Eddy viscosity	m^2/s
ρ	Density	kg/m^3
σ_{share}	Niche radius	m
τ_{ij}	Reynolds-stress tensor	kg/ms^2
φ	Arbitrary scalar quantity	$-$
φ_f	Value of an arbitrary quantity φ convected through face f	$-$
Ψ	Azimuthal rotor position	$^\circ$
ω	Angular velocity	rad/s
ω	Specific turbulence dissipation rate	$1/s$
ω_x	Axial vorticity	$1/s$

Subscripts

Adv	Advancing rotor blade
BSF	Blade-sleeve fairing
FFB	Full-fairing beanie
Ret	Retreating rotor blade
TR	Tail rotor
$mean$	Averaged quantity
nb	Neighboring cell
∞	Free-stream value

Acronyms and Abbreviations

ABC	Advancing Blade Concept
ADHeRo	Aerodynamic Design Optimisation of a Helicopter Fuselage including a Rotating Rotor Head
AER	Chair of Aerodynamics and Fluid Mechanics
AHF	Airbus Helicopters France
AMG	Algebraic Multigrid

AoA	Angle of Attack
AUSM	Advection Upstream Splitting Method
BERP	British Experimental Rotor Programme
BPF	Blade-Passing Frequency
BSF	Blade-Sleeve Fairing
BSL	Baseline
BVI	Blade Vortex Interaction
CAD	Computer Aided Design
CARD	Contribution to Analysis of Rotor-hub Drag reduction
CEAS	Council of European Aeropace Societies
CFD	Computational Fluid Dynamics
CFL	Courant-Friedrichs-Lewy
DAKOTA	Design Analysis Kit for Optimization and Terascale Applications
DES	Detached Eddy Simulation
DLR	Deutsches Zentrum für Luft- und Raumfahrt
DNS	Direct Numerical Simulation
EMS	Emergency Medical Service
FAI	Fédération Aéronautique Internationale
FFB	Full-Fairing Beanie
FFT	Fast Fourier Transformation
FRC	Fast Rotorcraft
FURADO	Full-Fairing Rotor Head Aerodynamic Design Optimization
FVM	Finite Volume Method
GA	Genetic Algorithm
GOAHEAD	Generation of Advanced Helicopter Experimental Aerodynamic Database for CFD code validation
HEMS	Helicopter Emergency Medical Service
HPC	High-Performance Computer/Computing
HPER	Hub Pylon Evaluation Rig
IADP	Innovative Aircraft Demonstrator Platform
ICAO	International Civil Aviation Organization
LES	Large Eddy Simulation
LHS	Latin Hypercube Sampling
LRZ	Leibniz Supercomputing Centre
LU-SGS	Lower-Upper Symmetric Gauss-Seidel
MOGA	Multi-Objective Genetic Algorithm
MRP	Moment Reference Point
MTOW	Maximum Take-Off Weight
NASA	National Aeronautics and Space Administration
PIV	Particle Image Velocimetry

RACER	Rapid And Cost-Effective Rotorcraft
RANS	Reynolds-averaged Navier-Stokes
RB	Rotor Blade
RH	Rotor Head
SAR	Search And Rescue
SIMPLE	Semi-Implicit Method for Pressure Linked Equations
SIMPLEC	Semi-Implicit Method for Pressure Linked Equations-Consistent
SME	Small and Medium-Sized Enterprise
SST	Shear-Stress Transport
STEP	Standard for the Exchange of Product Model Data
TCL	Tool Command Language
TEL	Twin-Engine Light
TUM	Technical University of Munich
TUM-AER	Chair of Aerodynamics and Fluid Mechanics of the Technical University of Munich
UDF	User-Defined Function
UP	Utopia Point
URANS	Unsteady Reynolds-averaged Navier-Stokes
VTOL	Vertical Take-Off and Landing

1 Introduction

1.1 Motivation

An almost seamless door-to-door mobility represents a valuable privilege of nowadays society. The mobility is reached by a combination of different transportation means including public and private vehicles with the corresponding infrastructures. One of the main transportation sectors is represented by the aviation industry. The growing demand for air travel is reflected by Fig. 1.1 giving an overview on the worldwide air passenger numbers from 2000 to 2018. The number of transported passengers has increased by 160 % within this time frame.

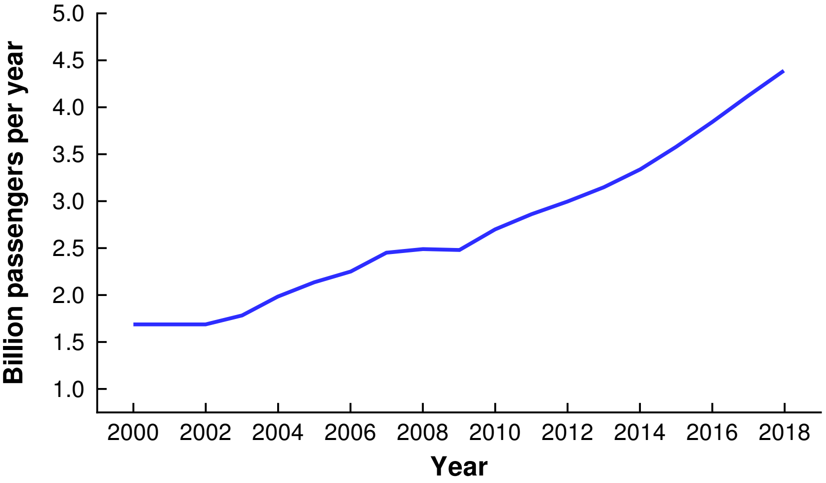

Figure 1.1: Total number of passengers transported by aircraft per year [1].

Consequently, the growing population and the increased demand for traveling lead to increased emissions. The most relevant emissions, which contribute to radiative forcing of climate, are given by carbon dioxide (CO_2), nitrogen oxides (NO_x) and aerosols. In order to reduce the environmental impact of aircraft, the development of environmentally friendly aircraft is a major topic. For this purpose, Europe has defined ambitious goals for future air transportation concepts within the framework of Horizon 2020 [26] and FlightPath 2050 [27]. Compared to aircraft available in the year 2000, a reduction of 75 % of CO_2 and 90 % of NO_x is targeted until 2050. Additionally, the perceived noise level of aircraft should be decreased by 65 %. In order to fulfill these requirements, a successive improvement of the aircraft performance has to be pursued. Therefore, the key properties of future vehicles comprise aerodynamically optimized shapes (e.g. fuselage, wing, empennage), enhanced engines and advanced light-weight structural design. Today, certain vehicles are dedicated to specific mission scenarios and they are optimized for their application purpose. Two major fields in aviation industry are represented by airplanes and rotorcraft. Airplanes provide high payload capacity for long-haul flights, at high speed and high altitude.

However, they require a large ground infrastructure including runways and taxiways. In contrast, helicopters are applied for short-haul travels and they are capable of vertical takeoff and landing (VTOL). This reduces the complexity in terms of ground infrastructure and enables the application in remote areas. The biggest drawback of conventional helicopters is that they do not achieve the cruise speed, payload and range of fixed-wing aircraft. Typical helicopter mission scenarios are given by Helicopter Emergency Medical Service (HEMS), Search And Rescue (SAR), logistic support on remote sites (e.g. offshore platforms) and parapublic missions. All of these scenarios have in common that time is a critical factor, which demands for high-speed helicopters. Therefore, the development of future helicopters is subject to the reduction of the environmental impact on the one hand and the expansion of the flight envelope towards higher cruising speeds on the other hand. At the current stage, conventional helicopter configurations have reached a limit in terms of speed, range and endurance. Besides the available power of the helicopter, there are two main reasons for the speed limitation, which are given by transonic effects on the advancing rotor blade and the retreating blade stall. During high-speed flight, reversed flow occurs in the blade root region of the retreating rotor blade. Additionally, high local angles of attack are applied to compensate the dynamic pressure deficit compared to the advancing rotor blade. If a certain angle of attack is exceeded, rotor-blade stall may occur. Moreover, if the retreating rotor blade does not generate sufficient lift, a significant lift asymmetry can be present on the rotor disk, which induces a roll moment [28]. In order to be able to tackle the physical speed limitation related to the rotor aerodynamics, an innovative rotor-blade shape is required, or the conceptual design of the entire rotorcraft must be changed.

There are several promising high-speed rotorcraft concepts available nowadays and by example, four of them are illustrated in Fig. 1.2. Figure 1.2a shows the Westland Lynx, which still holds the official speed record of the Fédération Aéronautique Internationale (FAI) for conventional helicopters reaching a forward flight speed of 216 knots. This record was achieved during a demonstration program in 1986. For this pupose, the helicopter was equipped with an advanced rotor blade, which was developed during the third phase of the British Experimental Rotor Programme (BERP III). The rotor blade features a unique blade-tip design, distributed cambered airfoils and a non-linear twist distribution providing high-speed capability [29]. The Sikorsky X2 is depicted in Fig. 1.2b and it features a coaxial rotor with thrust compounding. The X2 configuration uses the advancing blade concept (ABC) rotor system [30] to unload the retreating rotor blade at high cruise speeds. By using the ABC concept, the retreating blade stall can be avoided [31]. Moreover, the lateral rotor delivers additional thrust enabling the helicopter to reach a cruise speed of 250 knots. Figure 1.2c shows the X^3 demonstrator, which was developed by Eurocopter and had its first flight in September 2010 [32]. The X^3 demonstrator uses wing compounding to unload the main rotor and two lateral rotors at the wing tips to deliver thrust during forward flight.

Due to the additional lift generated by the wings during cruise flight, the rotational speed of the main rotor can be reduced, which avoids transonic effects at the advancing rotor blade. The X^3 compound helicopter reached a cruise speed of 255 knots in a steady horizontal flight. Hence, both, the Sikorsky X2 and the Eurocopter X^3, unofficially broke the FAI speed record of the Westland Lynx. Another concept applied for high-speed rotorcraft is the tiltrotor, which is illustrated in Fig. 1.2d showing the V-22 Osprey as a prominent example. The V-22 configuration has two large rotors mounted at the wing tips, which can be turned into a vertical and a horizontal position. Therefore, it provides vertical take-off and landing capabilities and it can be transformed into a turboprop aircraft for cruise flight. For this purpose, the rotors are gradually tilted forward in a transition phase. The tiltrotor concept makes the Bell-Boeing V-22 a multi-mission aircraft reaching a cruise speed of 270 knots.

(a) Westland Lynx (216 kts) [33].

(b) Sikorsky X2 (250 kts) [34].

(c) Eurocopter X^3 (255 kts) [35].

(d) Bell-Boeing V-22 (270 kts) [36, 37].

Figure 1.2: Overview of typical high-speed rotorcraft concepts.

Within the European Clean Sky 2 research initiative [38], the cruise-speed limitation is addressed by the Fast Rotorcraft Innovative Aircraft Demonstrator Platforms (FRC-IADP). As part of the FRC-IADP, an innovative compound helicopter, namely the Rapid And Cost-Effective Rotorcraft (RACER), is developed [4]. The RACER is based on the idea and the knowledge gained through the X^3 demonstration program, see Fig. 1.2c.

Hence, it combines the beneficial characteristics of fixed-wing aircraft and rotorcraft by enabling fast and efficient forward flight as well as vertical take-off and landing. Due to the high cruise speed, aerodynamic efficiency is a major challenge during the development of such high-speed helicopters. The basic fuselage and the rotor head of a helicopter represent the main drag sources, which has been indicated by several drag breakdown studies [3, 39, 40]. The importance of aerodynamic design optimization with respect to drag reduction is reflected by high research effort that has been put into this topic within the last decades, see Sec. 1.2. Depending on the weight class and the cruise speed of the helicopter, the rotor head roughly contributes between 25 and 40 percent of the total parasite drag. Previous investigations have revealed that the application of a rotor-head fairing can be promising in terms of rotor-head drag reduction [41–43]. Nowadays, full-fairing concepts are not applied on production type machines and they are still subject to current research. The present work is based on the results obtained during the FURADO project [44], which deals with the aerodynamic design optimization of a semi-watertight full-fairing rotor head with respect to drag reduction of the RACER compound helicopter [11, 44, 45]. A detailed description about the analyzed RACER configuration is given in Sec. 1.3 of the thesis. The full-fairing components are successively optimized by means of numerical flow simulations. Moreover, the impact of the newly developed fairing on the overall performance of the RACER demonstrator is evaluated. This work contributes to advance the maturity of full-fairing concepts for future helicopter designs and the results are of great value for the helicopter industry. The research findings support new solutions for efficient vehicles with positive impact on speed, fuel consumption, noise and emission.

1.2 State of the Art

In this section of the thesis, the research effort that has been put into helicopter drag reduction for the last 70 years is reflected. In the early stage of helicopter development, the focus of the engineers was mainly on flight mechanics, the design of the controls and the rotating components. The most critical topics were related to vibration, stability and adequate hover performance. Therefore, almost no attention was paid to the aerodynamic efficiency of the non-rotating helicopter parts [40]. In the early 1950s the potential benefits of helicopter parasite drag reduction were estimated by Harrington [46]. He stated that parasite drag reduction is possible but not necessarily profitable for all helicopter missions. It becomes more relevant for high-speed and long-range applications. The purpose of his work was to indicate the order of magnitude of possible drag-reduction benefits and to determine the main parasite-drag contributors for typical helicopters in use at that time. Moreover, Harrington mentioned that increased parasite drag can be acceptable for low-speed helicopters allowing for simple design and fabrication, which compensates the drag penalty.

Between 1959 and 1962, the NASA Langley wind tunnels were used for parasite-drag measurements of several helicopter configurations [47–49]. These investigations dealt with drag and stability characteristics of different helicopter fuselage models and the influence of the rotor hub on the overall performance of the helicopter. It was demonstrated that streamlining the fuselage through advanced design and faired landing skids can lead to a parasite drag reduction of 60 % for small helicopters. Regarding the rotor hub measurements, the obtained results indicated that the angle of attack, the hub rotational speed and the forward flight speed had only a minor impact on the equivalent flat plate area representing parasite drag. Brown and Drees [50] analyzed the need for increasing the maximum continuous cruise speeds of conventional helicopters in 1960. They studied the variation of the productivity with the design cruise speed. At this time they claimed that the maximum productivity of a transport helicopter is reached at a cruise speed of about 150 knots.

In the seventies, the oil crisis steamed up the research and development efforts spent on the analysis of helicopter parasite drag. Therefore, the evaluation of cost benefits related to drag reduction became more and more important. Duhon [51] mentioned that the influence of potential drag-reduction measures on empty weight, cost to manufacture, maintenance and operating costs must be taken into account during the helicopter development. Furthermore, the impact of reduced parasite drag on the fuel costs of a civil and a military helicopter fleet was reviewed by Rabbott and Stroub [52]. According to Williams and Montana [53], the parasite-drag level of a helicopter was six to ten times higher than for a fixed-wing aircraft at this time. Hence, the reduced cruise efficiency of the helicopter substantially degraded its mission capability and a comprehensive research and development plan was required to solve this problem. Therefore, several helicopter drag-reduction programs were set up during this time, see for example [53] and [42]. It was concluded that a drag reduction of 75 % could be reasonable for a heavy helicopter by the full implementation of technically mature designs. Furthermore, drag-reduction guidelines were defined for fuselage components, such as cabin, nose section, hub, landing gear and protuberances. The cruise speed of the helicopter has successively increased over time due to more engine power and enhanced rotor performance. With increasing speed, the parasite drag began to dominate the picture even more. The fuselage and the rotor hub represent the major parasite drag sources and therefore, a significant research effort has been put into the performance improvement of these components within the last decades.

The present work deals with the aerodynamic design optimization of rotor-hub fairings for the RACER compound helicopter. Nevertheless, the most relevant findings and achievements related to helicopter fuselage drag reduction are presented in this thesis, in order to complement the research efforts spent on low-drag helicopter design.

A typical utility helicopter fuselage features a complex bluff-body flow separation in the rear part, which is mainly related to the required backdoor-loading capability. It is important to correctly predict the nature of the flow separation in this region, because the drag significantly changes with the type of flow (e.g. vortex flow, eddy flow), which was demonstrated by Seddon [54]. Furthermore, Seddon determined the influence of the backdoor upsweep angle, the lateral tapering and the flight incidence angle on the fuselage drag. Comprehensive experimental and numerical investigations were conducted for different types of helicopters to better understand the flow around helicopter fuselages and to improve and validate numerical methods.

Within the ADHeRo (Aerodynamic Design Optimisation of a Helicopter Fuselage including a Rotating Rotor Head) project, numerous wind-tunnel experiments were performed for a twin-engine light utility helicopter including the measurements of forces, moments and surface pressure. Moreover, the wake-flow field was visualized by stereo particle image velocimetry (PIV). Figure 1.3a shows the ADHeRo model mounted in wind tunnel A of the Chair of Aerodynamics and Fluid Mechanics of the Technical University of Munich (TUM-AER). The experimental investigations were complemented by numerical flow simulations, see Fig. 1.3b. The work was focused on improving the aerodynamic design of the skid-landing gear and the fuselage in order to reduce the helicopter's parasite drag without significantly increasing the downforce, see Refs. [39,55–59] for more details.

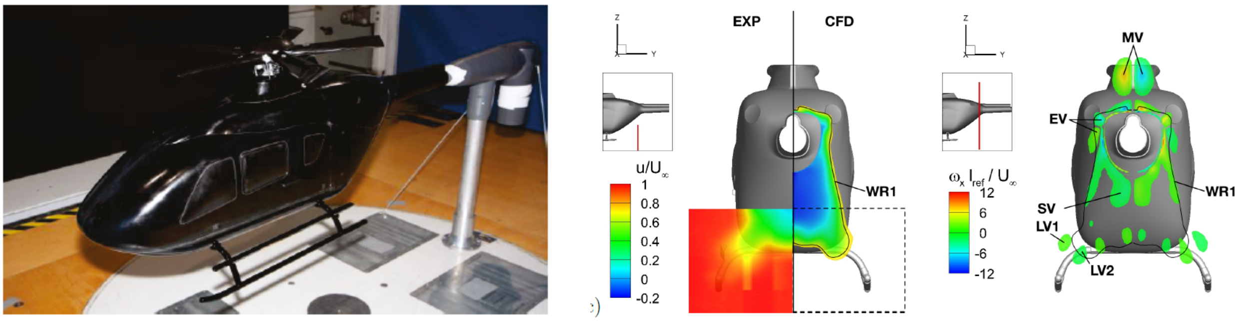

(a) ADHeRo wind-tunnel model mounted in wind tunnel A of TUM-AER [58].

(b) Comparison between experiment and CFD [59].

Figure 1.3: Experimental and numerical investigations performed within the ADHeRo project.

The European project GOAHEAD (Generation of Advanced Helicopter Experimental Aerodynamic Database for CFD code validation) dealt with the numerical and experimental investigation of a heavy transport helicopter, which is based on the NH90. A highly instrumented and very detailed wind-tunnel model was designed, which can be seen in Fig. 1.4a. GOHAED was initiated in 2005 by 15 partners including five national research centers, five universities and four helicopter manufacturers. A detailed description about the project is given by Pahlke [60].

The main objectives of this project were to improve the aerodynamic prediction capability regarding complete helicopter configurations, to create an experimental database for CFD-code validation and to establish best practice guidelines for numerical investigations of viscous flow around helicopters. In the first two years of the project, blind-test CFD activities were performed to assess state-of-the-art helicopter CFD codes used in Europe [61, 62]. Furthermore, Zhang et al. [63, 64] developed an adjoint-based optimization method for the fuselage backdoor geometry of a helicopter, which was applied to aerodynamically improve the GOAHEAD configuration. An overview of selected GOAHEAD project results is given by Schwarz and Pahlke [65]. Figure 1.4 shows the highly detailed GOAHEAD wind-tunnel model and exemplary results of the CFD blind-test activities.

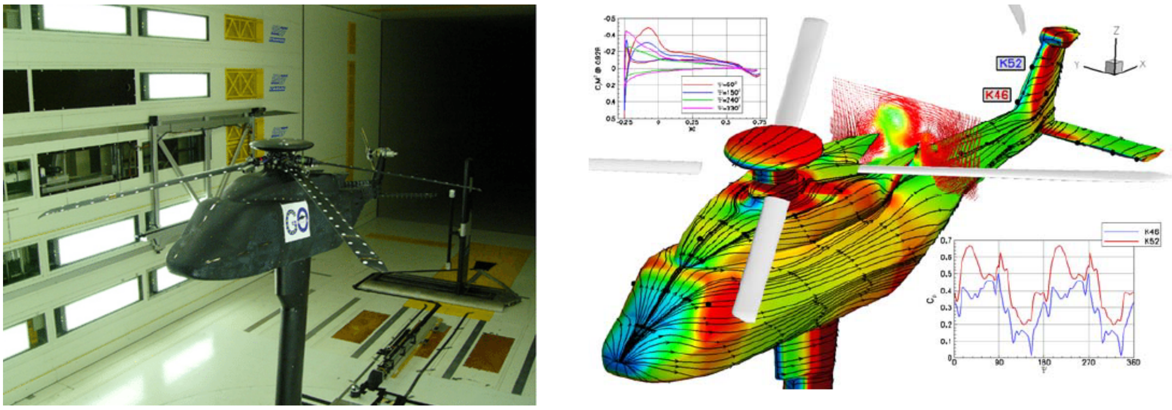

(a) GOAHEAD wind-tunnel model [65].

(b) Blind-test CFD activities [62].

Figure 1.4: Generation of an aerodynamic database for a heavy transport helicopter within the European project GOAHEAD.

Due to the fact that wind-tunnel measurements and flight testing are expensive as well as time consuming, numerical flow simulation has become an important tool for the aerodynamic design and performance evaluation of present and future rotorcraft, see Fig. 1.5. Several authors helped to introduce CFD to the industrial environment. In order to improve the numerical methods used for helicopter development, different flow solvers and aeromechanic tools have been compared to each other and validated against wind-tunnel measurements. Some examples for the industrial application of numerical flow simulation regarding the aerodynamic performance prediction of different helicopter configurations are given in Refs. [66–72].

In addition to the aerodynamic design optimization of the helicopter fuselage shape, passive and active flow control have been identified to effectively reduce drag. Boniface et al. [73] investigated different shapes and arrangements of vortex generators on a GOAHEAD-like fuselage, which can be seen in Fig. 1.6a. Promising vortex generator configurations reached a maximum drag reduction of 5 % in cruise flight, which is related to flow reattachment and static pressure recovery.

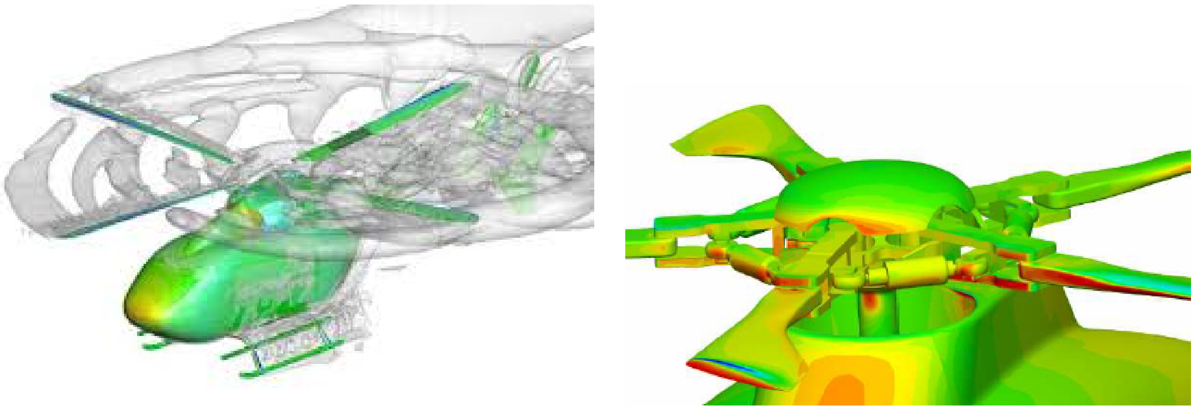

(a) Flow field of a complete helicopter configuration [67].

(b) Pressure distribution on a rotating rotor head [68].

Figure 1.5: Industrial application of numerical flow simulation for helicopter development.

Concerning active flow control, the pressure drag at the upswept ramp region of the helicopter can be decreased by momentum injection through slots in the fuselage shell, which is illustrated in Fig. 1.6b. This configuration was investigated by Martin et al. [74] and they achieved a drag reduction of 10 % by means of zero-net-mass-flux synthetic jet actuators located in the backdoor region. Similar investigations about the application of active flow control for helicopter drag reduction were conducted by several authors, see for example in Refs. [75–79].

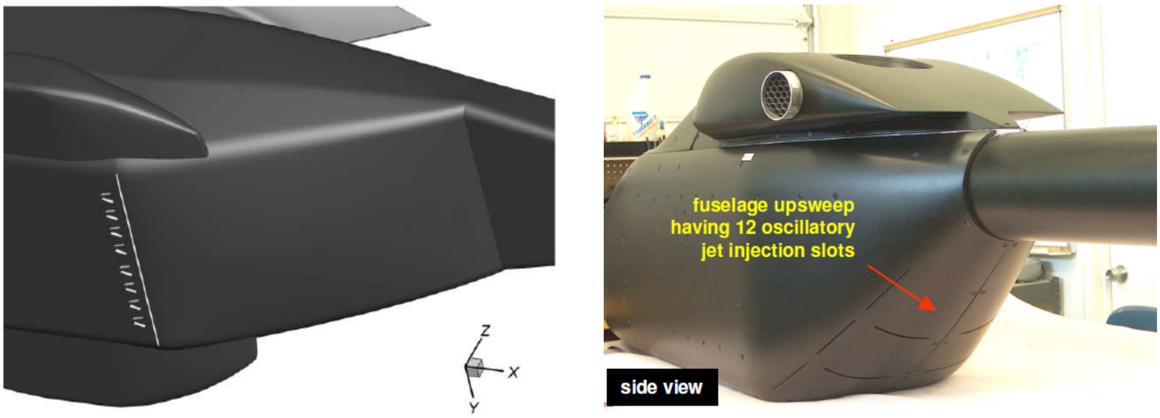

(a) Passive flow control by vortex generators [73].

(b) Active flow control by zero-net-mass-flux synthetic jet actuators [74].

Figure 1.6: Helicopter drag reduction by means of passive and active flow control.

Besides the helicopter fuselage, the rotor head represents a major parasite drag source. A general review on helicopter rotor hub drag data and methods for predicting hub drag were given by Sheehy [2, 80]. Figure 1.7 shows a summary of rotor hub drag trends depending on the helicopter gross weight and the complexity of the hub configuration, which can either be articulated, hingeless or faired.

It can be observed that the hub incremental drag can be reduced by approximately 70 % from an articulated rotor to a clean, faired hub. Moreover, Sheehy summarized the parameters having the main influence on rotor hub drag, which are for example given by the hub swept frontal area, the position of the hub on the pylon, the pylon shape, the Mach and Reynolds number, the fairing/pylon incidence, the fairing thickness to diameter ratio and the fairing/pylon aerodynamic seal [2].

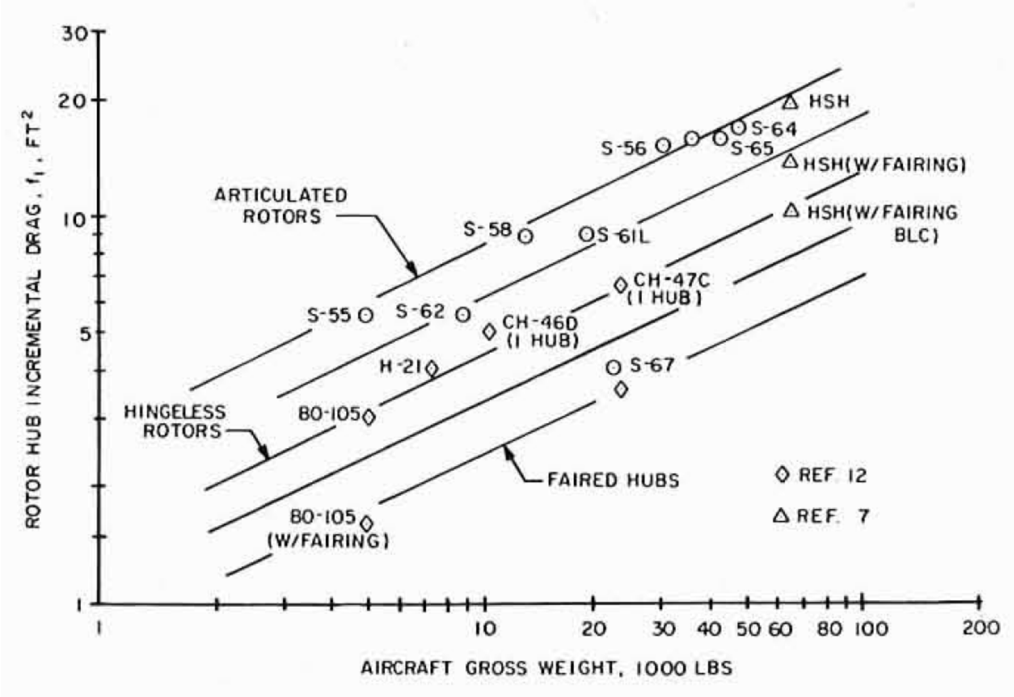

Figure 1.7: Incremental rotor-hub drag depending on the gross weight [2].

Montana performed wind-tunnel tests of different hub-fairing shapes and hub-pylon configurations [81, 82]. For this purpose he used the hub-pylon evaluation rig (HPER), which offered a facility for wind-tunnel experiments on large-scale helicopter rotor hub-pylon configurations. Several hub and shaft fairings were tested for different shaft angles and angles of attack using the HPER. Additional wind-tunnel tests aiming at hub- and pylon-fairing drag reduction were conducted at the NASA Ames Research Center [43, 83–87]. The tested configurations included cambered elliptical hub fairings, different shaft fairings and strakes applied on a single- and a coaxial-rotor helicopter. Furthermore, the hub/pylon interference drag was evaluated and the effect of the clearance between these fairings was determined. A comprehensive review of the research performed on rotor-hub drag and wake physics between 1954 and 2014 was given by Reich et al. [88].

Within the European Clean Sky project CARD (Contribution to Analysis of Rotor-hub Drag reduction), the influence of advanced rotor-head and pylon-fairing designs on the overall drag of an Airbus Helicopters H155 was determined. For this purpose, wind-tunnel tests and numerical flow simulations were performed [89]. The numerical flow simulations revealed that the implementation of the best fairing combination could lead to a drag reduction of 9.7 % of the baseline drag.

Today, aerodynamic drag reduction is still a major topic during the helicopter development. The main objectives are to reduce the environmental impact, to lower the operating costs and to expand the flight envelope towards higher cruising speeds. In order to identify the main drag sources of a state-of-the-art helicopter, the drag breakdown of an AS365-N3 "Dauphin" is examined in Fig. 1.8. The AS365-N3 represents a conventional, medium weight-class helicopter in operation today. The presented results were obtained by Desvigne and Alfano using unsteady numerical flow simulations to determine the influence of the complexification of the rotor-head geometry on the overall drag of the helicopter [3]. Figure 1.8a gives an overview on the components of the investigated helicopter and Fig. 1.8b shows the corresponding drag contribution. Additionally, the rotor head interference drag is illustrated in Fig. 1.8b. The main drag sources are given by the fuselage (28 %) and the rotor head (41 %). A significant part of the rotor-head drag can be related to the blade sleeves, the blade roots and the hub region.

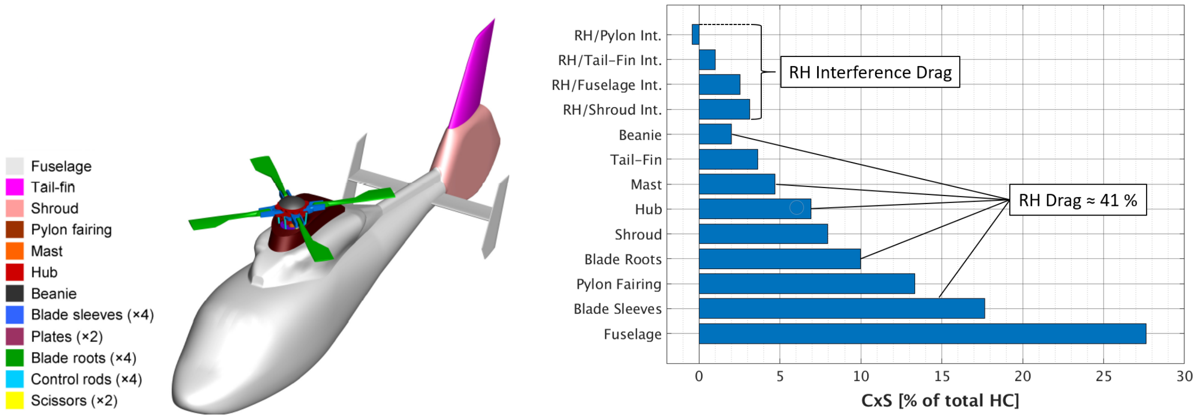

(a) Definition of the helicopter components.

(b) Mean-drag breakdown obtained by numerical flow simulation.

Figure 1.8: Aerodynamic drag analysis for an AS365-N3 Dauphin using CFD simulation [3].

1.3 Analyzed Compound Helicopter Configuration

This section introduces the RACER (Rapid And Cost-Effective Rotorcraft) compound helicopter, which is addressed within the present thesis. The RACER high-speed demonstrator is developed within the Clean Sky 2 research initiative, under the lead of Airbus Helicopters and together with industrial and academic partners. The RACER concept is based on the knowledge and experience gained through the X^3 program, which validated the feasibility of the compound helicopter design. Figure 1.9 gives an overview on the RACER demonstrator allowing to identify its main features.

Figure 1.9: Rapid And Cost-Effective Rotorcraft (RACER) [4].

The key objectives for this new compound helicopter are 50 % higher cruise speed and 25 % cost reduction per nautical mile compared to conventional helicopters. The targeted sea-level cruise speed is 220 knots. Furthermore, aeroacoustic investigations are performed to ensure a low-noise footprint. In terms of maximum take-off weight (MTOW), the RACER demonstrator is a medium weight-class helicopter, which is comparable to the Airbus Helicopters H160 and H175. It has a low-drag fuselage, which is optimized for Emergency Medical Service (EMS), Search And Rescue (SAR), transport and parapublic missions. Furthermore, the innovative box-wing design realizes an optimal interdisciplinary synergy between structure, system integration and aeromechanics. Two lateral rotors are placed behind the joined wings providing high safety characteristics regarding passenger transport and winch operation. The lateral rotors deliver thrust during cruise flight, generate anti-torque and enable yaw-control in hover. Additionally, the noise exposure in the cabin is decreased by this arrangement compared to forward looking lateral rotors. The stabilizers in H-type architecture provide pitch and yaw stability during cruise flight and reduce the structural excitation caused by the rotor wake flow. Moreover, a retractable landing gear is implemented, which is favorable in terms of parasite drag.

The asymmetric tailboom is optimized for better hover performance using the downwash of the main rotor to generate anti-torque. The vertical take-off and landing capability is achieved by a conventional, five-bladed main rotor. In cruise flight, the wings provide a significant portion of the lift and the main rotor can be unloaded. For this purpose, the rotational speed of the main rotor is decreased and the pitch angles are adapted accordingly. Hence, the retreating-blade stall as well as transonic effects on the advancing rotor blade can be avoided and high-speed flight becomes realizable [90].

In order to reduce the overall drag of the RACER demonstrator in cruise flight, aerodynamically optimized rotor head fairings are applied. Figure 1.10 shows the comparison between an Airbus Helicopters H175 rotor head without fairings and the RACER full fairing configuration. The main components of the RACER full-fairing concept are illustrated in Fig. 1.10b consisting of the blade-sleeve fairing, the full-fairing beanie and the pylon fairing. Within the present work, an aerodynamic design optimization is performed for the RACER blade-sleeve fairing considering a sea-level cruise flight with 220 knots. Furthermore, different full-fairing beanie shapes are examined in combination with the optimized blade-sleeve fairing. Finally, the best fairing combination is put to the test on the full RACER configuration and compared to an Airbus Helicopters reference rotor head to determine the performance benefit of the newly developed fairing.

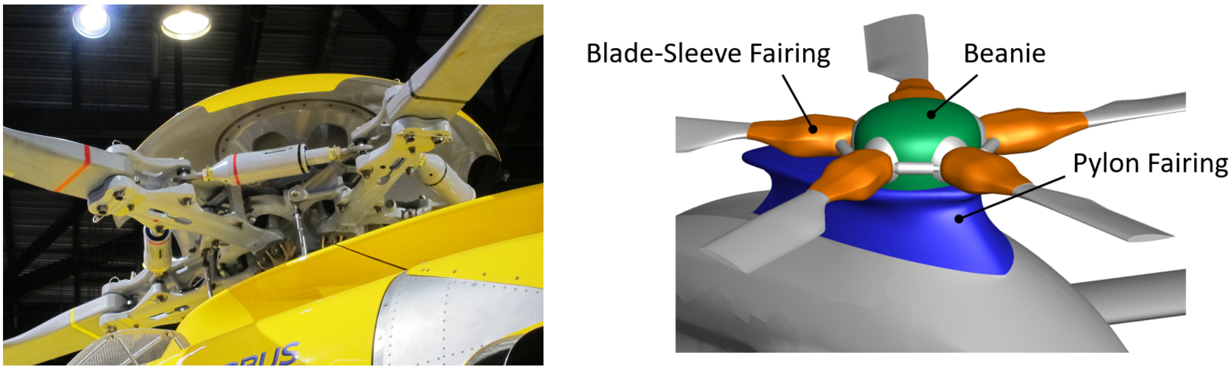

(a) Airbus Helicopters H175 rotor head [91]. (b) RACER full fairing components.

Figure 1.10: Comparison of a fully articulated Airbus Helicopters H175 rotor head and the RACER full-fairing concept.

1.4 Research Objectives and Thesis Outline

Introducing high-speed rotorcraft into the civil rotorcraft market represents an important step for next-generation helicopter design. The expansion of the helicopter flight envelope towards higher cruising speeds and ranges enables a cost-effective operation of a small helicopter fleet covering the same operational area as a larger fleet with conventional helicopters. Furthermore, typical helicopter mission scenarios include Search And Rescue (SAR) and Helicopter Emergency Medical Service (HEMS). Both scenarios have in common that time is a critical factor and life depends on fast response, which demands for high-speed rotorcraft. However, there are some major challenges to be tackled during the development, which include controlling the costs of operation and keeping the ecological footprint as low as possible. In order to reduce the required power to reach a desired cruise speed, drag mitigation is an important topic, which is addressed by the application of aerodynamically optimized shapes. The feasibility of compound helicopters using wings and lateral rotors to support the conventional main rotor was proven by the Eurocopter X^3 demonstrator platform. Based on this idea and the experience gained through this test bed, the current compound helicopter RACER is realized.

Nowadays, high-fidelity CFD has become a standard tool for helicopter development in the industrial environment. It can be used to partly replace expensive wind-tunnel measurements and flight tests providing reasonable accuracy. Therefore, CFD allows for the selection of relevant designs and flight conditions to be investigated experimentally. Today, the availability of computational resources and validated CFD software enables the engineers to perform computer aided design optimization by means of CFD simulation. One of the main objectives of the present thesis is the development of a CFD-based optimization tool chain providing a robust and modular framework for automated aerodynamic shape optimization. The modularity of the tool chain is ensured by the clear definition of interfaces and the corresponding data exchange between the different software components. This allows for a convenient implementation of additional or other software packages. Furthermore, parallelization enables the simultaneous evaluation of several designs, which significantly accelerates the design optimization process. The integration of the high performance computer SuperMUC of the Leibniz Supercomputing Centre (LRZ) allows to investigate computationally expensive, three-dimensional flow problems.

Besides the development of the optimization tool chain, the research work is dedicated to the aerodynamic design optimization of a full-fairing rotor head for the RACER compound helicopter. For this purpose, the sea-level cruise flight is considered, which represents the most relevant flight condition in terms of drag reduction. The newly developed tool chain is employed for the aerodynamic design optimization of the blade-sleeve fairing, which covers the hub region of the rotor blade.

This is done in a step-wise approach starting with the two-dimensional design optimization of selected radial blade-sleeve sections. The application of a genetic optimization algorithm provides a large database of optimized airfoil shapes representing the basis for the subsequent three-dimensional design optimization of the blade-sleeve fairing. The full-fairing concept of the RACER rotor head consists of two main components comprising the full-fairing beanie and the blade-sleeve fairing. Besides the design optimization of the blade-sleeve fairing, the impact of the full-fairing beanie shape (diameter/height) on the overall performance of the RACER demonstrator is evaluated. At first, the rotor-head fairings are examined on the isolated, five-bladed rotor head and thereafter, the most promising fairing combinations are investigated in more detail on the full RACER configuration incorporating all interference effects between the fuselage, the pylon fairing and the rotor head. Furthermore, the optimized blade-sleeve fairing is compared to a reference fairing, which was developed by Airbus Helicopters during the preliminary design phase of the RACER demonstrator. The performance benefit that can be expected by the application of the newly developed blade-sleeve fairing is demonstrated by the evaluation of the aerodynamic forces of the isolated rotor head as well as the full RACER configuration. The outcome of the present research includes a versatile, CFD-based optimization tool chain, which can be used for any kind of aerodynamic optimization problem. This tool chain has successfully been applied for the development of a new blade-sleeve fairing design, which is proposed as an aerodynamic upgrade for the RACER compound helicopter. Furthermore, the present thesis provides a workflow for the aerodynamic design optimization of rotor-head fairings by means of CFD simulations. Additionally, guidelines and best practices can be derived supporting the development of future helicopters.

The following paragraphs provide a brief outline on the present thesis. The fundamentals of helicopter aerodynamics and flight mechanics as well as the basics of optimization theory are introduced in Chapter 2. Helicopter design and control are briefly described in Sec. 2.1 giving an overview on the main components of a conventional helicopter and the cyclic pitch control of the main rotor. Furthermore, an introduction to rotor aerodynamics is provided and the flow phenomena occurring on the main rotor during cruise flight are illustrated. Section 2.2 is dedicated to optimization theory, which includes the formulation of an optimization problem, the characterization of the design and the objective space as well as an introduction to the basics of genetic optimization algorithms.

Chapter 3 is about the selected design optimization approach enabling the development of the RACER rotor-head fairing. First, the applied optimization tool chain is presented and its key components are described in detail.

Section 3.2 provides an overview on the applied optimization strategy, which includes the definition of the optimization problem and the theory about the applied multi-objective genetic optimization algorithm. Furthermore, Latin Hypercube Sampling (LHS) is introduced, which is used to derive a well-distributed, initial population of designs with respect to the available search space.

Chapter 4 describes the numerical approach that is used for the design optimization of the RACER blade-sleeve fairing as well as the detailed analysis of selected full-fairing concepts. Based on the complexity of the investigated flow problems, different mesh topologies are employed and therefore, a detailed description about the selected mesh generation strategy is given in Sec. 4.1. Moreover, Sec. 4.2 provides a short introduction to relevant CFD theory and fluid mechanic principals. Additionally, the applied flow solvers are briefly described and their main features are highlighted.

The aerodynamic design optimization of the RACER blade-sleeve fairing is presented in Chapter 5. The development of the new blade-sleeve fairing is performed in two steps. The first step deals with the two-dimensional design optimization of selected, radial blade-sleeve sections, which is described in Sec. 5.1. At the beginning, the rotor-head geometry as well as the parameterization of the blade-sleeve sections are introduced. Thereafter, the formulation of the optimization problem is stated and the applied numerical setup is described. Selected results of the design optimization process are illustrated and a detailed view on the most promising designs is given. Based on the optimized blade-sleeve sections, the three-dimensional design optimization of the blade-sleeve fairing is conducted, which is presented in Sec. 5.2. At first, the investigated geometry is introduced and the parameterization of the model is explained. Thereafter, the formulation of the optimization problem is provided, which is similar to the two-dimensional design optimization. The applied computational grid and the numerical setup are described in detail. Finally, selected results of the three-dimensional design optimization are presented including a detailed analysis of the objective space, the aerodynamic forces as well as the most relevant flow-field and surface quantities.

Chapter 6 deals with the evaluation of the optimized blade-sleeve fairing on the isolated rotor head as well as the full compound helicopter configuration. Section 6.1 introduces the investigated geometries and it provides a detailed description of the rotor-head fairing components. Furthermore, the simplifications that have been introduced for the present work are summarized in this section. The mesh generation approach and the applied computational grids are presented in Sec. 6.2. The numerical setup is described in Sec. 6.3 including an introduction to the implemented blade-pitch motion, the flow-solver settings and the required computational resources. The most relevant results and findings regarding the isolated rotor-head investigations are illustrated in Sec.6.4.

At first, the aerodynamic forces are analyzed including the evaluation of the total forces, the component forces and the frequency spectrum of the unsteady aerodynamic loads acting on the isolated rotor head. Additionally, selected surface and flow-field quantities are presented to illustrate the occurring flow phenomena. Finally, the impact of the optimized rotor-head fairing on the overall performance of the RACER compound helicopter is analyzed in Sec. 6.5. In total, three different rotor-head fairing configurations are compared to each other. The first configuration represents the reference geometry, which serves as the benchmark for the optimized fairing shape. The two remaining configurations feature the optimized blade-sleeve fairing together with two different full-fairing beanie geometries, which vary in terms of diameter and height. The focus of the analyses is set on the evaluation of the transient and the mean aerodynamic forces, in order to determine the performance benefit that can be expected by the newly developed blade-sleeve fairing. Moreover, a Fourier analysis of the aerodynamic forces is used to determine dominant frequencies and amplitudes acting on the rotor head. The main flow features are described by means of selected flow-field and surface quantities.

Finally, the thesis is concluded in Chapter 7 giving an overview on the design optimization process of the RACER blade-sleeve fairing and the corresponding analyses of the aerodynamic characteristics. Furthermore, an outlook on possible future tasks complementing the present work and finalizing the performance evaluation of the newly developed rotor-head fairing is given.

2 Fundamentals

This chapter introduces the relevant principles of helicopter aerodynamics and flight mechanics. Based on the subject of the present thesis, a special focus is set on the rotor aerodynamics of the helicopter. Additionally, a brief overview on optimization theory and the applied optimization algorithm is given.

2.1 Basics of Helicopter Aerodynamics and Flight Mechanics

Within this section, the design and control of a conventional, state-of-the-art helicopter are described. Furthermore, an introduction to rotor aerodynamics and flight mechanics is given. The occurring flow phenomena on the main rotor of a helicopter during forward flight are presented. Finally, the flow problems that must be tackled by the helicopter to reach high-speed forward flight are explained.

2.1.1 Helicopter Design and Control

Serving as an example for a modern, medium weight-class helicopter, the Airbus Helicopter H160 is illustrated in Fig. 2.1. Moreover, the main components of a typical, conventional transport helicopter are shown. The H160 represents a highly sophisticated and mature, multi-mission rotorcraft incorporating the key innovations and technologies obtained during research activities within the last decades. A conventional helicopter is characterized by a single main rotor and a tail rotor for yaw control.

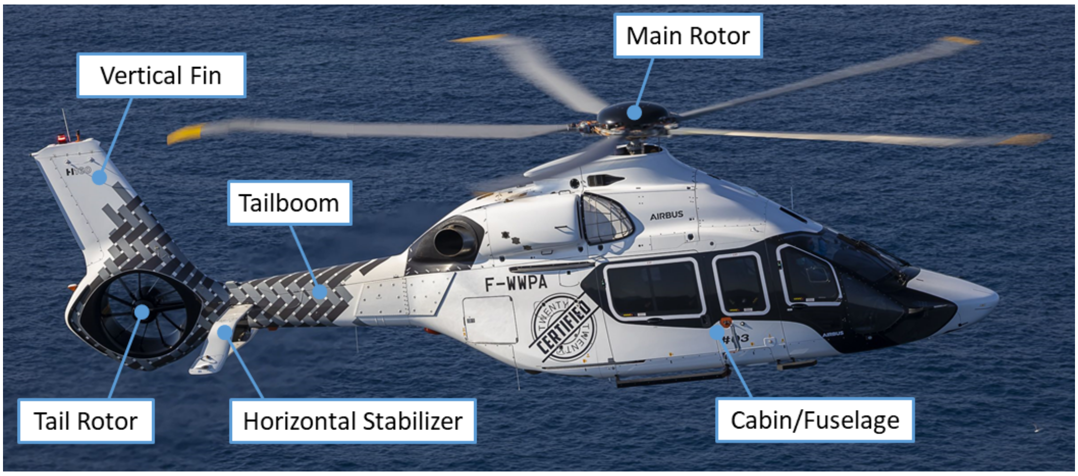

Figure 2.1: Main components of a conventional transport helicopter, adapted from [5].

The main rotor of a helicopter has three principal functions: (1) the generation of lift to compensate weight, (2) the generation of thrust to counteract drag and (3) the control of the flight attitude in the three-dimensional space. In order to achieve a steady cruise flight, the force equilibrium shown in Fig. 2.2a must be established. The rotor thrust (orange) can be divided into lift (blue) and forward thrust (green). The helicopter weight and additional downforces (violet), which originate from the flow around the vehicle, are compensated by lift. Moreover, the aerodynamic drag (red) is balanced by the forward thrust component of the rotor. Figure 2.2b shows the clockwise rotational movement of the main rotor by the blue colored arrow. In order to be able to realize the rotational movement, a certain driving torque must be transmitted via the rotor shaft. This induces a yawing moment on the helicopter, which is illustrated by the red arrow in Fig. 2.2b. During hover, the yawing moment is mainly compensated by the tail-rotor thrust in combination with a certain lever arm x_{TR}. Besides the generation of anti-torque, the variable pitch or rotational speed of the tail rotor is used for yaw control. In forward flight, the vertical fin provides additional anti-torque and directional stability.

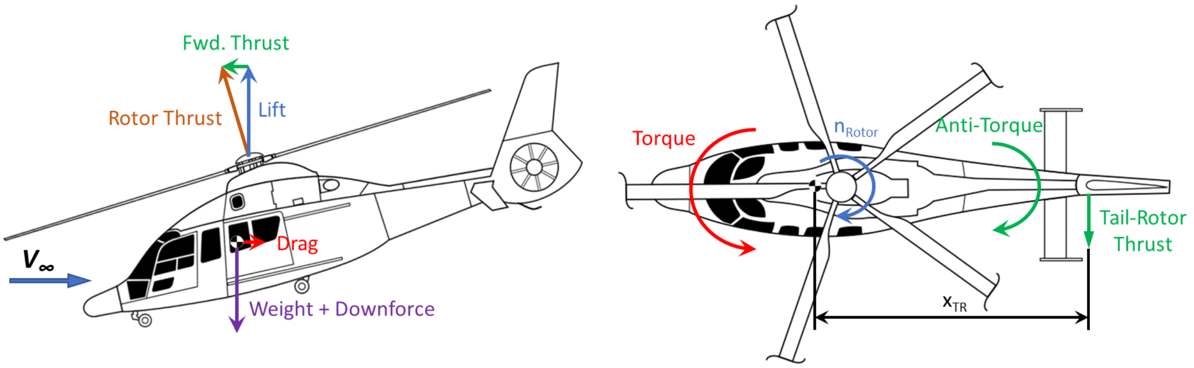

(a) Schematic overview of the force equilibrium during cruise flight.

(b) Effect of the tail-rotor thrust to generate anti-torque.

Figure 2.2: Overview of the main aerodynamic forces and moments acting on a conventional helicopter during cruise flight, adapted from [6].

Figure 2.3 gives an overview on the mechanical components of a typical rotor system. The pitch movement of the rotor blades is achieved by the swashplate system. It consists of two plates, which are connected via a bearing allowing for relative movement between each other. The upper plate rotates with the blades and it is connected to the blade sleeves by the pitch link and the pitch horn. In contrast, the lower part of the swashplate system is stationary and connected to the control rods, which are linked to the hydraulic actuators. Furthermore, scissor links are used to prevent the stationary plate from rotating with the upper one and to connect the upper, rotating swashplate with the rotor shaft. Scissor links are applied, because the swashplate assembly must be able to slide along the main rotor shaft.

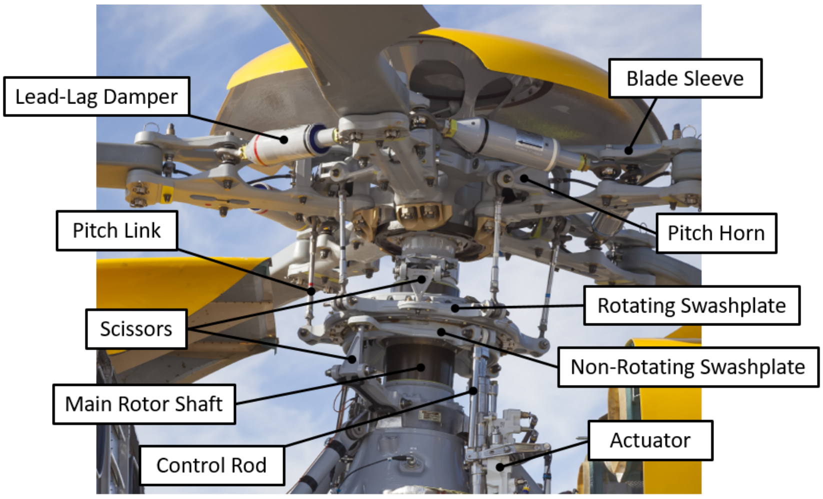

Figure 2.3: Mechanical components of the helicopter main rotor including the swashplate control system, adapted from [7].

The blade-pitch angles of the main rotor are adjusted by the collective and the cyclic pitch, which can schematically be seen in Fig. 2.4. The required main-rotor thrust is adjusted by the collective pitch, which changes all blade-pitch angles simultaneously by moving the swashplate up and down. In order to control the flight direction and the attitude of the helicopter, the rotor plane is tilted by the cyclic pitch, which continuously changes the blade-pitch angle during one rotor revolution. In Fig. 2.4, on the right hand side, the swashplate is exemplarily tilted forwards and backwards. Hence, the pitch and roll movement of the helicopter are realized by changing the direction of the main-rotor thrust vector through adjustment of the blade pitch via the swashplate assembly.

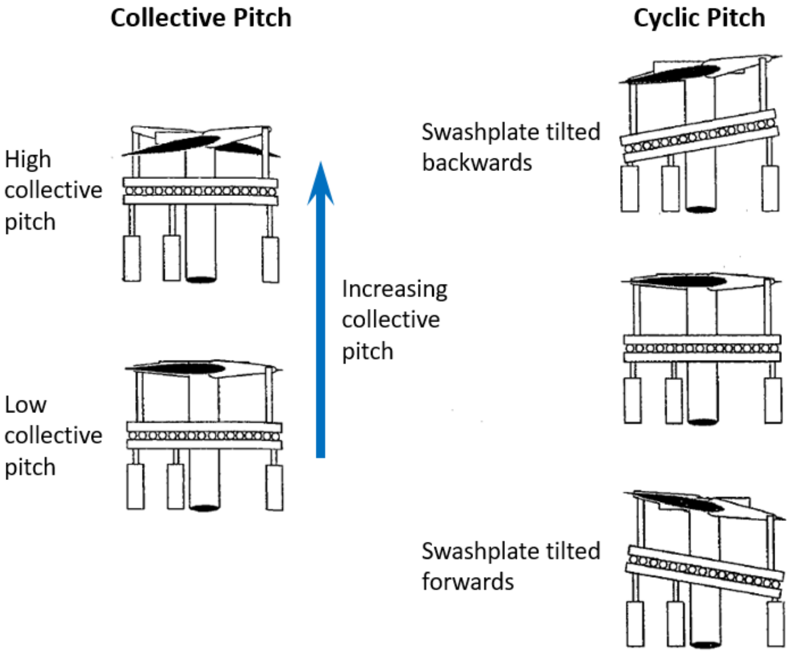

Figure 2.4: Collective and cyclic blade pitch change by the movement of the swashplate, adapted from [8].

According to Leishman [8], the blade-pitch motion can be described as a Fourier series:

$$\theta(r,\Psi) = \theta_{tw} \cdot r + \theta_0 + \theta_{1c} \cdot cos\Psi + \theta_{1s} \cdot sin\Psi + ... + \theta_{nc} \cdot cos(n\Psi) + \theta_{ns} \cdot sin(n\Psi) \quad (2.1)$$

θ_{tw} stands for the elastic deformations (twist) of the blade and r corresponds to the non-dimensional radial position on the blade. In Eq. 2.1, the control inputs are given by the collective pitch θ_0, the lateral cyclic pitch θ_{1c} and the longitudinal cyclic pitch θ_{1s}. θ_{1c} and θ_{1s} are the first harmonics of the Fourier series. The average, total rotor thrust is obtained by the average blade-pitch angle, which is controlled by the collective pitch θ_0. The orientation of the rotor disk can be adjusted by a combination of the two cyclic pitch controls. Within the present work, the elastic blade deformation and the higher harmonics of the Fourier series are neglected and Eq. 2.1 is simplified to:

$$\theta(\Psi) = \theta_0 + \theta_{1c} \cdot cos\Psi + \theta_{1s} \cdot sin\Psi \quad (2.2)$$

The blade pitch motion of a single rotor blade during forward flight is shown in Fig. 2.5. The definition of the azimuthal rotor position $\Psi = 0°$ corresponds to a downwind pointing rotor blade, which is depicted in Fig. 2.5a. Moreover, the blade-pitch angle depending on its azimuthal rotor position is illustrated in Fig. 2.5b for one rotor revolution ($0° \leq \Psi \leq 360°$). For demonstration purposes, arbitrary values of the collective and the cyclic pitch inputs were chosen.

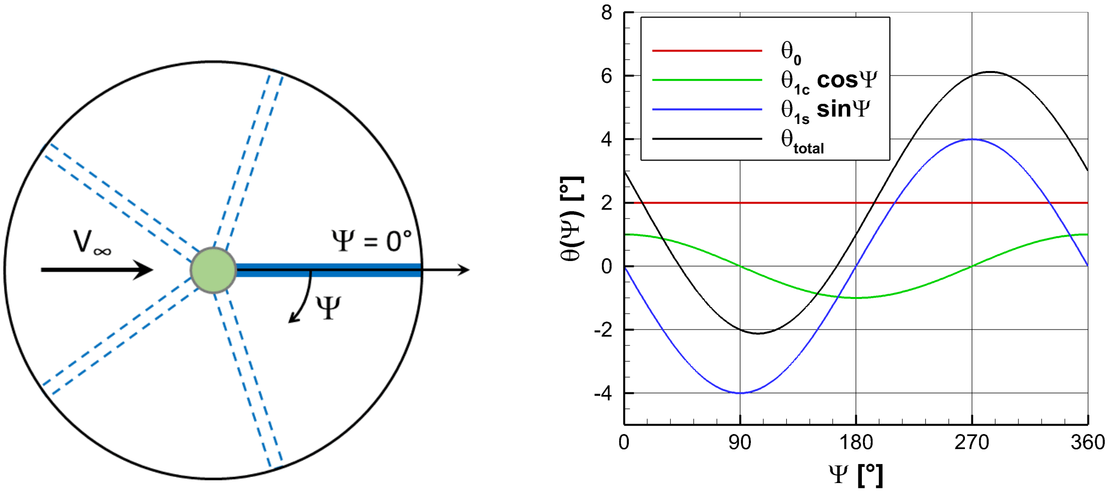

(a) Definition of the azimuthal blade angle for a clockwise rotating rotor.

(b) Blade-pitch angles for a single rotor blade depending on its azimuthal position.

Figure 2.5: Exemplary visualization of the rotor-blade pitch angles $\theta_0 = 2°$, $\theta_{1c} = 1°$ and $\theta_{1s} = -4°$ for one rotor revolution.

According to Eq. 2.2, the actual pitch angle θ_{total} is obtained by summing up the contributions of the collective pitch θ_0, the lateral cyclic pitch θ_{1c} and the longitudinal cyclic pitch θ_{1s}.

In order to be able to obtain the required pitch input for a given flight condition, the trim of the helicopter must be determined. A comprehensive overview on rotor-blade motion including an introduction to rotor trim is given by Leishman [8].

2.1.2 Rotor Aerodynamics

The flight conditions of a helicopter include hover, forward flight, vertical climb/descent, turning flight and transient maneuvers. In each flight condition, the main rotor thrust provides the required lift to counteract weight and downforce. The rotor thrust is based on the acceleration of an air mass flow through the rotor disk in opposite direction of the thrust vector, as schematically shown in Fig. 2.6 for hover flight.

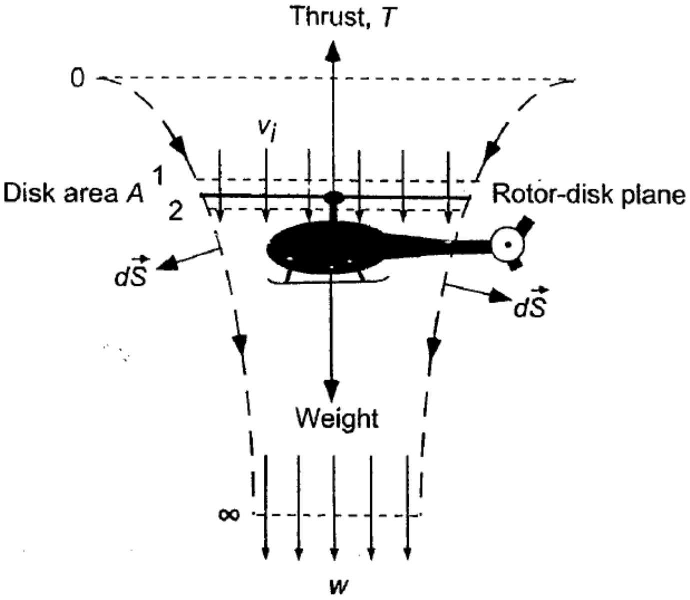

Figure 2.6: Actuator disk model used for the estimation of the rotor performance in hover flight [8].

The calculation of the aerodynamic rotor forces by means of mathematical models is quite challenging and not straight forward. However, analytical solutions with reasonable accuracy can be obtained for simplified flow conditions. For example, the basic hover performance of a rotor can be estimated by an actuator-disk concept, which is based on the Rankine-Froude momentum theory [92]. The first rotor-performance prediction for hover flight was published by Joukowsky in 1918 [93]. The actuator-disk approach can be used to estimate the required power and sizing of a rotor for a given thrust during the preliminary design phase. Regarding Fig. 2.6, a simplified mathematical approach can be used to estimate the rotor thrust assuming a quasi-steady, 1-D incompressible flow [8]. The surface S represents the boundary of the control volume that is used to set up the governing equations for hover flight. The cross section 0 is far upstream of the rotor, where the fluid is quiescent. Moreover, the cross sections 1 and 2 are located close to the rotor disk with the area A.

The far-wake region is given by cross section ∞, which is also called "vena contracta" due to the reduced cross-sectional area. At the rotor disk, an induced velocity v_i is present and in the far wake an increased velocity w can be observed. Mass conservation inside the control volume requires a constant mass flow rate $\dot{m}$ at each cross section, which is calculated according to Eq. 2.3, where ρ represents the density of the fluid.

$$\dot{m} = \rho A_\infty w = \rho A v_i \tag{2.3}$$

The conservation of momentum yields the relation between the rotor thrust and the change of the momentum within the control volume, which is given by Eq. 2.4. The vector $\vec{V}$ comprises the velocity components with respect to the given coordinate system.

$$T = \iint_\infty \rho \left(\vec{V} \cdot d\vec{S}\right) \vec{V} = \dot{m} w \tag{2.4}$$

Considering the conservation of energy, the energy gain of the fluid per time unit is equal to the work done on the rotor, which leads to Eq. 2.5

$$T v_i = \iint_\infty \frac{1}{2} \rho \left(\vec{V} \cdot d\vec{S}\right) \vec{V}^2 = \frac{1}{2} \dot{m} w^2 \tag{2.5}$$

The relation between the induced velocity v_i at the rotor disk and the velocity w in the wake region can be derived by combing the Eqs. 2.4 and 2.5 to $w = 2 \cdot v_i$. Furthermore, the mass conservation leads to $A_\infty = 0.5 \cdot A$.

In order to fully understand the rotor aerodynamics of a helicopter, detailed knowledge about the flow environment in which the rotor blade operates and the dynamic response is required. The generated lift of a rotor-blade section is defined by the local angle of attack (AoA) and the local dynamic pressure, which can significantly change depending on the flight condition of the helicopter. Figure 2.7 shows the flow velocity distribution on the rotor disk comparing hover and forward flight. Moreover, four different azimuthal rotor positions are illustrated, which are given by $\Psi = [0°, 90°, 180°, 270°]$. The assumed forward-flight condition corresponds to a sea-level cruise flight in ICAO standard atmosphere with $V_\infty = 255\ km/h$, which is equivalent to a Mach number of $M = 0.208$. The same rotor speed is applied for both flight conditions. Equation 2.6 shows the definition of the advance ratio μ, which yields the ratio between the freestream flow velocity V_∞ and the tip speed of the rotor blade due to the rotational movement ωR. For the given example, an advance ratio of $\mu = 0.3$ is applied.

$$\mu = \frac{V_\infty}{\omega R} \tag{2.6}$$

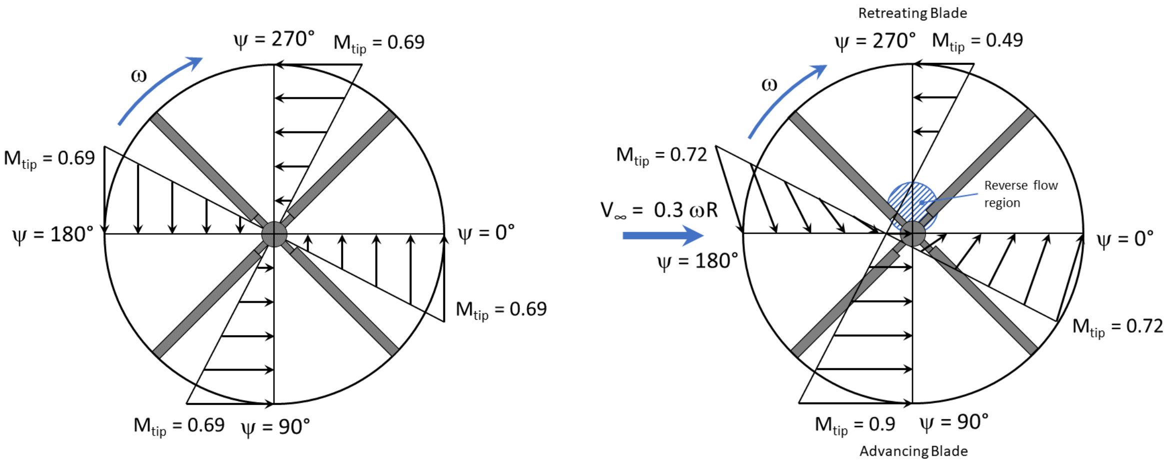

(a) Axisymmetric velocity distribution during hover flight.

(b) Non-uniform velocity distribution during cruise flight.

Figure 2.7: Influence of the forward flight speed and the rotational speed of the main rotor on the azimuthal velocity distribution on the rotor disk ($V_\infty = 255\ km/h$, $\mu = 0.3$).

Figure 2.7a illustrates the velocity distribution in hover flight, which is axisymmetric and changes linearly in radial direction reaching its peak value at the blade tip. Moreover, the flow velocity becomes zero at the rotational axis. Regarding cruise flight, which is depicted in Fig. 2.7b, a periodic change of the flow velocity can be observed. This leads to highly unsteady aerodynamic loads acting on the rotor blades as well as the entire rotorcraft depending on the structural coupling of the rotor assembly. The local tip speed of the rotor blade is calculated by superposing the rotational movement of the blade with the cruise speed of the helicopter, as shown in Fig. 2.8. Considering a blade-fixed coordinate system, the flow velocity can be divided into a tangential component V_t and a radial component V_r.

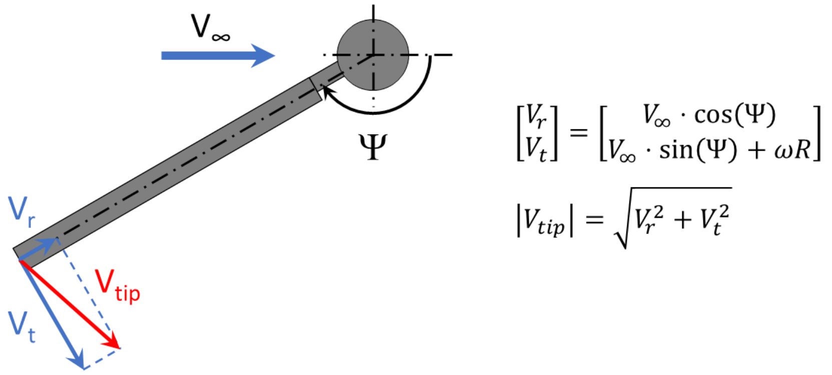

Figure 2.8: Radial and tangential velocity components at the rotor blade tip depending on the azimuthal position Ψ.

Regarding Fig. 2.7b, the highest flow velocity is obtained at the advancing rotor-blade tip ($\Psi = 90°$) reaching a Mach number of $M_{tip} = 0.9$ by assuming the flow conditions shown in Fig. 2.7. Therefore, the risk of potential transonic effects on the main rotor is measured by the tip Mach number of the advancing rotor blade, which is calculated by Eq. 2.7. Here, a represents the speed of sound, which is $a = 340\ m/s$ at sea-level in the ICAO standard atmosphere.

$$M^*_{90°} = \frac{V_\infty + \omega R}{a} \tag{2.7}$$

The critical Mach number represents the free-stream Mach number at which the flow locally reaches the speed of sound, but does not exceed it. If the flow regime at the advancing rotor blade is beyond the critical Mach number, shock induced flow separation and increased wave drag could occur. These effects would require much more power to drive the rotor head and should be avoided. Moreover, highly transient rotor-blade forces are expected above the critical Mach number, which intensify the vibrations and loads acting on the helicopter. This is accompanied by an amplified rotor noise level. Besides reducing the rotational speed of the main rotor to avoid transonic effects, the critical Mach number can be increased by using thin airfoils in the blade tip region. The mitigation of compressibility effects is always a trade-off between the the rotor speed and the forward flight speed.

Concerning the retreating rotor-blade tip ($\Psi = 270°$) in Fig. 2.7b, the lowest Mach number of $M_{tip} = 0.49$ is obtained and a region of reversed flow is present in the inboard section of the blade. In this region, the rotor speed ωR is smaller than the free-stream velocity V_∞. Comparing the advancing and the retreating rotor blade, the increased dynamic pressure on the advancing side would generate more lift at the same blade-pitch angle, which must be compensated in order to avoid lift asymmetry on the rotor disk. The possible lift asymmetry and the transonic effects are partially responsible for the cruise speed limitation of conventional helicopters. The lift inequality between the advancing and the retreating rotor blade is counteracted by a flapping movement of the rotor blade and a proper cyclic pitch input. The local blade-pitch angle of the retreating rotor blade is increased to compensate the lower dynamic pressure. However, a certain angle of attack must not be exceeded in order to avoid flow separation and dynamic stall. Due to the flapping movement, the rotor-blade radius is locally changed, which induces a lead-lag movement of the blade. For more details about rotor blade dynamics, the reader is referred to Leishman [8] and Prouty [94].

Regarding the upwind ($\Psi = 180°$) and the downwind ($\Psi = 0°$) pointing blade position, an inclined flow can be seen in Fig. 2.7b and the magnitude of the tip speed is calculated by $V_{tip} = \sqrt{(\omega R)^2 + V_\infty^2}$.

According to Johnson [28], a high-speed helicopter requires a high blade-tip Mach number and a high advance ratio. Figure 2.9 shows the relationship between these two parameters. The rotor speed of the main rotor is plotted against the forward flight speed for constant values of the advancing-tip Mach number $M^*_{90^\circ}$ and the advance ratio μ. This diagram allows to determine the maximum helicopter cruise speed for given limits of $M^*_{90^\circ}$ and μ [28]. Moreover, the exemplary cruise-flight condition of Fig. 2.7b featuring a blade-tip Mach number of $M^*_{90^\circ} = 0.9$ and an advance ratio of $\mu = 0.3$ is highlighted in blue in Fig. 2.9. For this flight condition, a blade-tip speed of $\omega R = 235.6\ m/s$ and a corresponding cruise speed of $V_\infty = 137.4\ kts$ $(255\ km/h)$ can be determined from the diagram.

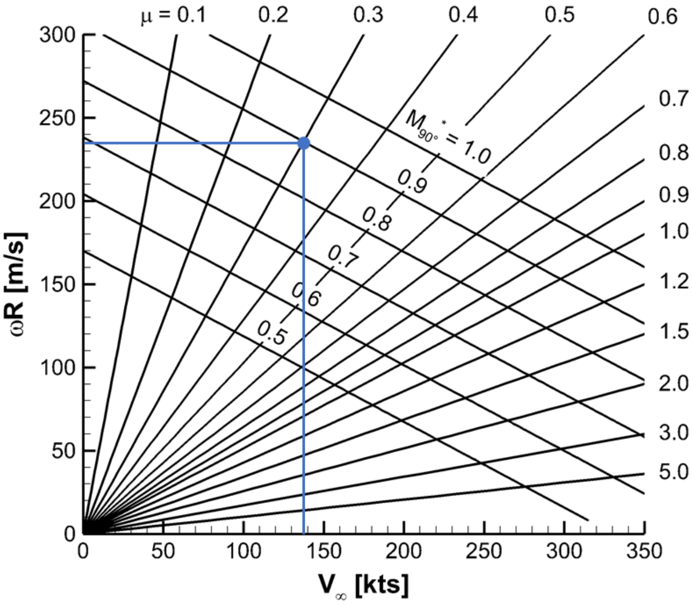

Figure 2.9: Rotor speed ωR vs. the forward flight speed V_∞ depending on the Mach number $M^*_{90^\circ}$ and the advance ratio μ.

The investigation of helicopter rotor aerodynamics is a challenging task, because several flow problems occur at the same time, which can be seen in Fig. 2.10. Here, the most significant flow phenomena related to main-rotor aerodynamics during forward flight are summarized. In addition to the flow problems related to the advancing and the retreating rotor blade, which were already mentioned, the blade-vortex interaction (BVI) represents an important flow phenomenon. BVI can typically be observed in the azimuthal region between the backward facing rotor blade ($\Psi = 0^\circ$) and the advancing rotor blade ($\Psi = 90^\circ$). It is an unsteady, three-dimensional flow problem, which appears when the rotor blade passes shed tip vortices from the preceding rotor blade. BVI can happen in forward flight and it is typically more pronounced in maneuver flight, vertical descent and forward flight descent.

Furthermore, the interaction of the vortex with the rotor blade is a major source of helicopter noise featuring highly unsteady loads. Therefore, BVI is an important topic during helicopter development, especially regarding helicopter noise reduction. More details about the fundamentals of rotor aerodynamics and helicopter theory can be found in Refs. [8, 9, 28, 95].

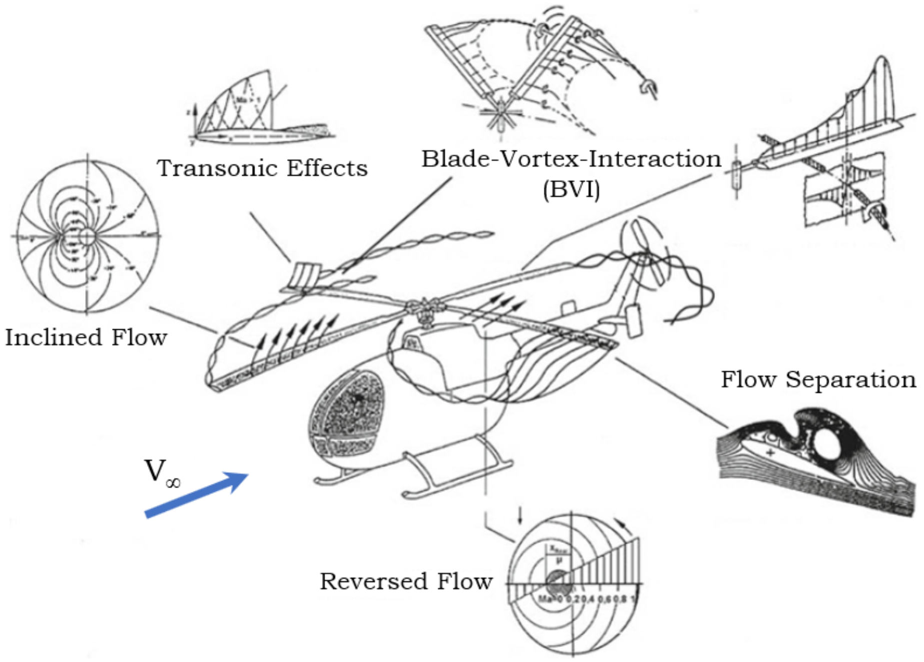

Figure 2.10: Schematic view showing the encountered aerodynamic problems on a helicopter in forward flight, adapted from [9].

2.2 Optimization Theory

This section of the thesis gives an introduction to optimization theory including the formulation of an optimization problem as well as the classification of the objective function. Optimization can be defined as a mathematical approach to find an optimal or near optimal solution for a given problem by selecting the appropriate design parameters. The optimum is found, if the minimum or maximum value of an objective function or a predefined threshold of improvement is reached. Usually, this cannot be done in a single step and therefore, an iterative process is applied, which, in the best case, guides the solution towards the optimum. According to Rothlauf [96], the commonly used steps for an optimization process include: recognizing and defining problems, constructing and solving models, evaluating and implementing solutions. The search for optimization potential is mostly initiated by external pressure (e.g. economical aspects) or changes in the environment. Moreover, the identification of such a potential is based on the availability of better alternatives compared to the current situation.

2.2.1 Problem Formulation

Each optimization task requires an appropriate formulation of the optimization problem. Figure 2.11 shows a schematic view on the main components defining an optimization problem. These include the design variables, the objective function and the design constraints, which can be used to limit the search space to a region of interest.

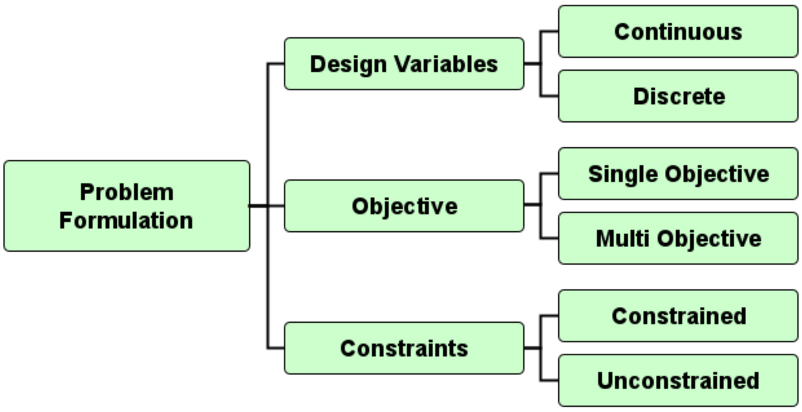

Figure 2.11: Problem formulation used for the classification of an optimization problem, adapted from [10].

The simplest form of an optimization task is given by a one-dimensional, unconstrained problem with a single objective function, which is illustrated in Fig. 2.12 showing the function $f(x)$ and the corresponding optimum. In this example, the minimum of $f(x)$ is searched. For such cases, highly efficient, gradient-based optimization algorithms are available, which lead to fast convergence in the iterative solution process.

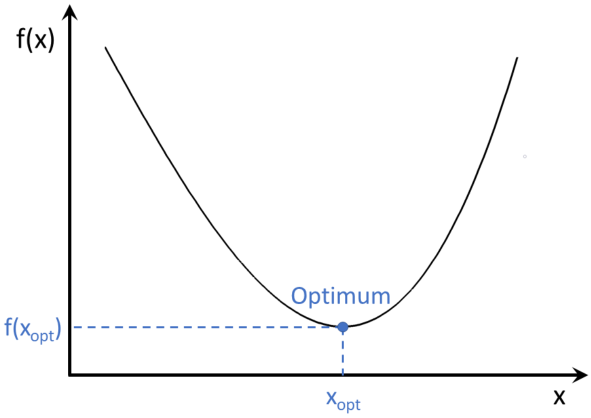

Figure 2.12: Example for a one-dimensional, unconstrained optimization problem with a single objective function.

Unfortunately, the majority of practical optimization tasks cannot be reduced to a one-dimensional problem with a single objective function. Therefore, more sophisticated optimization algorithms are usually required to be able to solve complex optimization problems.

A general formulation for an n-dimensional problem including multiple objective functions and design constraints is given by:

$$\begin{array}{lll} \text{min/max} & \mathbf{z} = f_i(\mathbf{x}), & i \in \{1,...,k\} \\ \text{subject to:} & g_i(\mathbf{x}) \leq 0, & i \in \{1,...,m\} \\ & h_i(\mathbf{x}) = 0, & i \in \{1,...,p\} \end{array}$$

where $f(\mathbf{x})$ is the particular objective function to be minimized or maximized and $\mathbf{x}$ represents the vector of n design variables $\mathbf{x} = \{x_1,...,x_n\}$. The design variables can either have continuous ($x \in \mathbb{R}^n$) or discrete ($x \in \mathbb{Z}^n$) values. A set of design variables represents a decision alternative for the given optimization problem. The number of available decision alternatives defines the difficulty of the resulting problem. Therefore, the selection of the most relevant design variables is an important aspect to keep the complexity within a reasonable frame. The objective function maps the set of design variables onto the objective space by providing an objective function value. With this value, the quality of the obtained result can be measured. Furthermore, design constraints can be applied to the optimization problem, which limit the search space to a region of interest. Here, they are given by $g(\mathbf{x})$ and $h(\mathbf{x})$ representing inequality and equality constraints, respectively. An example for a constrained, two-dimensional optimization problem is illustrated in Fig. 2.13. Three inequality constraints $g_1(\mathbf{x})$, $g_2(\mathbf{x})$ and $g_3(\mathbf{x})$ are shown in Fig. 2.13a. The objective space is defined by two design variables x_1 and x_2. Furthermore, the optimal solution for the underlying constraints is shown by x^*, which is located on the border of $g_1(\mathbf{x})$. The red area represents an infeasible region of the design space. The inequality constraint $g_1(\mathbf{x})$ is active for the given case and it can be seen that it includes both other inequality constraints making them gratuitous and inactive.

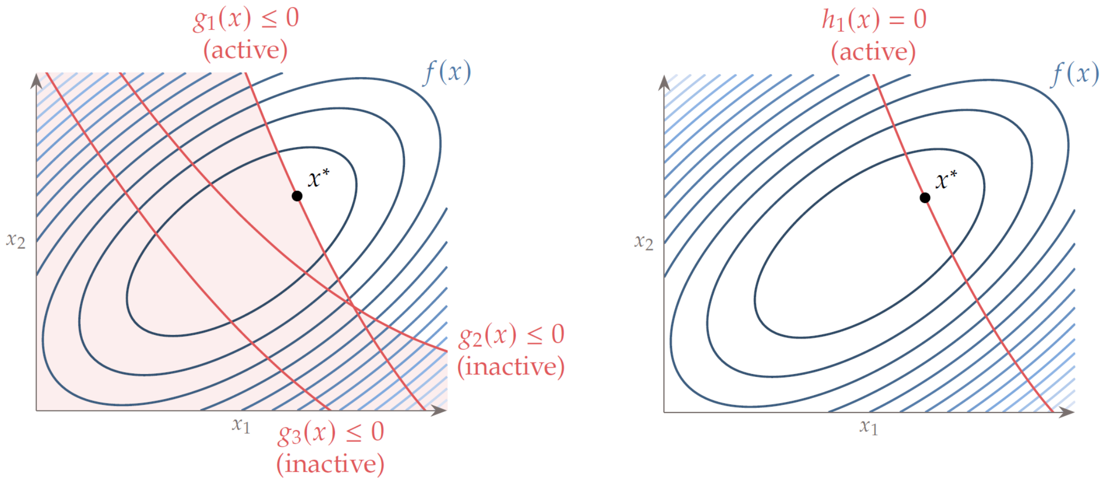

(a) Inequality Constraints. (b) Equality Constraint.

Figure 2.13: Example of a two-dimensional optimization problem showing two different types of design constraints. The red areas indicate infeasible reagions [10].

Figure 2.13b shows that the same optimum is found by using the equality constraint $h_1(\mathbf{x})$. Therefore, the solution is forced to be located on the red curve, which is defined by $h_1(\mathbf{x})$.

2.2.2 Objective Function Characteristics

In order to be able to choose an appropriate optimization algorithm, the characteristics of the objective space have to be identified. According to Martins and Ning [10], the most relevant properties of an objective function are illustrated in Fig. 2.14.

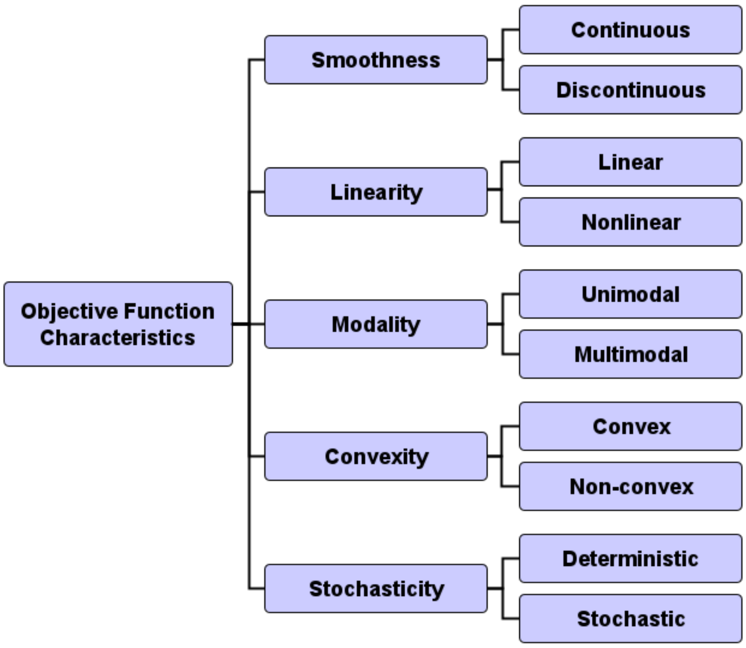

Figure 2.14: Main properties used for the characterization of an objective function, adapted from [10].

The smoothness of an objective function depends on the continuity of the function values as well as their derivatives. If the function value is varying continuously, the function is called C^0 continuous. Furthermore, if the first derivatives are changing continuously as well, the function is C^1 continuous, and so on. Figure 2.15 shows the comparison between a discontinuous and a C^2 continuous, one-dimensional objective function. The knowledge about the smoothness of an objective function is important, because discontinuities in the objective function values or derivatives can limit the applicability of certain optimization algorithms.

Furthermore, an optimization problem can either be linear or non-linear. A linear optimization problem is given, if the objective function and the applied constraints are linear. Originally, linear optimization was applied in operations research and the first numerical optimization algorithms were developed for such kind of problems.

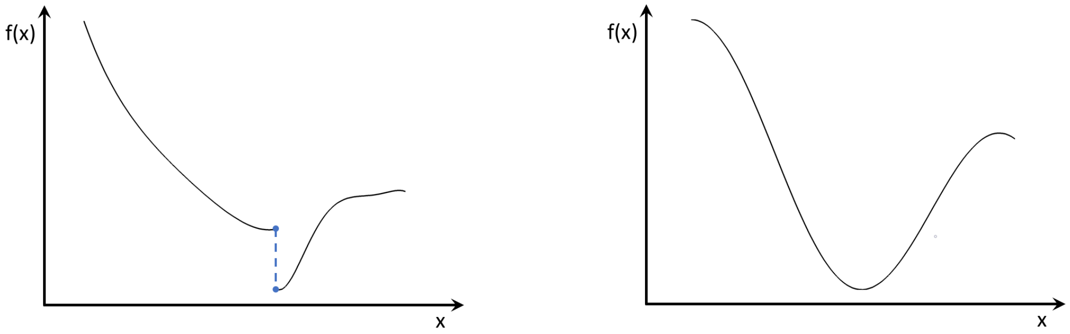

(a) Discontinuous objective function.

(b) C^2 continuous objective function.

Figure 2.15: Evaluation of the objective function smoothness considering a one-dimensional problem.

An example for a linear, two-dimensional optimization problem is given in Fig. 2.16. Here, one can see several iso-lines of the objective function and four inequality constraints limiting the feasible design space to the white region. Within this region, the maximum objective function value is obtained on the top right corner, which is marked by x^*. Within the present work, a CFD-based shape optimization is performed, which represents a non-linear optimization problem to be tackled by the selected optimization algorithm.

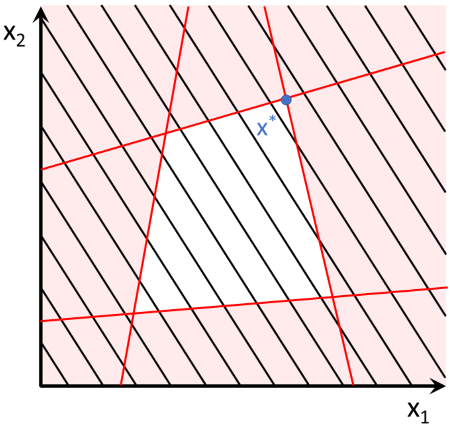

Figure 2.16: Example for a linear, two-dimensional objective function in combination with four, linear inequality constraints.

Regarding the modality of an objective function, one distinguishes between unimodal and multimodal functions. The objective function is unimodal, if it has a single, global minimum or maximum. In contrast, a multimodal function has several local minima or maxima. Therefore, it is not an easy task to find the global optimum of a multimodal function. It requires the exploration of the entire design space to prove that the encountered minimum/maximum is a global optimum. Furthermore, the convexity of an objective function is closely linked to its modality, which can be seen in Fig. 2.17 showing the comparison between a convex, unimodal and a non-convex, multimodal objective function.

Regarding convex optimization problems, every local minimum is always a global minimum, as shown in Fig. 2.17a. The red curve is randomly drawn and it can be seen that the intersection of this curve with the objective function $f(x)$ forms a closed and convex region with only one optimum. This characteristic makes it easier for an optimization algorithm to efficiently navigate to the optimal solution within a short time period. An introduction to convex optimization can be found in [97]. Furthermore, prominent examples for contemporary methods that are used for the solution of convex optimization problems are given by the gradient descent method, Newton's method, the interior point method, the simplex method, the cutting plane method and the ellipsoid method. Gradient-based optimization algorithms are well suited for convex optimization problems, because they efficiently navigate to the local optimum in the vicinity of the starting point. However, accurate gradient calculation is required, because inexact derivatives could cause failures in the search. Figure 2.17b shows a non-convex, multimodal optimization problem, which is characterized by several local maxima and minima. It can be seen that by intersecting the objective function with the red curve, convex and concave sub-regions are present. For such problems, gradient-based optimization algorithms are generally not suited, because they can get stuck in a local optimum and do not necessarily find the global one. A robust alternative for non-convex search spaces is given by global and derivative-free evolutionary/genetic optimization algorithms, which are described in detail in Sec. 2.2.3 of the thesis.

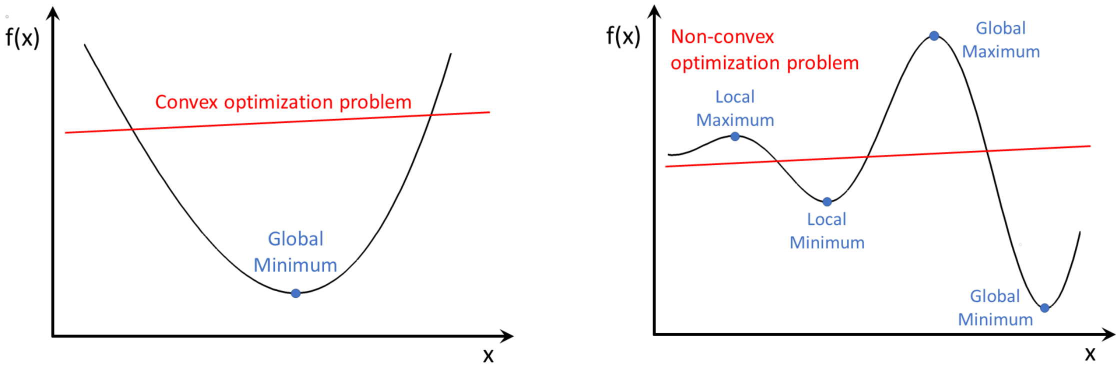

(a) Convex optimization problem. (b) Non-convex optimization problem

Figure 2.17: Comparison of different objective space characteristics and optimality conditions.

If randomness is a factor concerning the objective function or the applied constraints, stochastic effects must be taken into account during the optimization process. If the same set of design variables can repeatedly be tested and the objective function value does not change, the observed function is deterministic. In contrast, if the same input of design variables causes different objective function values, a stochastic behavior is present. A comparison between a deterministic and a stochastic objective function is illustrated in Fig. 2.18 for a one-dimensional problem. The objective function is repeatedly evaluated at x_{eval} demonstrating the influence of randomness on the objective function value.

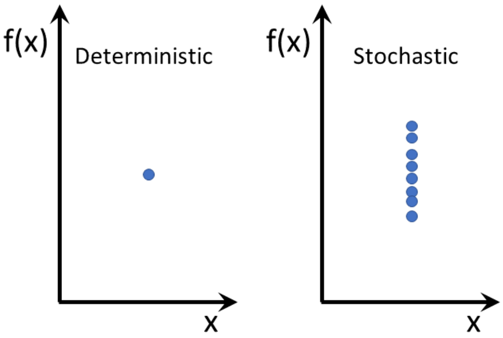

Figure 2.18: Comparison between a deterministic and a stochastic objective function.

Subsequent to the definition of the optimization problem, a convenient optimization algorithm has to be chosen. Therefore, it is important to understand the previously introduced characteristics of the search space. Furthermore, the capabilities and the requirements of the available algorithms must be well known. The following list summarizes important considerations for the selection of an optimization algorithm [98]:

- Type of design variables (continuous, discrete, mixed)
- Global or local search and design space smoothness
- Required constraint support (unconstrained, bound constrained, generally constrained)
- Convergence rate and robustness of the method

A comprehensive overview on local and global optimization algorithms of different fidelity is given in the literature, see for example in Refs. [99,100]. Regarding the aerodynamic design optimization of the RACER rotor head fairings, the characteristics of the objective space are unknown and a non-linear behavior of the aerodynamic forces can be expected when changing the shape of the geometry. For example, small adjustments in the geometrical shape of the fairing could lead to an instant change of the flow separation onset, which cannot be predicted beforehand. Moreover, the objective function is deterministic, because the evaluation of the same set of design variables by means of numerical flow simulations delivers the same objective function values. The complexity of the investigated optimization problem leads to the conclusion that a robust and global optimization algorithm is desired, which is capable of dealing with non-convex and multi-modal search spaces. Therefore, a genetic optimization algorithm is chosen for the present work, which is described in detail in Sec. 2.2.3 of the thesis.

2.2.3 Genetic Optimization Algorithms

Genetic optimization algorithms (GAs) are based on the idea of natural evolution and Darwin's principle of survival of the fittest. Sivanandam and Deepa [101] mentioned similarities between problems solved by biological species and classical optimization methods. In nature, several species are competing against each other searching for the same resources in an ecosystem. The fittest individuals, which are capable of acquiring resources, will survive and reproduce having numerous descendants in the future. As a result, the average fitness of the population increases from generation to generation and the individuals with weaker attributes are dying out. The same principle can be applied to practical optimization problems engineers are dealing with. The GA performs an efficient, directed search by the adaptation of successive generations consisting of a large number of individuals. When traditional search algorithms, like random walk or gradient descent, become exhaustive and impractical in large search spaces, the GA paves the way to find an optimal or near-optimal solution. However, GAs require a large number of function evaluations to cover a wide region of the design space ensuring diversity among the population. Therefore, the computational effort represents a major drawback of GAs compared to conventional optimization algorithms, which perform a point-wise search in the design space. Nevertheless, GAs provide a robust alternative in non-convex search spaces or whenever the characteristics of the search space are unknown. According to Goldberg [102], GAs differ from other optimization algorithms in four ways:

1. GAs work with a coding of the parameter set, not the parameters themselves.
2. GAs search from a population of points, not a single point.
3. GAs use payoff (objective function) information, not derivatives or other auxiliary knowledge.
4. GAs use probabilistic transition rules, not deterministic rules.

A population consists of several individuals, which represent feasible solutions in the optimization environment. Each individual is defined by its parameters and the corresponding fitness value. The parameters yield design variables, which are typically coded in a linear data structure, a vector or a string. A very common way of encoding design variables is given by binary strings, which are capable of representing integers as well as finite, real numbers. Moreover, the length of a binary string determines the possible accuracy. As an example, Fig. 2.19 shows the binary encoding and decoding of real-value design variables using a 10-bit string for demonstration purposes. The first bit defines the sign of the number ($1 =$ - and $0 = +$) and the remaining nine bits yield the value. Therefore, the design variable can be defined within a range of $-5.11 \leq x \leq +5.11$ considering an accuracy of 0.01 for the given example.

The binary representation enables an easy manipulation of the design parameters by simply flipping zeros and ones in the binary string.

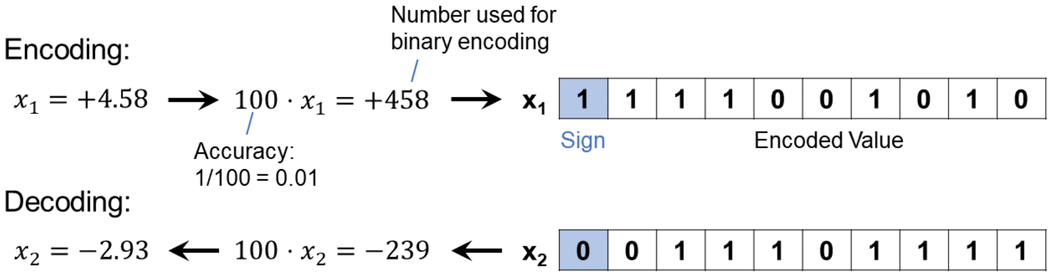

Figure 2.19: Example showing the binary coding commonly used by genetic optimization algorithms.

A big advantage of GAs is that they start their search for the optimal solution from a population of points and not a single one. Therefore, the risk of getting caught in a local optimum is significantly reduced. Furthermore, robustness concerning non-convex optimization problems can be ensured. The individuals of the first population are typically distributed over the entire design space in a random manner. Figure 2.20 shows a comparison between the initial population of a global GA and the single starting point of a local optimization algorithm.

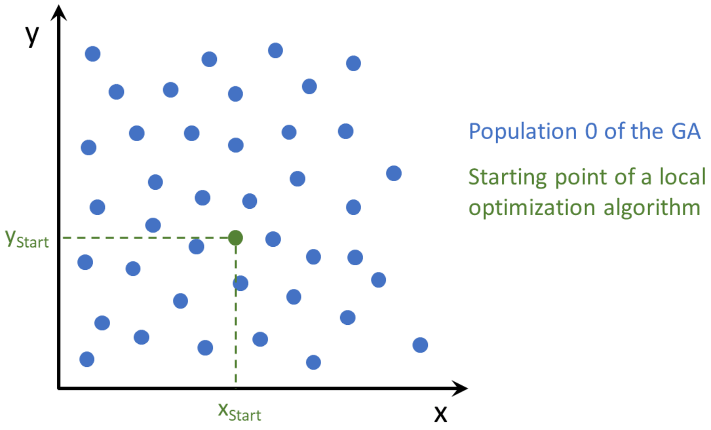

Figure 2.20: Initial population of a GA compared to the starting point of a local optimization algorithm (e.g. gradient-based algorithm).

Furthermore, GAs do not require any auxiliary information, like gradients or hessians. The evaluation of the fitness of each individual is only based on the derived objective function value. Therefore, the computational effort of a single function evaluation can be reduced. Subsequent to the examination of each candidate in the current generation, the quest towards search space with likely improvement is guided by probability based decision making. Moreover, a set of simple operations is applied to each population leading to a successive improvement of the individuals over time.

A common GA is composed of three operators: Selection (Reproduction), Crossover (Recombination) and Mutation. Selection is the process of choosing parents from the current population for crossing over genetic information. The purpose of selection is to emphasize fit parents, which could contribute offspring in the hope for an even higher fitness level in the subsequent generation. There are several algorithms available for the selection process and the most common ones are given by the rank-based selection and the biased roulette wheel [102]. The selected candidates are replicated and put into a mating pool, which is used for reproduction and further genetic operations. Within the next step, the candidates of the mating pool are randomly combined and each pair of strings (e.g. binary coded parameters) is crossed over leading to the generation of offspring. The simplest way of crossing over genetic information is to randomly choose a crossover point where the binary strings are cut, which can be seen in Fig. 2.21. Here, the information after the cut is exchanged between the parents generating two children.

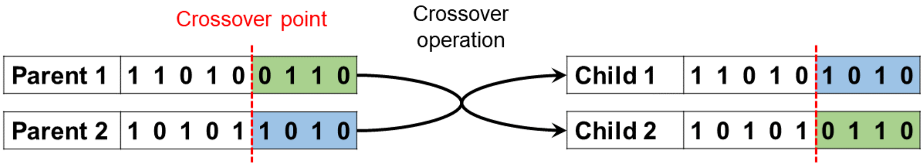

Figure 2.21: Crossover operation for two parents generating two children.

The selection and the crossover operations already provide much of a GA's power. However, the mutation operator is crucial as well, because it introduces potentially useful genetic material. During mutation, values of the coded parameter strings are randomly changed at certain string positions. Nevertheless, mutation rates in a simple GA are usually small (e.g. 0.1 %), which leads to the conclusion that mutation plays only a secondary role within the genetic evolution. Similar mutation rates are observed in natural populations, which justifies the assumption that mutation can be considered as a secondary mechanism [102].

3 Design Optimization Approach

The optimization tool chain, which is applied for the aerodynamic design optimization of the RACER rotor head fairings, and the selected optimization strategy are introduced within this section of the thesis. A detailed description about the optimization process and the main modules of the tool chain is provided. Furthermore, the selected multi-objective genetic optimization algorithm (MOGA) is explained and the principle of using Latin Hypercube Sampling (LHS) for the initialization of the first population of designs is presented.

3.1 Optimization Tool Chain

The introduction to the optimization tool chain is based on the author's publication in the Aeronautical Journal of the Council of European Aerospace Societies (CEAS) in 2019 [11].

The framework of the optimization tool chain is inspired by the work of Winkler [103] in his doctoral thesis at TUM-AER. The current tool chain is highly modular, robust and it allows for the parallel evaluation of multiple designs at the same time. Furthermore, the high-performance computer SuperMUC is integrated, which is the supercomputer of the Leibniz Supercomputing Centre [104]. A schematic view on the optimization tool chain and the five main modules involved in the design optimization process is given in Fig. 3.1. The five modules include an optimizer (A) providing state-of-the-art optimization algorithms, a CAD software (B), a mesh generator (C), a flow solver (D) and an analysis module (E) used to derive the objective function values. The communication and data exchange between the different modules is realized by dedicated Python scripts. Furthermore, a main Python routine represents the core part of the optimization tool chain managing the parallel execution of the optimization process and invoking the required subroutines in the different modules.

The applied CAD software Catia V5R21 requires a windows operating system. Therefore, the tool chain is split up in two parts, which can be seen in Fig. 3.2 showing the system architecture. The local network features two independently running Python processes working on a Windows and a Linux operating system. The two operating systems have a shared network drive, which is used for data exchange. Regarding Fig. 3.1, the Linux part of the tool chain deals with the modules A as well as C-E and the Windows part provides the CAD-based shape generation of module B. Moreover, the software packages implemented in the optimization tool chain are shown in Fig. 3.2.

In order to be able to investigate complex and computationally expensive flow problems, a remote HPC network is available for the optimization purpose and the communication is realized via a network connection between the local Linux work station and the remote supercomputer.

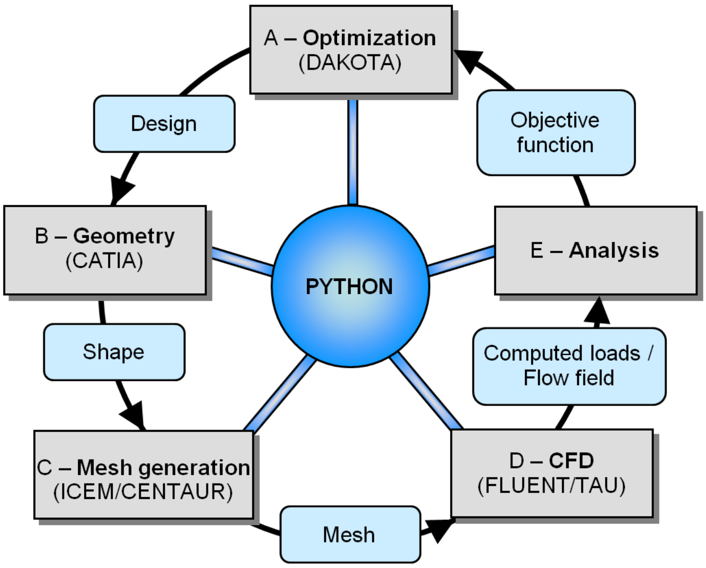

Figure 3.1: Schematic overview on the main modules of the aerodynamic design optimization tool chain [11].

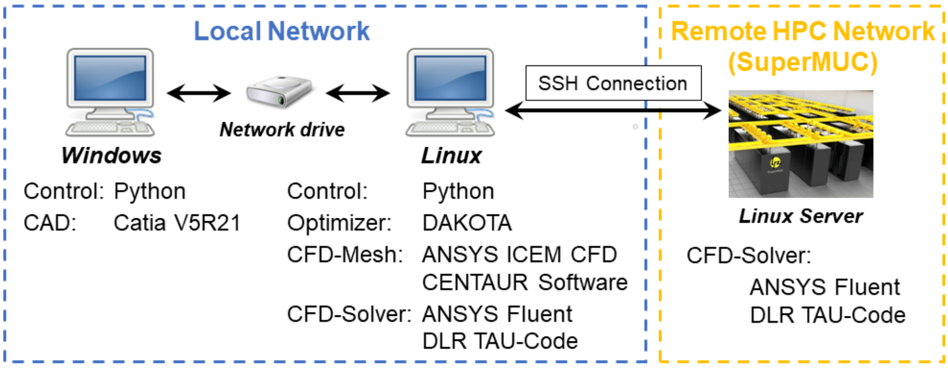

Figure 3.2: System architecture of the optimization tool chain and applied software packages, adapted from [11].

Python offers a versatile, general-purpose programming language, which is widely used in engineering applications. The simple syntax in combination with an extensive documentation and a large standard library makes Python well suited for the present optimization tool chain. The principle code structure of the developed tool chain is schematically shown in Fig. 3.3. The main Python routines are given by the green boxes and the orange boxes represent Python subprograms, which are invoked by the main process. The subprograms contain functions for the evaluation of design constraints, the generation of CAD shape files, the computational mesh generation, the automated flow simulations and the evaluation of objective functions, which are fed back to the optimizer.

Moreover, the required data exchange between the different software packages is shown in Fig. 3.3. Case-dependent parameters are provided by a user-defined input file and the optimization setup, which are highlighted by blue-colored boxes. These files include information about the simulation architecture, the optimization setup, the mesh generation, the flow simulation setup and the executables of the applied software packages. Furthermore, logfiles are generated throughout the optimization process allowing to follow each work step and enabling convenient debugging in case of an error in one of the modules.

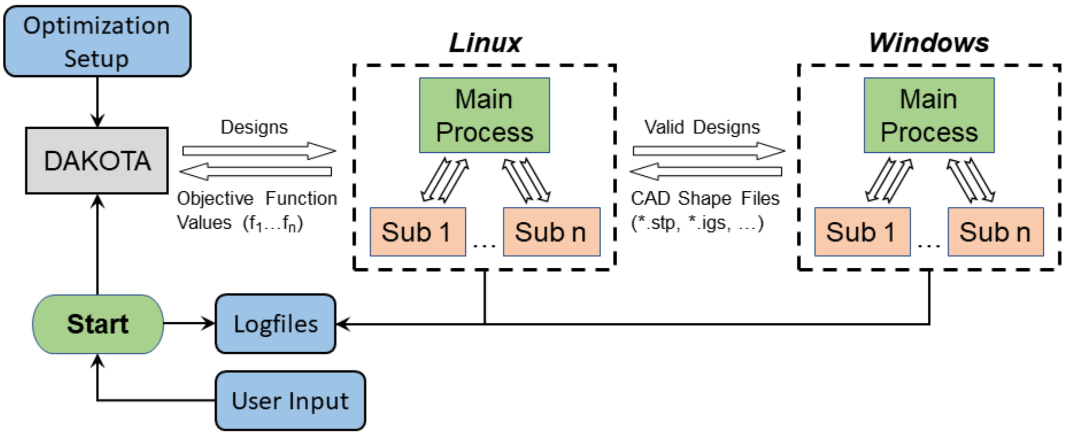

Figure 3.3: Visualization of the optimization process showing the main python routines and the required data exchange between the different modules, adapted from [11].

In the following, the implemented software packages and the corresponding modules (A-E) of the optimization tool chain are introduced.

Optimizer (A)

Regarding the optimization software, the Design Analysis Kit for Optimization and Terascale Applications (DAKOTA [98]), which is developed by Sandia National Laboratories, is applied. DAKOTA represents an optimization toolbox containing state-of-the art optimization algorithms ranging from local, gradient-based to global, evolutionary algorithms. Moreover, it provides a flexible interface between iterative analysis methods and simulation codes. DAKOTA is the starting point of each optimization process invoking the Python-based analysis driver, which is the core part of the optimization tool chain. Furthermore, the design points to be evaluated within the optimization process are generated by DAKOTA at the beginning of each optimization task. Some optimization algorithms allow for the simultaneous evaluation of different design points, which can be exploited by the parallelized optimization tool chain. This significantly accelerates the design optimization process and the maximum number of parallel processes is only limited by the availability of computational resources.

The optimizer can be seen as a black box, because it generates the design points as the input for the optimization tool chain and it retrieves the evaluated objective functions in the end. DAKOTA requires a setup file containing information about the optimization environment (e.g. graphical output, tabular data format), the applied method, the design variables (e.g. discrete, continuous), the interfaces and the responses (e.g. objective function values). More detailed information about the DAKOTA optimization toolbox is available in [98].

Shape Generator (B)

At the beginning of each optimization process, DAKOTA provides a design point, which represents a set of design variables. This design point is first checked for any violation of design constraints. If the design is valid, it is passed on to the Windows part of the optimization tool chain. For this purpose, the shared network drive is used and the main Python process running on the Windows work station continuously checks for any new designs in the transfer directory. The automated shape generation is conducted by using the CAD software Catia V5R21. This requires a paramterized CAD model of the investigated geometry, which can be manipulated via a design table. Hence, the design table is updated according to the present set of design variables. The CAD software is executed in batch mode using a predefined macro, which is prepared in the Catia-specific scripting language CATScript. The macro performs three tasks, which include: load the parameterized CAD model, update the shape according to the design table, write the shape file in the required data format. Within the present work, the widely used data exchange format STEP is used. The new shape file is returned to the Linux part of the optimization tool chain initiating the mesh generation process.

Mesh Generator (C)

Regarding mesh generation, two different software packages are implemented. These are given by the commercial mesh generators Ansys ICEM CFD [105] and CENTAUR from CentaurSoft [106]. Within the present work, ANSYS ICEM CFD is used to generate block-structured hexahedral meshes and CENTAUR can be applied to create hybrid, unstructured grids consisting of a mixture of prisms, hexahedra and tetrahedra. In order to run the mesh generators in batch mode, predefined macros in the corresponding scripting language are required. The high-level, general-purpose Tool Command Language (TCL) is applied for the automation of the mesh generation with ANSYS ICEM CFD. The TCL macro contains Linux shell script commands, which are used to determine temporary variable names and values (e.g. design number), as well as ICEM-specific commands. The latter can be recorded during the initial, manual mesh generation for a baseline geometry using the graphical user interface of ICEM CFD.

Hence, the manually created macro serves as the template containing all the necessary steps for subsequent automated mesh generation during the design optimization process. The second mesh generator CENTAUR requires several input files to be run automatically in batch mode. The main file contains a list of sequentially executed commands, which determine the automated mesh generation process. The workflow comprises the geometry import, the execution of a CAD cleaning tool, the import of the necessary input files for mesh generation (surface mesh, prism mesh, tetrahedral mesh) and the export of the mesh files. Furthermore, there are additional parameter files containing information about the geometry features (zones and groups), the definition of the boundary conditions and the parameters used for the successive generation of the surface, the prism and the tetrahedral mesh.

Flow solver (D)

The optimization tool chain offers two different flow solvers. These are given by the commercial flow solver ANSYS Fluent [107] and the DLR TAU-Code [108,109], which is developed by the German Aerospace Center. Each of the flow solvers can be combined with any of the mesh generators, which in total yields four different setups in the optimization tool chain. Therefore, depending on the selected flow solver, the required mesh format and the corresponding input files are generated by dedicated Python scripts. The flow simulation setup for ANSYS Fluent is defined by a journal file containing information about the flow solver parameters, the boundary conditions and the variables to be monitored for post-processing. In comparison, the DLR TAU-Code requires a parameter file and a boundary mapping file. The TAU parameter file is used to define the pre-processing, the setup of the flow solver and the post-processing. The optimization tool chain allows for parallel flow simulations to be conducted either on the local workstation or remote on the high-performance computer SuperMUC.

Analysis (E)

The successful termination of a flow simulation is marked by the presence of specific results files. Therefore, the main Python routine is regularly checking the current work directory for the availability of these files. Post-processing is conducted by means of dedicated Python scripts, which must be adapted according to the required objective functions. The analysis of the flow simulation results and the evaluation of the objective functions finalize the optimization loop for the current design. The objective function values are fed back to the optimizer and the next design is dispatched, which triggers the next loop of the optimization process.

3.2 Optimization Strategy

The focus of the aerodynamic design optimization is on the development of a low-drag blade-sleeve fairing for the RACER demonstrator. The unsteady numerical flow simulation of the full rotor head with cyclic pitch movement represents a complex, three-dimensional flow problem, which requires high computational effort to evaluate the aerodynamic forces. Hence, it is not feasible to conduct unsteady flow simulations of the full RACER rotor head for each blade-sleeve fairing design during the optimization. Therefore, a single, steady rotor blade is considered and a step-wise optimization strategy is employed. First, a two-dimensional design optimization of selected, radial blade-sleeve fairing sections is conducted. Thereafter, a refined aerodynamic design optimization of the three-dimensional blade-sleeve fairing shape is performed. Within this section of the thesis, the general formulation of the optimization problem and the corresponding design constraints are presented. Furthermore, the applied multi-objective genetic optimization algorithm (MOGA) and the basic principles of Latin Hypercube Sampling (LHS), which is used for the initialization of the first population of designs, are introduced. A detailed description about the two- and the three-dimensional design optimization of the blade-sleeve fairing is given in Sec. 5.1 and Sec. 5.2, respectively.

3.2.1 Definition of the Optimization Problem

As part of the RACER full-fairing rotor head development, the blade-sleeve fairing is aerodynamically optimized within the present thesis. For this purpose, a sea-level cruise flight with 220 knots is considered. During cruise flight, the flow conditions acting on a rotor blade are continuously changing over one rotor revolution leading to unsteady aerodynamic forces. Figure 3.4 shows the drag coefficient C_D of a single rotor blade depending on its azimuthal position ($0° \leq \Psi \leq 360°$). Moreover, the influence of the cyclic blade-pitch movement on the drag characteristics can be observed.

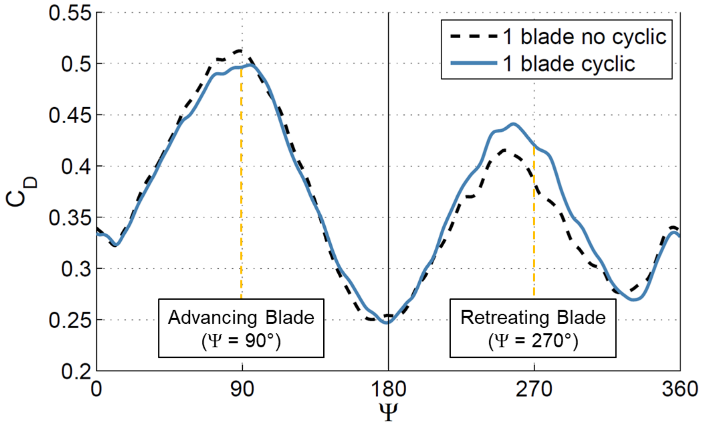

Figure 3.4: Drag coefficient C_D shown for a single rotor blade depending on its azimuthal position (with and without cyclic pitch), adapted from [11].

The highest drag values are obtained at $\Psi = 90^\circ$ and close to $\Psi = 270^\circ$, which corresponds to the advancing and the retreating rotor blade, respectively. The flow conditions at these azimuthal positions are the most relevant ones to be taken into account during the design optimization process, because drag reduction is the primary target of the blade-sleeve fairing development. Due to the fact that two rotor positions are considered for the design optimization task, it was decided to employ two independent objective functions. Regarding the advancing rotor blade, the aerodynamic efficiency, which is given by the lift-to-drag ratio L/D, is maximized, which includes both, the reduction of drag and the increase of lift. At the retreating rotor-blade position, reversed flow occurs in the inboard region of the blade-sleeve fairing and therefore, no lift contribution is expected and the minimization of drag is at focus. The two objective functions are competing with each other and they are independently evaluated. The general formulations of the applied objective functions are given by Eq. 3.1 and Eq. 3.2.

$$\textit{maximize} \quad f_1(\mathbf{x}) = L/D \tag{3.1}$$

$$\textit{minimize} \quad f_2(\mathbf{x}) = D \tag{3.2}$$

Furthermore, design constraints regarding the minimum and maximum permissible design space of the blade-sleeve fairing are employed, which can be seen in Fig. 3.5. The blue volume, which is located close to the rotor-blade attachment region, defines the minimum size and the green volume specifies the maximum permissible size of the blade-sleeve fairing. Moreover, the red, dashed lines illustrate the radial positions of the blade-sleeve sections addressed within the two-dimensional design optimization of the blade-sleeve fairing. At these positions, aerodynamically optimized supporting airfoils are used to define the three-dimensional shape of the fairing.

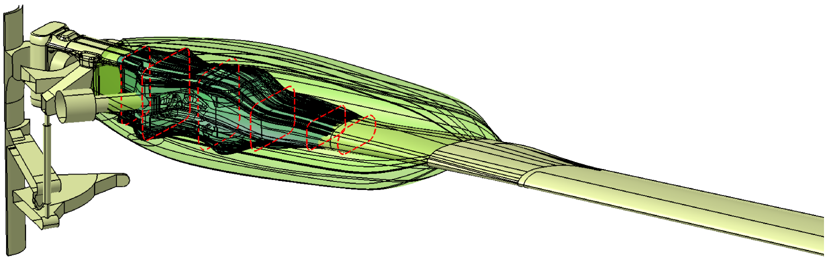

Figure 3.5: Visualization of the design constraints defining the permissible design space and radial positions of the investigated blade-sleeve fairing sections (red dashed lines).

Regarding the minimum design space, the movement of the mechanical rotor head parts inside the fairing requires a certain clearance to avoid contact and abrasion, which could reduce the lifetime of the fairing.

Additionally, the maximum design space must not be exceeded in the optimization process to prevent interference with surrounding rotor head elements and the RACER pylon fairing. A detailed description about the applied objective functions and the design constraints is given in Sec. 5.1 for the two-dimensional design optimization and in Sec. 5.2 for the three-dimensional design optimization of the RACER blade-sleeve fairing.

3.2.2 Multi-Objective Genetic Algorithm (MOGA)

Many practical optimization problems involve more than one objective function to be optimized. In most cases, the objective functions are competing with each other and there is no single, shared optimal solution. A typical example for such an optimization task is given by the maximization of the performance of a car and the simultaneous reduction of the fuel consumption. One can imagine that a high-performance race car will look different than an economic car. Hence, there is always a tradeoff between the applied objective functions leading to compromise solutions.

Multi-objective problems can be combined into a single-objective one by using weighting factors (e.g. $f = 0.7 \cdot f_1 + 0.3 \cdot f_2$). However, this approach requires a priorization of the objective functions before the optimization, which is subjective and not an easy task. A proper alternative is given by a multi-objective genetic algorithm (MOGA), which is capable of capturing multiple optimal solutions within a population of designs. Deb [110] and Goldberg [102] contributed valuable input for the development of MOGAs and they provide comprehensive theoretical knowledge about the principals of these kind of optimization algorithms. The nature of genetic optimization algorithms makes them well suited for multi-objective problems, because they search from a population of points and not a single one, which ensures diversity among the search space. Regarding a multi-objective problem, the best performing designs of the final population are located on the so called Pareto front. In contrast, the previously mentioned weighted sum approach featuring a combined objective function would only find a single point near or on the Pareto front. Therefore, many optimizations with different weights would have to be performed to obtain a parametric understanding of the influence of the weights.

Figure 3.6 shows a sketch of an exemplary objective space for two concurring objective functions. The blue points represent solutions from the feasible objective space and the green points compose a set of non-dominated designs forming the Pareto front. A comparison between two solutions from the Pareto front reveals that none of them can be identified to be better than the other one regarding both objective functions.

According to Deb [110], two conditions must be true for a non-dominated set of solutions:

1. Any two solutions of the set must be non-dominated with respect to each other.
2. Any solution not belonging to the non-dominated set is dominated by at least one member of this set.

The orange point in Fig. 3.6 represents the utopia point, which is obtained by connecting the best values of both objective functions. The utopia point is a theoretical solution combining the best of both objective functions. However, this solution can never be reached and therefore, it is located in an infeasible region of the objective space.

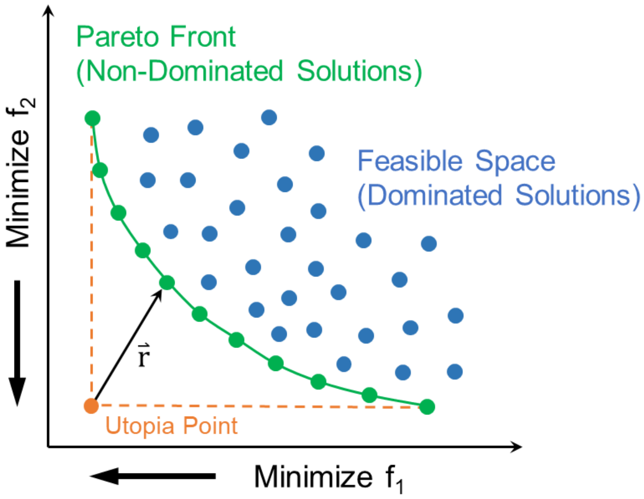

Figure 3.6: Schematic view on a two-dimensional objective space showing the Pareto front consisting of non-dominated solutions.

The vector $\vec{r}$ yields the distance between the utopia point and other designs, which can be taken into account for the selection of relevant solutions. However, normalized objective function values have to be considered for the calculation of the absolute value of $\vec{r}$ to equally weight both objective functions. Hence, the distance to the utopia point is calculated according to Eq. 3.3. From a mathematical point of view, the candidate with the minimum distance to this theoretical point offers the best compromise between the applied objective functions.

$$|\vec{r}| = \sqrt{\left(\frac{f_{1,\ Design\ x} - min(f_1)}{max(f_1) - min(f_1)}\right)^2 + \left(\frac{f_{2,\ Design\ x} - min(f_2)}{max(f_2) - min(f_2)}\right)^2} \tag{3.3}$$

The MOGA provides a successive development of non-dominated designs in each population. For this purpose, the fitness of each design is assessed and a selection operation is conducted to determine the candidates to be kept in the population.

Within the present thesis, the applied MOGA from the optimization toolbox DAKOTA uses a domination count and a below-limit selector to determine relevant designs in the present population. This means that the number of designs dominating another one is counted and used to rank the solutions as illustrated in Fig. 3.7. The green, hatched area shows an exemplary region containing two designs dominating the one of rank 3. Furthermore, the best performing designs yield a non-dominated set of rank 1.

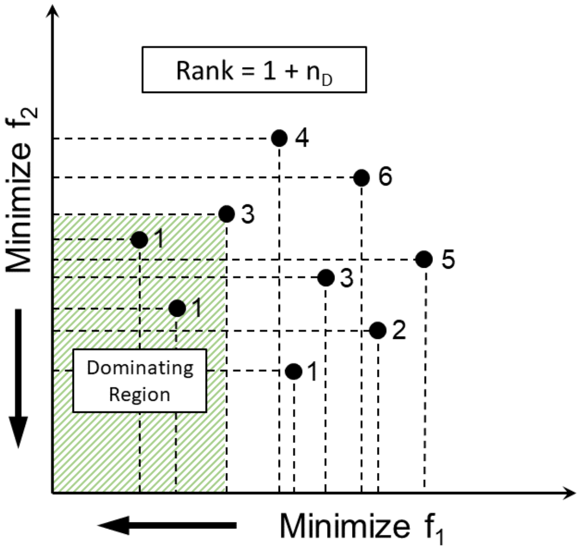

Figure 3.7: Ranking of designs according to their domination count.

Regarding the selection process, a maximum number of dominating designs is chosen. If this number is exceeded by the present design, it is discarded from the population and does not contribute offspring. However, to avoid an excessive reduction of the population size, a shrinkage percentage is defined, which relaxes the strictness of the below-limit selector, if necessary. This determines the minimum number of selections taking place for the current population. Moreover, niching is applied as a secondary operation to encourage differentiation along the Pareto front avoiding clustering of design points. Niching is also known as fitness sharing and it was introduced by Goldberg and Richardson [111]. Horn et al. [112] state that the fitness value f_i of an individual is degraded by a niche count m_i to achieve a better distribution of designs in the search space. The degradation is achieved by dividing f_i by m_i leading to the shared fitness f_i/m_i. The niche count m_i determines how crowded the neighborhood of a certain individual is and it is calculated according to Eq. 3.4 [112].

$$m_i = \sum_{j=1}^{n_{Pop}} Sh\left(d\left[i{,}j\right]\right), \tag{3.4}$$

where n_{Pop} is the size of the current population, $Sh(d)$ represents the sharing function and $d[i{,}j]$ yields the distance between the individuals i and j.

A typical sharing function is given by Eq. 3.5 using the distance between the individuals $d[i,j]$ and the desired niche radius σ_{share} to calculate the contribution to the niche count m_i. Therefore, the niche radius σ_{share} defines the desired separation between the solutions, because individuals within this distance reduce each others fitness.

$$d \leq \sigma_{share}: \quad Sh(d) = 1 - \frac{d}{\sigma_{share}} \tag{3.5}$$

$$d > \sigma_{share}: \quad Sh(d) = 0 \tag{3.6}$$

A detailed description about the MOGA-setup used within the present thesis is provided in the particular sections about the design optimization of the RACER blade-sleeve fairing. Furthermore, an extensive documentation about the applied multi-objective genetic algorithm is available in the DAKOTA manual [98].

3.2.3 Latin Hypercube Sampling (LHS)

Prior to the optimization process, the initial population of designs is generated by multidimensional parameter sampling. The main goal of this approach is to derive a widespread distribution of candidates covering a large region of the search space. Moreover, unintentional clustering of designs can be avoided by the application of a suitable sampling method.

Within the present work, Latin Hypercube Sampling (LHS) is employed for the generation of the first population of designs. Furthermore, the design constraints are evaluated for the LHS-sampled candidates generating only valid designs for the first generation. LHS was originally developed by McKay et al. [113] in 1974 as a method for selecting values of input variables in the analysis of output from a computer. The basic principle of LHS is to divide the range of each variable x_1,...x_k into N non-overlapping strata of equal marginal probability $1/N$, which leads to a k-dimensional sampling space. It is sampled once from each stratum leading to a sample x_{kj} for $j = 1$,...,N. The components of all variables x_k are then matched at random.

An illustrative explanation for LHS is given by Olsson et al. [12] showing a possible sampling plan for two input variables ($K = 2$) and five realizations ($N = 5$), which can be seen in Fig. 3.8. They define a matrix **S** according to Eq. 3.7, which consists of the matrices **P** and **R**. Here, **S** represents the basic sampling plan for the given example. **P** is an $N \times K$ matrix and each of the K columns yields a random permutation of 1,...,N. Moreover, **R** is an $N \times K$ matrix containing independent random numbers from 0 to 1.

$$\mathbf{S} = \frac{1}{N} \cdot (\mathbf{P} - \mathbf{R}) \tag{3.7}$$

According to Eq. 3.8, each element of S is mapped onto its target marginal distribution by using the inverse of the target cumulative distribution function F_{xj}^{-1} for variable j. The vector $\hat{x}_i = [\hat{x}_{i1} \quad \hat{x}_{i2} \quad \ldots \quad \hat{x}_{ik}]$ contains the input data for one computation.

$$\hat{x}_{ij} = F_{xj}^{-1}\left(S_{ij}\right) \tag{3.8}$$

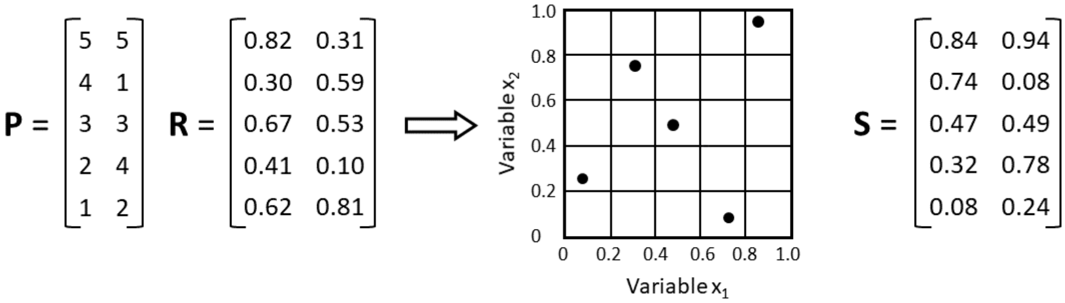

Figure 3.8: Example for Latin Hypercube Sampling (LHS) considering a two-dimensional problem (K=2) with five realizations (N=5), adapted from [12].

According to Olsson et al. [12], there is a certain risk of spurious correlation by the presented approach, which is exemplarily shown on the left-hand side of Fig. 3.9. However, it has been shown that the risk of clustering in the search space can be reduced by the modification of the permutation matrix **P** [114, 115]. More details about the correlation reduction of the standard LHS are given in the literature [12].

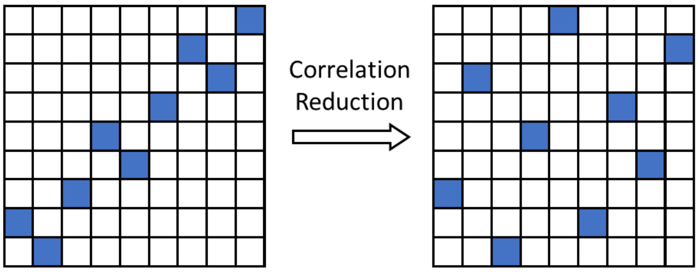

Figure 3.9: Reduction of undesired clustering/correlation in the sampling plan, adapted from [12].

The combined approach of preliminary design constraint evaluation and parameter sampling using LHS provides a sound database for the evolutionary algorithm and represents a good starting point for the design optimization process. The careful selection of reasonable input variables is crucial to keep the number of investigated designs as low as possible and as high as necessary.

4 Numerical Approach

Within this chapter, the mesh generation approach and the selected flow solvers with the corresponding numerical methods are introduced. Regarding mesh generation, block-structured hexahedral as well as hybrid unstructured meshes are applied depending on the complexity of the investigated geometry. Additionally, an introduction to overset mesh, which is used to realize the cyclic pitch movement of the RACER main rotor, is provided. Two different flow solvers are used, which are given by the commercial flow solver ANSYS Fluent and the DLR-TAU code. Therefore, the main characteristics of each flow solver and the applied numerical schemes are briefly described.

4.1 Computational Mesh

CFD is based on the finite volume method (FVM), which requires the spatial discretization of the fluid domain by a finite number of simple elements, like tetrahedra or hexahedra. These elements form the computational mesh, which is essential for the numerical solution of the partial differential equations related to the considered flow problem. The grid structure provides discrete points for the calculation of the flow variables using a system of algebraic equations. Hereby, the accuracy of the numerical solution strongly depends on the quality of the spatial discretization. Based on the complexity of the investigated flow problem and the characteristics of the selected flow solver, different types of computational meshes are available. Section 4.1.1 provides the motivation for the selection of the mesh topology depending on the investigated flow problem. A detailed description of each computational mesh is given in the corresponding results chapter of the present thesis.

4.1.1 Selection of the Mesh Topology

The most common mesh topologies include structured, block-structured, unstructured and hybrid unstructured grids. Within the present work, block-structured hexahedral and hybrid unstructured grids are used. Therefore, the focus is set on these two types of grids. The selection of the mesh topology depends on several factors including the meshing experience of the user, the complexity of the investigated geometry, the available time for the mesh generation process as well as the designated computational resources. The generation of structured grids usually requires much more time and experience compared to unstructured ones. However, the elements of a structured grid are mostly aligned with the flow direction, which leads to high mesh quality, low numerical dissipation, more accurate results and better convergence in the flow simulations. The alignment of the grid lines with the main flow direction is implicitly achieved, because both follow the contour of the geometry for attached flows.

Moreover, the structured mesh almost provides full control of all node locations allowing to precisely generate the desired computational grid. Additionally, it requires less elements than an unstructured grid considering the same spatial resolution, which reduces the computational effort. Unstructured meshes also need more memory to store the elements/nodes and their connectivity information. In contrast, a certain pattern is used to define the structured mesh, which does not require the storage of a connectivity table and therefore reduces the computation time. The major benefits of unstructured grids include a fast grid generation, the ability to handle complex geometries and the fact that less experience is required for the grid generation process. Moreover, unstructured grids typically allow for automated, local mesh refinement based on specific flow quantities, like pressure or velocity gradients. Within the last decades, the exponential growth of computational ressources and the increased complexity of the investigated flow problems have made unstructured grids more attractive. Hence, the time-saving factor and the simplicity of the unstructured grid generation typically supersede the computational benefits of the structured mesh. Additionally, there are several unstructured mesh generators available that allow for the usage of structured mesh blocks in selected regions.

During previous work at TUM-AER, numerical flow simulations were conducted by Stuhlpfarrer et al. [13] for a twin-engine light (TEL) utility helicopter using block-structured hexahedral meshes, which can be seen in Fig. 4.1. The blocking of the rotor disk and a single rotor blade are depicted in Fig. 4.1a and a detailed view on the surface mesh of the rotor head is given in Fig. 4.1b. The movement of the rotor blades was realized by a sliding-mesh interface in combination with deforming mesh for the cyclic blade-pitch movement.

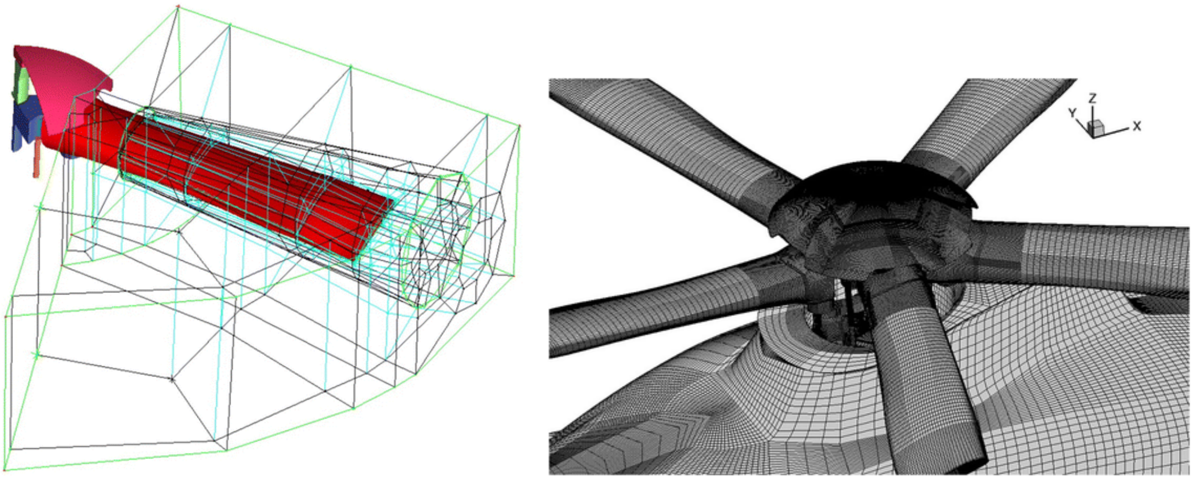

(a) Blocking of the rotor disk and the embedded rotor blade.

(b) Detailed view on the surface mesh of the rotor head with truncated rotor blades.

Figure 4.1: Spatial discretization of a conventional helicopter configuration using a block-structured mesh topology [13].

The experience and knowledge gained through Stuhlpfarrer et al. in terms of block-structured mesh generation for helicopter applications served as the basis for the selection of the proper meshing strategy within the present thesis.

Regarding the present work, four different flow problems are addressed, which are schematically shown in Fig. 4.2. They are ordered from the lowest complexity on the left-hand side to the highest complexity on the right-hand side. Starting with the two-dimensional flow simulation of selected blade-sleeve fairing sections during the initial phase of the design optimization process, the complexity is successively increased up to the full RACER configuration featuring a moving rotor head with cyclic blade-pitch input. A block-structured hexahedral mesh approach is chosen for the two-dimensional blade-sleeve fairing sections, the single rotor blade and the five-bladed, isolated rotor head. These structured meshes are generated with ANSYS ICEM CFD. Concerning the numerical flow simulations of the full RACER configuration, the block-structured rotor head mesh is integrated into a hybrid-unstructured mesh of the compound helicopter. The unstructured mesh generation is performed with ANSYS Fluent Meshing.

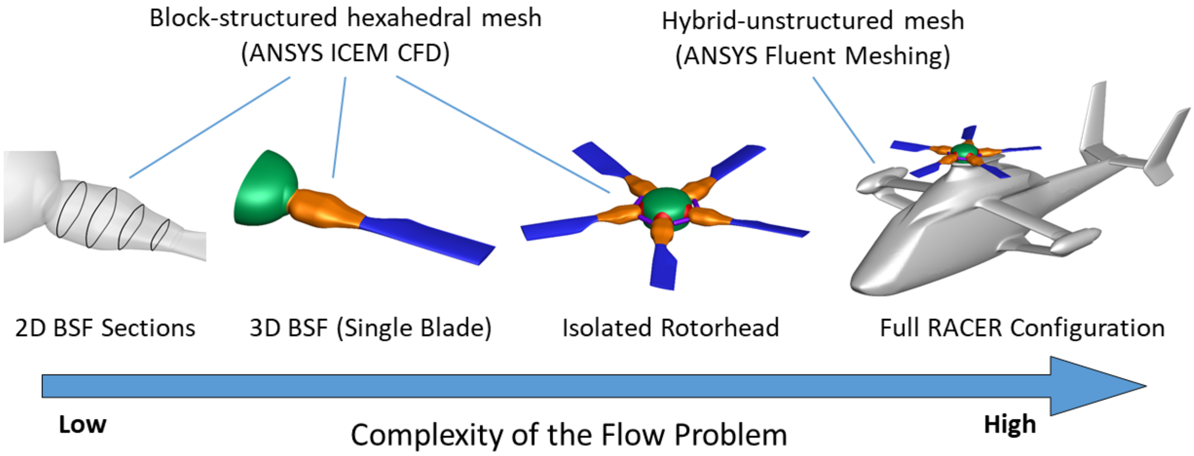

Figure 4.2: Selection of the mesh topology depending on the complexity of the investigated flow problem.

4.1.2 Overset Mesh Interpolation

An overset mesh approach is used to realize the cyclic blade-pitch movement of the RACER main rotor. The introduction to overset mesh interpolation is based on the author's publication in the Aerospace Journal in 2021 [14].

Overset mesh is also known as Chimera and it represents a numerical strategy that allows to subdivide a fluid domain into several overlapping regions, which can be independently meshed from each other. This significantly reduces the mesh generation effort for complex geometries. Benek et al. [116] first introduced the Chimera technique in 1983. The main idea of this technique is to connect the overlapping cell zones by an overset interface, which allows to exchange information between the sub-domains at the newly formed cell-zone boundaries. An exemplary 2D overset mesh case consisting of three component grids is illustrated in Fig. 4.3. The component meshes are embedded in the background mesh overlapping each other. Furthermore, the blue cell zone is protruding the boundary at the bottom side of the background mesh. The overset boundaries and the wall boundaries of the component meshes are marked in Fig. 4.3a. Benek et al. [117] mention that a hierarchical embedding process is employed during the overset mesh generation to manage the data exchange among the grids. Embedded grids are on a lower hierarchical level than the grids in which they are embedded. Hence, the background mesh of the present example is on the highest hierarchical level and the three component meshes are on the same level. The hierarchical approach proved to be beneficial concerning the generation of the data structure and the limitation of the search effort to find points in other grids that can be used to interpolate boundary data. Regarding Fig. 4.3a, it can be observed that some points of the background mesh lie within the solid boundary of the component meshes. These points must be discarded from the solution process, because they lie outside of the computational domain.

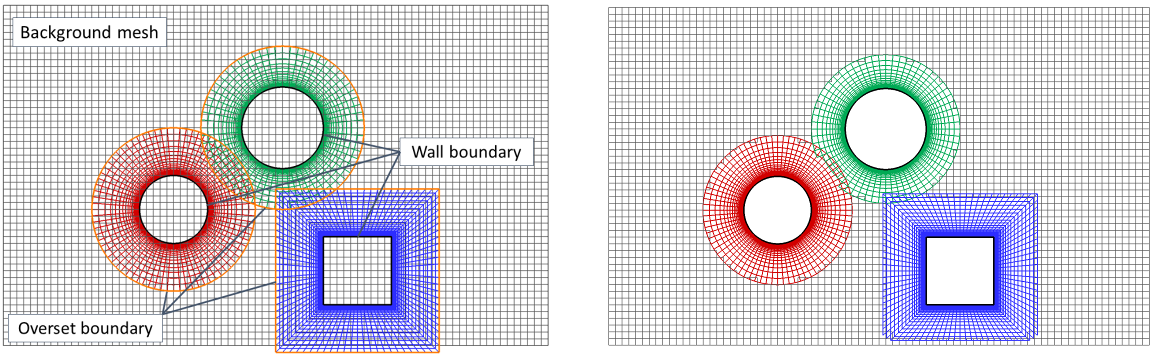

(a) Background mesh and three embedded component meshes.

(b) Solve cells after the initialization of the overset mesh.

Figure 4.3: Exemplary visualization of the overset mesh generation using a background mesh with three component meshes [14].

If the background mesh has a lot of points in common with the component mesh, it is necessary to discard irrelevant points from the solution process in order to avoid time consuming data interpolation and update processes. Furthermore, Lombard and Venkatapathy [118] mention that an extensive interpolation between the different mesh components can highly degrade the global accuracy. This is even intensified, if there is a large discrepancy between the spatial resolutions of the considered meshes. In order to avoid these problems, only the boundary of each component mesh is updated at each time step.

The so called "hole cutting" process is used to exclude certain cells from the solution process during the initialization of the overset mesh. Figure 4.3b shows the overset mesh after hole cutting for the given 2D example. In the final mesh that is used for the flow simulation, regions of different cell types are present, which can be seen in Fig. 4.4. The background mesh after hole cutting is given on the left-hand side of Fig. 4.4. The corresponding component meshes are shown on the right-hand side of the figure. The blue colored areas represent blanked/masked cells, which are discarded from the solution process on the respective grid level. Moreover, the green cells are used to calculate the flow equations and therefore, they are denoted as "computed" cells. Based on the interpolation method between the different component meshes, a certain overlap must be guaranteed to enable an interpolation at the hole boundary. The communication between the background and the component meshes is achieved by donor (red) and receiver (cyan) cells. The donor cells constitute a subset of the computed cells and provide data to the receiver cells of the neighboring domain. In order to reduce interpolation errors at the overset boundaries, a similar mesh resolution should be provided in the transition region between the mesh components.

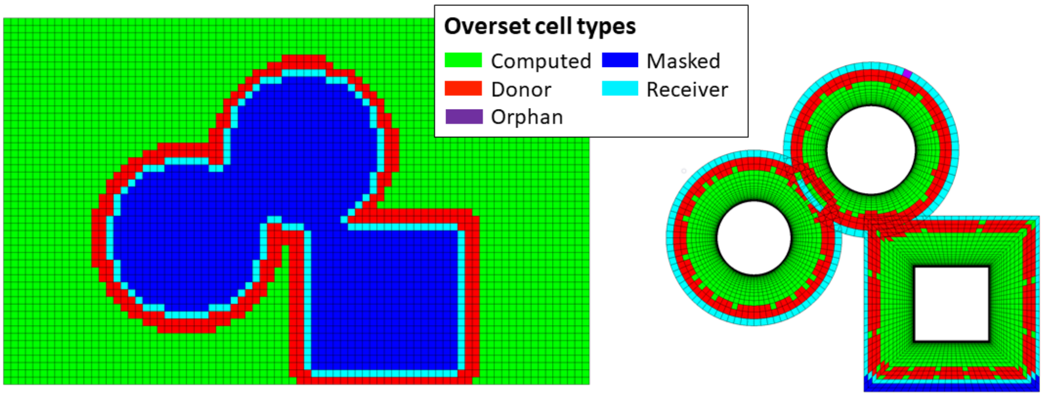

Figure 4.4: Overset mesh cell types and visualization of the hole cutting process forming a new boundary used for data interpolation between the mesh components [14].

The definition of the overset mesh connectivity is finalized by the donor search. For this purpose, valid compute cells are determined, which contain the cell centroids of the corresponding receiver cells. At least one valid donor cell is required for each receiver. According to the ANSYS Fluent user guide [107], four or more cells are required in the overlap region of both meshes to enable a successful donor search. Finally, the receiver cells form the fringe layer of a mesh zone defining the transition region to the opposing mesh. A valid mesh overlap is depicted in Fig. 4.5 for two component meshes. If the donor search fails and the receiver cell cannot find a valid donor, it becomes an orphan cell. The presence of orphan cells indicates an insufficient overlap between the meshes or a too large discrepancy in the mesh resolution.

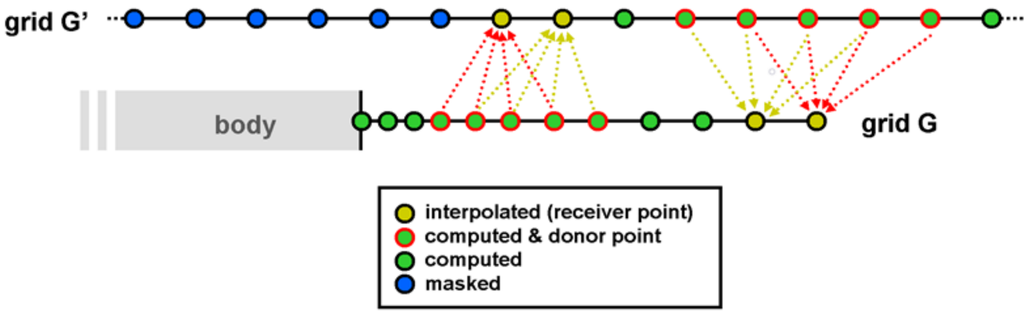

Figure 4.5: Sketch of a valid mesh overlap leading to a successful donor search for two mesh components [3].

4.2 Computational Fluid Dynamics

This section provides a short introduction to the principles of computational fluid dynamics (CFD) and the underlying methods used within this thesis.

According to Anderson [15], there are three main fields in fluid dynamics, which are schematically shown in Fig. 4.6. These include the classical domains of experiments and analytical methods as well as the most recent field of CFD. CFD was first introduced in the 1960s, and before that time, the major advancements in fluid mechanics were achieved by experiments in combination with theoretical analyses [15]. A major drawback of theoretical analyses is that simplifications are introduced to reach a closed-form solution, which typically does not include all flow physics properly. At this point, a remedy is found by CFD, which is continuously gaining importance in engineering applications. A state-of-the-art numerical flow simulation is capable of capturing complex flow phenomena with high accuracy using sophisticated mathematical models for the governing equations of mass, momentum and energy. These equations represent the basis for all CFD applications. Nowadays, CFD is complementing wind-tunnel experiments and theoretical analyses to support the solution of complex problems in fluid mechanics. However, due to the fast development of computers and the fact that CFD is economically cheaper than wind-tunnel measurements, it is partly replacing experiments during the preliminary design phase of new aircraft. The accuracy of a CFD simulation strongly depends on the implemented physical models and the boundary conditions. Furthermore, truncation errors of the applied solution algorithm can compromise the accuracy of the CFD results. Therefore, wind-tunnel measurements are still being used to validate numerical flow simulations and to fine-tune the final design of the aircraft [15].

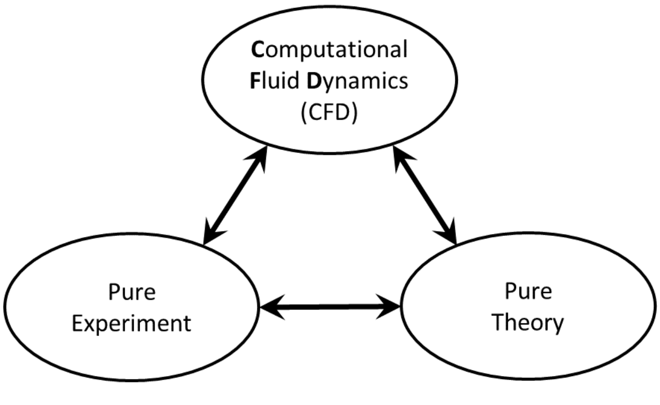

Figure 4.6: The three main fields of fluid dynamics, adapted from [15].

4.2.1 Principles of Fluid Mechanics

The mathematical description of fluid dynamics is based on the fundamental governing equations for continuity, momentum and energy, which are also known as the Navier-Stokes equations, see Ferziger and Peric [119]. In general, the Navier-Stokes equations are nonlinear, partial differential equations that can be used to describe any kind of problem in fluid mechanics. However, the mathematical treatment of these equations can be quite challenging and exact solutions are only available for simplified flow problems. The definition of a general mathematical model, which can be used to calculate any fluid mechanics problem, is unpractical or even impossible. Therefore, different models are derived and they are tailored for their application purpose in the numerical solution process.

In order to be able to classify the investigated flow problems, two dimensionless quantities are mainly used, which are given by the Mach number M and the Reynolds number Re. According to Eq. 4.1, the Mach number is defined as the ratio between the free-stream velocity V_∞ and the speed of sound a. It serves as a measure for the compressibility of the investigated flow problem.

$$M = \frac{V_\infty}{a} \tag{4.1}$$

where:

M = Mach number [-]
V_∞ = Free-stream velocity [m/s]
a = Speed of sound [m/s]

The typical classification of flow regimes at different Mach numbers is depicted in Fig. 4.7. The flow can be incompressible ($M << 1$), subsonic ($0 < M < 1$), transonic ($M \approx 1$), supersonic ($M > 1$) or hypersonic ($M >> 1$) [120].

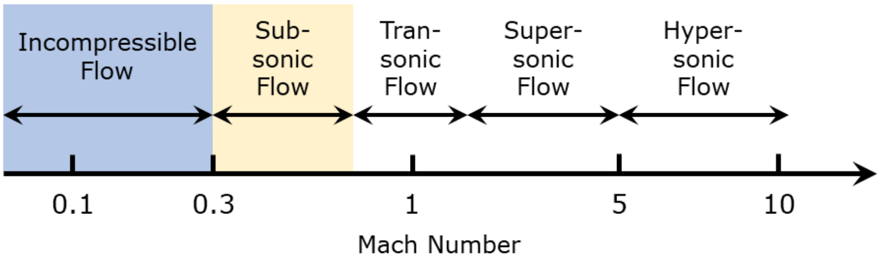

Figure 4.7: Flow regimes depening on the Mach number, adapted from [16].

The targeted sea-level cruise speed of the RACER demonstrator corresponds to a Mach number of $M \approx 0.33$. Therefore, compressible flow is assumed for all CFD simulations within the present work.

The highest flow velocities are obtained at the blade tip of the advancing rotor blade, which is related to the superposition of the helicopter cruise speed with the circumferential speed of the rotor. The tip region of the advancing rotor blade usually operates close to the transonic flow region. Hence, special attention must be paid to the local Mach numbers to avoid transonic effects, like shock-induced flow separation. Regarding the present thesis, truncated rotor blades are considered keeping the observed flow within a subsonic, compressible flow regime.

The Reynolds number Re is applied to characterize the boundary layer and the turbulent flow patterns for a given flow problem. Moreover, it serves as a reference to estimate whether the expected flow is laminar or turbulent. The definition of the Reynolds number is given by Eq. 4.2. Depending on the free-stream velocity, the characteristic length scale of the investigated geometry and the viscosity of the fluid, different boundary layer characteristics and turbulent flow structures can be observed. The influence of the Reynolds number on the boundary layer of a flat plate is illustrated in Fig. 4.8. The boundary layer consists of a laminar region in the front part, a transition region in the middle part and a turbulent region in the back part of the plate.

$$Re = \frac{V_\infty \cdot L}{\nu} \tag{4.2}$$

where:

Re = Reynolds number [-]
V_∞ = Free-stream velocity [m/s]
L = Characteristic length scale [m]
ν = Kinematic viscosity [m^2/s]

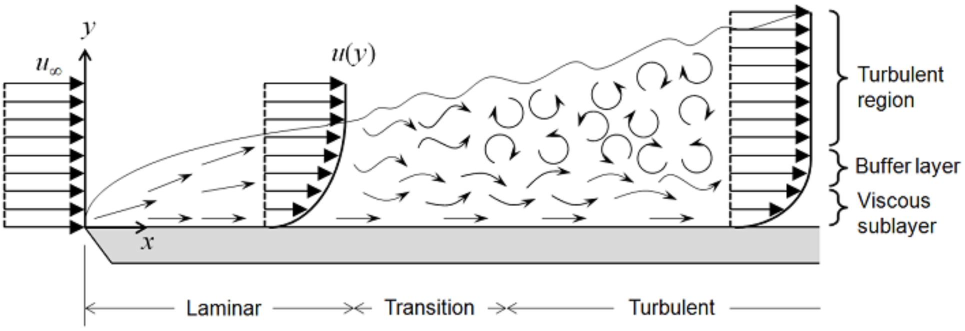

Figure 4.8: Flat-plate boundary layer showing the transition from laminar to turbulent flow [17].

Furthermore, the type of boundary layer has a strong impact on the drag of a body, as depicted in Fig. 4.9 for the given example. The drag coefficient C_d is shown for different Reynolds numbers Re. It can be seen that up to $Re \approx 500.000$ the drag coefficient is decreasing and thereafter, a sudden change in the drag characteristic can be detected.

This is related to the transition from laminar to turbulent flow. It can be seen that the drag coefficient is also decreasing for turbulent flow with increasing Reynolds number. However, the gradient of the curve is weaker than for the laminar flow.

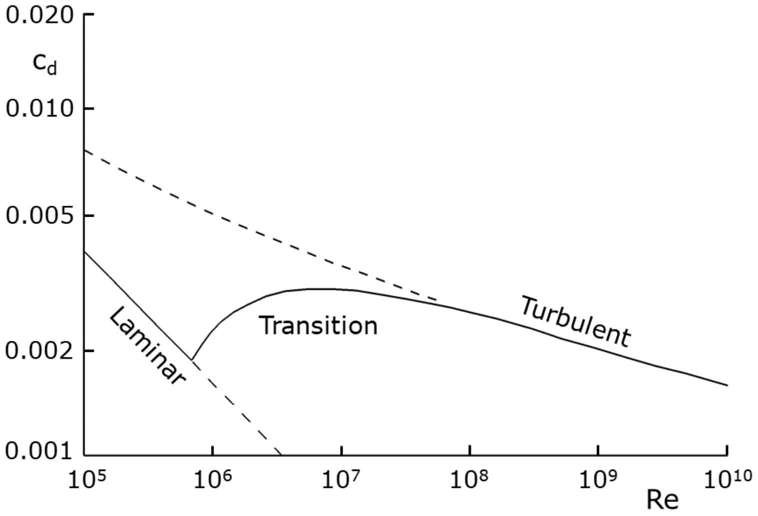

Figure 4.9: Drag coefficient C_d of the flat plate depending on the Reynolds number Re, adapted from [18].

Regarding the numerical flow simulations of the present thesis, fully turbulent flow is assumed for all cases due to the high cruise speed of the RACER demonstrator, which leads to a Reynolds number per meter of $Re_m \approx 7.7 \cdot 10^6$.

The correct prediction of turbulent flow is a major challenge in CFD. This is caused by the fact that turbulent flow exhibits a wide range of flow structures with different length scales and energy levels. Figure 4.10 shows the energy spectrum of the turbulent kinetic energy from the largest to the smallest turbulent length scales. The size of the respective eddies is defined by the wave number k. The largest flow structures are given by the integral length scales in the energy-containing range of the spectrum. Turbulent flow structures of intermediate size are located in the inertial subrange and the smallest eddies are given in the dissipation range. The energy cascade transfers energy from the large flow structures to the smaller ones. The turbulent kinetic energy is then dissipated by flow structures of the Kolmogorov length scale representing the smallest scale in the turbulent spectrum.

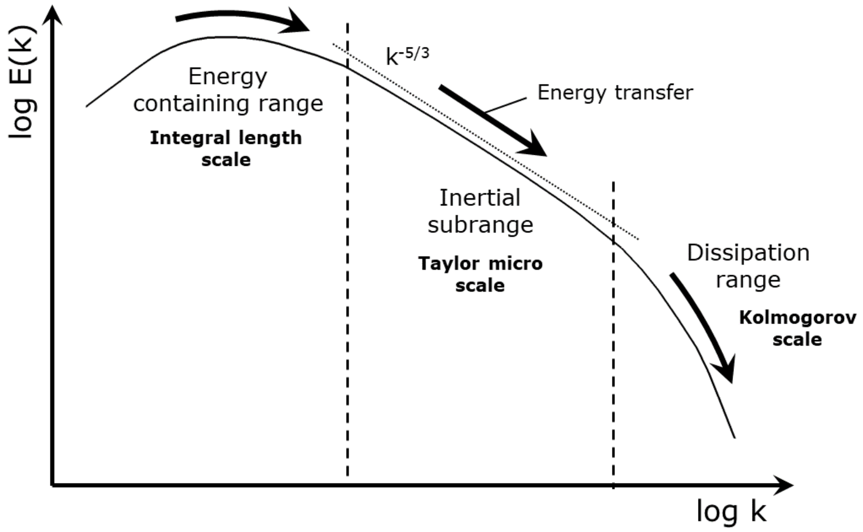

Figure 4.10: Characteristics of the turbulent kinetic energy spectrum, adapted from [19].

There are several methods available to calculate turbulent flow in CFD and the most common ones are depicted in Fig. 4.11. These methods are ordered from the lowest to the highest complexity, which correlates with the computational effort and the numerical accuracy. The three basic methods include the Reynolds-averaged Navier-Stokes (RANS) equations, the Large-Eddy Simulation (LES) and the Direct Numerical Simulation (DNS). Additional methods are given by the unsteady Reynolds-averaged Navier Stokes (URANS) equations and a hybrid approach combining RANS and LES, which is also known as Detached Eddy Simulation (DES).

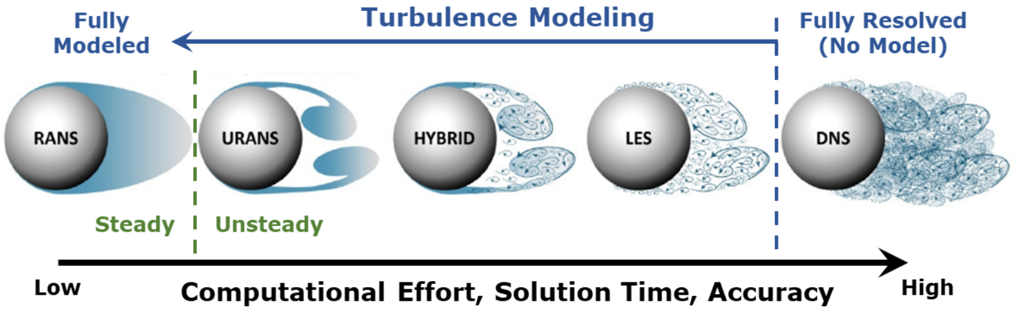

Figure 4.11: Overview of the main methods used to calculate turbulent flow in CFD and their characterization, adapted from [20].

If the temporal and spatial resolution of the numerical flow simulation is fine enough to capture all turbulent flow structures up to the Kolmogorov length scale, one speaks about DNS. This method is the most accurate one, which does not require any turbulence modeling and directly solves the Navier-Stokes equations. However, the application of DNS is limited to basic research and low Reynolds numbers, because the computational effort increases with $\mathcal{O}(Re^3)$ [21].

Regarding LES, the smallest length scales are ignored by low-pass filtering the Navier-Stokes equations. Hence, the small-scale information is removed from the flow-field solution. The filtering operation can be seen as a temporal and spatial averaging of the numerical solution. The influence of the unresolved, small-scale turbulence is incorporated by modeling the residual stress tensor in the LES equations. For this purpose, sub-grid scale models are employed [21]. In terms of computational effort, LES lies between DNS and RANS simulations.

The Detached Eddy Simulation (DES), which is referred to as Hybrid in Fig. 4.11, uses RANS for the near-wall flow with attached boundary layer and LES for the free shear flow. Hence, the computational effort for complex geometries and high Reynolds numbers can be significantly reduced compared to pure LES. Moreover, the accuracy of the scale-resolving LES delivers accurate results for the turbulent flow field in the wake of the investigated body.

Based on the complexity of the investigated flow problems, the high Reynolds numbers and the applied numerical methods, steady and unsteady RANS simulations are performed within the present work. RANS models are widely used in engineering applications, because they yield a reasonable balance between computational efficiency and numerical accuracy. Moreover, the main focus lies on the evaluation of the aerodynamic forces and moments to determine the cruise flight performance of the RACER demonstrator. The impact of the rotor-head wake on the tail of the helicopter is of less interest and therefore, it is not required to accurately capture all length and time scales of the turbulent flow structures. This allows for the application of coarser meshes and bigger time steps, which significantly reduces the computational effort and enables the evaluation of a large number of designs within a reasonable time frame. RANS is based on the idea that turbulent flow can be decomposed into a mean and a fluctuating component, as illustrated by Fig. 4.12 and Eq. 4.3 for a single velocity component $u_i(t) (i = 1,2,3)$.

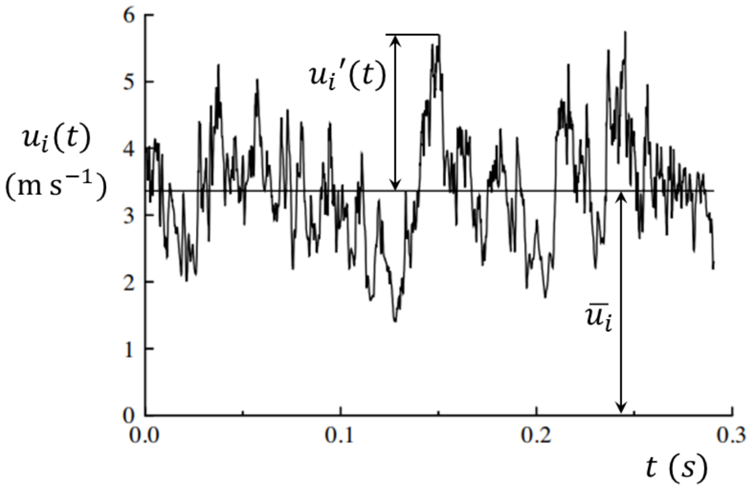

Figure 4.12: Turbulent velocity signal $u_i(t)$ decomposed into the mean velocity $\overline{u_i}$ and the fluctuation $u_i'(t)$, adapted from [21].

$$u_i(t) = \overline{u}_i + u_i'(t) \tag{4.3}$$

The decomposition of pressure and other scalar quantities is done in the same manner. The flow variables from the instantaneous Navier-Stokes equations are replaced by the decomposed components. Subsequently, Reynolds-averaging is conducted, which leads to the RANS equations [22]:

Continuity equation:

$$\frac{\partial \rho}{\partial t} + \frac{\partial}{\partial x_i}\left(\rho \overline{u}_i\right) = 0 \tag{4.4}$$

Momentum equation:

$$\frac{\partial}{\partial t}\left(\rho \overline{u}_i\right) + \frac{\partial}{\partial x_j}\left(\rho \overline{u}_i \overline{u}_j\right) = -\frac{\partial \overline{p}}{\partial x_i} + \frac{\partial}{\partial x_j}\left[\mu\left(\frac{\partial \overline{u}_i}{\partial x_j} + \frac{\partial \overline{u}_j}{\partial x_i} - \frac{2}{3}\delta_{ij}\frac{\partial \overline{u}_k}{\partial x_k}\right)\right] + \frac{\partial}{\partial x_j}\left(-\rho\overline{u_i' u_j'}\right) \tag{4.5}$$

Compared to the original Navier-Stokes equation, Eq. 4.5 contains an additional term, which represents the divergence of the Reynolds-stress tensor $\tau_{ij} = \rho\overline{u_i' u_j'}$. This symmetric tensor incorporates the effect of turbulent motions on the mean stresses of the flow field. The diagonal elements of the tensor τ_{ij} represent the normal stresses and the off-diagonal elements yield the shear stresses. The Reynolds-stress tensor introduces six additional unknowns to the system of equations leading to a closure problem for the RANS equations. In order to be able to solve this problem, a suitable modeling approach for the Reynolds stresses is required, which allows for the expression of the Reynolds stresses by mean flow quantities. For this purpose, a wide range of turbulence models is available and the most common ones are summarized by Pope [21]. Within the present work, an eddy viscosity turbulence model is employed and a detailed description about this model is given in Sec. 4.2.2.

4.2.2 Turbulence Modeling

Concerning RANS simulations, there are two main types of turbulence models, which are given by eddy-viscosity models and Reynolds-stress models [21]. Within the present work, an eddy-viscosity turbulence model was chosen. These kind of models are widely used in engineering applications and they are based on the idea that the Reynolds-stress tensor $\tau_{ij} = \rho\overline{u_i' u_j'}$ can be modeled as a function of the mean shear rate S_{ij} and the eddy viscosity ν_t. The eddy viscosity represents the momentum transfer by turbulent eddies and acts in a similar way as the molecular viscosity, which describes the momentum transfer by molecular diffusion.

Equation 4.6 shows the eddy viscosity hypothesis, which is also known as the Boussinesq approximation [121]. This hypothesis is used to replace the Reynolds-stress tensor in Eq. 4.5.

$$\overline{u_i'u_j'} - \frac{2}{3}k\delta_{ij} = -2\nu_t S_{ij} \tag{4.6}$$

According to Eq. 4.7, the trace of the Reynolds-stress tensor yields twice the turbulent kinetic energy k. Furthermore, the mean shear stress tensor S_{ij} is defined by Eq. 4.8.

$$k = \frac{1}{2}\left(\overline{u_i'u_i'}\right) \tag{4.7}$$

$$S_{ij} = \frac{1}{2}\left(\frac{\partial \overline{u}_i}{\partial x_j} + \frac{\partial \overline{u}_j}{\partial x_i}\right) \tag{4.8}$$

The newly introduced eddy viscosity ν_t is calculated by the turbulence model. For this purpose, several types of eddy-viscosity models are available and the most common ones are summarized by [122]. These models include algebraic, one-equation and two-equation models. For the present thesis, the shear-stress transport (SST) k-ω model was selected, which was developed by Menter as an improvement of the baseline (BSL) k-ω model in 1994 [123]. Both models introduce two additional transport equations for the turbulent kinetic energy k and the specific dissipation rate ω. Furthermore, the standard Wilcox k-ω model is sensitive regarding the free-stream conditions of k and ω outside the shear layer. Therefore, the BSL and the SST model use a blending function between the k-ω formulation in the near-wall region and k-ϵ formulation in the far field.

The transport equations for k and ω are given by Eq. 4.9 and Eq. 4.10, respectively. The equations are presented as they are implemented in the flow solver ANSYS Fluent [22, 107].

$$\frac{\partial}{\partial t}(\rho k) + \frac{\partial}{\partial x_i}(\rho k \overline{u}_i) = \frac{\partial}{\partial x_j}\left(\Gamma_k \frac{\partial k}{\partial x_j}\right) + G_k - Y_k + S_k \tag{4.9}$$

$$\frac{\partial}{\partial t}(\rho \omega) + \frac{\partial}{\partial x_i}(\rho \omega \overline{u}_i) = \frac{\partial}{\partial x_j}\left(\Gamma_\omega \frac{\partial \omega}{\partial x_j}\right) + G_\omega - Y_\omega + D_\omega + S_\omega \tag{4.10}$$

The term G_k represents the production of turbulent kinetic energy k and G_ω yields the generation of the specific dissipation rate ω. The effective diffusivity of k and ω is given by Γ_k and Γ_ω, respectively. Y_k and Y_ω represent the dissipation of k and ω due to turbulence.

Furthermore, D_ω is the cross-diffusion term and S_k as well as S_ω are user-defined source terms. A detailed description about each term in Eq. 4.9 and Eq. 4.10 is given in the Fluent theory guide [22].

The SST k-ω turbulence model includes all features of the BSL model. Moreover, it considers the transport of the turbulent shear stress in the definition of the eddy viscosity. Therefore, the SST model is more accurate and reliable than the standard k-ω and the BSL k-ω model. The SST model better predicts the onset and the development of flow separation from smooth surfaces, which is related to the consideration of the turbulent shear-stress transport. The BSL model typically overpredicts the eddy viscosity and therefore, the SST model uses a limiter for the formulation of the eddy viscosity, as defined by Eq. 4.11.

$$\mu_t = \frac{\rho k}{\omega} \frac{1}{max\left[\frac{1}{\alpha^*}, \frac{SF_2}{a_1 \omega}\right]} \tag{4.11}$$

S is the strain rate magnitude and α^* damps the turbulent viscosity acting as a low-Reynolds number correction. The definition of α^* is given by Eq. 4.12.

$$\alpha^* = \alpha^*_\infty \left(\frac{\alpha^*_0 + Re_t/R_k}{1 + Re_t/R_k} \right) \tag{4.12}$$

where:

$$Re_t = \frac{\rho k}{\mu \omega},\ R_k = 6,\ \alpha^*_0 = \frac{\beta_i}{3},\ \alpha^*_\infty = 1,\ \beta_i = 0.072$$

Furthermore, the function F_2 is calculated by:

$$F_2 = tanh\left(\phi_2^2\right) \tag{4.13}$$

$$\phi_2 = max\left[2\frac{\sqrt{k}}{0.09\omega y}, \frac{500\mu}{\rho y^2 \omega}\right] \tag{4.14}$$

where y represents the distance to the next surface. All model constants of the k-ω SST turbulence model are summarized in the ANSYS Fluent theory guide [22, p. 64].

4.2.3 Flow Solvers

In order to provide enhanced modularity and flexibility of the optimization tool chain, two different flow solvers are implemented. These are given by the commercial flow solver ANSYS Fluent and the DLR-TAU code, which is developed and maintained by the German Aerospace Center (DLR). The integration of different mesh generators and flow solvers enables its application within a wide range of the aerospace domain supporting the aerodynamic design optimization of future aircraft. Regarding the present work, both flow solvers are used during the design optimization of the RACER blade-sleeve fairing. Hence, the main characteristics and capabilities of both flow solvers are briefly introduced within this section.

ANSYS Fluent

ANSYS Fluent is a commercial, state-of-the-art CFD software used to model fluid flow for complex geometries. Furthermore, heat transfer and chemical reactions can be investigated. A comprehensive overview of the physical models in ANSYS Fluent is given by the theory guide [22]. The software is written in C language, which enables true dynamic memory allocation, flexible solver control and efficient data structures. ANSYS Fluent is an unstructured solver using an internal data structure to order cells, faces and grid points. Hence, it does not require ijk-indexing to determine the neighboring cells. This offers full flexibility in terms of mesh structure and topology. Supported mesh types include 2D triangular/quadrilateral, 3D tetrahedral/hexahedral/pyramid/wedge/polyhedral and mixed (hybrid) meshes. Moreover, the computational mesh can be refined based on the flow solution during a simulation run. ANSYS Fluent offers a meshing and a solution mode. The meshing mode can be used to generate unstructured grids consisting of tetrahedral, hexahedral, polyhedral, prismatic or pyramidal cells. Within the present work, the ANSYS Fluent mesh generator was used to create the computational mesh for the core geometry of the RACER demonstrator. Combined with the structured rotor head mesh, the full RACER compound helicopter mesh is obtained. In order to realize the rotational movement of the rotor head within the numerical flow simulations, ANSYS Fluent offers time-accurate mesh-motion techniques.

There are two different flow solvers available in ANSYS Fluent, which are given by the pressure-based and the density-based solver. From a historical point of view, the pressure-based solver was developed for low-speed, incompressible flows and the density-based solver was intended to be used for high-speed, compressible flows. However, both solvers have been reformulated and extended allowing them to be used for a wide range of flow conditions reaching from incompressible to highly compressible flow. Nevertheless, the density-based flow solver provides an accuracy advantage for high-speed compressible flows.

In the present thesis, the pressure-based solver is chosen for all flow simulations, because mildly compressible flow problems are addressed and faster convergence is obtained in comparison to the density-based solver. Using this solver, the pressure field is calculated by solving a pressure equation that is derived by manipulating the continuity and momentum equations. In general, the numerical solution is obtained by solving the integral governing equations for mass, momentum and, if necessary, energy as well as other scalar quantities such as turbulence. The solver is based on a finite-volume method and the pressure-based version uses an algorithm that belongs to a class of methods known as projection method [124]. Regarding the projection method, the continuity equation, which yields the mass conservation of the velocity field, is satisfied by a pressure-corrected velocity field. Due to the fact that the governing equations are coupled and nonlinear, an iterative solution process is required.

The pressure-based solver contains two different solution algorithms, which are given by the segregated and the coupled algorithm. The working principles of both algorithms are demonstrated by Figure 4.13.

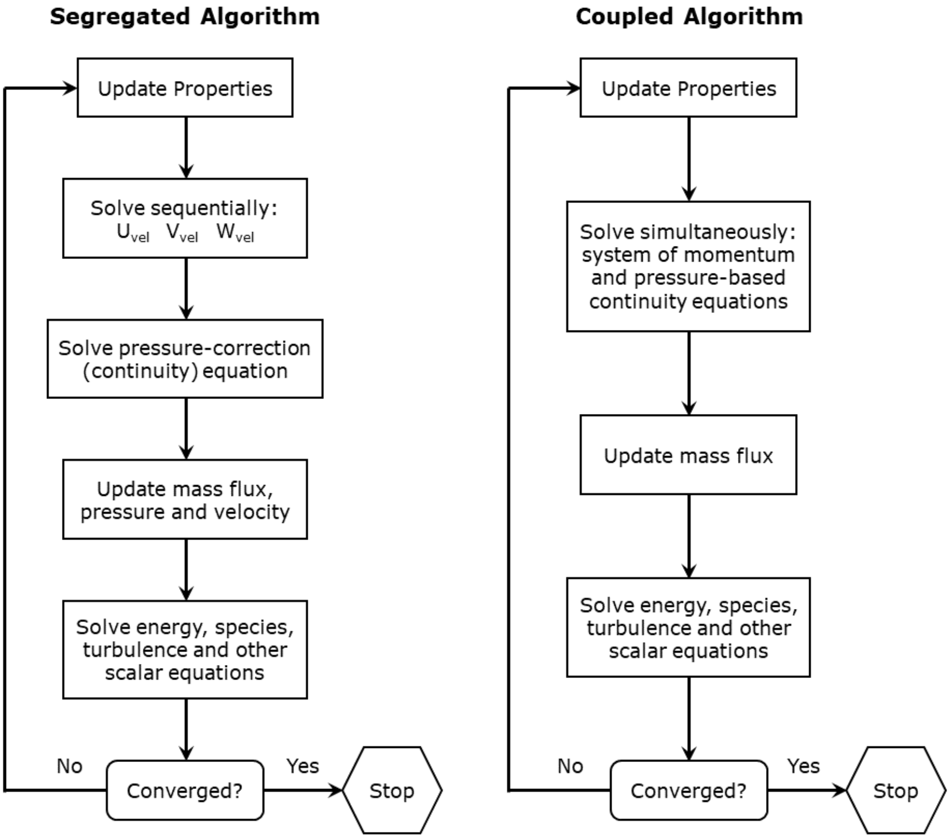

Figure 4.13: Workflow of the pressure-based solution algorithms, adapted from [22].

Regarding the segregated algorithm, all governing equations are sequentially solved, which offers a memory efficient approach. However, slower convergence is obtained and it is less stable than the coupled algorithm for complex flow problems.

Comparing both algorithms, it can be seen that the second and third step of the segregated algorithm are replaced by a single one dealing with the solution of a coupled system of equations for continuity and momentum. Moreover, the coupled approach accelerates the solution convergence, but it increases the memory requirement by 1.5-2 times. Additional transport equations such as the ones for turbulence are solved in a decoupled manner as for the segregated algorithm. In order to demonstrate the discretization of the governing equations and their solution in ANSYS Fluent, an unsteady transport equation for an arbitrary scalar quantity φ is employed, which is given by Eq. 4.15. This equation is applied to each cell (control volume) of the computational domain.

$$\int_V \frac{\partial \rho\varphi}{\partial t} + \oint \rho\varphi\vec{v} \cdot d\vec{A} = \oint \Gamma_\varphi \nabla\varphi \cdot d\vec{A} + \int_V S_\varphi dV \tag{4.15}$$

where:

ρ = Density
$\vec{v}$ = Velocity vector
$\vec{A}$ = Surface area vector
Γ_φ = Diffusion coefficient for φ
$\nabla\varphi$ = Gradient of φ
S_φ = Source of φ per unit volume

The discretization of Eq. 4.15 for an arbitrary control volume is illustrated by Fig. 4.14. Two control volumes with the cell centers c_0 and c_1 are shown. Furthermore, the face normal vector $\vec{A}_f$ of the triangular cell and the two displacement vectors ($\vec{r_0}$, $\vec{r_1}$) are marked.

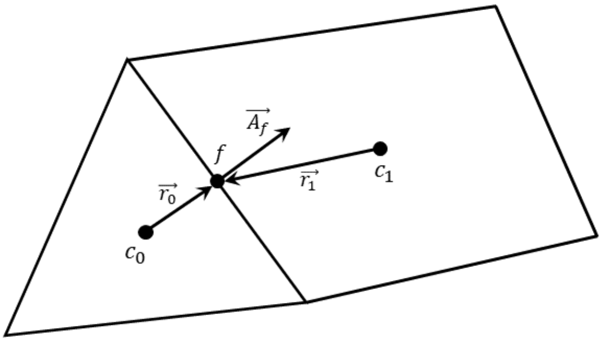

Figure 4.14: Illustration of the discretization of a scalar transport equation for an arbitrary control volume, adapted from [22].

Based on the example shown in Fig. 4.14, the numerical discretization of Eq. 4.15 is given by Eq. 4.16. Here, the term $\frac{\partial \rho \varphi}{\partial t} V$ represents the temporal discretization, which is described later in this section.

$$\frac{\partial \rho \varphi}{\partial t} V + \sum_{f}^{N_{faces}} \rho_f \vec{v}_f \varphi_f \cdot \vec{A}_f = \sum_{f}^{N_{faces}} \Gamma_\varphi \nabla \varphi_f \cdot \vec{A}_f + S_\varphi V \tag{4.16}$$

where:

N_{faces} = Number of faces enclosing the cell
φ_f = Value of φ convected through the face f
$\rho_f \vec{v}_f \cdot \vec{A}_f$ = Mass flux through the face f
$\vec{A}_f$ = Area vector of the face f
$\nabla \varphi_f$ = Gradient of φ at the face f
V = Cell Volume

In general, Eq. 4.16 will be nonlinear with respect to the unknown variables and therefore, a linarization is performed leading to Eq. 4.17. The subscript nb corresponds to neighboring cells and a_P as well as a_{nb} yield the linearized coefficients for the variables φ and φ_{nb}. The number of cell neighbors is defined by the mesh topology and usually corresponds to the number of cell faces, except for the boundary cells.

$$a_P \varphi = \sum_{nb} a_{nb} \varphi_{nb} + b \tag{4.17}$$

The application of Eq. 4.17 to all cells of the computational domain leads to a system of algebraic equations with a sparse coefficient matrix. An implicit Gauss-Seidel solver [125] is employed together with an algebraic multigrid (AMG) method [126] to solve this linear system of equations.

Spatial Discretization

The actual value of the quantitiy φ is stored at the cell center of each control volume. In order to be able to calculate the convection terms, the face values φ_f are required. For this purpose, ANSYS Fluent applies an upwinding scheme to derive the face values by interpolating the cell center values. Within the present work, a second-order upwind and a bounded central differencing scheme are mainly used.

Regarding the second-order upwind scheme, the face value φ_f is calculated by Eq. 4.18.

$$\varphi_f = \varphi + \nabla\varphi \cdot \vec{r} \tag{4.18}$$

where:

φ = Cell-centered value in the upstream cell
$\nabla\varphi$ = Gradient of the cell-centered value in the upstream cell
$\vec{r}$ = Displacement vector from the upstream centroid to the face centroid

The central-differencing scheme provides improved accuracy, especially for scale-resolving simulations, and it is defined by Eq. 4.19. The indices 0 and 1 are referred to the cells $c0$ and $c1$ sharing the face f, see Fig. 4.14.

$$\varphi_f = \frac{1}{2}\left(\varphi_0 + \varphi_1\right) + \frac{1}{2}\left(\nabla\varphi_0 \cdot \vec{r}_0 + \nabla\varphi_1 \cdot \vec{r}_1\right) \tag{4.19}$$

where:

φ_i = Cell-centered value of the variable φ for the cell c_i
$\nabla\varphi_i$ = Reconstructed gradient at the cell c_i
$\vec{r}_i$ = Vector from the cell centroid to the face centroid of the cell c_i

The gradient $\nabla\varphi$ of each cell is determined by a least squares cell-based approach. For more details about the gradient reconstruction, the reader is referred to the ANSYS theory guide [22].

Temporal Discretization

If transient flow simulations are performed, the governing equations must be discretized in space and time. The spatial discretization is the same as for steady-state flow simulations and the temporal discretization deals with the integration of the equations over a time step Δt. In general, the temporal evolution of a scalar quantity φ can be written as:

$$\frac{\partial\varphi}{\partial t} = F(\varphi) \tag{4.20}$$

where the function F represents the spatial discretization. For the present work, an implicit time integration scheme was chosen, which means that the function $F(\varphi)$ is evaluated at a future time level according to Eq. 4.21.

$$\frac{\varphi^{n+1}-\varphi^{n}}{\Delta t}=F\left(\varphi^{n+1}\right) \tag{4.21}$$

In Eq. 4.21, n represents the value at the current time level t and $n+1$ is related to the next time level $t+\Delta t$. Above mentioned method is called implicit, because the scalar quantity φ^{n+1} of the actual cell depends on φ^{n+1} of the neighboring cells. An iterative solution process is employed at each time level to solve the implicit equation Eq. 4.22 before moving on to the next time step.

$$\varphi^{n+1}=\varphi^{n}+\Delta t F\left(\varphi^{n+1}\right) \tag{4.22}$$

For the numerical flow simulations of the present thesis, the second-order time integration scheme of ANSYS Fluent is employed. Furthermore, a fixed time-step size is used leading to the temporal scheme according to Eq. 4.23.

$$\frac{3\varphi^{n+1}-4\varphi^{n}+\varphi^{n-1}}{2\Delta t}=F\left(\varphi\right) \tag{4.23}$$

DLR TAU-Code

The DLR TAU-Code is a CFD software that is developed and maintained by the German Aerospace Center (DLR). It is a modular software system consisting of three main modules, which are given by the pre-processing module, the flow solver and the grid adaptation module. The solver allows to predict flow about complex geometries ranging from low subsonic to hypersonic flow regimes. Moreover, inviscid and viscous flow problems can be addressed. A finite volume scheme is employed to solve the three-dimensional, compressible Reynolds-averaged Navier-Stokes (RANS) equations. In order to extend its use to incompressible flows, a Low-Mach-number preconditioning is implemented. A hybrid unstructured computational grid is used consisting of tetrahedrons, prisms, pyramids and hexahedrons. Moreover, the DLR TAU-Code includes two classes of turbulence models, which are given by pure RANS and hybrid RANS/LES models. The hybrid models are often known as Detached Eddy Simulation (DES) models and they combine scale-resolving methods in the farfield with RANS turbulence models in the near-wall region. The main modules of the DLR TAU-Code can either be used as stand-alone tools or within a Python scripting framework allowing for communication between the modules without file-I/O. An introduction to the DLR TAU-Code is provided by Schwamborn et al. [127] and a detailed description is available in the technical documentation of the flow solver [128].

Preprocessing

The primary grid must be generated by a third-party software and it serves as the input for the TAU pre-processing module. Furthermore, the primary grid is required for adaptive mesh generation and for the visualization of the data during post processing. The TAU-Code is based on a dual-mesh approach and therefore, a secondary grid is generated, which contains all the mesh data that is relevant for the flow solver. The arrangement of the control volumes and the corresponding points to store the flow variable values are defined by the applied grid metric. The DLR TAU-Code provides a cell-vertex and a cell-centered grid metric, which are schematically shown in Fig. 4.15. It can be seen that the cell-centered grid metric leads to the same control volumes for the primary and the secondary grid. Hence, the flow variables are associated with the cell centers. In contrast, the cell-vertex grid metric stores the flow variables at the primary grid vertices and the control volumes of the secondary grid are formed around each primal grid node by connecting the cell centers. However, both grid metrics share the same edge-based data structure to store the connectivity of the control volume. The edge-based data structure makes the flow solver independent of the element types in the primary grid and allows for the application of a multi-grid technique [128].

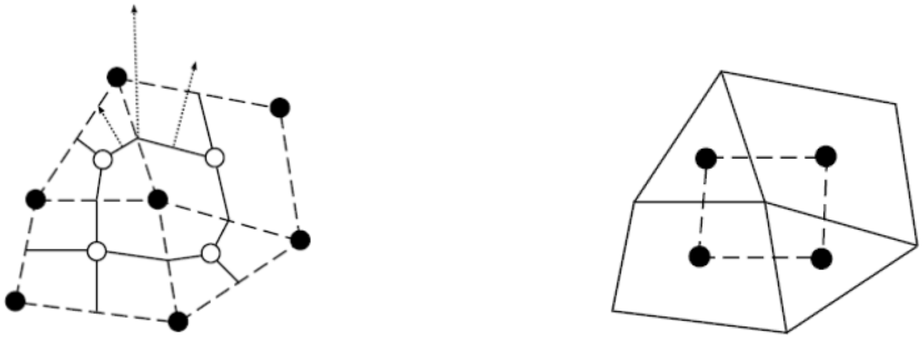

(a) Cell-vertex metric.

(b) Cell-centered metric.

Figure 4.15: Compuational meshes for a cell-vertex and a cell-centered grid metric [23].

Spatial Discretization

Regarding the spatial discretization, schemes of first and second order are available. In the present section, the continuity equation is used to explain the principle idea behind the implemented upwind and central schemes. In general, the governing equations are approximated by finite-difference quotients, as shown by Eq. 4.24 for the continuity equation.

$$\frac{\partial \rho}{\partial t} + \frac{\partial (\rho u)}{\partial x} = 0 \tag{4.24}$$

If a constant velocity u is assumed, Eq. 4.24 becomes a linear convection equation for the transport of mass with the velocity u, which leads to Eq. 4.25.

$$\frac{\partial \rho}{\partial t} + u\frac{\partial \rho}{\partial x} = 0 \tag{4.25}$$

The mathematical description for the flux balance around the cell point i using a first-order upwind scheme is given by Eq. 4.26. For the given example, a forward time-differencing scheme is assumed and the superscript n denotes the actual time step. Moreover, it can be seen that the quantity ρ_i is only depending on the upwind located cell i-1. There are several different functions implemented in the TAU-Code, which can be used for the flux discretization in an upwind scheme. Prominent examples are given by the van Leer [129], the hybrid AUSM-Van Leer [130], the AUSMDV [131] and the Roe [132] upwind scheme.

$$\frac{\rho_i^{n+1} - \rho_i^n}{\Delta t} = -\frac{u}{\Delta x}\left(\rho_i^n - \rho_{i-1}^n\right) \tag{4.26}$$

Besides the upwind schemes, a central scheme is implemented in the flow solver, which can be used in combination with a model for scalar or matrix dissipation. In order to reach a second-order central scheme for the spatial discretization, the variable values from the upwind and the downwind located cells are used according to Eq. 4.27. Again, a simple forward differencing scheme in time is used for the time derivative in the given example.

$$\frac{\rho_i^{n+1} - \rho_i^n}{\Delta t} = -\frac{u}{\Delta 2x}\left(\rho_{i+1}^n - \rho_{i-1}^n\right) \tag{4.27}$$

Temporal Discretization and Solution Techniques

The DLR TAU-Code provides explicit Runge-Kutta and implicit Backward-Euler schemes, which can be used to derive steady-state and time-accurate solutions. Regarding explicit schemes, the numerical solution at a later time is only depending on the solution at the current time, which means that all necessary quantities are known to advance in time. Explicit methods can easily be solved numerically and they feature low memory requirements during the flow simulation. However, the maximum permissible time-step size is quite limited and it has to fulfill a certain requirement concerning the Courant-Friedrichs-Lewy number (CFL number) [133] to provide numerical stability. This criterion is typically given by $CFL \leq 1$. In contrast, implicit methods are much more stable, which allows for significantly larger time steps.

Hence, faster convergence of the numerical solution can be obtained. However, the implementation of implicit methods is complex and the computational cost is much higher than for explicit methods. For each time step, an iterative solution process has to be employed, which requires much more computational time and memory.
Regarding steady-state problems, a fictitious pseudo-time t^* is introduced to compute the time-independent solution and local time stepping is employed to accelerate the convergence. The local time stepping allows for different time-step sizes in each control volume depending on the local CFL number. Furthermore, there are several techniques available that can be used to further accelerate the convergence to the steady-state solution. These are given by Residual Smoothing and Multigrid. Details about these acceleration techniques can be found in the technical documentation of the DLR TAU-Code [128].

Regarding time-accurate computations, global time stepping and dual time stepping [134] are implemented. In the present work, dual time stepping is used for the CFD simulations. It represents a combined approach introducing pseudo time steps in addition to the physical time steps. This means that for every physical time step, the partial differential equations are iteratively solved using the pseudo time step t^*. Therefore, the time-dependent solution is reached by solving a sequence of steady-state problems. Moreover, acceleration techniques, like Local Time Stepping and Multigrid, can also be applied. The selection of the physical time-step size is based on the time-dependent flow features that should be resolved.

5 Blade-Sleeve Fairing Design Optimization

This chapter presents the aerodynamic design optimization of a new blade-sleeve fairing (BSF), which is part of the RACER full-fairing concept. The investigated RACER rotor head is based on the fully-articulated, five-bladed H175 rotor head [135], which can be seen in Figure 5.1. This fairingless H175 rotor head is equipped with a conventional hub cap, which will be replaced by a full-fairing beanie on the RACER demonstrator.

Figure 5.1: Airbus Helicopters H175 with the fairingless rotor head serving as the basis for the RACER rotor head [24].

The BSF is aerodynamically optimized for a steady sea-level cruise flight. For this purpose, the optimization tool chain, which is described in Sec. 3.1 is employed. The aerodynamic design optimization is performed in two steps. The first optimization step consists of an airfoil optimization for selected blade-sleeve sections and its process is described in Sec. 5.1. The rotor head geometry as well as the parameterization of the blade-sleeve sections are introduced. Furthermore, the formulation of the optimization problem and the numerical setup are described. Thereafter, selected results of the design optimization process are presented and a detailed view on the best performing candidates is given. The newly developed blade-sleeve sections are compared to the sectional shapes of the reference BSF, which was developed at Airbus Helicopters during the preliminary design phase of the RACER compound helicopter. The optimized blade-sleeve sections yield the supporting structure for the definition of the three-dimensional fairing shape.

Within the second optimization step, the three-dimensional BSF shape is optimized by using a selected subset of the previously optimized blade-sleeve sections. Section 5.2 deals with the three-dimensional design optimization of the RACER BSF.

At first, the investigated geometry is introduced, which represents a simplified model of the RACER rotor head. A stationary, single rotor blade is considered and therefore, interactional effects with the surrounding helicopter components as well as blade-vortex interactions are neglected during the design optimization process to achieve a suitable computational effort. The parameterization of the geometry is described in detail and the formulation of the optimization problem, which is similar to the two-dimensional design optimization, is provided. Based on the fact that the two-dimensional blade-sleeve sections fulfill the applied design constraints, an unconstrained design optimization is conducted. Regarding the numerical setup, the block-structured computational grid is illustrated and the flow solver settings are introduced. Finally, selected results of the three-dimensional BSF design optimization are presented including a detailed analysis of the objective space, the evaluation of the aerodynamic forces for the most promising designs and the evaluation of relevant flow-field and surface quantities.

5.1 Two-dimensional Design Optimization

This section of the thesis is based on the author's publication in the CEAS Aeronautical Journal [11].

The blade-root region of the rotor head is divided into six sections (S1-S6), which can be seen in Fig. 5.2. The last section in radial direction S6 is located close to the first aerodynamic section of the rotor blade. Furthermore, it is manually designed to fit the rotor-blade contour at this position and to ensure a smooth transition from the BSF to the rotor blade. The most inboard section S1 is manually designed as well to provide a proper transition to the full-fairing beanie. This means that the remaining four blade-sleeve sections S2-S5 are taken into account during the automated aerodynamic design optimization process. Regarding the placement of the sections, it can be seen that the second section S2 is located at the thickest part of the blade root and that, besides the first and the last section, the remaining ones are evenly distributed.

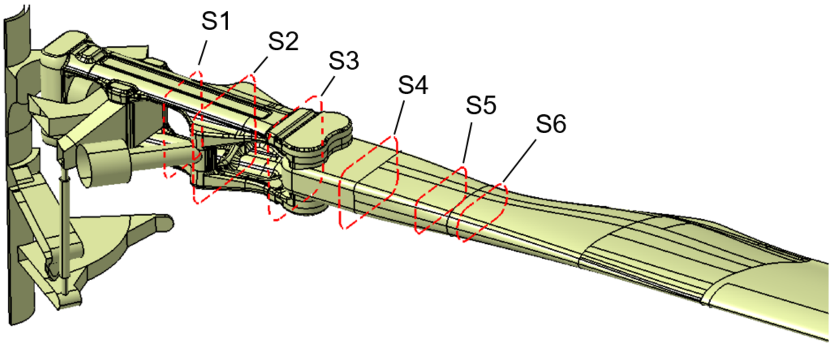

Figure 5.2: Geometrical arrangement of the blade-sleeve fairing sections to be optimized.

The available design space for the BSF is based on the rotor head geometry on the one hand, and design constraints provided by Airbus Helicopters on the other hand. These design constraints are depicted in Fig. 5.3 showing the minimum (green) and the maximum (orange) permissible design space. The design constraints are derived from the movement of the rotor blade and its mechanical components. Furthermore, cooling requirements are limiting the minimum size of the fairing shape, because major cooling issues could arise when covering the rotor head. Hence, this point must be addressed during the design process. The increased temperature under the fairing is caused by hot air coming from the engine compartment and friction heat originating from the movement of the mechanical components. Some rotor-head parts are sensitive to high temperatures and sufficient cooling must be provided, which is a dimensioning parameter for the minimum design space. In order to fulfill the design constraints, the geometry of the fairing must be located between the two surfaces shown in Fig. 5.3.

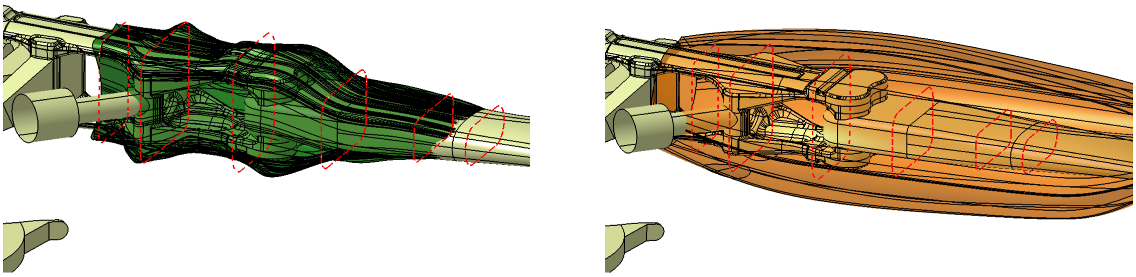

(a) Minimum permissible design space. (b) Maximum permissible design space.

Figure 5.3: Design constraints showing the limits for the minimum and maximum permissible design space of the blade-sleeve fairing.

5.1.1 Geometry Parameterization

The investigated, two-dimensional geometry is parameterized by third-order Bézier curves [136,137]. This parameterization method was originally developed by Bézier and Casteljau for CAD programs in French car companies. Today, Bézier curves represent the mathematical basis for many CAD systems and they provide a fundamental tool for curve and surface description.

The principal idea of a Bézier curve is that it can be described by a set of control points P_0 to P_n , where n represents the order of the curve ($n = 1$ linear, $n = 2$ quadratic, etc.). The mathematical definition of a Bézier curve is given by Eq. 5.1.

$$B(t) = \sum_{i=0}^{n} b_{i,n}(t) P_i \qquad 0 \leq t \leq 1 \tag{5.1}$$

P_i represents the coordinates of the control points and $b_{i,n}(t)$ is the Bernstein basis polynomial of the degree n, which is defined as:

$$b_{i,n}(t) = \frac{n!}{i!\,(n-i)!} t^i\,(1-t)^{n-i} \qquad 0 \leq i \leq n \tag{5.2}$$

where t is the local coordinate of the actually considered curve segment. There are three main properties of the Bernstein polynomial, which are given by [136]:

- partition of unity: $\sum_{i=0}^{n} b_{i,n}(t) = 1$
- positivity: $b_{i,n}(t) \geq 0$ for $t \in [0,1]$
- recursion: $b_{i,n} = (1-t) \cdot b_{i,n-1}(t) + t \cdot b_{i-1,n-1}(t)$

Figure 5.4 shows the parameterization of an arbitrary third-order Bézier curve using the Bernstein polynomial $b_{i,n}(t)$ as the basis function. A third-order curve is derived by four control points ($P_0 - P_3$), as illustrated in Fig. 5.4b. Here, the control polygon is shown by the blue line forming a convex hull containing the actual Bézier curve, which is given by the black curve. The weighting of the control points is obtained by the basis functions shown in Fig. 5.4a. Based on this weighting approach, the starting point and the end point of the Bézier curve coincide with the control points $P0$ and $P3$.

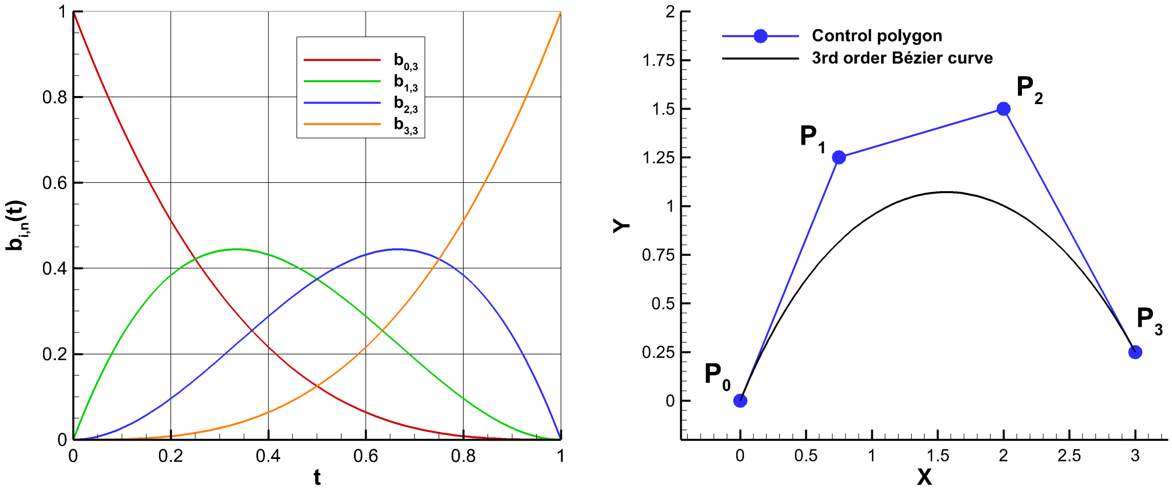

(a) Basis functions for a third-order Bézier curve.

(b) Third-order Bézier curve based on the control polygon $P_0 - P_3$.

Figure 5.4: Geometry parameterization by third-order Bézier curves, adapted from [11].

Figure 5.5 shows the parameterization of an exemplary blade-sleeve section by four third-order Bézier curves ($B_1 - B_4$) and two straight lines on top and bottom. Furthermore, the applied design constraints are schematically shown by the red dotted lines. The coordinates of the Bézier control points (B_iP_{jx}, B_iP_{jz}) yield the design variables for the optimization problem. The black arrows in Fig. 5.5 represent the degrees of freedom of the corresponding control point.

The straight lines on top and bottom of the shape are defined to satisfy mechanical constraints regarding the attachment of the sleeve fairing on the actual rotor head. The axial position (x-direction) of these lines is fixed and only vertical movement is allowed by varying B_1P_{2z} and B_3P_{2z}. This guarantees an easy attachment of the fairings to the rotor hub later in the design process and reduces the complexity of the mounting structure inside the fairing. The horizontal and vertical alignment of the control points enables a tangential transition between the curves of the two-dimensional fairing shape. As demonstrated in Fig. 5.5, the applied design constraints, which are schematically shown by the red dotted lines, consist of a rounded rectangular geometry on the inside and an elliptic geometry on the outside. Depending on the examined radial section, the size and shape of these constraints vary.

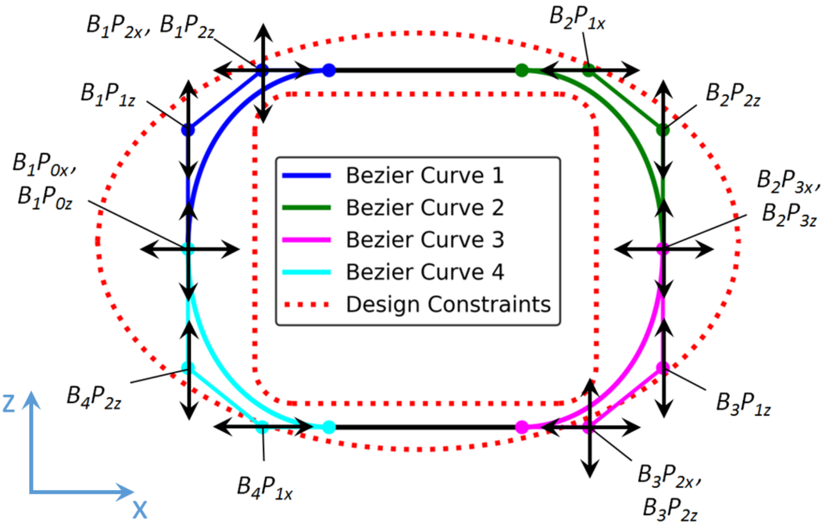

Figure 5.5: Parameterization of the blade-sleeve section by four third-order Bézier curves [11].

5.1.2 Optimization Problem

The aerodynamic design optimization of the RACER rotor-head fairings is conducted for a sea-level cruise flight. As mentioned in Sec. 3.2.1 of the thesis, the advancing and the retreating rotor-blade position are considered to be the most relevant ones to be taken into account during the design optimization process. Therefore, two concurring objective functions are employed, which are given by:

$$maximize \quad f_1(\mathbf{x}) = C_l/C_d \quad (Advancing\ blade) \tag{5.3}$$

$$minimize \quad f_2(\mathbf{x}) = C_d \quad (Retreating\ blade) \tag{5.4}$$

The objective function for the advancing rotor blade is defined by the maximization of the lift-to-drag ratio, which is also known as the aerodynamic efficiency. Regarding the retreating rotor blade, the minimization of drag is the focus, because reversed flow occurs at this azimuthal rotor position. The design variables for the present optimization problem are given by the coordinates of the Bézier control points, as illustrated in Fig. 5.5. Overall, 14 design variables are used to define the shape of the particular blade-sleeve section:

$$\begin{aligned}\mathbf{x} = \{&B_1P_{0x},\, B_1P_{0z},\, B_1P_{1z},\, B_1P_{2x},\, B_1P_{2z},\, B_2P_{1x}, B_2P_{2z}\\ &B_2P_{3x},\, B_2P_{3z},\, B_3P_{1z},\, B_3P_{2x},\, B_3P_{2z},\, B_4P_{1x},\, B_4P_{2x}\}\end{aligned}$$

In Fig. 5.5, it can be seen that on each side of the control polygon four control points are aligned in vertical and horizontal direction. This alignment ensures a tangential transition between the curves. Besides the design space constraints, which are depicted in Fig. 5.3, four additional inequality constraints are applied to the optimization problem. These are given by:

$$\begin{aligned}\textit{subject to} \qquad\qquad & g_1(\mathbf{x}) = B_1P_{0z} - B_1P_{1z} < 0\\ & g_2(\mathbf{x}) = B_2P_{3z} - B_2P_{2z} < 0\\ & g_3(\mathbf{x}) = B_3P_{1z} - B_2P_{3z} < 0\\ & g_4(\mathbf{x}) = B_4P_{2z} - B_1P_{0z} < 0\end{aligned}$$

The inequality constraints are necessary to ensure convexity of the Bézier curves and to avoid unfavorable, peaky contour shapes. Regarding the design constraints shown in Fig. 5.3, any design space violation is fed back to the optimizer by means of a penalization of the objective function values. In order to be able to measure the degree of violation, the portion of the Bézier curve that is intruding into an unfeasible design space and the corresponding distance to the boundary of the violated design constraint are determined. For this purpose, the Bézier curves are discretized by a certain number of points and the position of each point is compared to the design constraint functions. The distance of each invalid point to the permissible design space is contributing to a penalty function. Therefore, the number of points violating the design constraints and the distance of each point to the permissible design space determine the value of the penalty function that is fed back to the optimization algorithm.

5.1.3 Computational Grid

The grid generation for the two-dimensional blade-sleeve fairing shapes is conducted with ANSYS ICEM CFD [105]. This mesh generation software can be used to create multi-block structured, unstructured or hybrid meshes. Furthermore, geometry manipulation and preparation for the mesh generation process can be performed. For the present flow problem, a block-structured, two-dimensional computational mesh with hexahedral elements is generated. A fully resolved boundary layer is provided by a dimensionless wall distance of $y^+ \leq 1$ on the entire geometry. The computational domain and the applied boundary conditions are depicted in Fig. 5.6. The geometry is placed inside a circular domain with a diameter of $d = 40 \cdot L_c$, where L_c is the chord length. A pressure-farfield boundary condition is chosen to define the ambient conditions and the investigated Mach number with the corresponding flow direction.

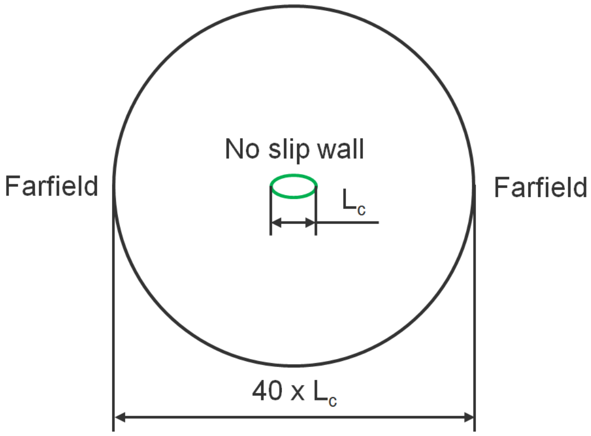

Figure 5.6: 2D computational domain and the applied boundary conditions [11].

A mesh-sensitivity study is performed to determine the impact of the spatial discretization on the numerical solution. For this purpose, the symmetric reference geometry from Fig. 5.5 is used and the mean aerodynamic forces are compared to each other for the advancing and the retreating blade case. The results of the mesh-sensitivity study are summarized in Tab. 5.1. Overall, four different mesh sizes are evaluated ranging from 68.000 to 437.000 elements. The computational mesh with 276.000 elements is chosen for the automated optimization process, because it offers a feasible compromise between numerical accuracy and computational effort. Regarding the advancing blade case, a discrepancy of 1.65 percent in lift and 0.47 percent in drag can be observed in comparison to the finest mesh with 437.000 elements. The largest deviation is observed for the lift of the retreating blade case with $\Delta C_{l,Ret} = 3.54\,\%$, which is still reasonable considering the large number of flow simulations that have to be performed during the design optimization process. Additionally, the absolute value of the generated lift is small on the retreating fairing, which leads to a larger relative discrepancy. The predicted drag of the retreating blade case reveals a minor deviation of $\Delta C_{d,Ret} = 0.34\,\%$.

Furthermore, the discretization errors are negligible compared to the sensitivity of the parameters in the optimization process between different design points. This justifies the selected mesh to be fit-for-purpose.

Mesh Size	$\Delta C_{l,Adv}$ [%]	$\Delta C_{d,Adv}$ [%]	$\Delta C_{l,Ret}$ [%]	$\Delta C_{d,Ret}$ [%]
437000	-	-	-	-
276000	1.65	0.47	3.54	0.34
138000	4.23	0.99	5.41	1.27
68000	64.51	25.48	89.77	23.80

Table 5.1: Mesh-sensitivity study regarding the spatial discretization [11].

5.1.4 Applied Numerical Setup

For the aerodynamic investigations of the blade-sleeve sections, compressible URANS simulations are conducted using the commercial flow solver ANSYS Fluent [107]. Compressibility effects are taken into account, because the Mach number of the advancing blade case exceeds $M = 0.3$. At first, a steady-state solution is generated providing the initial flow field for the transient simulation. Turbulence modeling is realized by the two-equation $k - \omega$ SST model [123]. The turbulence properties at the farfield are set to provide a turbulence intensity of $Tu = 0.3\,\%$ directly in front of the geometry. The Semi-Implicit Method for Pressure-Linked Equations (SIMPLE) algorithm is used for pressure-velocity coupling. Second-order upwind schemes are chosen for the spatial discretization of density, momentum, turbulent kinetic energy, specific dissipation rate and energy. Moreover, the pressure interpolation is achieved by the standard pressure scheme of ANSYS Fluent. A least squares cell-based formulation is applied for the gradient calculation. Regarding the temporal discretization, a bounded, second-order implicit scheme is chosen.

Besides the mesh sensitivity study related to the spatial discretization, a time-step size study is performed to determine the influence of the temporal discretization on the numerical solution. For this purpose, the selected computational mesh with 276.000 elements is examined. The convergence behavior as well as the aerodynamic forces and moments are evaluated and compared to each other to determine a reasonable time-step size. The results of this study are summarized in Tab. 5.2. It can be seen that the advancing and the retreating blade case are addressed within this study. Overall, four different time-step sizes within a range of $0.05\,ms \leq \Delta t \leq 0.4\,ms$ are considered. The smallest time-step size of $\Delta t = 0.05\,ms$ serves as the reference solution for the other cases. It can be seen that the simulation results using $\Delta t = 0.1\,ms$ are in good agreement to the solutions of the reference time step, especially in terms of the predicted drag. The largest deviation can be observed for the lift coefficient of the advancing blade case, which differs by $\Delta C_{l,Adv} = 2.32\,\%$.

Regarding the two other time-step sizes of $\Delta t = 0.2\,ms$ and $\Delta t = 0.4\,ms$, much larger discrepancies are present for both, lift and drag of the two investigated cases. Therefore, the time-step size of $\Delta t = 0.1\,ms$ is selected for the production runs offering a good compromise between numerical accuracy and computational effort. Additionally, it is less important to obtain the most accurate numerical solution within the optimization process, because relative differences are compared to each other. Furthermore, the time-saving factor plays a major role due to the large number of investigated shapes in the automated design optimization process.

$\Delta t\,[ms]$	$\Delta C_{l,Adv}$ [%]	$\Delta C_{d,Adv}$ [%]	$\Delta C_{l,Ret}$ [%]	$\Delta C_{d,Ret}$ [%]
0.05	-	-	-	-
0.1	2.32	0.66	1.18	0.42
0.2	6.49	1.02	2.87	1.12
0.4	8.04	1.03	4.13	0.93

Table 5.2: Time-step size study for the selected computational mesh with 276.000 elements [11].

Based on the convergence of the aerodynamic forces, a total simulation time of $t_{sim} = 0.25\,s$ is chosen leading to a total number of 2500 time steps for the selected time-step size of $\Delta t = 0.1\,ms$. The aerodynamic forces and moments are averaged over a time interval of $t_{ave} = 0.125\,s$ leading to a converged solution for all investigated geometries and allowing the comparison between the different shapes.

5.1.5 Results and Analysis

Within this section, the flow-simulation results for the two-dimensional design optimization of the BSF sections are presented and analyzed. A detailed evaluation of the objective space for each of the four optimized BSF sections is given. The previously introduced optimization tool chain is used in combination with a multi-objective genetic algorithm to generate the necessary data. The objective functions are given by the lift-to-drag ratio of the advancing rotor blade (f_1) and the drag coefficient of the retreating rotor blade (f_2).

The fitness of each design is determined by a domination count, which can be used to order the population members. For this purpose, the negative value of the number of candidates dominating a specific design is assigned, which keeps with the convention that higher fitness is better. Furthermore, a below-limit replacement value of six is chosen, which sorts out designs that are dominated by more than this specified number. In combination with a shrinkage percentage of 95 %, the candidates that are allowed to contribute offspring to the next generation are determined. The selected shrinkage percentage allows for a maximum reduction of five percent in the population size from on generation to the other.

If the below-limit replacement value would discard too many designs in the current population, its value is increased until the minimum required amount of candidates is found. Additionally, a niching algorithm is employed to avoid strong clustering along the Pareto-frontier. In particular, a radial nicher is chosen, which enforces a minimum Euclidean distance between two candidates in the objective space. The input for the radial nicher is defined by a vector of the length according to the number of applied objective functions. Furthermore, the elements of the vector are defined by a percentage of the non-dominated range of the objectives. In the present case, a value of 0.02 is chosen for both elements of the radial niching vector. A random crossover operation is employed creating a random shuffle of the design variables of the parents for the respective children. Depending on the amount of mixing that is desired during crossing over the parental information, the relative number of children and parents is set. In the present case, two parents produce two children and a crossover rate of 0.8 is chosen. This means that the number of crossover operations is 80 % of the population size. In order to introduce random diversity in each generation of designs, mutation is employed. For this purpose, the *replace uniform* algorithm of the optimization toolbox is chosen, which randomly assigns a new, valid value to a randomly selected design variable of a random design. Moreover, a mutation rate of five percent of the population size is applied. The main parameters of the optimizer setup are summarized in Tab. 5.3.

No. of Objective Functions	2	No. of Parents	2
Fitness Type	Domination Count	No. of Children	2
Replacement Type	Below Limit	Crossover Rate	0.80
Replacement Value	6	Niching Radius (f_1/f_2)	0.02/0.02
Crossover Type	Random Shuffle	Mutation Rate	0.05
Shrinkage Percentage	0.95		

Table 5.3: Summary of parameters used for the setup of the genetic optimization algorithm.

The initial population (population 0) for each of the four optimization runs contains 120 candidates that are evenly distributed in the permissible design space by using a Latin Hypercube Sampling (LHS) approach according to the description given in Sec. 3.2.3 of the present thesis. The best performing designs of each blade-sleeve section are compared to the reference shapes of the original Airbus Helicopters BSF. For this purpose, angle-of-attack polars are examined allowing to determine the robustness of the newly developed BSF sections in terms of varying inflow conditions. Additionally, the sectional pressure distributions are compared to each other and the main differences are highlighted. Finally, selected flow field quantities are shown and the main flow features are presented.

Analysis of the Objective Space

The objective space for the given optimization problem is spanned by the two objective functions f_1 and f_2. These objective functions are normalized by the respective objective function values of the reference BSF sections leading to $f_{1,norm}$ and $f_{2,norm}$. This enables a direct comparison between the newly developed designs and the reference shapes. The design optimization results for section S2 are illustrated in Fig. 5.7. All investigated designs that are located within the feasible objective space are shown in Fig. 5.7a. These candidates do not violate any of the given design constraints. It can be seen that the feasible objective space lies within a range of $-1.5 \leq f_{1,norm} \leq 0.67$ and $0.68 \leq f_{2,norm} \leq 5.8$. The orange symbol marks the reference design, which is located at $f_{1,norm} = -1$ and $f_{2,norm} = 1$.

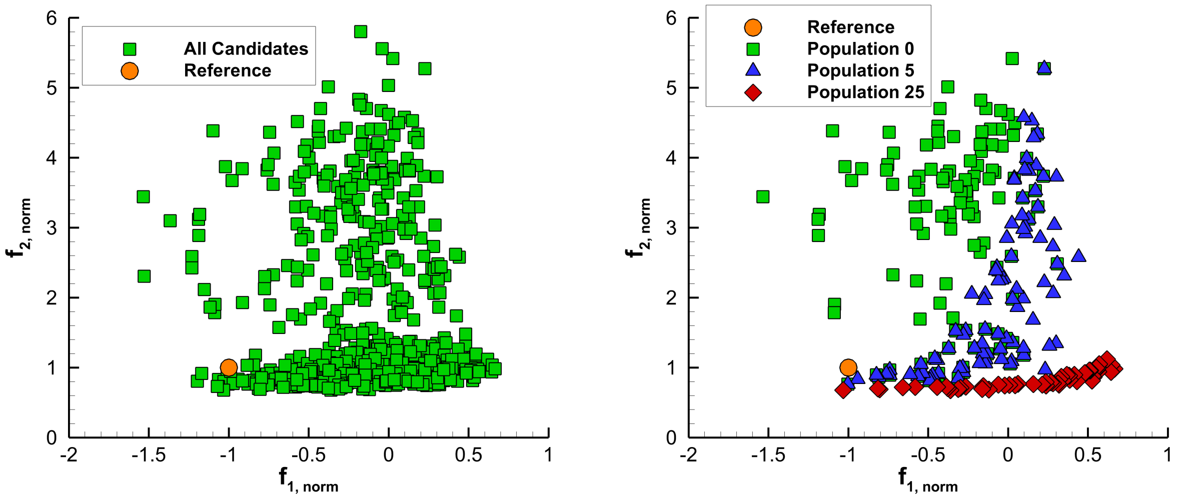

(a) All investigated designs in the feasible objective space.

(b) Generation-wise development from population 0 to population 25.

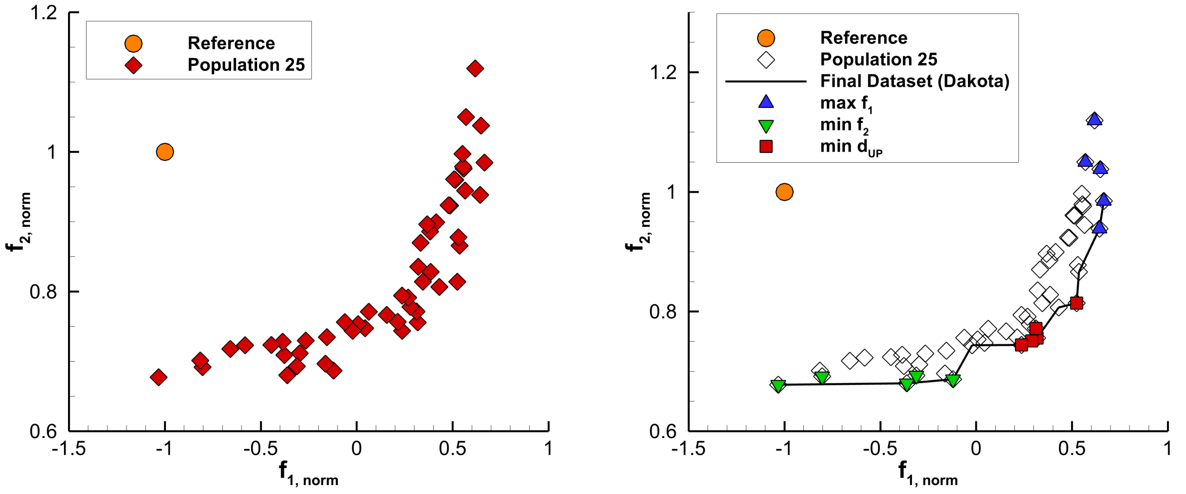

(c) Detailed view on the Pareto front of the final population.

(d) Best performing designs and final dataset from DAKOTA.

Figure 5.7: Evaluation of the objective space for the second blade-sleeve section S2.

Overall, a total number of 1510 geometries have been investigated in 25 generations, and 619 valid candidates can be derived, which are analyzed by means of CFD simulations. The remaining 891 designs violate one or more design constraints and are therefore rejected from the flow simulation process. Hence, a penalized objective function value is directly fed back to the optimization algorithm for these designs. The optimization task is terminated after 25 generations, because no big changes can be observed within the last three generations. This maximum number of populations is also used for the optimization of the other blade-sleeve sections. Figure 5.7b illustrates the evolutionary development from population 0 to population 25. The initial set of candidates consists of 120 individuals and it is shown by the green squares. As an intermediate result, the fifth generation is depicted by the blue triangles and the final population is given by the red diamonds. The last population (population 25) consists of 52 solutions forming a Pareto front, which is shown in Fig. 5.7c. The designs with the highest lift-to-drag ratios reach $f_{1,norm} \approx 0.67$ for the advancing blade case. However, this can only be achieved in combination with penalized drag values for the retreating blade case. In comparison to the reference design, a reduction of the drag coefficient of $\Delta f_{2,norm} = 32\,\%$ can be achieved. Figure 5.7d summarizes the best performing designs from the final population. The five best candidates from each region of the Pareto front are marked. These include high lift-to-drag ratio designs for the advancing blade case ($max(f_1)$), low-drag designs for the retreating blade case ($min(f_2)$) and designs offering a good compromise between the applied objective functions ($min(d_{UP})$). Furthermore, the proposed final dataset from the optimization toolbox Dakota is shown in Fig. 5.7d.

An overview about the optimization results for blade-sleeve section S3 is given in Fig. 5.8. For this section, a total number of 1500 designs have been analyzed in 25 successive generations. The pool of candidates contains 1195 permissible solutions that do not violate the applied design constraints. The feasible objective space is defined within a range of $-1.65 \leq f_{1,norm} \leq 1.38$ and $0.45 \leq f_{2,norm} \leq 5.4$. The generation-wise development of the sectional shapes for S3 can exemplarily be seen in Fig. 5.8b showing the generations 0, 5 and 25. A detailed view on the final generation of the optimization process is given in Fig. 5.8c. There is a sparsely populated region of designs providing the highest lift-to-drag ratios ($f_{1,norm}$) at the design point for the advancing blade case. However, this beneficial performance in terms of objective function $f_{1,norm}$ is only achieved in combination with a compromised objective function $f_{2,norm}$. Therefore, these designs do not provide a good compromise between the applied objective functions. In contrast, there are many designs available on the Pareto front that offer almost the same lift-to-drag ratio for the advancing rotor blade in combination with a much lower drag value for the retreating rotor blade. The five best designs from each region of the Pareto front as well as the final dataset proposed by the optimization toolbox Dakota are summarized in Fig. 5.8d.

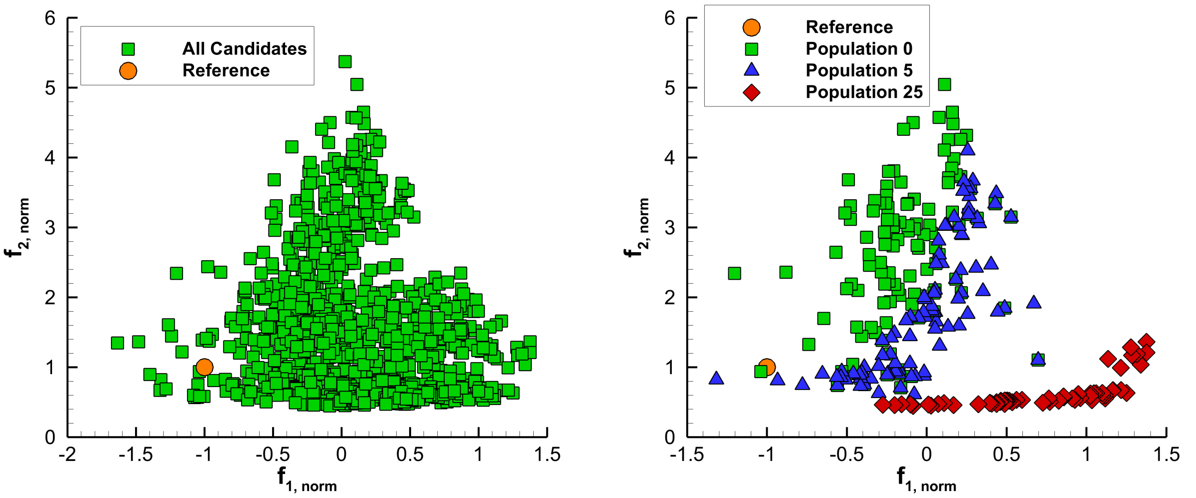

(a) All investigated designs in the feasible objective space.

(b) Generation-wise development from population 0 to population 25.

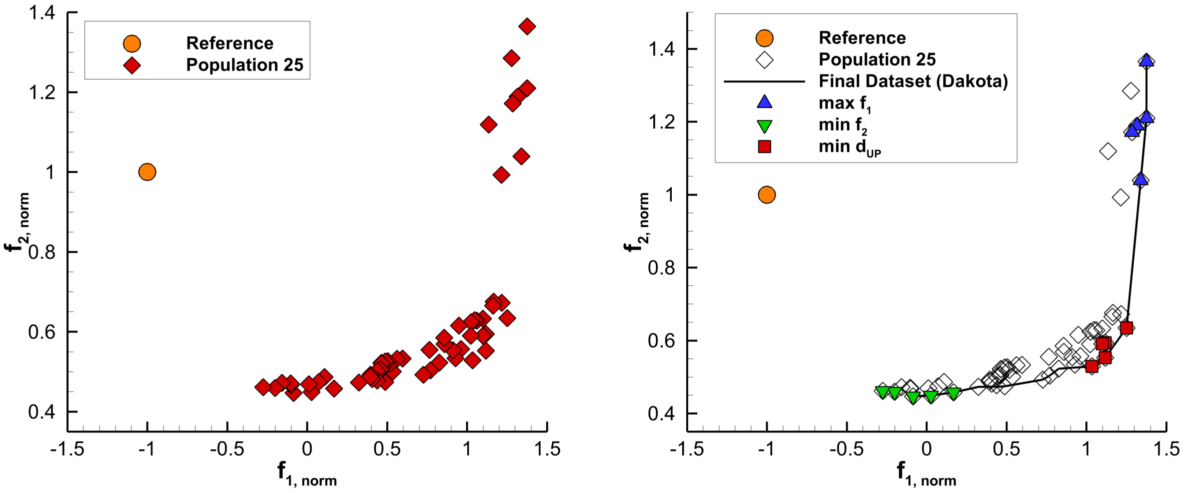

(c) Detailed view on the Pareto front of the final population.

(d) Best performing designs and final dataset from DAKOTA.

Figure 5.8: Evaluation of the objective space for the third blade-sleeve section S3.

The optimization results for section S4 are illustrated in Fig. 5.9. In total, 1594 designs are evaluated and 1294 valid designs are derived, which are depicted in Fig. 5.9a. The feasible objective space is defined within a range of $-3.6 \leq f_{1,norm} \leq 1.45$ and $0.73 \leq f_{2,norm} \leq 16$. It can be seen that a large number of candidates generates much more drag than the reference design, which leads to the conclusion that the reference shape already provides a reasonable low-drag design for the retreating blade case. Nevertheless, the design optimization process for section S4 led to an improvement of the performance for this BSF section. A drag reduction potential of about 25 % can be observed in combination with much higher lift-to-drag ratios at the advancing rotor blade. The shape with the lowest drag coefficient for the retreating blade case reaches a normalized objective function value of $f_{2,norm} = 0.73$. Furthermore, a maximum lift-to-drag ratio of $f_{1,norm} = 1.45$ can be achieved.

The successive development from the initial to the final population is shown in Fig. 5.9b. Concerning the fifth generation of designs, the performance improvement is limited to objective function f_1 and the reference shape is still superior in terms of objective function f_2. Hence, the drag reduction for the retreating blade case takes much longer than for the previous sections S2 and S3, which substantiates the fact that the reference shape already provides a good low-drag design at this radial station of the blade sleeve. The final population consists of 64 candidates and a detailed view on the Pareto front is given in Fig. 5.9c. Furthermore, the best performing designs are illustrated in Fig. 5.9d providing subsets of five candidates for each region of the Pareto front. The reference shape is dominated by the low-drag designs on the bottom left of the Pareto front and the candidates closest to the utopia point $(min(d_{UP}))$. In contrast, the designs with the highest lift-to-drag ratios regarding the advancing blade case are inferior concerning objective function f_2.

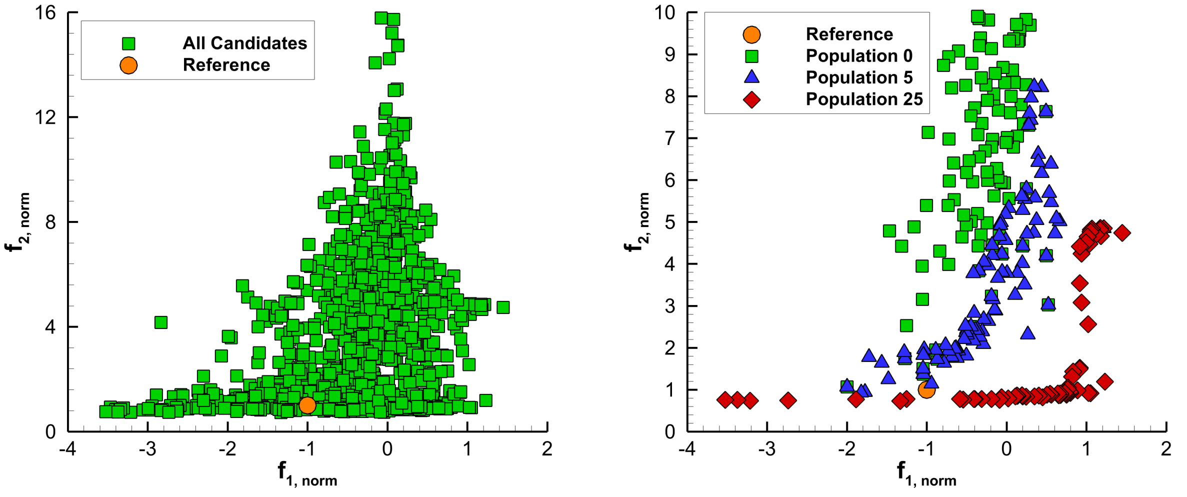

(a) All investigated designs in the feasible objective space.

(b) Generation-wise development from population 0 to population 25.

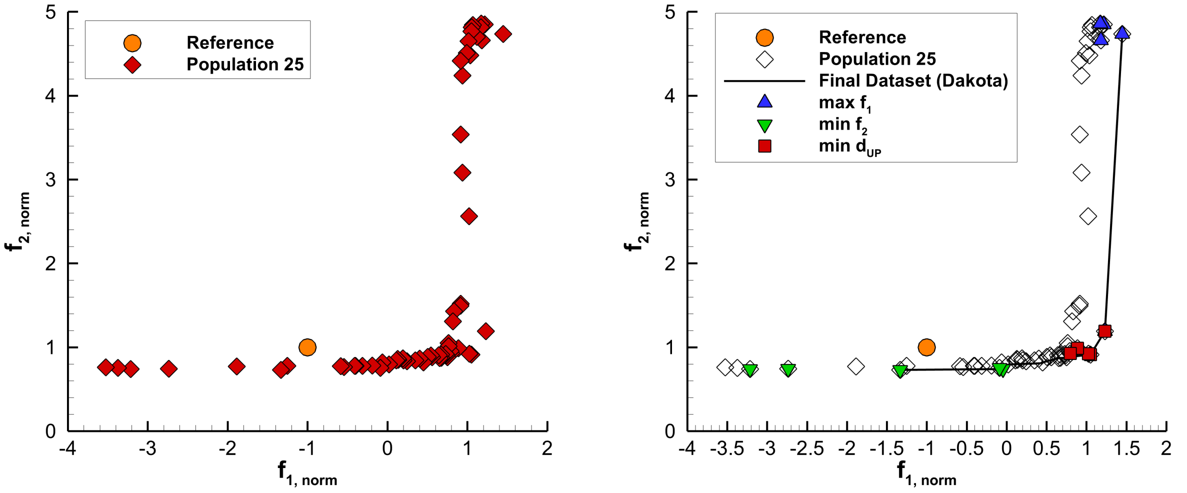

(c) Detailed view on the Pareto front of the final population.

(d) Best performing designs and final dataset from DAKOTA.

Figure 5.9: Evaluation of the objective space for the fourth blade-sleeve section S4.

Figure 5.10 summarizes the optimization results for BSF section S5. For this section, a total number of 1495 different designs are evaluated and 322 candidates violate one or more design constraints. The remaining 1173 valid shapes are investigated by means of CFD simulations and the corresponding objective space is depicted in Fig. 5.10a. For this BSF section, the feasible objective space is defined within a range of $-3.6 \leq f_{1,norm} \leq 1.45$ and $0.73 \leq f_{2,norm} \leq 16$. With regard to the objective function f_1, the majority of candidates outperforms the reference shape, whereas only a minor part of the designs leads to a lower objective function value f_2. The evolutionary development from population 0 to population 25 is illustrated in Fig. 5.10b showing the fifth generation as an intermediate result of the design optimization process. Figure 5.10c gives a detailed view on the final population consisting of 55 individuals.

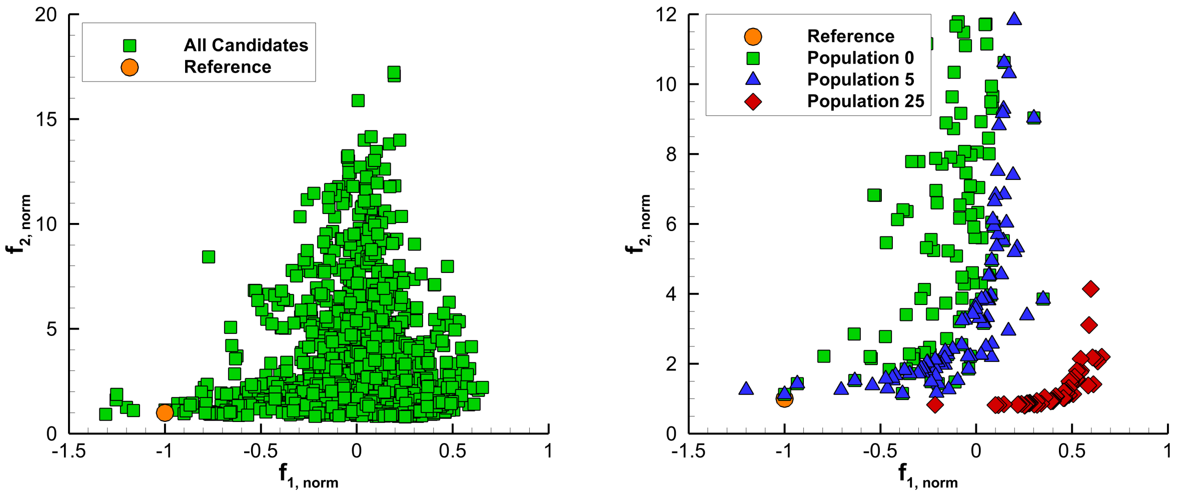

(a) All investigated designs in the feasible objective space.

(b) Generation-wise development from population 0 to population 25.

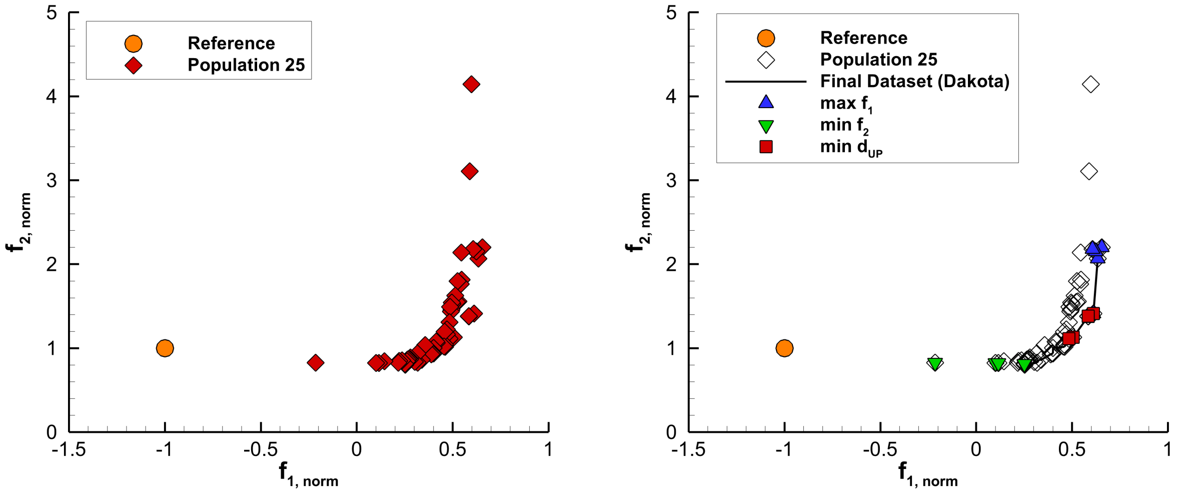

(c) Detailed view on the Pareto front of the final population.

(d) Best performing designs and final dataset from DAKOTA.

Figure 5.10: Evaluation of the objective space for the fifth blade-sleeve section S5.

It can be seen that no designs are located close to the reference shape in the objective space. This is related to the fact that, except for one design, the newly developed shapes generate lift for the advancing blade case, which is reflected by positive values for objective function f_1. The design with the highest lift-to-drag ratio for the advancing blade case reaches $f_{1,norm} = 0.65$. Moreover, the best low-drag shape with respect to the retreating blade case yields $f_{2,norm} = 0.80$.

The preliminary aerodynamic design optimization of the blade-sleeve sections serves as the basis for subsequent tasks. A large database of two-dimensional shapes has been generated for the four blade-sleeve sections with a total number of 4281 valid designs. In order to be able to continue with the three-dimensional design optimization of the BSF, a subset of promising candidates must be chosen to reduce the number of design variables to a reasonable level. The three-dimensional design optimization process is initially set up for a baseline geometry and the preliminary work includes the parameterization of the three-dimensional fairing shape in CAD, the automated mesh generation, the setup of the flow simulation as well as the automated post-processing. The sectional shapes offering the best compromise between the applied objective functions are chosen for the definition of the baseline fairing, because both objective functions are equally weighted. Regarding the objective space, these individuals are located at the bottom right corner of the Pareto front yielding the minimum distance to the utopia point ($\min(\mathrm{d}_{UP})$).

Figure 5.11 shows the optimized designs, which are selected for the definition of the initial, three-dimensional blade-sleeve fairing shape. Furthermore, the design constraints regarding the minimum and maximum permissible design space are illustrated by the red dashed lines. It can be seen that the selected designs from the current optimization process stay inside the permissible design space for all sections. Regarding section S2, the design constraints are strongly limiting the available design space, which can be seen in Fig. 5.11a. Hence, the contour of the new design is almost touching the boundaries of the design constraints at several positions. The remaining sections S3-S5 are mainly influenced by the design constraints for the minimum permissible design space. Therefore, the main drivers for the performance improvement of the blade-sleeve sections are given by the thickness and the bluntness of the profiles.

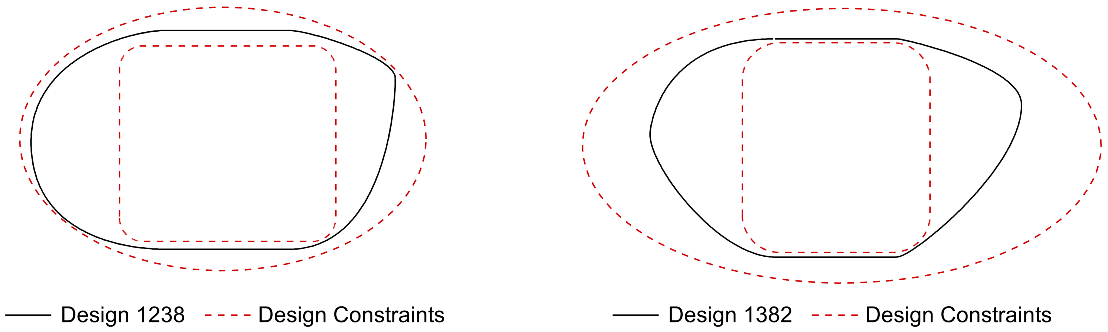

(a) Section S2. (b) Section S3.

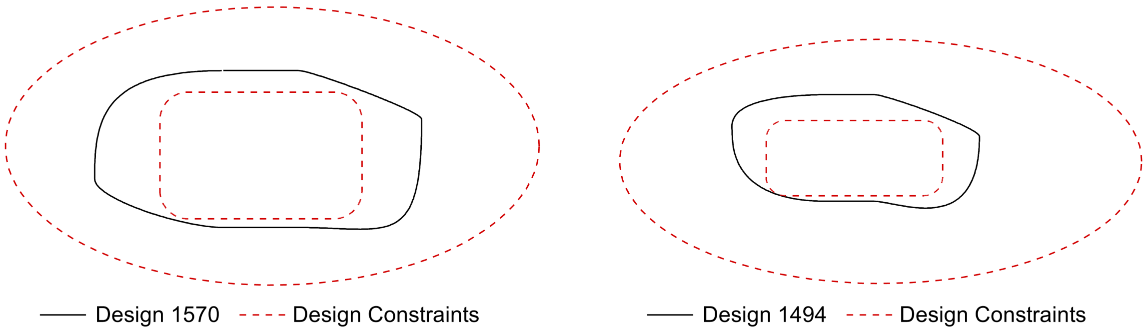

(c) Section S4. (d) Section S5.

Figure 5.11: Sectional shapes used for the definition of the initial three-dimensional blade-sleeve fairing. The applied design constraints are given by the red dashed lines.

Evaluation of the Aerodynamic Forces

In this section, the aerodynamic forces of the blade-sleeve sections, which have been used for the definition of the initial three-dimensional blade-sleeve fairing shape, are investigated. The corresponding designs yield the best compromise between the applied objective functions and their geometrical shapes are illustrated in Fig. 5.11. The blade-sleeve sections are optimized for a certain operating point corresponding to the flow conditions of the advancing and the retreating rotor blade during a sea-level cruise flight with 220 knots. Therefore, a single angle of attack is taken into account during the design optimization for each rotor-blade position. This angle of attack is defined by the cyclic blade-pitch law and an estimation of the flow deflection caused by the fuselage. However, it is desired to develop a robust BSF concerning varying inflow conditions, because the angle of attack as well as the flow velocity are continuously changing during one rotor revolution.

In order to evaluate the performance and the robustness of the selected sectional shapes, a series of angle-of-attack polars in the range of $-20° \leq \alpha \leq +20°$ is examined. Furthermore, a direct comparison to the aerodynamic forces of the reference shapes is given.

The investigated aerodynamic forces are derived from transient simulation runs and they are averaged over the last ten percent of the flow-simulation time. Regarding section S2, design 1238 is selected for the baseline fairing and the aerodynamic forces of this two-dimensional shape are illustrated in Fig. 5.12 for the advancing and the retreating blade case, respectively. The results include the lift- and drag coefficients as well as the lift-to-drag ratio. The red curves with the squared symbols represent the aerodynamic forces of the reference design and the green curves with the triangular symbols correspond to the aerodynamic forces of the selected design 1238. All forces are normalized by a reference value, which does not reveal the absolute values of the force coefficients, but enables a qualitative comparison between the optimized and the reference geometry.

The evaluation of the advancing blade case shows that the newly developed design generates a higher lift coefficient within the angle-of-attack (AoA) range of $-16° < \alpha < +8°$, which can be seen in Fig. 5.12a. The maximum lift is reached at $\alpha = +16°$ for both designs with a higher lift coefficient for the reference shape. Furthermore, the newly developed design reveals a sudden loss of lift at $\alpha = 8°$, which is recovered with increasing AoA. Figure 5.12c shows the comparison of the drag coefficients for the advancing blade case. The new design leads to a reduction of the drag coefficient within the entire AoA range. Furthermore, the drag coefficient is continuously decreasing with increasing AoA, whereas it stays within a narrow range for the reference design. A sudden drag reduction can be seen at $\alpha = +8°$ for design 1238, which is accompanied by a loss of lift as shown in Fig. 5.12a. Beyond this AoA, an almost constant drag coefficient is observed within the range of $+8° \leq \alpha \leq +16°$. The combination of increased lift and reduced drag leads to a higher lift-to-drag ratio for the newly developed design, which is illustrated in Fig. 5.12e. This lift-to-drag ratio of the advancing rotor blade case yields the first objective function f_1 of the design optimization process. Regarding both designs, a linear increase of the lift-to-drag ratio can be observed up to $\alpha = +16°$ with an almost constant offset between the two curves in the AoA range of $-10° \leq \alpha \leq +16°$. The reference shape achieves a higher lift-to-drag ratio at $\alpha < -14°$ and shows a different characteristic within this AoA regime.

The evaluation of the aerodynamic forces for the retreating blade case of section S2 reveals that design 1238 shows a more robust and predictable behavior in terms of lift and drag, compared to the reference design. The AoA polar for the lift coefficient is depicted in Fig. 5.12b and for the drag coefficient it is given in Fig. 5.12d. The lift curve for design 1238 shows an almost linear characteristic within the range of $-16° \leq \alpha \leq +16°$, whereas the lift of the reference design seems to be quite sensitive concerning the angle of attack. In a small range between $\alpha = -6°$ and $\alpha = +2°$, the reference shape shows a similar characteristic as the newly developed design, but above $\alpha = +2°$ it completely differs. The drag coefficient of the retreating blade case represents the second objective function f_2 and the corresponding force polar is illustrated in Fig. 5.12d.

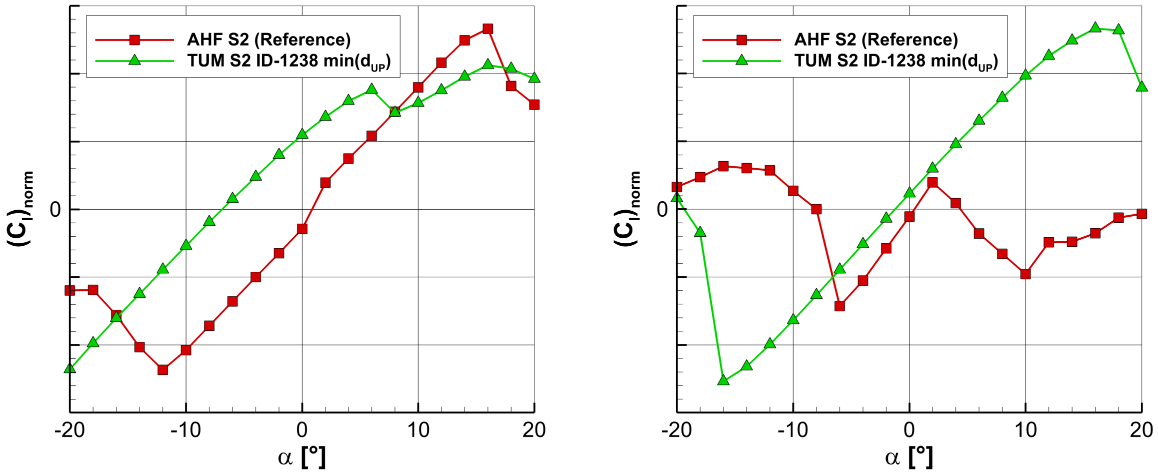

(a) $(C_l)_{norm}$ - Advancing Blade. (b) $(C_l)_{norm}$ - Retreating Blade.

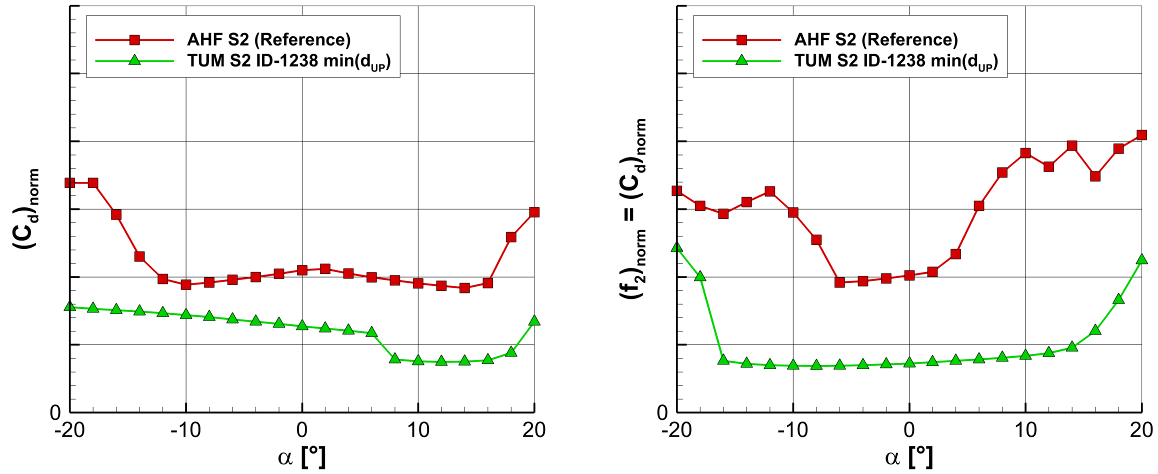

(c) $(C_d)_{norm}$ - Advancing Blade. (d) $(C_d)_{norm}$ - Retreating Blade.

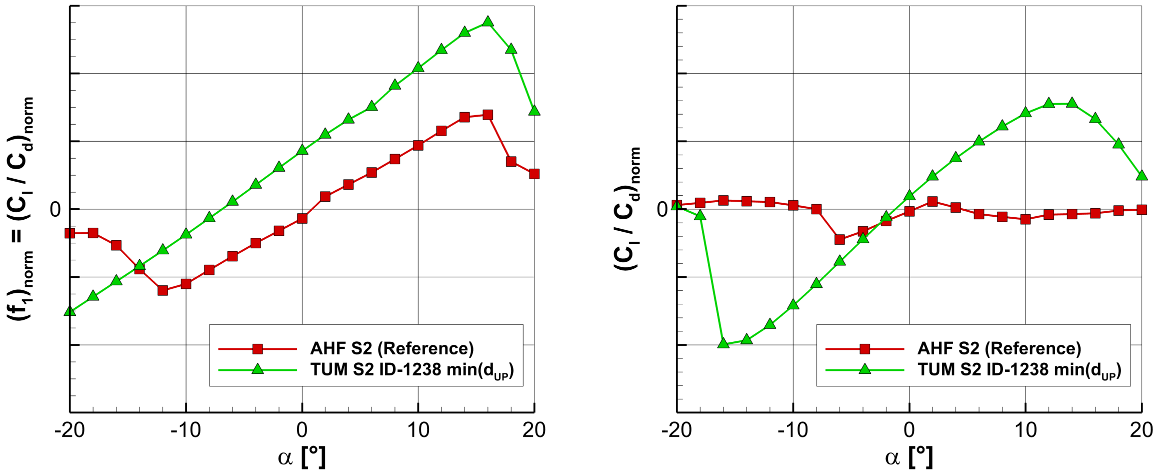

(e) $(C_l/C_d)_{norm}$ - Advancing Blade. (f) $(C_l/C_d)_{norm}$ - Retreating Blade.

Figure 5.12: Mean aerodynamic force polars for the advancing and the retreating blade case of section S2 showing a comparison between design 1238 of the current optimization process and the reference shape.

It can be seen that the new shape generates much less drag than the reference design within the entire AoA range. Moreover, it is quite robust in terms of drag, because almost the same drag values are obtained within a wide range of $-16° \leq \alpha \leq +12°$. In contrast, the reference shape shows a limited robustness within a much smaller AoA range of $-6° \leq \alpha \leq +2°$. Beyond this AoA range, the drag benefit of design 1238 becomes even bigger. Furthermore, a better lift-to-drag ratio is obtained for the new design above $\alpha = -2°$.

Regarding the third blade-sleeve section S3, design 1382 is selected for the evaluation of the aerodynamic forces. The mean force polars are summarized in Fig. 5.13 showing the comparison between the new design and the reference geometry. The evaluation of the lift coefficient for the advancing blade case, which is illustrated in Fig. 5.13a, reveals that the optimized shape delivers a higher lift coefficient up to $\alpha = +12°$. The drag polar for the advancing blade case is shown in Fig. 5.13c and it can be seen that the new design provides similar drag coefficients within the range of $-2° \leq \alpha \leq +4°$, whereas it generates higher values at negative AoAs and slightly increased values above $\alpha = +4°$. The comparison of the normalized lift-to-drag ratio for the advancing rotor blade is given in Fig. 5.13e. The previously mentioned lift- and drag characteristics yield a better lift-to-drag ratio for design 1382 within a wide AoA range. However, the performance benefit in terms of the aerodynamic efficiency vanishes above $\alpha = +10°$.

With respect to the retreating blade case, the focus lies on the drag coefficient, which is illustrated in Fig. 5.13d. At $\alpha = 0°$, almost the same drag coefficient is observed for both geometries, but the optimized design achieves much lower values below and above this AoA. Additionally, a nearly constant drag coefficient is present within the range of $-8° \leq \alpha \leq +16°$ for design 1382, which is an indication for good robustness in terms of varying inflow conditions. The comparison of the lift polar in Fig. 5.13b shows that the new design generates lift above $\alpha = -6°$, whereas the reference shape causes a down force above $\alpha = 0°$. Hence, much better lift-to-drag ratios are achieved for positive AoAs, which can be seen in Fig. 5.13f.

Regarding section S4, design 1570 provides the minimum distance to the utopia point in the objective space. Hence, it is selected to be investigated in more detail and used for the initial three-dimensional BSF shape. The mean aerodynamic forces for design 1570 are shown in Fig. 5.14 for the advancing and the retreating blade case, respectively. For this section, a very non-linear drag characteristic is derived for the advancing blade case, which can be seen in Fig. 5.14c.

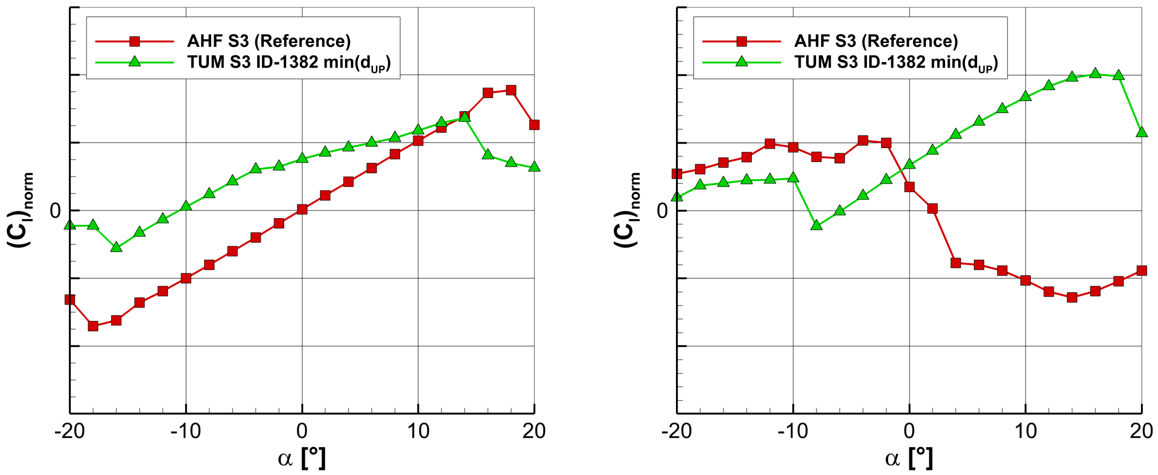

(a) $(C_l)_{norm}$ - Advancing Blade. (b) $(C_l)_{norm}$ - Retreating Blade.

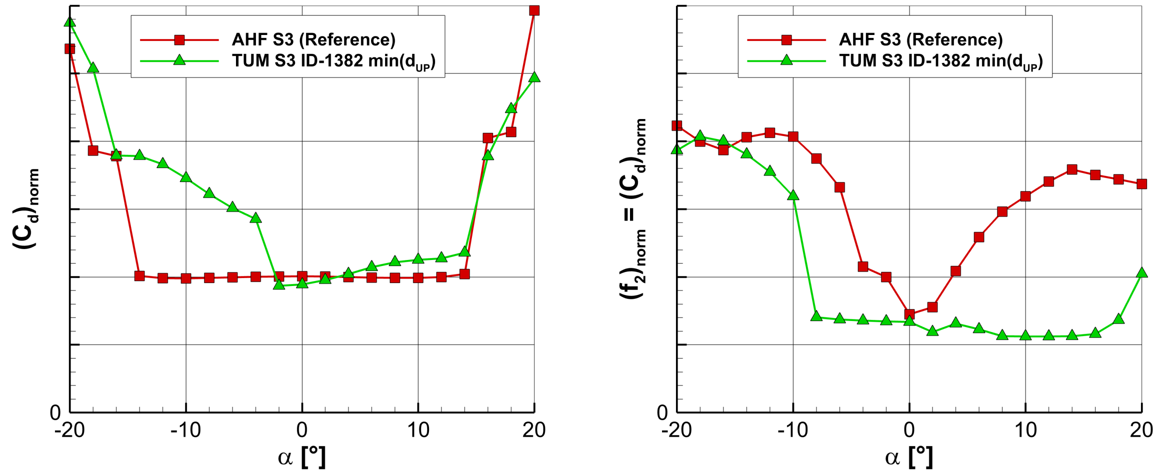

(c) $(C_d)_{norm}$ - Advancing Blade. (d) $(C_d)_{norm}$ - Retreating Blade.

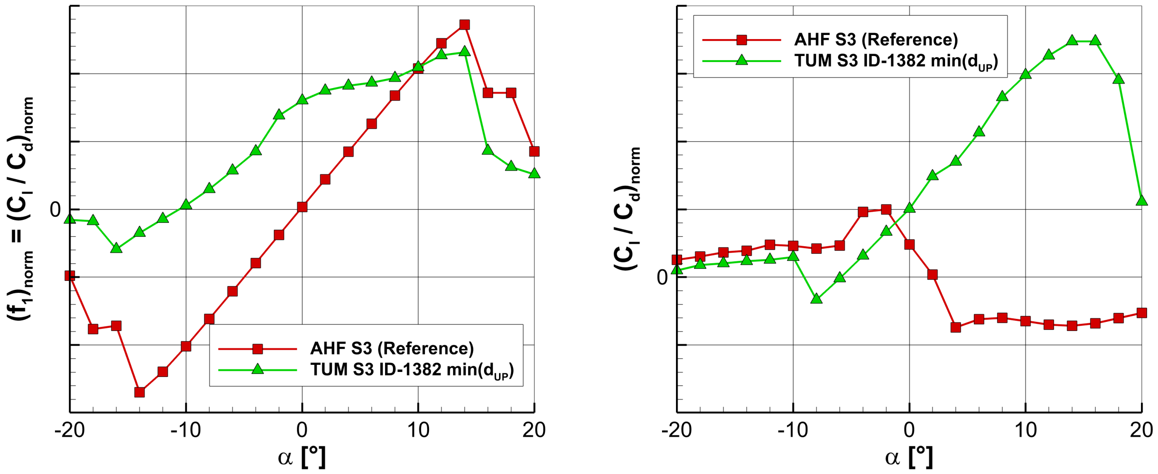

(e) $(C_l/C_d)_{norm}$ - Advancing Blade. (f) $(C_l/C_d)_{norm}$ - Retreating Blade.

Figure 5.13: Mean aerodynamic force polars for the advancing and the retreating blade case of section S3 showing a comparison between design 1382 of the current optimization process and the reference shape.

In the AoA ranges of $-4° \leq \alpha \leq +0°$ and $+8° \leq \alpha \leq +10°$ a sudden increase of the drag coefficient occurs, which could be related to a change in the flow separation characteristics. However, no detailed flow-field analyses have been performed in these angle-of-attack regions for section S4. Nevertheless, the impact of unsteady flow separation on the aerodynamic forces is discussed in detail during the analysis of the flow physics for selected blade-sleeve sections. Regarding the aerodynamic efficiency, design 1570 is beneficial within an AoA range of $-14° < \alpha < +4°$, which can be seen in Fig. 5.14e. The numerical investigation of the retreating blade case reveals that the AHF reference shape provides more lift in the AoA range of $-14° < \alpha \leq +20°$. Furthermore, the evaluation of the drag characteristics in Fig. 5.14d shows that design 1570 generates less drag in the negative AoA regime and up to $\alpha = 0°$. In contrast, lower drag coefficients are observed for the reference shape at positive AoAs.

The best compromise for both objective functions concerning the design optimization of the fifth blade-sleeve section is achieved by design 1494. Therefore, the aerodynamic forces of this design are analyzed in more detail and compared to the AHF reference shape. The force polars for the advancing and the retreating blade case are depicted in Fig. 5.15. It can be seen in Fig. 5.15a that design 1494 reaches a higher lift coefficient within an AoA range of $-18° \leq \alpha \leq +12°$. The drag polar for the advancing blade case, which is illustrated in Fig. 5.15c, shows that the minimum drag coefficient for the newly developed design is shifted to negative angles of attack. This can be related to the pronounced curvature in the rear part of the geometry leading to a strong redirection of the flow. Therefore, high lift and drag values are observed at $\alpha = 0°$ for this shape, see Fig. 5.15a and Fig. 5.15c. Furthermore, very high drag values are obtained for design 1494 at positive angles of attack, whereas the reference shape causes much less drag in the same region. Hence, it seems that the reference shape is more robust in terms of varying inflow direction. However, during cruise flight, the advancing rotor blade is operated at low AoAs and the new shape has been specifically optimized for one operating point in this regime. Therefore, the lift-to-drag ratio of design 1494 is superior within the AoA region of $-16° \leq \alpha \leq +02°$, which is depicted in Fig. 5.15e.

Regarding the retreating blade case, the focus is set on the drag coefficient, which is illustrated in Fig. 5.15d. It can be seen that design 1494 causes higher drag coefficients in the investigated AoA region and therefore, it performs worse with respect to the second objective function f_2 of the design optimization process. Figure 5.15b shows the corresponding lift polars for both designs. The reference shape reveals a linear lift increase with a constant gradient from $\alpha = -16°$ to $\alpha = +16°$. In contrast, the linear lift increase is limited to a smaller AoA range for design 1494. Additionally, the maximum lift coefficient is reached at $\alpha = +10°$ and beyond this AoA, a plateau of almost constant lift is observed.

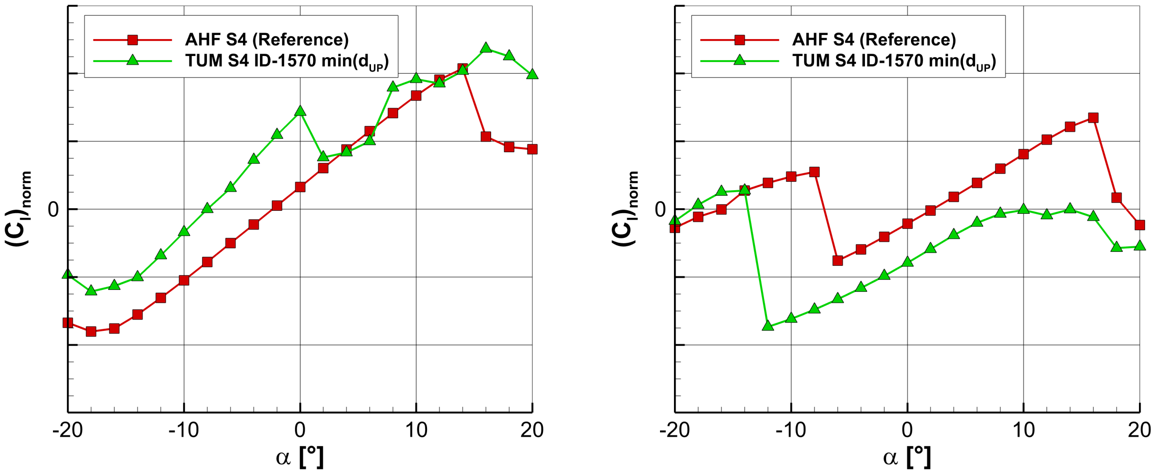

(a) $(C_l)_{norm}$ - Advancing Blade. (b) $(C_l)_{norm}$ - Retreating Blade.

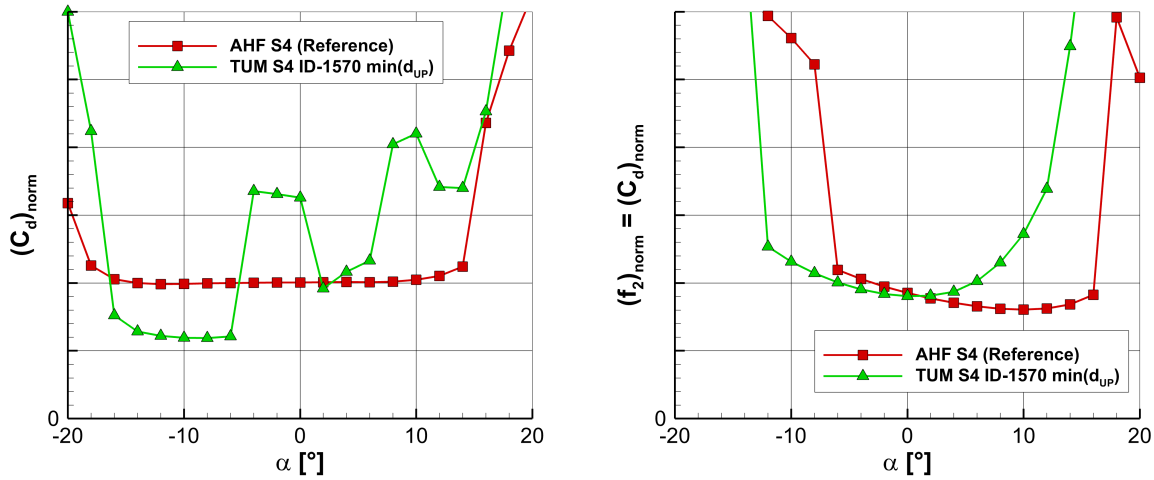

(c) $(C_d)_{norm}$ - Advancing Blade. (d) $(C_d)_{norm}$ - Retreating Blade.

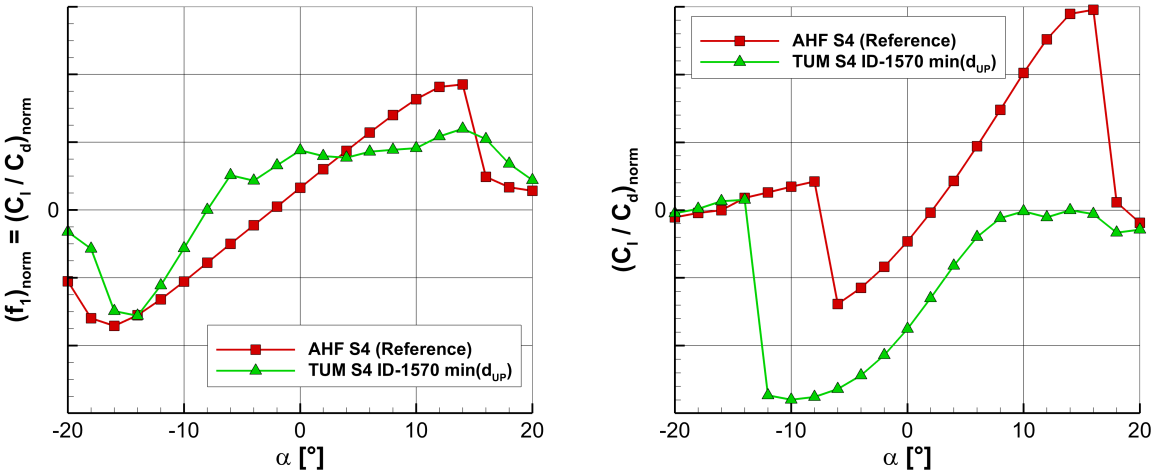

(e) $(C_l/C_d)_{norm}$ - Advancing Blade. (f) $(C_l/C_d)_{norm}$ - Retreating Blade.

Figure 5.14: Mean aerodynamic force polars for the advancing and the retreating blade case of section S4 showing a comparison between design 1570 of the current optimization process and the reference shape.

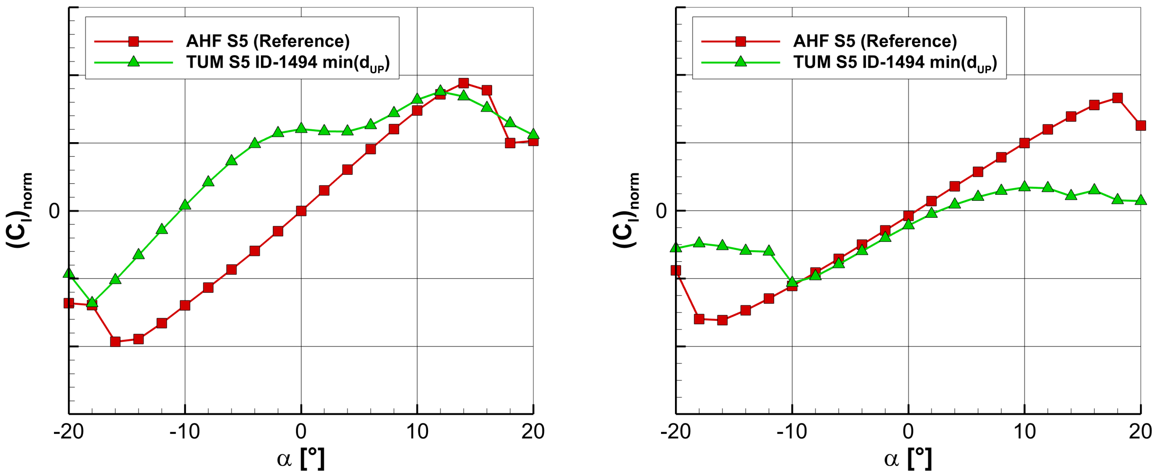

(a) $(C_l)_{norm}$ - Advancing Blade. (b) $(C_l)_{norm}$ - Retreating Blade.

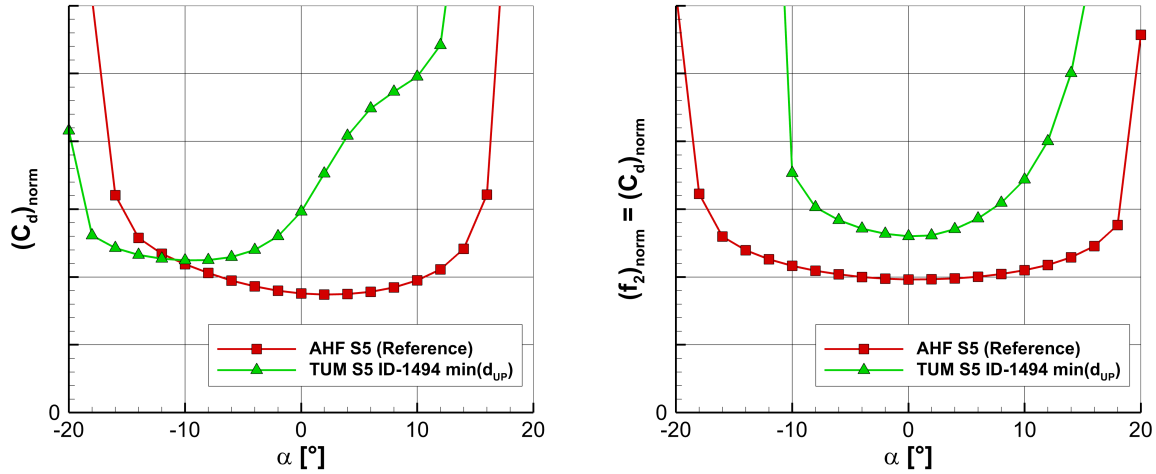

(c) $(C_d)_{norm}$ - Advancing Blade. (d) $(C_d)_{norm}$ - Retreating Blade.

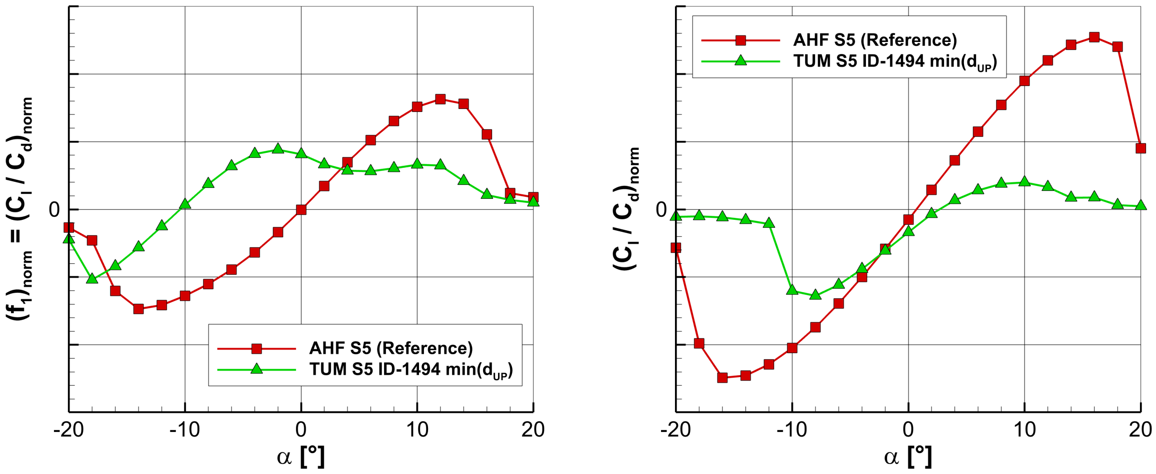

(e) $(C_l/C_d)_{norm}$ - Advancing Blade. (f) $(C_l/C_d)_{norm}$ - Retreating Blade.

Figure 5.15: Mean aerodynamic force polars for the advancing and the retreating blade case of section S5 showing a comparison between design 1494 of the current optimization process and the reference shape.

Analysis of the Flow Physics

In order to complement the analyses of the aerodynamic forces, selected flow field quantities are presented in this section. The comparison of the steady and unsteady flow-simulation results from the design optimization process reveal that transient flow phenomena, like vortex shedding, can strongly influence the mean aerodynamic forces of the two-dimensional blade-sleeve fairing shapes. Hereby, the occurrence of periodic vortex shedding depends on the shape of the investigated body, the flow velocity as well as the applied angle of attack. In order to be able to describe the flow mechanics of the oscillating flow, the Strouhal number is used, which is defined by Eq. 5.5. It represents the ratio between the frequency of vortex shedding f multiplied by a characteristic length l, and the flow velocity U. The characteristic length is typically the diameter of a cylinder or, as in the present case, the thickness of the respective blade-sleeve section.

$$St = \frac{f \cdot l}{U} \tag{5.5}$$

Regarding the flow around a cylinder, the Strouhal number St strongly depends on the Reynolds number Re, which is illustrated in Fig. 5.16. The plot shows two curves corresponding to the Strouhal numbers for smooth and rough cylinder surfaces, respectively. It can be seen that there is a strong deviation between the two characteristics within the Reynolds number range of $2 \cdot 10^5 < Re < 2 \cdot 10^6$, which is known as the transitional range [25]. The two curves in Fig. 5.16 are derived from the research work of Achenbach and Heinecke [138], who conducted experimental investigations with respect to vortex shedding from smooth and rough cylinders.

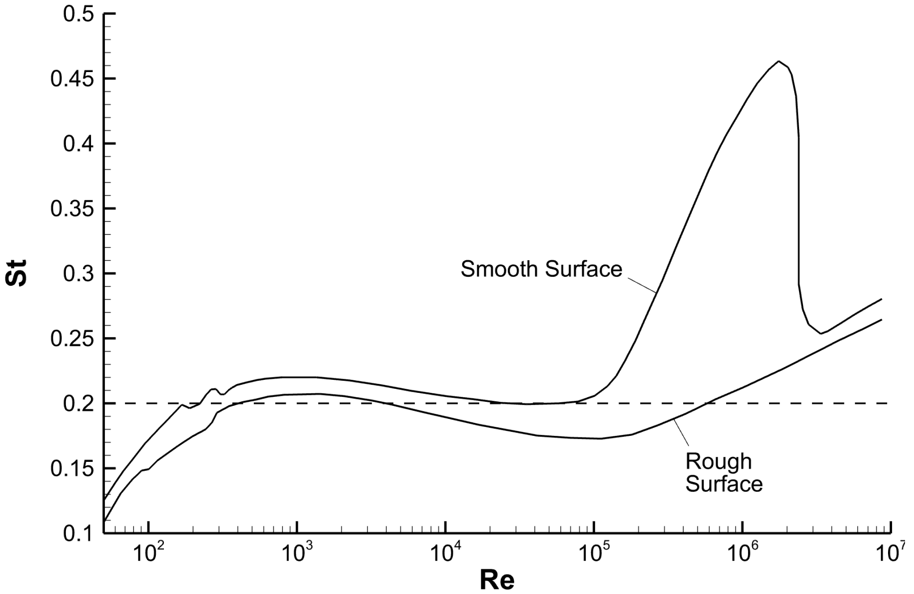

Figure 5.16: Relation between the Strouhal number St and the Reynolds number Re for a cylinder depending on the wall roughness [25].

They have shown that smooth surface cylinders generate a chaotic and high-frequency wake reaching a maximum Strouhal number of $St = 0.5$. In contrast, rough surface cylinders, with a surface roughness of $\epsilon/D = 3 \times 10^{-3}$ or higher, lead to well organized and periodic wakes with Strouhal numbers of $St \approx 0.25$. Here, ϵ represents the characteristic surface roughness and D the diameter of the cylinder.

During the design optimization, certain designs of the second and the third radial blade-sleeve sections (S2 & S3) have shown major differences between the steady and the unsteady flow-simulation results. These two sections have a much higher relative thickness than the remaining ones, which seems to trigger periodic vortex shedding in the transient flow simulations. This flow phenomena can lead to a misjudgment of the aerodynamic forces and must therefore be taken into account during the performance evaluation of the respective designs. In order to demonstrate the impact of vortex shedding on the aerodynamic forces, Fig. 5.17 shows the comparison between the steady and the transient forces of design 1238 from the second blade-sleeve section S2. Furthermore, lift and drag of the advancing as well as the retreating blade case are given. Design 1238 is selected, because it offers the best compromise between the applied objective functions and it is used as a supporting airfoil for the initial three-dimensional blade-sleeve fairing shape.

The steady flow-simulation results are used for the initialization of the transient flow simulations. Hence, it can be seen in Fig. 5.17 that the steady and the transient forces coincide at the beginning and start to deviate from a certain simulation time. Regarding lift and drag of the advancing blade case, a discrepancy of $\Delta L = +345\,\%$ and $\Delta D = +166\,\%$ can be observed. Additionally, the evaluation of the retreating blade case shows a difference of 158 % in lift and 16 % in drag. However, it must be taken into account that the absolute values of the forces are quite small leading to very high relative differences between the steady and the unsteady flow-simulation results. The dominating frequencies of the oscillations and the corresponding flow velocities at the investigated design points lead to Strouhal numbers of $St = 0.32$ for the advancing and $St = 0.38$ for the retreating blade case.

The fourth and the fifth radial blade-sleeve section (S4 & S5) have a much smaller relative thickness than S2 and S3, compare Fig. 5.11. The reduced relative thickness leads to a smooth boundary-layer separation for most of the investigated designs, which generates a steady flow field around the respective blade-sleeve sections. Regarding section S4, the design with the best compromise between the applied objective functions is given by design 1570 and for section S5 it is design 1494. The evaluation of the flow field for these two candidates reveals a smooth boundary-layer separation without vortex shedding for both shapes.

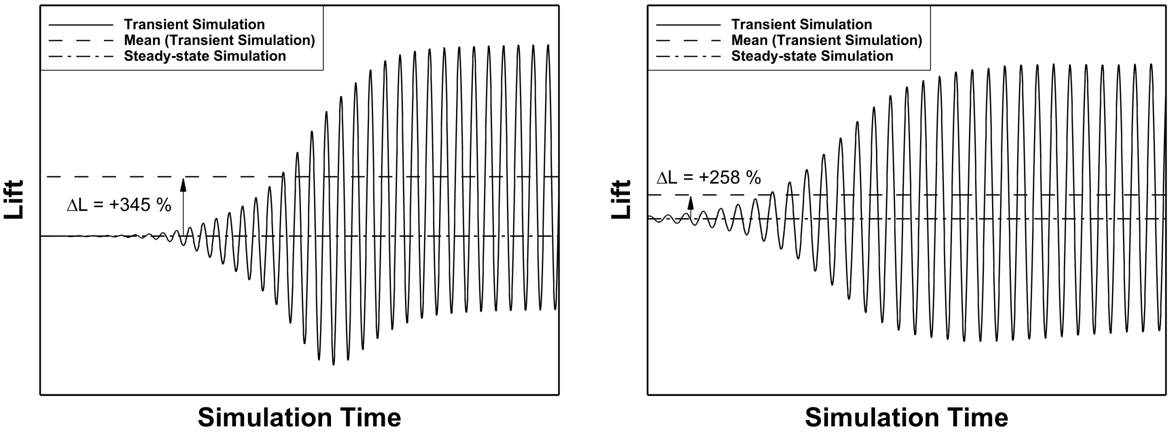

(a) Lift - Advancing Blade. (b) Lift - Retreating Blade.

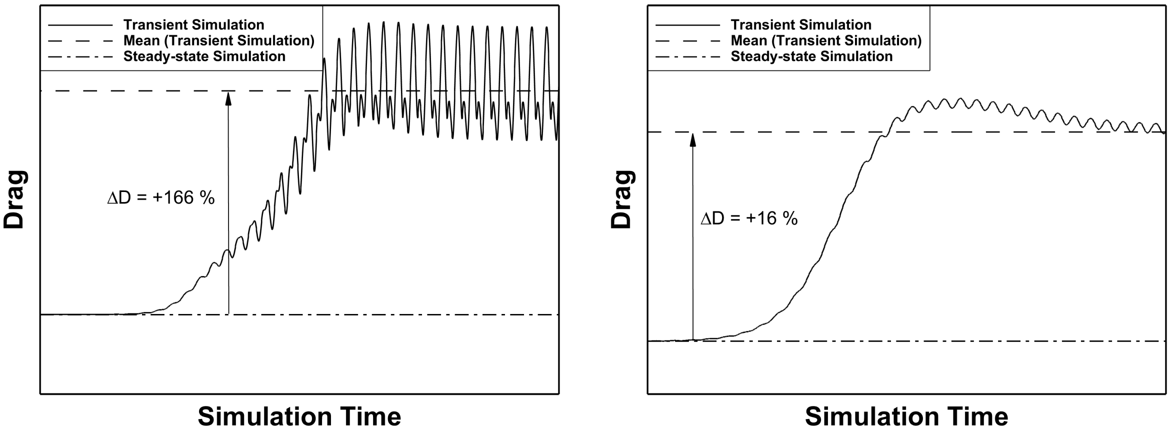

(c) Drag - Advancing Blade. (d) Drag - Retreating Blade.

Figure 5.17: Comparison of the aerodynamic forces for the advancing and the retreating blade case of design 1238 (Section S2) along the simulation time.

Hence, comparable aerodynamic forces are obtained for the steady and the unsteady flow-simulation results. In order to demonstrate the effect of periodic vortex shedding on the flow field, the flow-simulation results for the advancing blade case of design 1238 (Section S2) are depicted in Fig. 5.18. Moreover, the steady-state, the mean-transient and the transient flow-simulation results are shown for comparison. The respective distribution of the pressure coefficient C_p is illustrated on the left-hand side and the corresponding normalized, axial flow velocity u/V_∞ is depicted on the right-hand side of Fig. 5.18. The velocity distribution from the steady-state flow simulation in Fig. 5.18b shows a large region of reversed flow in the wake of the body. In contrast, the size of this region is significantly reduced for the mean, transient flow field in Fig. 5.18d, which is caused by the fact that the alternating vortices are strongly mixing the wake-flow field. Furthermore, the comparison between the steady-state pressure distribution in Fig. 5.18a and the mean, transient pressure distribution in Fig. 5.18c reveals the upstream effect of periodic vortex shedding.

It can be seen that the suction regions on the upper and the lower side of the blade-sleeve section are much more pronounced in Fig. 5.18c. Additionally, lower, average pressure levels are observed at the rear part of the body within the transient simulation. The instantaneous pressure coefficient for the last time-step of the transient flow simulation is depicted in Fig. 5.18e and the corresponding normalized, axial flow velocity is given in Fig. 5.18f. The periodic vortex shedding can clearly be identified by examining the respective pressure and velocity field.

As an example for the smooth and steady boundary-layer separation in the outboard region of the blade-sleeve fairing, the flow field of the fourth blade-sleeve section S4 is analyzed. Figure 5.19 shows the flow-simulation results for the advancing blade case of design 1570. The comparison between the steady-state and the transient flow simulation exhibits almost no differences in the flow field with respect to the pressure and velocity distributions. Even the instantaneous flow field from the last time-step of the transient flow simulation, which can be seen in Fig. 5.18e and Fig. 5.18f, provides the same pressure and velocity distribution as the steady-state simulation. Therefore, it can be concluded that a steady-state solution is obtained for design 1570 and negligible oscillations in the aerodynamic forces can be observed. As a result, the steady-state and the mean, transient solution could both be used to evaluate the objective function values during the design optimization process. However, it is impossible to know the aerodynamic characteristics of such blunt shapes beforehand and therefore, the approach of using more computationally expensive transient flow simulations to derive the mean aerodynamic forces is justified to ensure meaningful results in terms of the objective function values.

In order to determine the main reasons for the performance benefits of the newly developed shapes in comparison to the reference shapes from Airbus Helicopters, detailed flow-field analyses are conducted for relevant designs of each blade-sleeve section. For this purpose, the mean, transient flow-simulation results for the advancing and the retreating blade case are taken into account. In order to give an example for the flow field analyses at this point, the flow-simulation results for design 1238 of the second blade-sleeve section S2 and design 1570 of the fourth blade-sleeve section S4 are presented. As previously introduced, these designs offer the best compromise between the applied objective functions and they are representative for the inboard and outboard cross-sections of the blade-sleeve fairing.

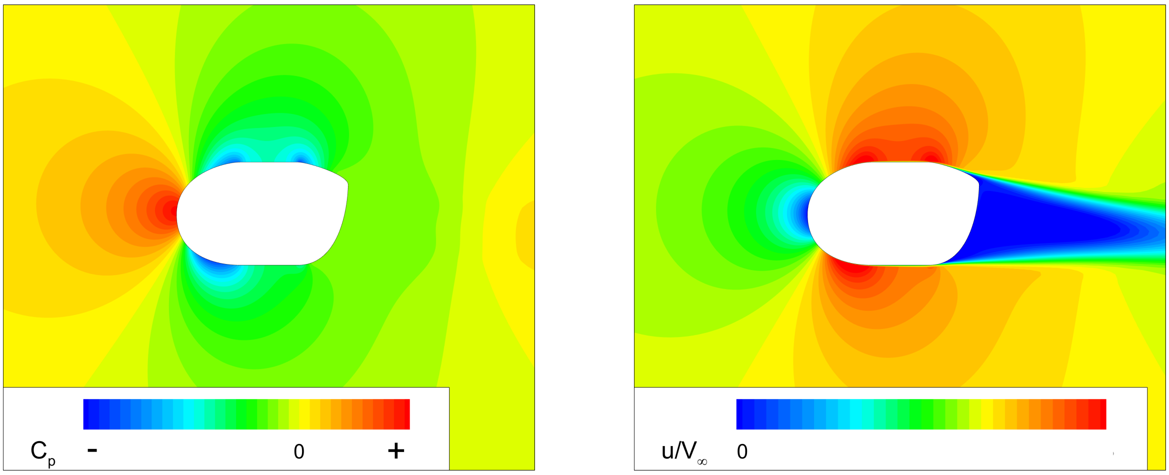

(a) Pressure coefficient C_p - Steady-state flow simulation.

(b) Normalized, axial flow velocity u/V_∞ - Steady-state flow simulation.

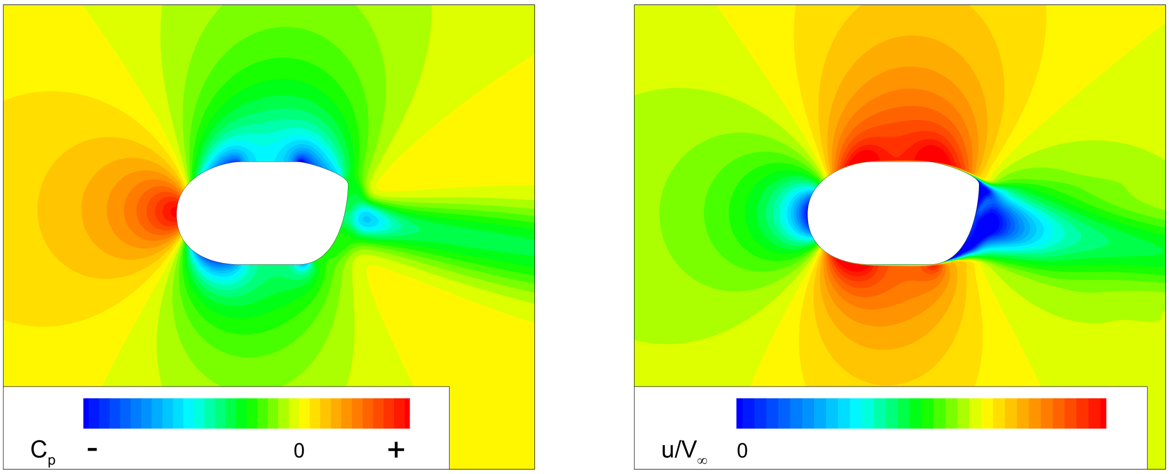

(c) Mean pressure coefficient C_p - Transient flow simulation.

(d) Mean, normalized, axial flow velocity u/V_∞ - Transient flow simulation.

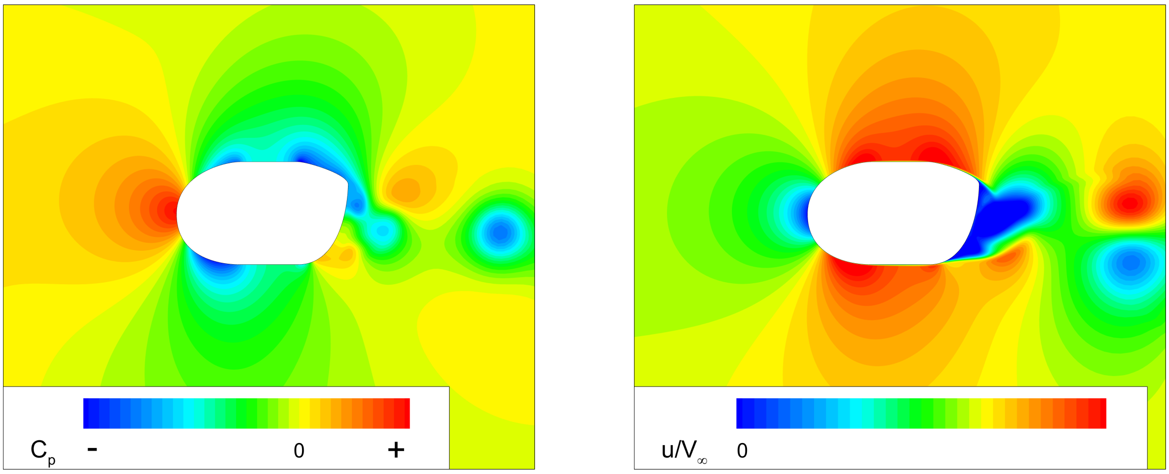

(e) Pressure coefficient C_p for the last time step of the transient flow simulation.

(f) Normalized, axial flow velocity u/V_∞ for the last time step of the transient flow simulation.

Figure 5.18: Comparison of the steady-state and the transient flow-simulation results regarding the advancing blade case of design 1238 (Section S2).

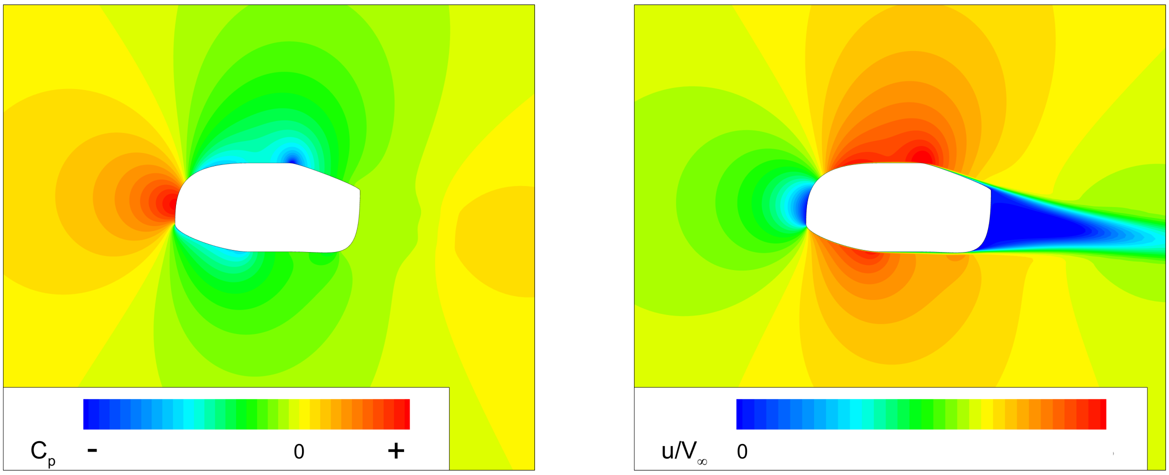

(a) Pressure coefficient C_p - Steady-state flow simulation.

(b) Normalized, axial flow velocity u/V_∞ - Steady-state flow simulation.

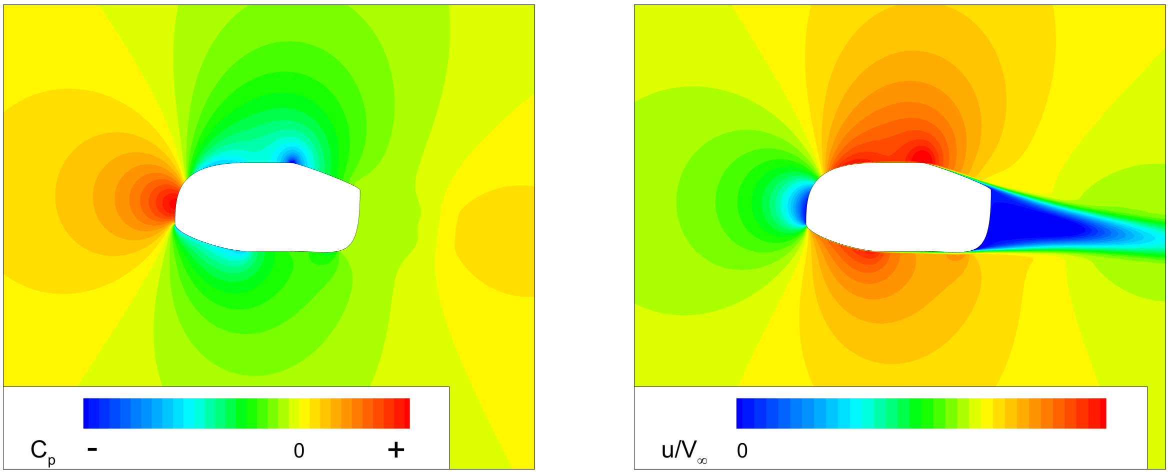

(c) Mean pressure coefficient C_p - Transient flow simulation.

(d) Mean, normalized, axial flow velocity u/V_∞ - Transient flow simulation.

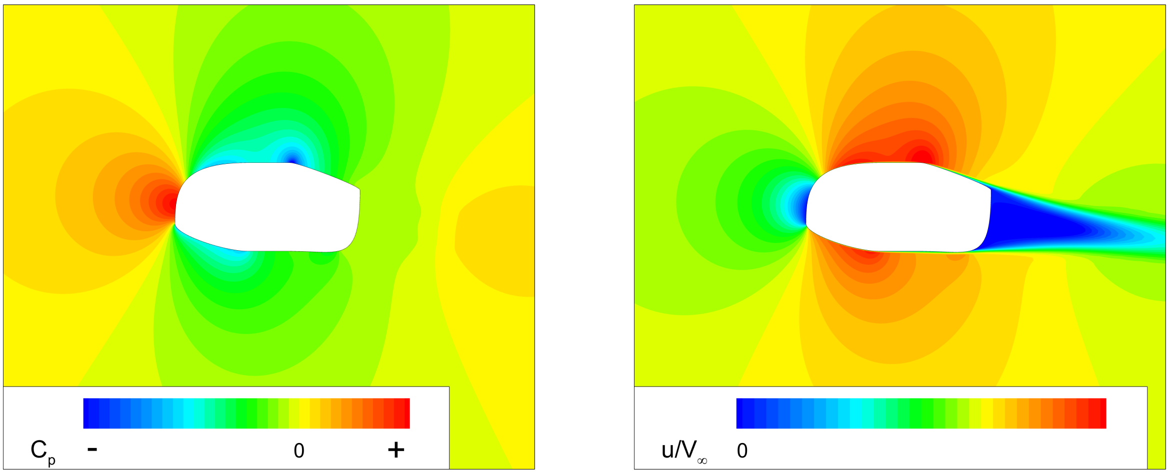

(e) Pressure coefficient C_p for the last time step of the transient flow simulation.

(f) Normalized, axial flow velocity u/V_∞ for the last time step of the transient flow simulation.

Figure 5.19: Comparison of the steady-state and the transient flow-simulation results regarding the advancing blade case of of design 1570 (Section S4).

Figure 5.20 shows the evaluation of the flow-simulation results for the advancing and the retreating blade cases of design 1238 (Section S2). The mean pressure distribution $C_p(x,y)$ for both cases is illustrated in Fig. 5.20a and Fig. 5.20b. The corresponding surface-pressure distribution $C_p(x/c)$ is depicted in Fig. 5.20c and Fig. 5.20d, respectively. Furthermore, the evaluation of the axial skin-friction coefficient $C_{fx}(x/c)$ complements the flow-field analysis, see Fig. 5.20e and Fig. 5.20f. The green curves with the triangular symbols represent the flow-simulation results for design 1238 and the red curves with the square symbols belong to the reference shape. Additionally, the curves for the upper and the lower surface of the blade-sleeve fairing are marked by U (upper) and L (lower), respectively. The evaluation of the surface-pressure distribution for the advancing blade case allows to identify the main reasons for the improved lift-to-drag ratio of design 1238. The pressure distribution on the reference design generates a downforce, because the pressure on the upper side is higher than on the lower side within a wide range. Additionally, there is a strong suction peak at $x/c = 0.1$ causing a significant downforce. In the rear part of the reference geometry there is only a minor pressure difference between the upper and the lower side, which does not generate a considerable amount of lift. Furthermore, flow-separation onset can be seen at $x/c \approx 0.8$ on both sides of the geometry, which is characterized by a plateau of constant pressure and confirmed by the negative axial skin-friction coefficient ($C_{fx} < 0$), see Fig. 5.20e. In comparison to the reference shape, the newly developed design prevents the large pressure difference in the front part of the geometry and therefore, a much smaller downforce is generated in the range of $0.0 \leq x/c < 0.27$. The pressure distribution on the remaining part of the geometry produces lift. Especially in the rear part of the geometry there is a major difference between the optimized and the reference shape. It can be seen that the flow starts to separate at $x/c \approx 0.8$ on the lower side of design 1238, whereas it stays attached on the upper side. Hence, a major pressure difference is achieved in this region, which results in an increase of lift. Moreover, a better pressure recovery can be identified for design 1238, which reduces the drag and contributes to a better lift-to-drag ratio.

Regarding the retreating rotor-blade case, the focus is on drag reduction. Due to the fact that reversed flow occurs on the blade-sleeve fairing at this azimuthal rotor position, any additional lift represents a beneficial secondary effect. However, as a primary objective, the optimized geometry should provide good pressure recovery in the aft-body region to reduce the parasite drag as much as possible. Figure 5.20d illustrates the surface-pressure distribution for the retreating blade case showing the reference design as well as the newly developed design 1238. The evaluation of the respective pressure distributions leads to the conclusion that both geometries create almost no lift and that design 1238 achieves better pressure recovery in the aft-body region, which reduces drag. With respect to design 1238, the flow separation onset can be seen at $x/c \approx 0.8$, whereas it is slightly delayed for the reference design.

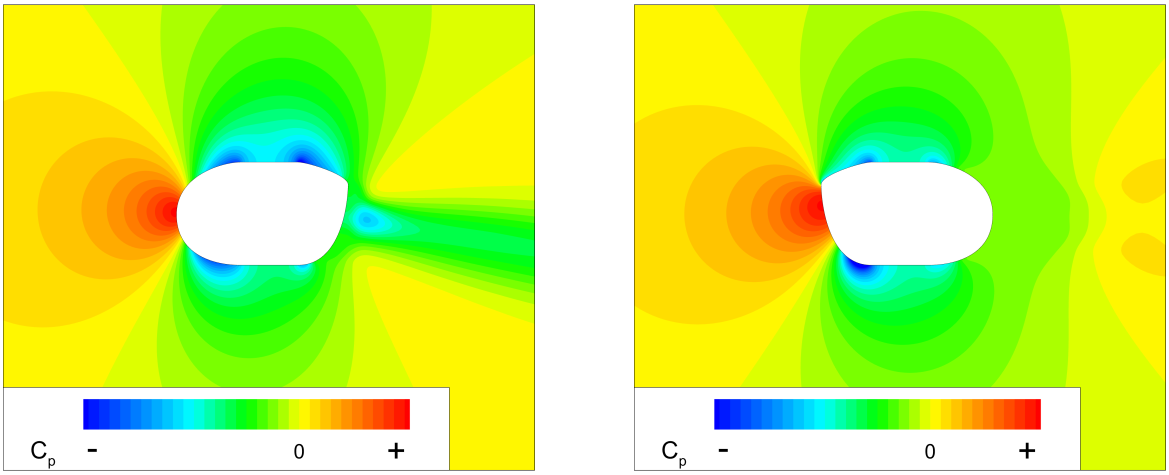

(a) Flow-field pressure distribution $C_p(x,y)$ - Advancing Blade.

(b) Flow-field pressure distribution $C_p(x,y)$ - Retreating Blade.

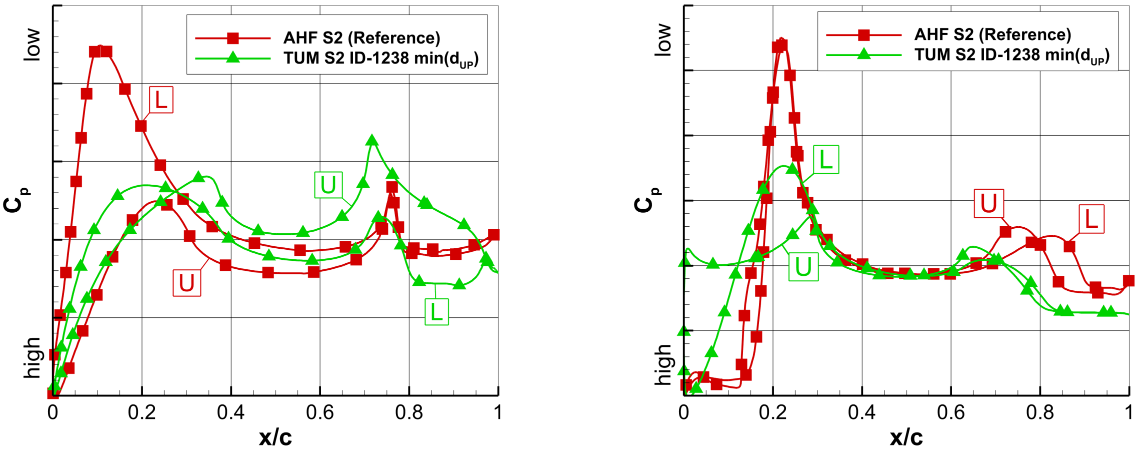

(c) Comparison of the surface-pressure coefficient $C_p(x/c)$ - Advancing Blade.

(d) Comparison of the surface-pressure coefficient $C_p(x/c)$ - Retreating Blade.

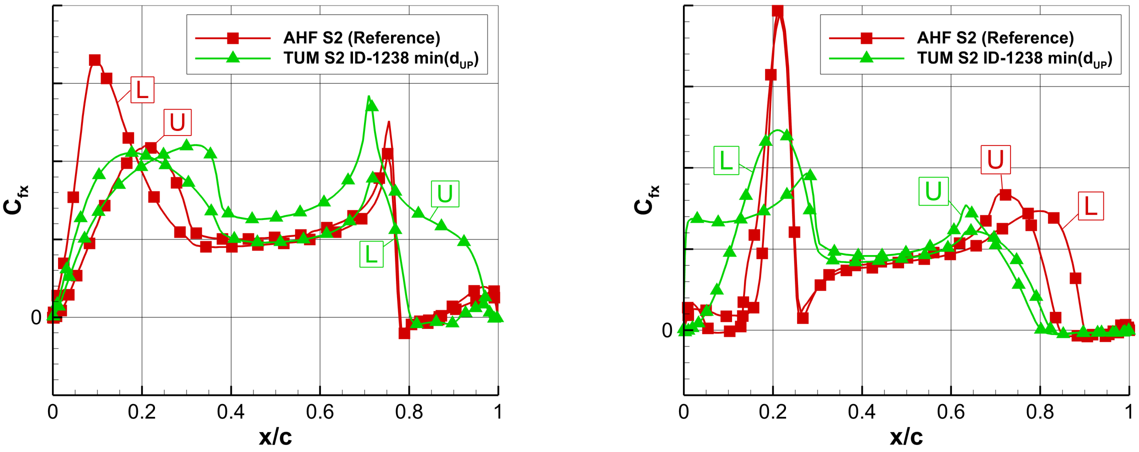

(e) Comparison of the axial skin-friction coefficient $C_{fx}(x/c)$ - Advancing Blade.

(f) Comparison of the axial skin-friction coefficient $C_{fx}(x/c)$ - Retreating Blade.

Figure 5.20: Evaluation of the mean, transient flow field and the surface quantities for the advancing as well as the retreating blade case of design 1238 (S2) showing a direct comparison to the original reference shape.

Figure 5.21 depicts the flow-simulation results for the advancing and the retreating blade-case of design 1570, which is used as the initial shape for section S4 on the three-dimensional blade-sleeve fairing. As previously shown for section S2, the presented results include the flow-field pressure distribution $C_p(x,y)$, the chord-wise surface-pressure distribution $C_p(x/c)$ and the axial skin-friction coefficient $C_{fx}(x/c)$. Furthermore, a direct comparison to the surface quantities of the reference geometry is given to be able to determine the main reasons for the performance improvement of the optimized shape.

The pressure distribution for the advancing blade case of design 1570 is illustrated in Fig. 5.21a and it shows a pronounced suction region on the upper surface at $x/c = 0.63$. This suction region is provoked by a strong surface curvature at this chord-wise position that accelerates the fluid flow and does not cause flow separation. The evaluation of the chord-wise surface pressure distribution in Fig. 5.21c shows that the strong suction peak at $x/c = 0.63$ supports a valuable pressure difference between the upper and the lower surface, which generates lift. In contrast, the integration of the surface pressure distribution for the reference shape leads to a downforce, because the pressure on the upper side is higher than on the lower side up to an axial position of $x/c = 0.6$. Concerning pressure recovery, a slightly better characteristic is obtained for design 1570 leading to parasite drag reduction. Furthermore, a delayed flow separation can be seen in comparison to the reference shape. The surface-pressure distribution and the axial skin-friction coefficient, which is illustrated in in Fig. 5.21e, indicate flow separation for the reference geometry at $x/c = 0.78$ on the upper side and $x/c = 0.72$ on the lower side. Regarding design 1570, the flow separation onset is detected at $x/c = 0.90$ on the lower side and on the upper side the flow follows the contour up to the trailing edge. Based on the increased lift and the reduced drag, the performance improvement concerning the lift-to-drag ratio of the advancing blade case is achieved.

The flow-field pressure distribution for the retreating blade case of design 1570 shows a strong suction region on the lower side of the geometry, as illustrated in Fig. 5.21b. This low-pressure region is located at $x/c = 0.08$, which can be seen in Fig. 5.21d. The pressure difference between the upper and the lower side causes a significant local downforce in this region. In comparison, the reference geometry features a stronger and more distinct suction peak at $x/c = 0.28$, but due to the reduced size of the low-pressure region, less downforce is generated. In terms of pressure recovery, similar pressure levels are observed for both geometries leading to comparable drag contributions. The evaluation of the axial skin-friction coefficient in Fig. 5.21f reveals that the flow-separation onset for design 1570 is located at $x/c = 0.86$. Regarding the reference shape, the flow separation on the upper side occurs at $x/c = 0.87$ and on the lower side it takes place at $x/c = 0.79$. Based on the given results for the retreating blade case of the two outboard blade-sleeve sections S4 and S5, it can be concluded that a limited drag reduction potential can be exploited for these shapes in comparison to the reference geometries.

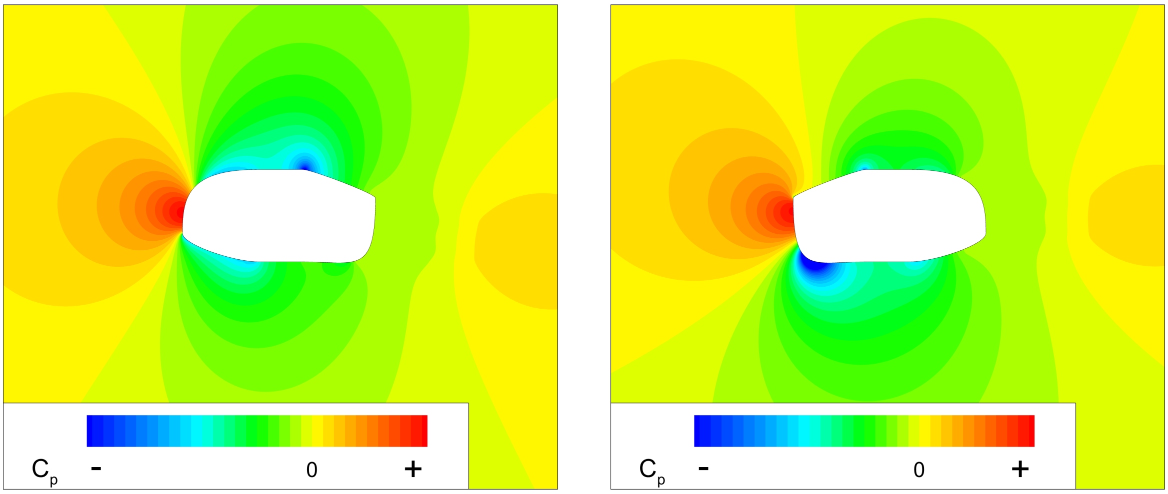

(a) Flow-field pressure distribution $C_p(x,y)$ - Advancing Blade.

(b) Flow-field pressure distribution $C_p(x,y)$ - Retreating Blade.

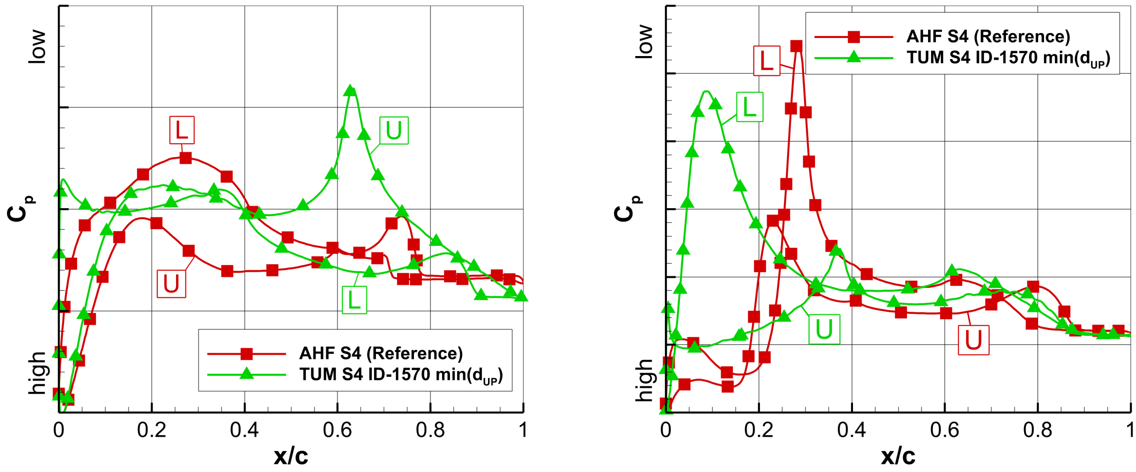

(c) Comparison of the surface-pressure coefficient $C_p(x/c)$ - Advancing Blade.

(d) Comparison of the surface-pressure coefficient $C_p(x/c)$ - Retreating Blade.

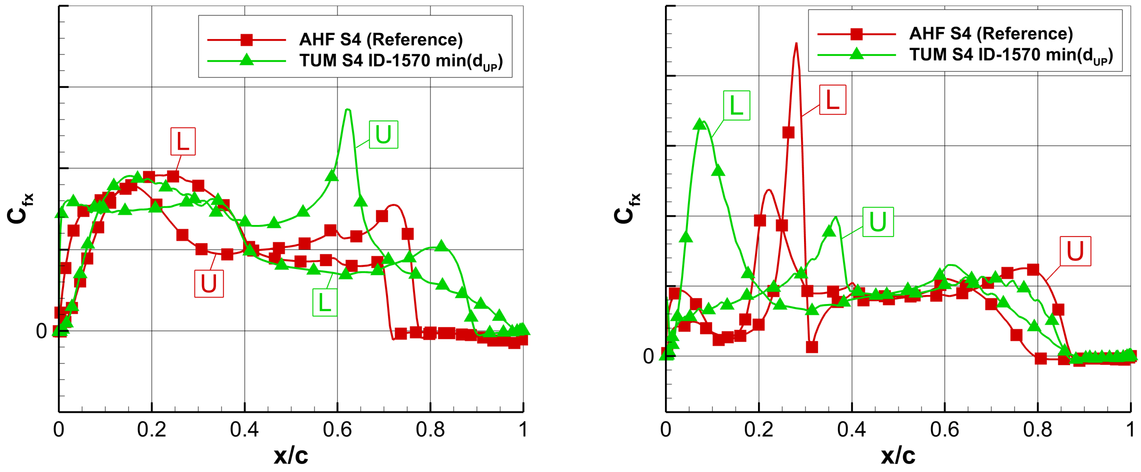

(e) Comparison of the axial skin-friction coefficient $C_{fx}(x/c)$ - Advancing Blade.

(f) Comparison of the axial skin-friction coefficient $C_{fx}(x/c)$ - Retreating Blade.

Figure 5.21: Evaluation of the mean, transient flow field and the surface quantities for the advancing as well as the retreating blade case of design 1570 (S4) showing a direct comparison to the original reference shape.

5.2 Three-dimensional Design Optimization

This section of the thesis is based on the author's publication in the Aeronautical Journal [45].

The large database of airfoils from the two-dimensional design optimization of the blade-sleeve sections (S2-S5) serves as the basis for the three-dimensional design optimization of the blade-sleeve fairing. For this purpose, selected subsets of airfoils are used to define the supporting structure of the blade-sleeve fairing. The shape modification is realized by exchanging specific airfoils at the respective blade-sleeve sections (S2-S5). The present optimization task is performed using an isolated rotor head with a single, stationary rotor blade. Moreover, two different azimuthal rotor positions are considered, which are given by the advancing and the retreating rotor-blade case. The flow conditions for the respective simulation cases are derived from the superposition of an average circumferential velocity in the blade-sleeve region with the cruise speed of the helicopter. Furthermore, an average angle of attack is applied, which is based on the cyclic blade-pitch angle as well as the local flow deflection due to the presence of the fuselage. The aerodynamic design optimization of the blade-sleeve fairing is performed with the optimization tool chain that has been developed in the course of the present thesis, see Sec. 3.1. Moreover, the optimization problem is tackled with a global, multi-objective optimization algorithm.

5.2.1 Geometry Parameterization

A simplified CAD model of the investigated rotor head is illustrated in Fig. 5.22. It consists of three components, which are given by the full-fairing beanie (FFB), the blade-sleeve fairing (BSF) and a truncated rotor blade (RB). Hence, an isolated rotor head is considered and interference effects with the pylon fairing as well as the fuselage are neglected. However, the effect of the fuselage flow deflection is incorporated, because the change in the local flow direction is considered in the applied angle of attack.

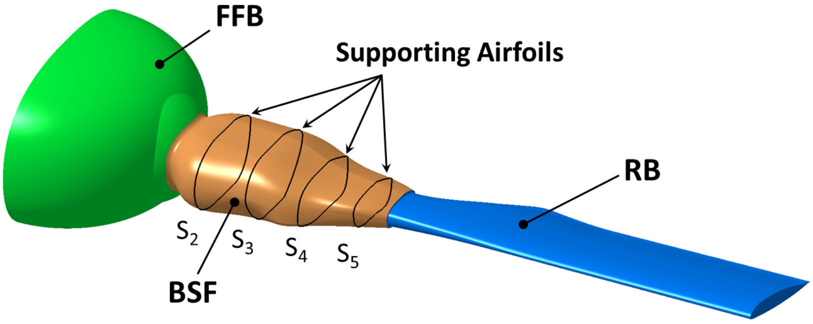

Figure 5.22: CAD model of the single rotor blade used for the design optimization of the RACER blade-sleeve fairing.

Due to the fact that a single, stationary rotor blade is examined, the effect of blade-vortex interaction is neglected. The simplification of the rotor head is necessary to achieve reasonable computational effort during the automated design optimization of the fairing.

Figure 5.23 illustrates the supporting structure that is used for the definition of the three-dimensional blade-sleeve fairing shape. It consists of six radial blade-sleeve sections (S1-S6) and additional supporting curves. The most inboard and outboard blade-sleeve sections S1 and S6 are illustrated by black lines. These two cross-sections are geometrically fixed to provide a proper transition between the full-fairing beanie, the blade-sleeve fairing and the rotor blade. The shape variation during the design optimization is achieved by replacing the four supporting airfoils S2-S5, which are depicted by the blue-colored lines. For this purpose, a selected subset of airfoils from the two-dimensional design optimization is used for each of the four blade-sleeve sections. The supporting airfoils are located at fixed radial stations within a range of $0.078 \leq r/R \leq 0.149$, where R corresponds to the rotor radius. The green-colored lines in Fig. 5.23 consist of straight lines and tangentially attached splines, which are connected through predefined points. The axial positions of these prescribed points are manually set to fulfill clearance and mounting requirements. Furthermore, the supporting airfoils are aligned according to the placement of these points, because they partially represent the control points of the Beziér curves, which are used for the definition of the sectional shapes. The supporting structure of the blade-sleeve fairing is filled by four tangential surface patches in the front, back, top and bottom. The automated shape generation during the design optimization is enabled by a parameterized CAD model in Catia V5R21. The design parameters are summarized in a design table, which is updated for each candidate according to the selected set of supporting airfoils. Finally, a predefined Catia macro is used to update the CAD model according to the modified design table.

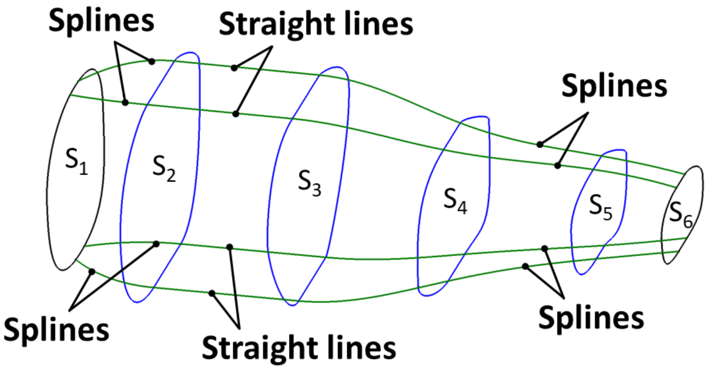

Figure 5.23: Supporting structure for definition of the three-dimensional blade-sleeve fairing shape.

5.2.2 Optimization Problem

The RACER blade-sleeve fairing is aerodynamically optimized for cruise flight, which is the most relevant flight condition in terms of drag reduction. During the preliminary design optimization of the blade-sleeve sections (S2-S5), two specific azimuthal rotor positions have been taken into account, which are given by the advancing ($\Psi = 090°$) and the retreating ($\Psi = 270°$) blade case. The same rotor positions are used for the present optimization task. The typical flow-velocity profiles along the rotor-blade axis during cruise flight are depicted in Fig. 5.24 for both cases. Regarding the advancing rotor blade, high Mach numbers are observed in the blade-tip region and in order to avoid transonic effects at the blade tip, the main rotor speed must be kept within a certain range depending on the cruise speed of the helicopter. Contrary to the advancing rotor blade, the retreating blade suffers from reversed flow in the blade-root region where the blade-sleeve fairing is located. The size of this reversed flow region depends on the main-rotor speed as well as the cruise speed of the helicopter. The RACER demonstrator uses an adaptive main-rotor speed to enable the expansion of the flight envelope towards the high-speed regime while maintaining vertical take-off and landing capabilities.

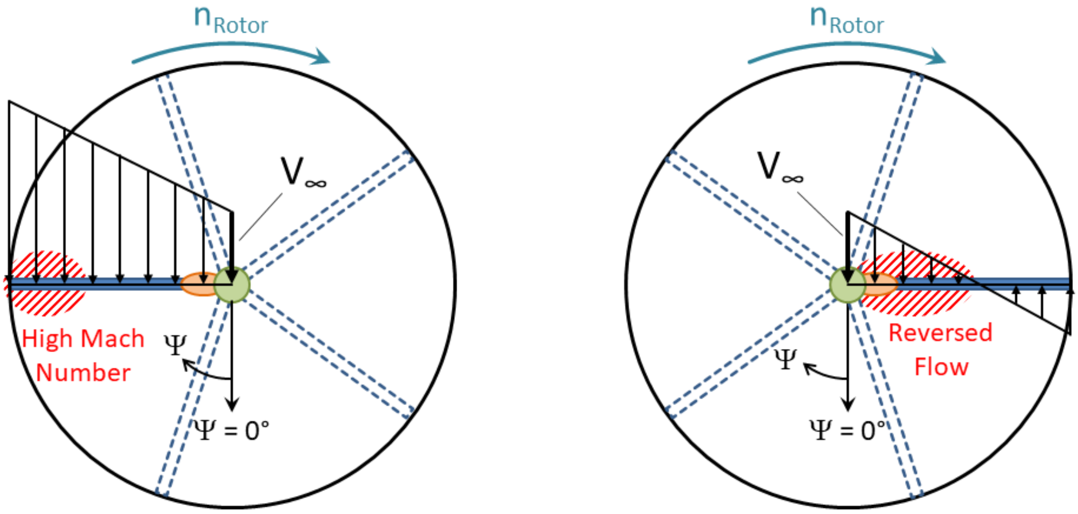

(a) Advancing rotor blade ($\Psi = 090°$). (b) Retreating rotor blade ($\Psi = 270°$).

Figure 5.24: Comparison of the radial flow-velocity profiles for the advancing and the retreating blade-case during cruise flight.

The applied objective functions are similar to the ones used for the two-dimensional design optimization, and their mathematical descriptions are given by Eq. 5.6 and Eq. 5.7. The main objective of the design optimization lies on drag reduction for cruise flight. However, lift is also taken into account in the objective function for the advancing rotor blade, which is given by the maximization of the aerodynamic efficiency C_L/C_D. Any additional lift that is generated by a favorable blade-sleeve fairing design without deteriorating drag would be beneficial for the overall performance of the entire configuration.

During cruise flight, the retreating blade-sleeve fairing lies within a region of reversed flow and therefore, the main objective is to minimize drag according to Eq. 5.7. The objective function f_2 is calculated by normalizing the drag of the retreating blade-sleeve fairing with the dynamic pressure. Hence, no reference surface is required to derive the objective functions.

$$maximize \quad f_1(\mathbf{x}) = C_L/C_D \qquad (Advancing\ Blade) \tag{5.6}$$

$$minimize \quad f_2(\mathbf{x}) = C_D \cdot S \qquad (Retreating\ Blade) \tag{5.7}$$

The design variables for the given optimization problem represent specific geometries of the supporting airfoils S2-S5. Hence, four discrete design variables are used according to the following mathematical description:

$$\mathbf{x} = \{S_2, S_3, S_4, S_5\} \quad with \quad \{S_i \in \mathbb{Z} \mid 1 \leq S_i \leq 12\} \tag{5.8}$$

Based on the preliminary design optimization of the blade-sleeve sections, a large database of optimized airfoils is available for the current optimization task. In order to reduce the computational effort to a reasonable level, the twelve best performing candidates are chosen for each of the four blade-sleeve sections (S2-S5). For this purpose, the final population can be divided into three regions, which can exemplarily be seen in Fig. 5.25 for blade-sleeve section S2. The first region consists of the "low-drag" shapes from the retreating blade case (green). The second region contains the "high lift-to-drag ratio" candidates from the advancing blade case (orange). The third region represents designs offering the best compromise between the applied objective functions. However, the main focus of the current optimization task is on drag reduction and therefore, shapes providing low-drag values for the advancing as well as the retreating blade case are chosen.

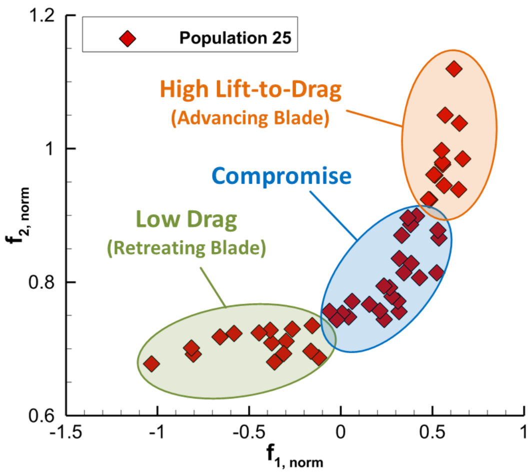

Figure 5.25: Population 25 of blade-sleeve section S2 showing the three different regions of the Pareto front.

For each of the two regions with low-drag shapes, four candidates are selected. Additionally, four designs are picked amongst the shapes offering the best compromise between the two objective functions. This provides a database of 48 specific shapes for the current optimization task, which yields a total number of 20.736 possible shape combinations.

The evaluation of all possible blade-sleeve fairing shapes is not feasible within a reasonable time-frame and the characteristics of the design space are unknown. Therefore, a robust, multi-objective genetic optimization algorithm is used to find promising designs for the RACER blade-sleeve fairing. During the preliminary optimization of the blade-sleeve sections, design constraints were employed, which should automatically be met by the three-dimensional blade-sleeve fairing. Hence, an unconstrained design optimization can be conducted. However, due to the interpolation between the blade-sleeve sections, minor violations of the design constraints could occur, which require a final, manual check of the most promising designs subsequent to the optimization process.

5.2.3 Computational Grid

The mesh generation is conducted with Ansys ICEM CFD and the fluid domain is discretized by block-structured, hexahedral elements. The advancing and the retreating blade case represent two different flow problems, which are both solved on the same computational mesh. The mesh is composed of 182 blocks yielding a total number of 7.2 million elements. The applied mesh resolution provides a good compromise between computational effort and numerical accuracy. The boundary layer is fully resolved featuring a dimensionless wall distance of $y^+ \leq 1$. Furthermore, a growth rate of 1.2 is employed in wall-normal direction to capture the near-wall flow properly. Figure 5.26 shows the dimensions of the applied computational domain, which is specified in multiples of the full-fairing beanie diameter d_{FFB}. Additionally, a detailed view on the surface mesh in the region of the blade-sleeve fairing is given. A farfield boundary condition is used on the front, back, top and bottom surface of the computational domain. Regarding the two remaining sides of the domain, a symmetry boundary condition is employed for the surface that is connected to the investigated geometry and a free-slip wall boundary condition is chosen for the opposite side. In order to enable an automated mesh generation, a tool command language (*.tcl) script is defined. For this purpose, the initial computational mesh is generated manually for a baseline geometry to derive the necessary ICEM commands that can be incorporated into the *.tcl script. Thereafter, this predefined script can be used to automatically mesh new geometries. The automated mesh generation process consists of several steps including the import of the new geometry, the re-association of the faces, edges and vertices as well as the export of the mesh in the desired format (e.g. *.msh, *.grid). Additionally, the distribution of the nodes as well as the mesh resolution can be updated if necessary in the meshing script.

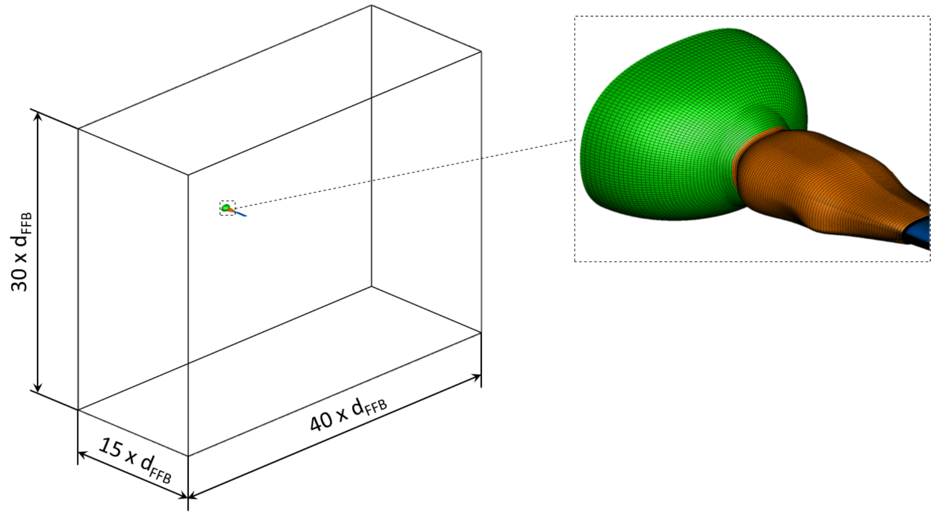

Figure 5.26: Size of the computational domain and detailed view on the surface mesh of the full-fairing beanie (green) and the blade-sleeve fairing (orange).

5.2.4 Applied Numerical Setup

Regarding the numerical investigation of the three-dimensional blade-sleeve fairing shape, two different flow solvers are used, which are given by the DLR TAU-Code and ANSYS Fluent. Therefore, the applied numerical setup for both flow solvers is summarized within this section. Due to the fact that faster convergence could be observed for the pressure-based solver of ANSYS Fluent concerning unsteady flow simulations, this solver is employed to derive time-accurate solutions of selected cases. Regarding the three-dimensional design optimization of the blade-sleeve fairing, steady-state flow simulations are performed using the DLR TAU-Code. This flow solver is not limited in terms of HPC licenses and therefore enables the parallel evaluation of multiple designs. Furthermore, the applicability of this flow solver within the optimization tool chain can be demonstrated on a complex three-dimensional optimization problem. The flexibility regarding the applied mesh-generation software and the implemented flow solvers enable a versatile exploitation of the optimization tool chain.

DLR TAU-Code

The numerical flow simulations for the design optimization of the three-dimensional blade-sleeve fairing shape are conducted with the DLR TAU-Code. A steady-state solution is generated solving the compressible Reynolds-Averaged Navier-Stokes (RANS) equations. Furthermore, a cell-vertex grid metric is employed and dual grid allows for the application of a multi-grid approach to stabilize and accelerate the solution process. Regarding turbulence modeling, fully turbulent flow is assumend and the SST k-g model is used, which represents a re-implemented version of the Menter SST model [123, 139].

The mean-flow equations are discretized by the standard TAU average of flux central scheme and a Roe second-order scheme is applied for the convective fluxes of the turbulence equations. Gradient reconstruction is achieved by a Green-Gauss algorithm. The system of equations is solved using a Lower-Upper Symmetric-Gauss-Seidel (LU-SGS) method. Moreover, a scalar dissipation model is selected as the numerical dissipation scheme. In general, the normalized density residual is reduced by four orders of magnitude, but the convergence behavior of the flow simulation strongly depends on the investigated geometry as well as the quality of the automatically generated computational mesh.

ANSYS Fluent

The commercial flow solver ANSYS Fluent is used for detailed investigations of selected three-dimensional blade-sleeve fairing shapes on the isolated rotor blade. For this purpose, steady as well as unsteady flow simulations are performed. The considered freestream Mach numbers lie within a range of $0.3 \leq Ma \leq 0.4$ and therefore, compressibility effects are taken into account. The compressible, unsteady Reynolds-Averaged Navier-Stokes (URANS) equations are solved. The transient flow simulations are initialized with the steady-state solutions. A pressure-based solver is used in combination with the SIMPLEC algorithm to achieve pressure-velocity coupling. The pressure interpolation is derived by the standard pressure scheme of ANSYS Fluent and turbulence modeling is realized by the two-equation k-ω SST model [123]. Furthermore, second-order upwind schemes are chosen for the spatial discretization of density, momentum, turbulent kinetic energy, specific dissipation rate and energy. The gradients are calculated by using a least-squares cell-based formulation. Additionally, a second-order implicit scheme is employed for the temporal discretization. The time-step size for the time-accurate flow simulations is set to $\Delta t = 0.1\,ms$, which offers a reasonable temporal resolution for the observed oscillations of the aerodynamic forces. All normalized residuals are reduced by at least four orders of magnitude. This is achieved within approximately ten inner iterations, depending on the investigated geometry. During preliminary tests concerning the applied temporal discretization, it was observed that doubling the time-step size leads to an increase of the number of inner iterations of 60 %. Additionally, the selected time-step size of $\Delta t = 0.1\,ms$ provides a more stable and robust convergence behavior. Concerning the fluid properties, air ideal gas is used and the ambient conditions are set according to a sea-level cruise flight in ICAO standard atmosphere.

5.2.5 Results and Analysis

An overview about selected results of the three-dimensional design optimization is given in the present section. The design optimization task is performed with the same genetic optimization algorithm that has been used for the two-dimensional design optimization of the blade-sleeve sections. Furthermore, the same parameters are employed to tune the optimization algorithm accordingly. The investigated objective functions are given by the maximization of the lift-to-drag ratio for the advancing rotor blade and the minimization of drag for the retreating rotor blade, see Eq.5.6 and Eq. 5.7.

Based on the applied optimization setup, the fitness of each candidate is evaluated by a domination count, which is used to order the population members. A design is dominating another one, if it is better in both objective functions. Hence, a ranking can be derived for each population. In the present optimization task, a replacement value of six is applied, which means that the number of candidates dominating a certain design must be lower than this value, otherwise it is rejected. In order to avoid an excessive reduction of the population size, a shrinkage percentage of 95 % is chosen, which means that the size of the subsequent population is reduced by five percent. If the optimization algorithm does not find enough designs to comply with the shrinkage percentage requirement, the below-limit selector is automatically adapted to higher values. In order to reach a reasonable distribution of candidates along the Pareto frontier, radial niching is employed, which ensures a minimum Euclidean distance between the candidates in the objective space. The niching vector consists of two elements and for each element a relative distance of two percent of the respective non-dominated objective function range is chosen. The crossover operation of the genetic optimization algorithm is realized by randomly shuffling the design-variable values of the parents. The relative number between parents and children defines the amount of mixing that is occurring within the population. For the current optimization problem, two parents produce two children. The crossover rate is set to 0.8, which means that the number of crossover operations corresponds to 80 % of the respective population size. Random diversity is introduced by a mutation rate of five percent of the population size. The selected mutation algorithm randomly assigns new design-variable values to randomly selected candidates. The main parameters of the optimizer setup are summarized in Tab. 5.4.

The presented results include an analysis of the objective space and a comprehensive overview of the best performing blade-sleeve fairing designs from the final population. A single, promising design is selected from the Pareto front and investigated in more detail. For this purpose, steady-state and transient flow-simulation results are evaluated and compared to a reference blade-sleeve fairing. Furthermore, a flow-field analysis is conducted and relevant surface quantities are shown.

Finally, the influence of three-dimensional flow phenomena on the aerodynamic characteristics of the blade-sleeve fairing is discussed.

No. of Objective Functions	2	No. of Parents	2
Fitness Type	Domination Count	No. of Children	2
Replacement Type	Below Limit	Crossover Rate	0.80
Replacement Value	6	Niching Radius (f_1/f_2)	0.02/0.02
Crossover Type	Random Shuffle	Mutation Rate	0.05
Shrinkage Percentage	0.95		

Table 5.4: Summary of parameters used for the setup of the genetic optimization algorithm.

Analysis of the Objective Space

The results of the design optimization are summarized in Fig. 5.27 showing the two-dimensional objective space for all investigated blade-sleeve fairing shapes. The objective functions are calculated from the lift and drag of the blade-sleeve fairing. The aerodynamic forces of the beanie and the truncated rotor blade are neglected. The objective functions are normalized by the respective aerodynamic forces of the reference blade-sleeve fairing, which was developed by Airbus Helicopters. During the automated design optimization process, a total number of 811 blade-sleeve fairings are investigated. Moreover, the first population is randomly initialized and it consists of 150 designs.

Figure 5.27a gives a global view on all investigated fairing shapes. The reference blade-sleeve fairing (AHF Reference) is illustrated by the orange circle and it is located at $f_1 = -1$ and $f_2 = 1$ due to the applied normalization. Besides the AHF reference fairing, an additional fairing is manually designed, which is designated as *TUM Reference*. The construction of this fairing is based on the sectional shapes offering the best compromise between the applied objective functions of the two-dimensional design optimization. These sectional shapes provide the minimum distance to the utopia point (min d_{UP}). The geometry of the TUM reference fairing is depicted in Fig. 5.28 including a detailed view on the selected supporting airfoils. Besides the geometries, the applied design constraints are illustrated by the red dashed lines. Furthermore, the final population of the two-dimensional design optimization is shown for each of the sections. Additionally, the location of the selected candidates is marked by a triangular symbol in the respective objective space. The evaluation of the objective space shows that simply combining the min d_{UP} sectional shapes does not necessarily provide the most performant three-dimensional blade-sleeve fairing shape. It can be seen that the majority of candidates shows improved objective functions. In comparison to the AHF reference, all investigated candidates reveal enhanced objective functions in both dimensions, which can be related to the previously optimized 2D sectional shapes.

The observed objective-function values lie within a range of $-1.03 \leq f_{1,norm} \leq 2.10$ and $0.69 \leq f_{2,norm} \leq 0.87$ considering the steady-state TAU simulation results. The *TUM Reference* blade-sleeve fairing is located at $f_{1,norm} = 1.07$ and $f_{2,norm} = 0.85$. Figure 5.27b shows the successive development of the designs from population 0 to population 20, which is the final population for the current optimization task. As an intermediate result and to visualize the development during the optimization, the fifth generation of the optimization run is illustrated. A detailed view on the final population is given in Fig. 5.27c, which consists of 62 candidates. The formation of a Pareto front amongst the best performing shapes can clearly be seen. Figure 5.27d depicts the final dataset of the design optimization run. Moreover, the best candidates from each region of the Pareto front are marked.

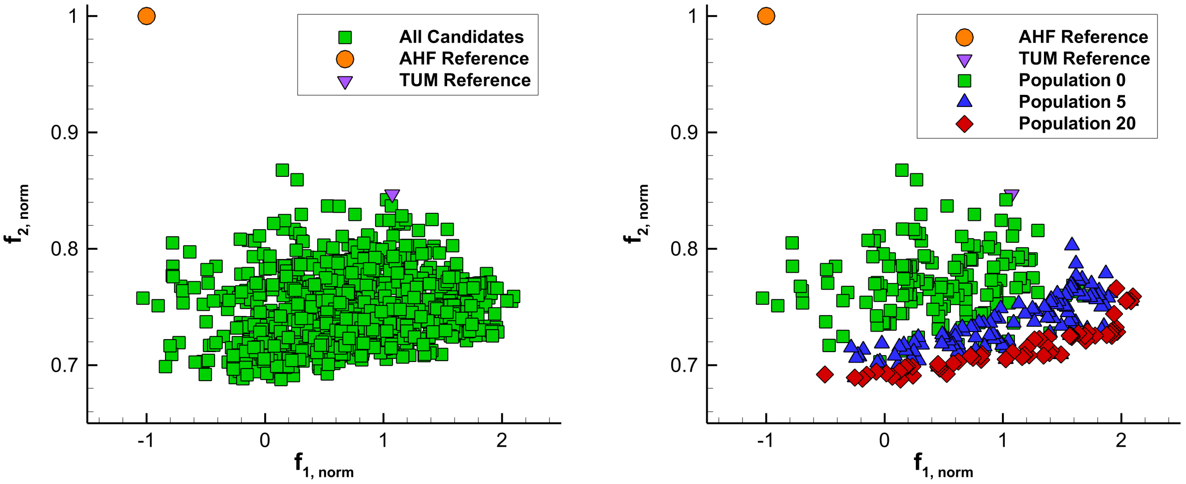

(a) All investigated designs in the feasible objective space.

(b) Generation-wise development from population 0 to population 20.

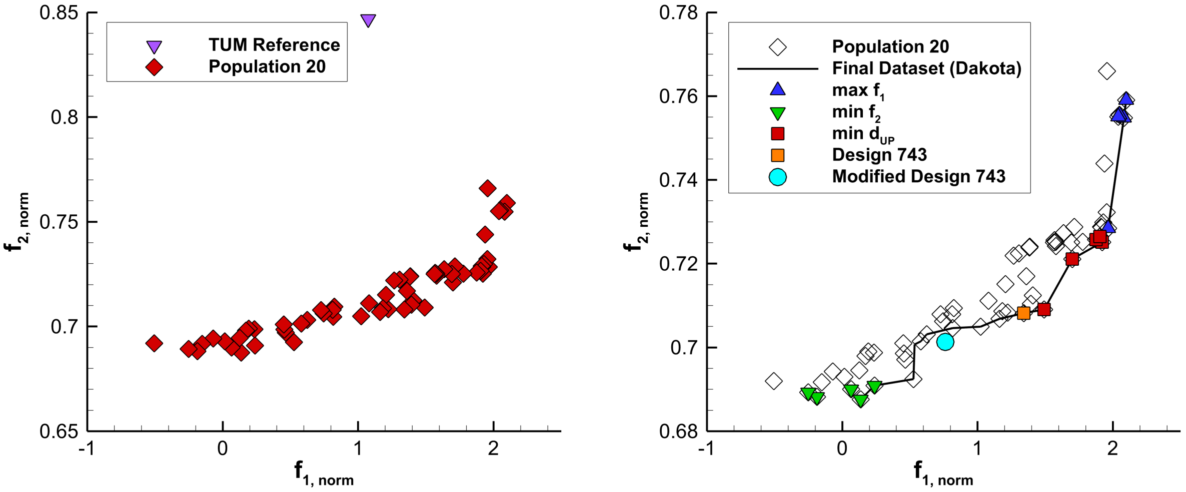

(c) Detailed view on the Pareto front of the final population.

(d) Best performing designs and final dataset from DAKOTA.

Figure 5.27: Evaluation of the objective space from the three-dimensional design optimization of the RACER blade-sleeve fairing.

These include the high lift-to-drag ratio shapes for the advancing blade case ($max\ f_1$), the low-drag shapes for the retreating blade case ($min\ f_2$) as well as the blade-sleeve fairings offering the best compromise between both objective functions ($min\ d_{UP}$).

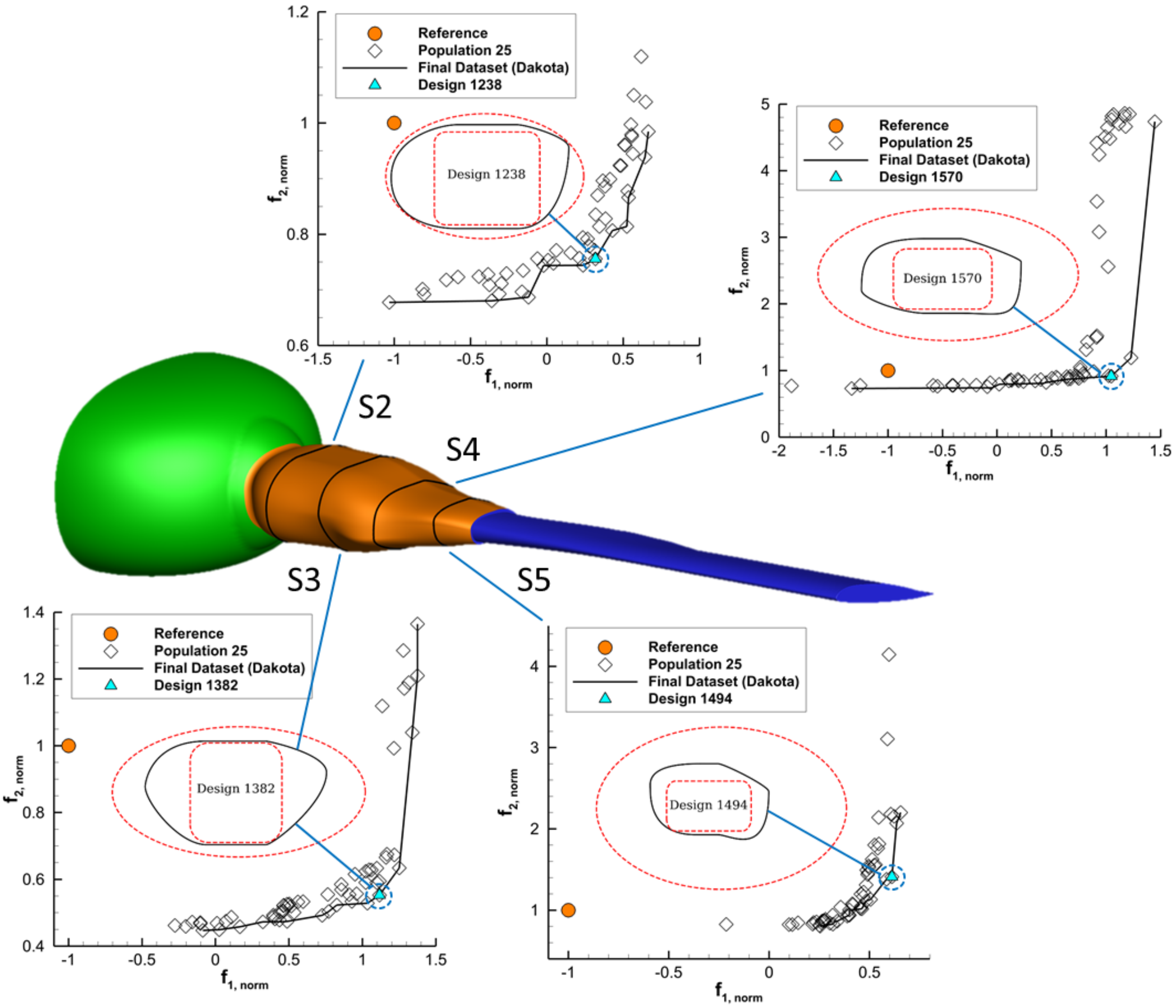

Figure 5.28: TUM reference blade-sleeve fairing showing the selected supporting airfoils and the corresponding objective spaces.

A detailed evaluation of promising candidates is conducted to choose a single blade-sleeve fairing from the Pareto front, which is investigated in more detail. Besides the aerodynamic forces, several additional assessment criteria are taken into account for the selection of the fairing including the smoothness of the geometry, the manufacturability and the mountability of the fairing. Based on these criteria, design 743 is chosen from the $min\ d_{UP}$ region of the Pareto front. Hence, this shape offers a good compromise between both objective functions and it is illustrated by the orange, squared symbol in Fig. 5.27d. Compared to the reference blade-sleeve fairing, the lift-to-drag ratio for the advancing blade case can be increased by $\Delta f_1 = +2.34$ and the drag of the retreating blade-case can be reduced by $\Delta f_2 = -0.29$.

Figure 5.29 shows blade-sleeve fairing 743 on the isolated rotor blade. Moreover, the supporting airfoils are illustrated and the corresponding objective spaces from the two-dimensional design optimization are presented.

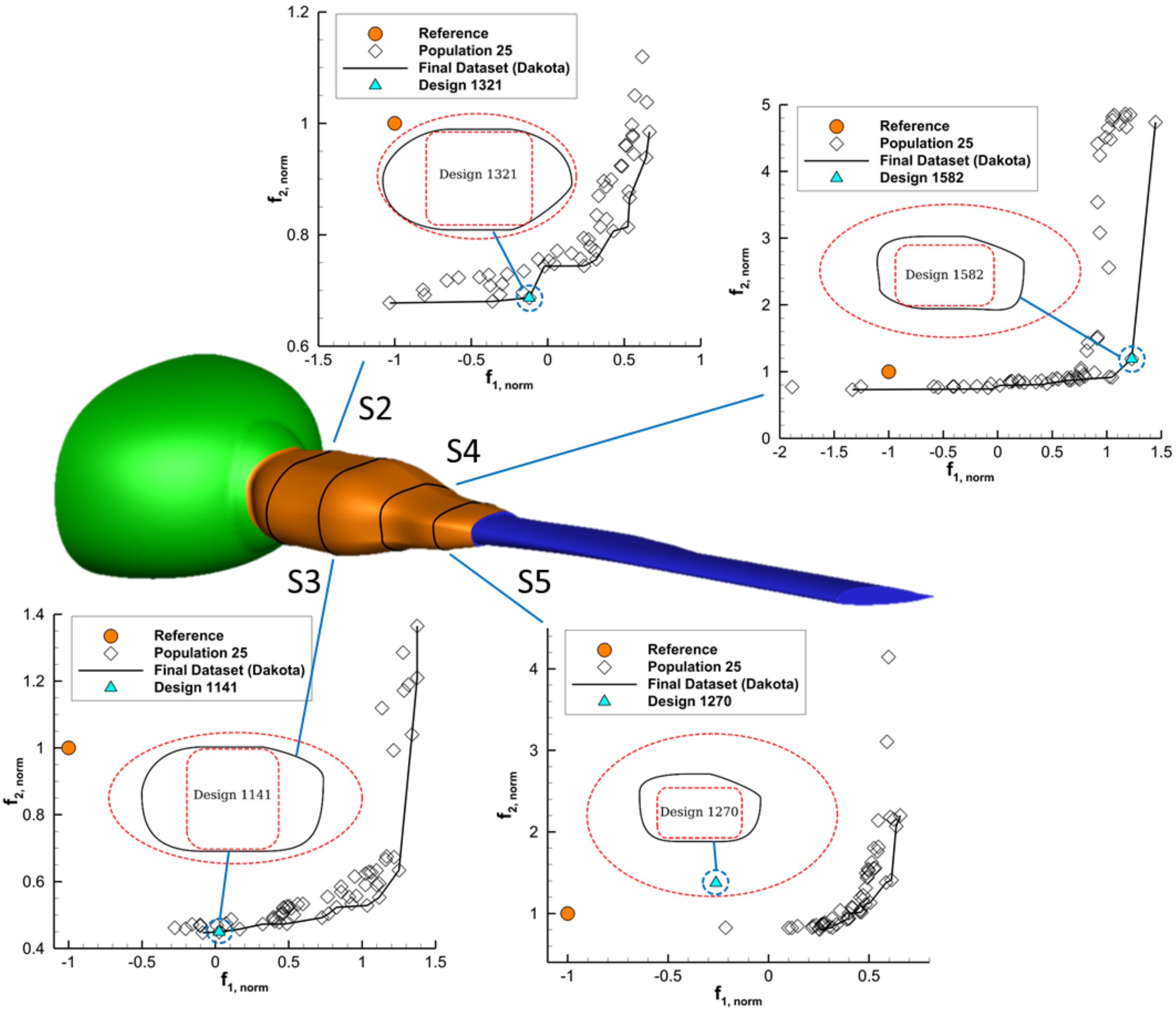

Figure 5.29: Blade-sleeve fairing design 743 offering the best compromise between the applied objective functions.

A detailed view on the outer shape of design 743 reveals some dents and bumps in the geometry, which are caused by the automated shape generation in combination with the applied design parameterization. There is no relation between the size and position of the blade-sleeve sections. Furthermore, the transition between the sections and their axial/vertical position are not part of the parameterization, which can cause a non-smooth shape. In order to enhance the outer shape of the selected blade-sleeve fairing, a manual smoothing is performed leading to a slightly modified shape of design 743, which is illustrated in Fig. 5.30. Additionally, the modified sectional shapes are presented. The change of the geometry leads to different objective function values, which can be seen in Fig. 5.27d, where the modified design 743 is represented by the turquoise circle. Hence, the finally selected blade-sleeve fairing design reaches normalized objective function values of $f_{1,norm} = 0.76$ and $f_{2,norm} = 0.70$.

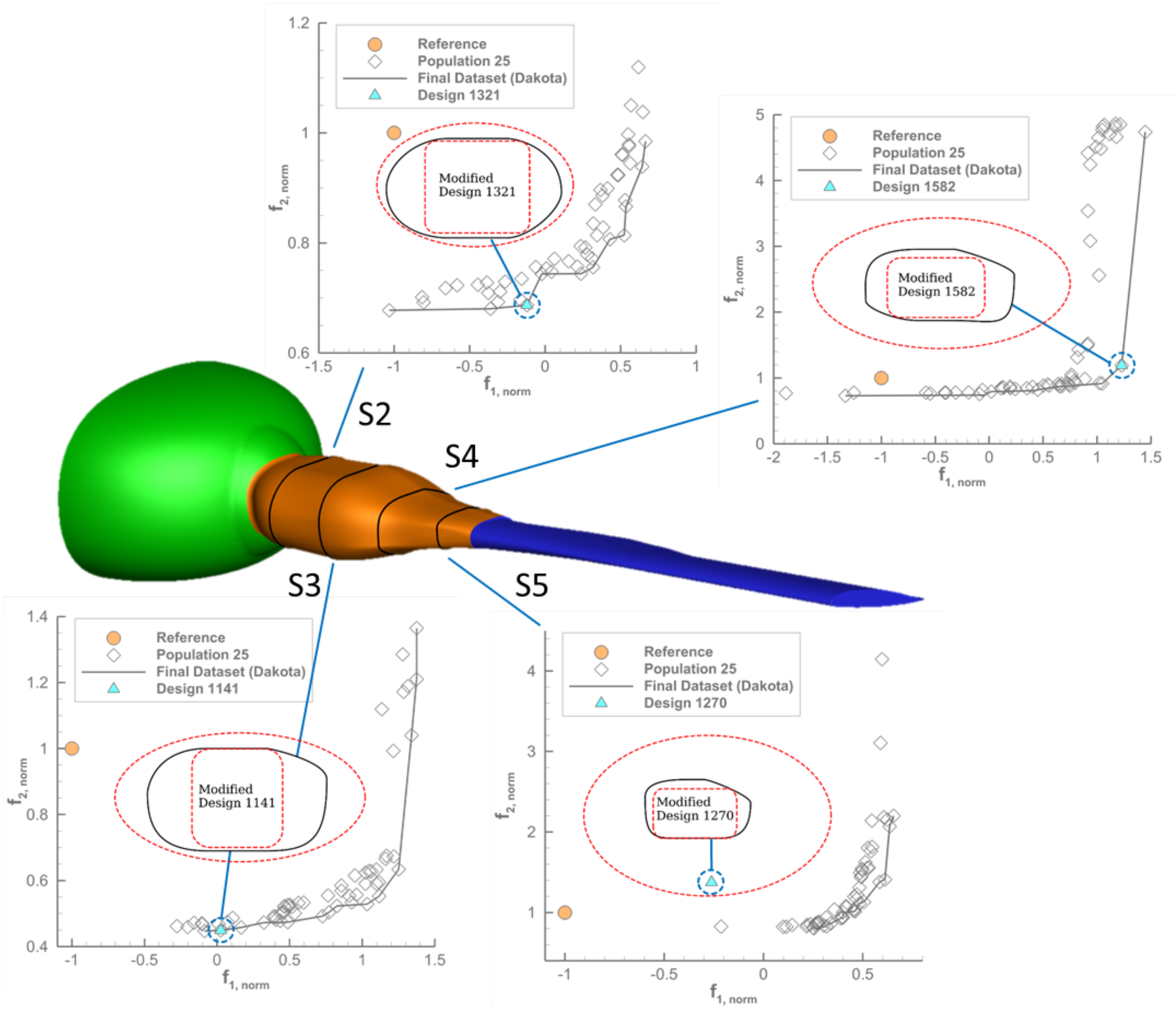

Figure 5.30: Modified blade-sleeve fairing design 743.

Within Chapter 6, the modified blade-sleeve fairing design 743 is investigated in more detail on the five-bladed, isolated rotor head featuring cyclic-pitch motion. The results are compared to the rotor head with the AHF reference blade-sleeve fairing. A detailed view on the AHF reference blade-sleeve fairing is given in Fig. 5.31 and the newly developed fairing is depicted in Fig. 5.32.

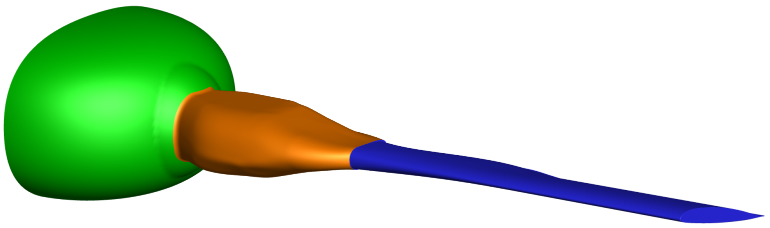

(a) Front view.

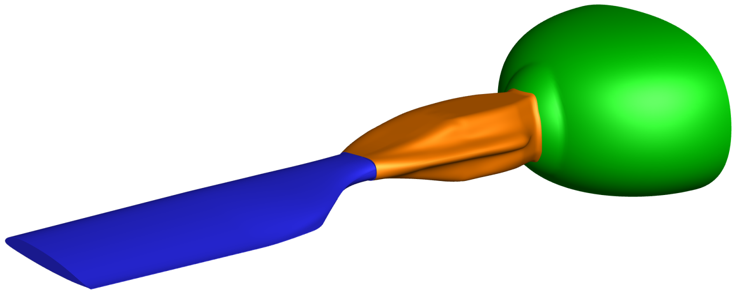

(b) Rear view.

Figure 5.31: Detailed view on the AHF reference blade-sleeve fairing.

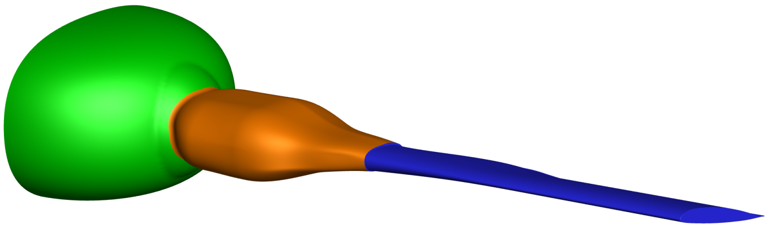

(a) Front view.

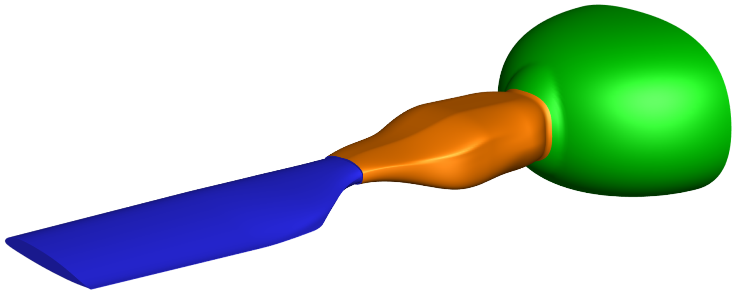

(b) Rear view.

Figure 5.32: Detailed view on the modified blade-sleeve fairing design 743.

Evaluation of the Aerodynamic Forces

In order to evaluate the performance benefit that can be expected by the newly developed blade-sleeve fairing, the aerodynamic forces are analyzed and compared to the AHF reference blade-sleeve fairing. First, the TAU steady-state flow simulations are examined, which can be seen in Tab. 5.5. The table includes the forces of the TUM reference fairing, design 743 and the modified design 743. Moreover, the integral forces are only given for the blade-sleeve fairing, because the rotor blade and the beanie are not taken into account for the evaluation of the objective functions during the design optimization process. Regarding the advancing blade case, the TUM reference fairing provides a lift increase of $\Delta L = +213.6\,\%$ and a slightly higher drag leading to $\Delta D = +5.7\,\%$. Hence, objective function f_1 is improved by $\Delta f_1 = +207.4\,\%$ compared to the AHF reference blade-sleeve fairing. The analysis of the retreating blade case shows a lift increase of $\Delta L = +85.6\,\%$ and a drag reduction of $\Delta D = -15.3\,\%$, which represents objective function f_2.

The automatically generated blade-sleeve fairing design 743 reveals a lift increase of $\Delta L = +231.5\,\%$ and a drag reduction of $\Delta D = -2.0\,\%$ regarding the advancing blade case, which leads to $\Delta f_1 = +234.2\,\%$. Furthermore, the evaluation of the retreating blade case shows a drag reduction of $\Delta D = -29.2\,\%$ in combination with a lift increase of $\Delta L = +76.2\,\%$ for the optimized design. The manual shape modification of design 743 shows a stronger impact on the advancing blade case, whereas the aerodynamic forces of the retreating blade case are comparable to the original shape of design 743. Regarding the advancing blade case, the modified design reduces lift by $\Delta L = -59.9\,\%$ and drag by $\Delta D = -4.0\,\%$ compared to the original geometry. The analysis of the retreating blade case shows a marginal lift increase of $\Delta L = +0.2\,\%$ and a minor drag reduction of $\Delta D = -0.7\,\%$ with respect to design 743.

TAU Steady-state		Advancing Blade			Retreating Blade	
		ΔLift	ΔDrag	Δf_1	ΔLift	ΔDrag $\widehat{=}\,\Delta f_2$
Fairing	Comp.	[%]	[%]	[%]	[%]	[%]
TUM Reference	BSF	+213.6	+5.7	+207.4	+85.6	-15.3
Design 743	BSF	+231.5	-2.0	+234.2	+76.2	-29.2
Modified Design 743	BSF	+171.6	-6.0	+176.2	+76.4	-29.9

Table 5.5: Evaluation of the aerodynamic forces for the TUM reference blade-sleeve fairing, design 743 and the modified design 743 based on the TAU steady-state simulations. The forces are given relative to the AHF reference blade-sleeve fairing.

Besides the steady-state TAU simulations, transient flow simulations are performed with ANSYS Fluent for above-mentioned blade-sleeve fairings to capture the unsteady flow field properly in a time-resolved manner. The results are summarized in Tab. 5.6 giving an overview on the mean aerodynamic forces of the blade-sleeve fairing (BSF) as well as the total forces including the contribution of the beanie, the blade-sleeve fairing and the truncated rotor blade. The forces are averaged over the last 20 % of the simulation time and they are given relative to the AHF reference blade-sleeve fairing. It can be seen that there is a large discrepancy between the steady-state and the transient solutions for all investigated fairings. From a global point of view, the transient flow simulations predict reduced lift and increased drag for the blade-sleeve fairing compared to the steady-state solutions. This discrepancy can be related to unsteady flow-separation characteristics, which differ the flow-separation onset as well as the development of the turbulent wake-flow field. A similar behavior is observed for the two-dimensional flow simulations of the blade-sleeve sections, see Sec. 5.1.5.

FLUENT Transient		Advancing Blade			Retreating Blade	
		ΔLift	ΔDrag	Δf_1	ΔLift	ΔDrag $\widehat{=}\, \Delta f_2$
Fairing	Comp.	[%]	[%]	[%]	[%]	[%]
TUM Reference	BSF	+188.5	+11.0	+179.7	+34.1	+5.3
	Total	+41.8	-2.7	+43.9	+11.6	-3.1
Design 743	BSF	+132.3	+16.4	+127.7	-25.9	+9.0
	Total	+23.5	-0.9	+23.1	-5.6	-1.9
Modified Design 743	BSF	+171.1	+18.4	+160.1	-19.3	+3.2
	Total	+34.8	-3.6	+38.2	-3.9	-5.9

Table 5.6: Evaluation of the aerodynamic forces for the TUM reference blade-sleeve fairing, design 743 and the modified design 743 based on the transient FLUENT simulations. The forces are given relative to the AHF reference blade-sleeve fairing.

Regarding the TUM reference blade-sleeve fairing, lift and drag are increased by $\Delta L = +188.5\,\%$ and $\Delta D = +11.0\,\%$, which leads to $\Delta f_1 = +179.7\,\%$ for the advancing blade case. Additionally, the evaluation of the retreating blade case reveals a difference in lift of $\Delta L = +34.1\,\%$ and additional drag of $\Delta D = \Delta f_2 = +5.3\,\%$. If all components of the geometry are taken into account for the calculation of the total forces, higher lift and lower drag values are observed for both cases.

The automatically optimized design 743 generates about 132.3 % more lift and +16.4 % more drag than the AHF reference fairing. This corresponds to an improvement in objective function f_1 of $\Delta f_1 = +127.7\,\%$. With respect to the total forces, lift is increased by $\Delta L = +23.5\,\%$ and drag slightly reduced by $\Delta D = -0.9\,\%$, which yields $\Delta f_1 = +23.1\,\%$. For the retreating blade case, design 743 delivers less lift ($\Delta L = -25.9\,\%$) and higher drag ($\Delta D = +9.0\,\%$) concerning the blade-sleeve fairing component. Regarding the total forces, lift is decreased by $\Delta L = -5.6\,\%$ and drag can be lowered by $\Delta D = -1.9\,\%$.

The manual shape modification of design 743 leads to an increased lift and slightly higher drag for the advancing blade case, which yields an improvement in objective function f_1 of 160.1 % compared to the AHF reference blade-sleeve fairing. Regarding the total forces, the newly developed fairing enhances the lift-to-drag ratio of the isolated rotor blade by 38.2 %. The evaluation of the retreating blade case shows that the blade-sleeve fairing itself reduces lift by 19.3 % and raises drag by 3.2 %. However, the total forces show a minor loss of lift with $\Delta L = -3.9\,\%$ and a drag reduction of $\Delta D = -5.9\,\%$ in comparison to the AHF reference fairing.

Analysis of the Flow Field and Surface Quantities

The flow field of the isolated rotor blade is shown for the modified blade-sleeve fairing design 743, which is considered as the final, optimized shape for further investigations within the FURADO project. The newly developed blade-sleeve fairing provides decent performance improvements and it fulfills all design requirements. This means that the fairing is fully compliant with the design constraints, it is manufacturable and it can be easily mounted on the RACER demonstrator, because major parts of the original supporting structure can be reused.

The flow field analyses are performed by means of averaged, transient flow-simulation results. The averaging is conducted over the last 20 % of the simulation time. Figure 5.33 illustrates the mean, axial flow velocity $V_{x,mean}$, which is normalized by the free-stream velocity V_∞. Five streamwise sections are shown for the advancing and the retreating blade case, respectively. In order to limit the sectional contour plots to a relevant region in the vicinity of the geometry, a cut-off value of $V_{x,mean}/V_\infty = 0.99$ is applied.

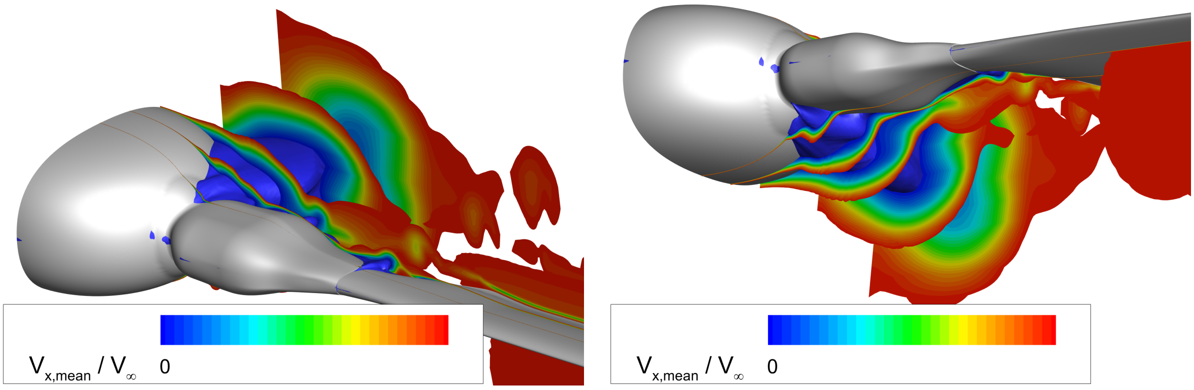

(a) Advancing rotor-blade case.

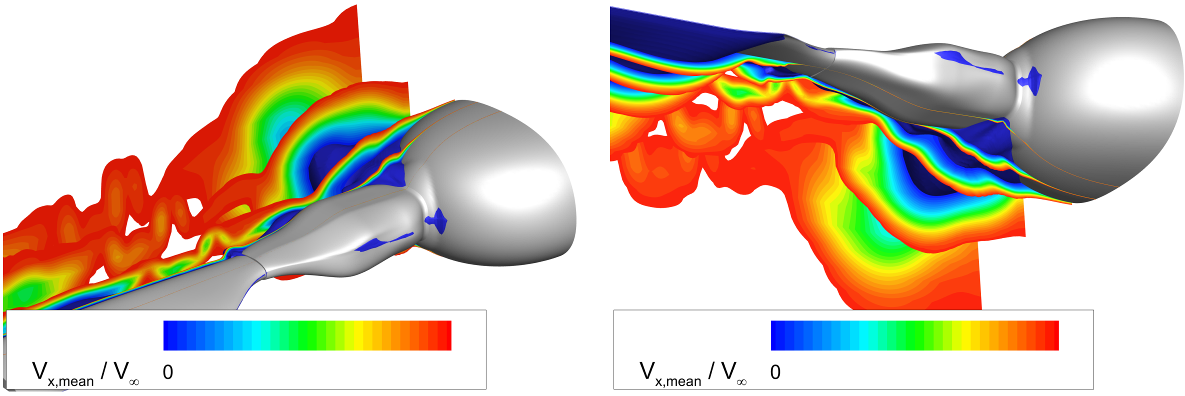

(b) Retreating rotor-blade case.

Figure 5.33: Flow-field visualization for the modified design 743 showing the mean, normalized axial flow velocity $V_{x,mean}/V_\infty$ in streamwise sections and a blue-colored iso-surface with $V_{x,mean}/V_\infty = 0$.

Additionally, a blue-colored iso-surface with $V_{x,mean}/V_{\infty} = 0$ is drawn to make regions of flow separation visible. It can be seen that an extensive flow separation occurs in the transition region between the blade-sleeve fairing and the full-fairing beanie. Regarding the bottom view of the retreating blade-case, additional flow separation can be seen on the lower side of the truncated rotor blade.

The mean surface-pressure distribution for the selected design is illustrated in Fig. 5.34 for both flow conditions. Moreover, the top and the bottom surface of the investigated geometry are shown. The direction of the incoming flow is drawn for better understanding of the contour plots. Due to the bluntness of the beanie and the blade-sleeve fairing, a large high-pressure region is present on the leading-edge of the respective case. Furthermore, strong curvatures in the fairing geometry are accompanied by pronounced low pressure regions. The large-scale flow separation between the beanie and the blade-sleeve fairing leads to almost constant pressure levels in the inboard, downstream part of the fairing.

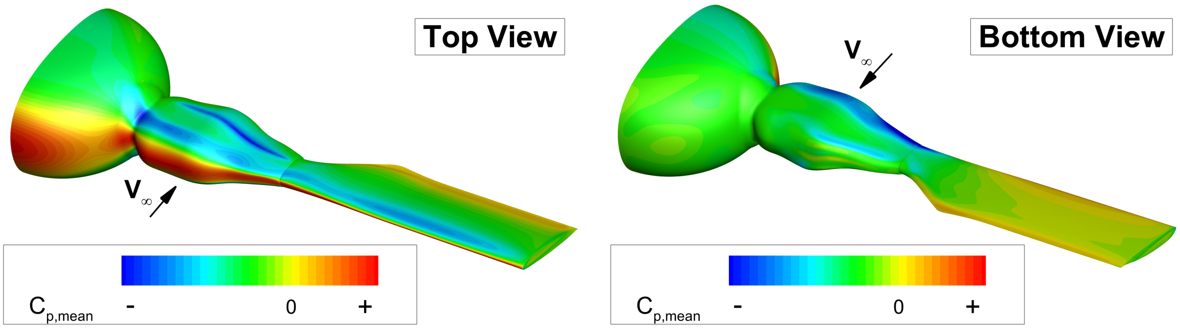

(a) Advancing rotor-blade case.

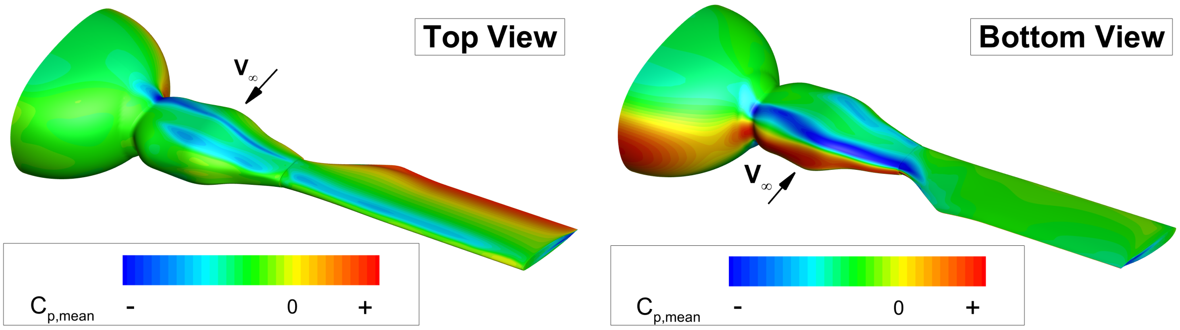

(b) Retreating rotor-blade case.

Figure 5.34: Mean surface-pressure coefficient $C_{p,mean}$ shown for the modified design 743.

In order to evaluate the impact of the manual shape modification on the aerodynamic characteristics of design 743, the chordwise surface-pressure distributions of the original and the modified shape are examined and compared to each other at the blade-sleeve sections S2-S5. The chordwise pressure distributions for the advancing blade case are depicted in Fig. 5.35 and for the retreating blade case they are given in Fig. 5.36.

The blade-sleeve fairing is divided into an upper and a lower side, which is marked by U for upper and L for lower, respectively. Regarding the advancing blade case, the most inboard section S2 shows only minor differences between the two geometries. The pressure distribution on the lower side is almost identical showing the same low pressure region in the front part and a plateau of rather constant pressure within the range of $0.4 \leq x/c \leq 1.0$. On the upper side, the largest discrepancies are present at $x/c = 0.3$ and $x/c = 0.7$, where the modified geometry generates slightly lower pressure levels.

Concerning the third blade-sleeve section S3, no geometry modifications are introduced and therefore, no mentionable differences can be seen in the pressure distribution. The geometry modification at blade-sleeve section S4 reduces the pressure difference between the upper and the lower side in the front part of the fairing ($x/c < 0.35$). Moreover, the suction peak at $x/c \approx 0.85$ is a bit stronger for the modified shape. The modified blade-sleeve section S5 shows a more pronounced suction peak on the lower surface at $x/c \approx 0.1$ and a slightly reduced pressure level on the upper surface. Downstream of this position, the pressure distributions are quite comparable.

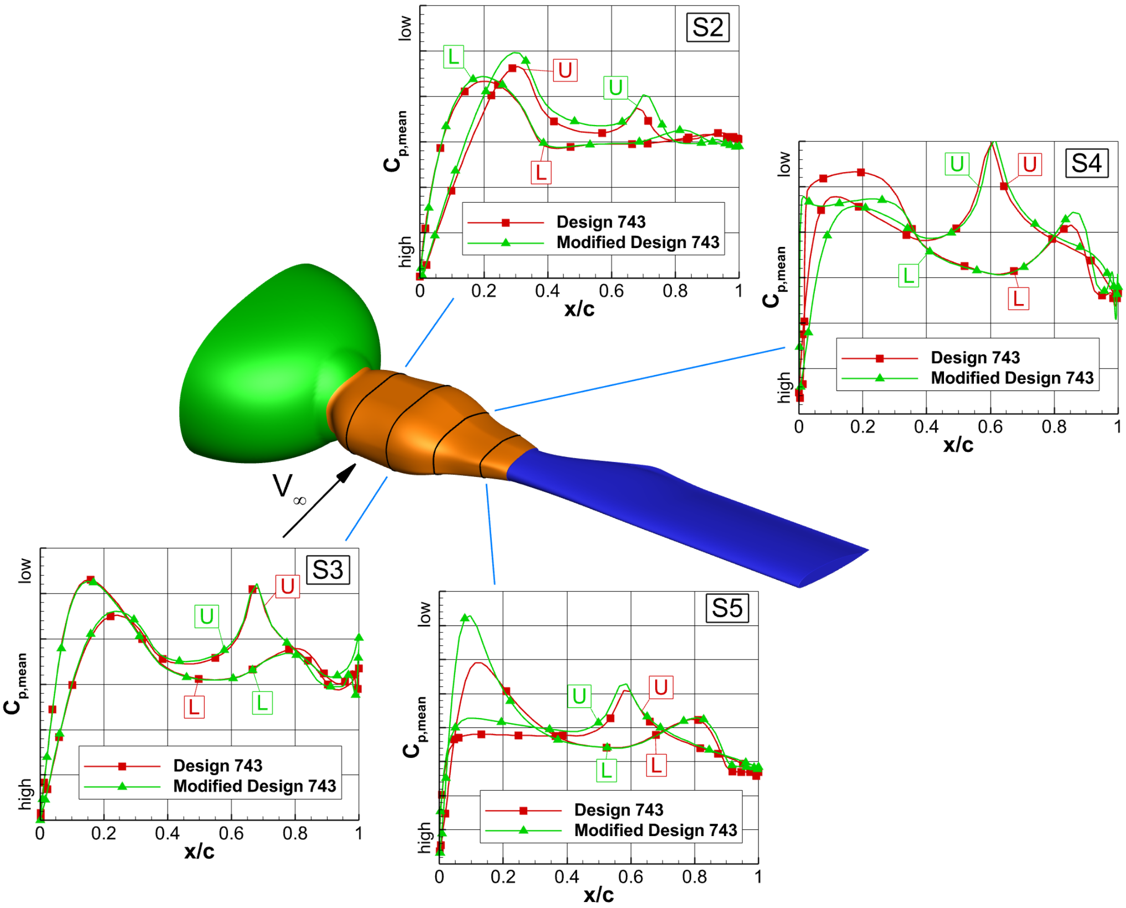

Figure 5.35: Evaluation of the mean, chordwise surface-pressure distribution $C_{p,mean}(x/c)$ at the blade-sleeve sections S2-S5 comparing the results of the original and the modified blade-sleeve fairing design 743 for the advancing blade case.

For the retreating blade case, which is depicted in Fig. 5.36, the x-axis of the chordwise surface pressure distribution is mirrored following the rule that the leading-edge is located at $x/c = 0$. Regarding section S2, it can be seen that the suction peaks on the lower and the upper surface are shifted more upstream by $\Delta x/c = 0.05$. Additionally, the modified shape generates a stronger suction peak on the upper side, whereas the same value is reached on the lower side. The difference in the pressure distribution for blade-sleeve section S3 is negligible. Furthermore, blade-sleeve section S4 shows marginal discrepancies between the two geometries. The biggest differences are present in the rear part of the fairing at $x/c > 0.6$. The evaluation of the most outboard section S5 reveals marginally stronger suction peaks at $x/c \approx 0.12$ for the lower and $x/c \approx 0.43$ for the upper side. Furthermore, the pressure recovery in the rear part of the fairing looks slightly different, but the same pressure levels are reached.

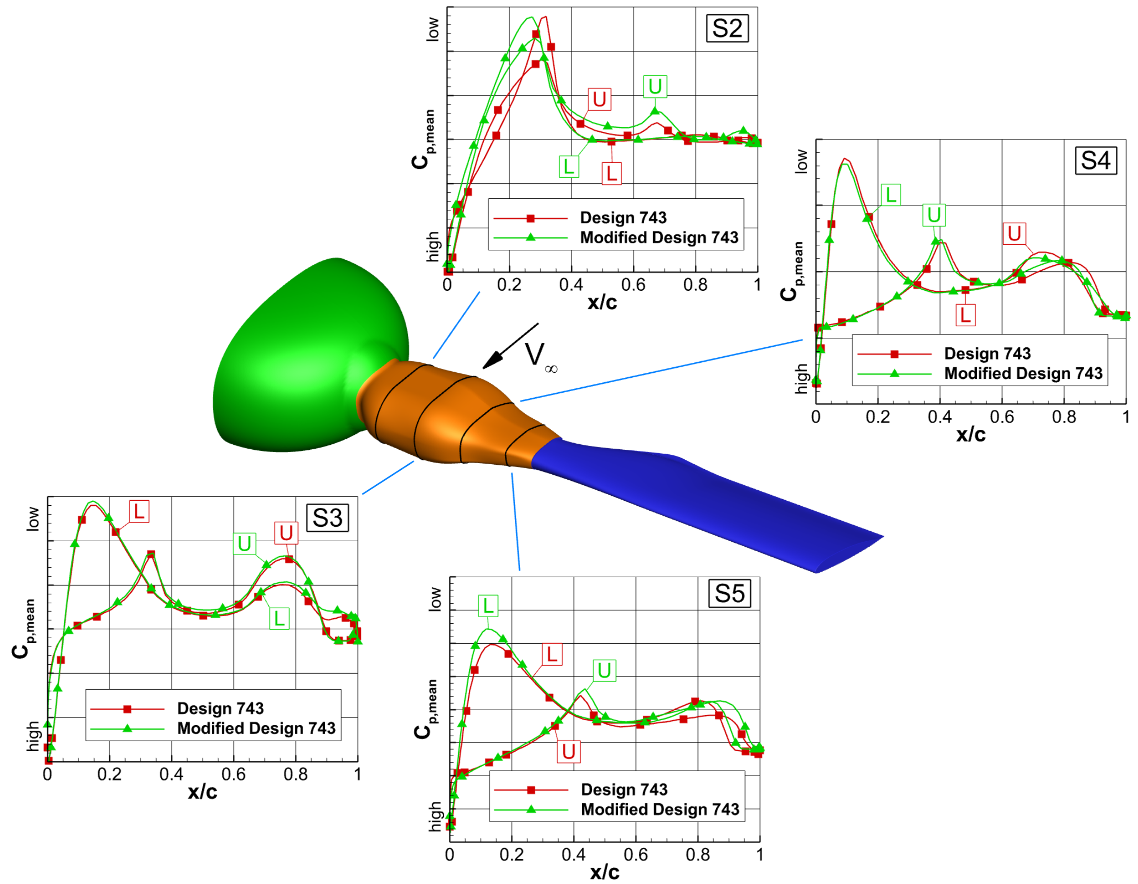

Figure 5.36: Evaluation of the mean, chordwise surface-pressure distribution $C_{p,mean}(x/c)$ at the blade-sleeve sections S2-S5 comparing the results of the original and the modified blade-sleeve fairing design 743 for the retreating blade case.

Besides the evaluation of the chordwise pressure distribution at the blade-sleeve sections S2-S5, the radial pressure distribution is analyzed as well. For this purpose, three chordwise positions are considered in the front (F), middle (M) and rear (R) part of the fairing, which can be seen in Fig. 5.37 for the advancing blade case. The radial position is specified relative to the length of the blade-sleeve fairing $l_{y,BSF}$, where the most inboard position is located at $y/l_{y,BSF} = 0$.

Regarding the most forward section F, the radial pressure distribution on the lower surface shows almost no difference between the two geometries in the inboard region ($y/l_{y,BSF} < 0.45$). In contrast, the wavy pressure distribution in the outboard region of the original geometry is smoothed by the shape modification. Concerning the upper surface of section F, larger discrepancies are present in the inboard as well as the outboard region. However, within the range of $0.4 < y/l_{y,BSF} < 0.7$ similar pressure levels are observed for both geometries. In general, only the inboard part of section F generates lift, whereas the outboard region creates a downforce. In this regard, the modified design provides more lift in the inboard region ($0.0 \leq y/l_{y,BSF} \leq 0.45$) and less downforce in the outboard region ($0.45 < y/l_{y,BSF} \leq 0.80$) compared to the original design 743. The pressure distribution of the middle section M reveals minor differences between the two geometries on the upper surface, in the inboard region of the fairing. The modified design reaches lower pressure levels on the upper side and in combination with a comparable pressure distribution on the lower side, more lift is achieved. In the rearward section R, very similar pressure characteristics are observed on both sides of the fairing. Therefore, the shape modification has a minor impact on the pressure distribution in this region. However, the original design 743 shows a slightly increased pressure on the lower surface within the range $0.15 < y/l_{y,BSF} < 0.30$. In contrast, higher pressure levels are obtained in the outboard part of the fairing for the modified shape ($y/l_{y,BSF} > 0.85$). Based on the observed pressure difference between the upper and the lower surface of both geometries in section R, lift is generated in the inboard region ($0.15 < y/l_{y,BSF} < 0.70$) and a downforce is derived for $y/l_{y,BSF} > 0.70$.

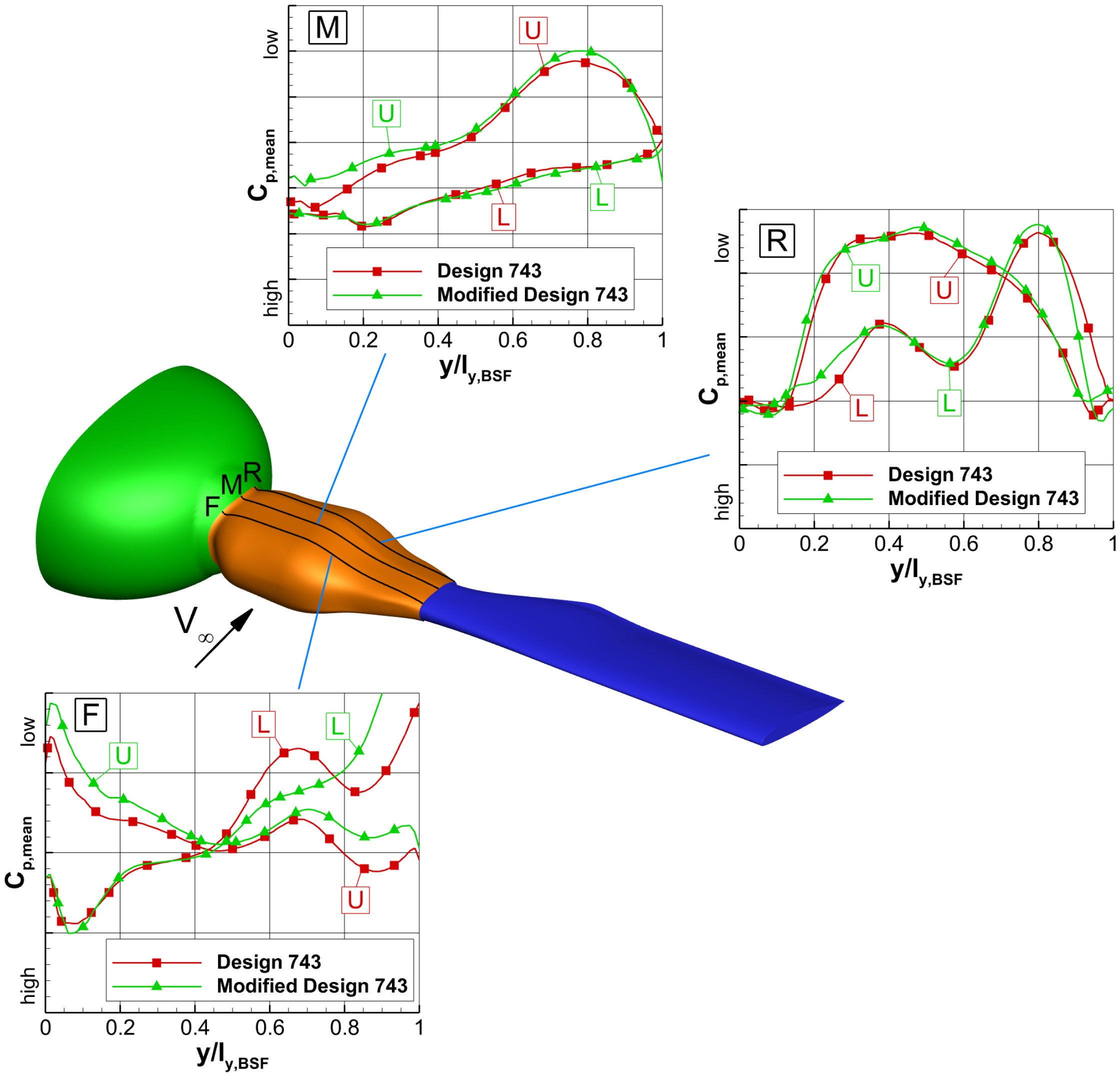

Figure 5.37: Evaluation of the mean, radial surface-pressure distribution $C_{p,mean}(y/l_{y,BSF})$ at three chordwise sections comparing the results of the original and the modified blade-sleeve fairing design 743 for the advancing blade case.

Figure 5.38 illustrates the radial surface-pressure distributions for the retreating blade case. Due to the reversed flow, the most forward section F is now located at the most downstream position of the fairing. The comparison of the pressure distribution in section F shows that the modified shape yields reduced pressure on the upper surface of the fairing in almost the entire range. Moreover, no differences are present in the inboard region of the lower surface ($y/l_{y,BSF} < 0.55$) and limited difference can be seen further outboard. However, the modified shape reduces the downforce that is generated in the outboard region due to the altered pressure difference between the upper and lower surface of the geometry. In the middle section M, the biggest effect of the shape modification is observed on the upper surface of the fairing, where the modified design 743 reaches significantly lower pressure levels, especially in the inboard region and within the range $0.7 < y/l_{y,BSF} < 0.9$.

In combination with an almost unchanged pressure distribution on the lower surface of the fairing, more lift is generated in this region by the modified shape. Regarding the most upstream section R, the pressure distribution on the upper surface shows the strongest deviation from the original pressure distribution within the radial range of $0.05 \leq y/l_{y,BSF} < 0.40$. In this region, reduced pressure levels are obtained for the modified design. The remaining part of the fairing reveals almost no discrepancies between the two geometries on the upper surface. Regarding the lower surface of the modified fairing, no differences can be seen in the range $0.27 \leq y/l_{y,BSF} \leq 0.75$ and reduced pressure levels are obtained upstream and downstream of this region for the modified shape.

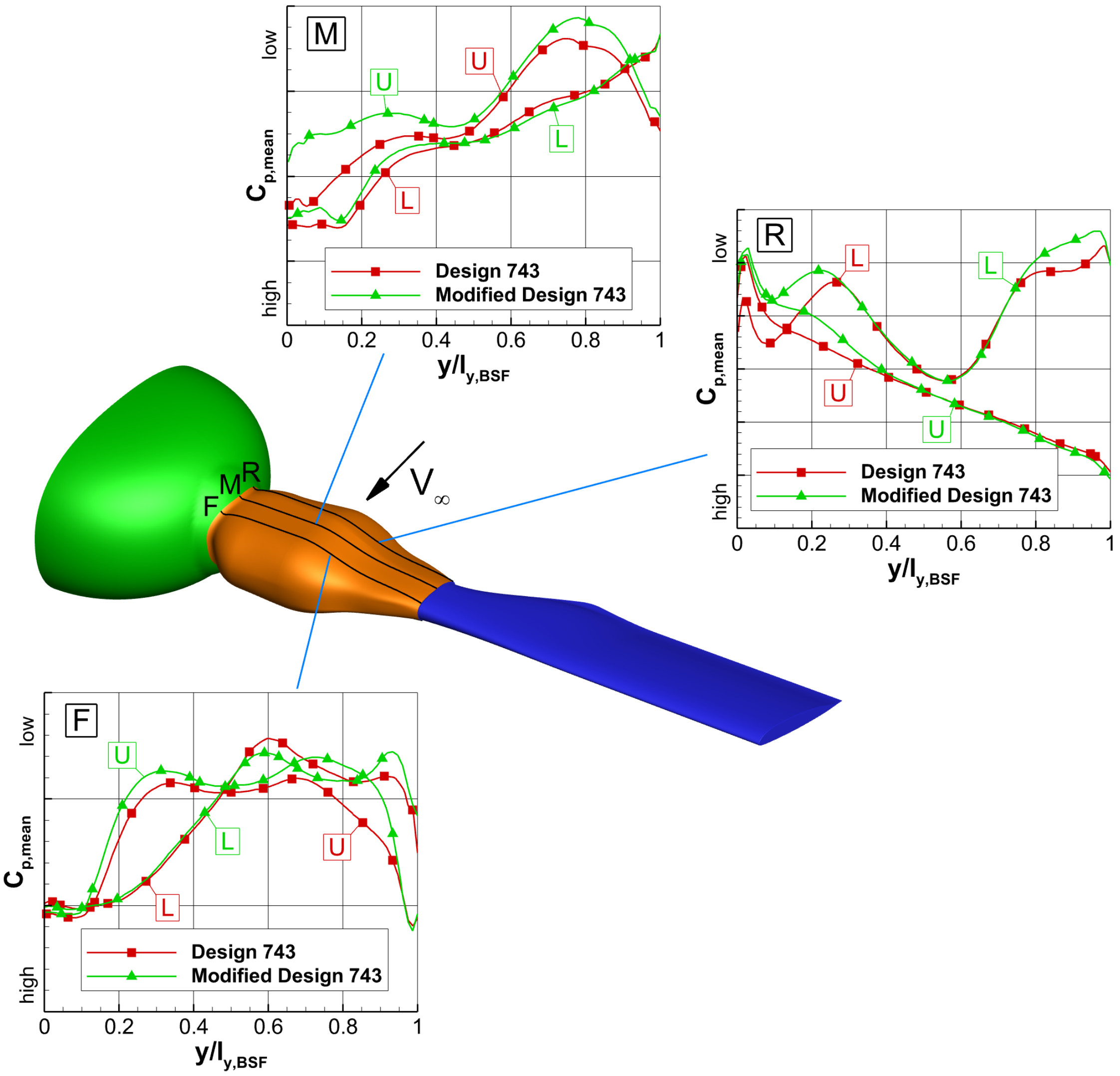

Figure 5.38: Evaluation of the mean, radial surface-pressure distribution $C_{p,mean}(y/l_{y,BSF})$ at three chordwise sections comparing the results of the original and the modified blade-sleeve fairing design 743 for the retreating blade case.

In order to estimate the influence of three-dimensional effects on the surface quantities of the blade-sleeve fairing, the flow-simulation results from the preliminary design optimization of the blade-sleeve sections are compared to the current three-dimensional flow-simulation results. For this purpose, the TUM reference blade-sleeve fairing is taken into account and the respective surface-pressure and skin-friction distributions are compared to each other. The analysis of the three-dimensional effects is exemplarily conducted for the advancing blade case, because similar characteristics have been observed for the retreating blade case.

The surface-pressure distribution for the advancing blade case is illustrated in Fig. 5.39 for all blade-sleeve sections. Complementary to the sectional surface-pressure distribution, the mean, axial skin-friction coefficient $C_{fx,mean}$ is shown in Fig. 5.40, which can be used to determine flow separation onset ($C_{fx,mean} = 0$) and regions of reversed flow ($C_{fx,mean} < 0$).

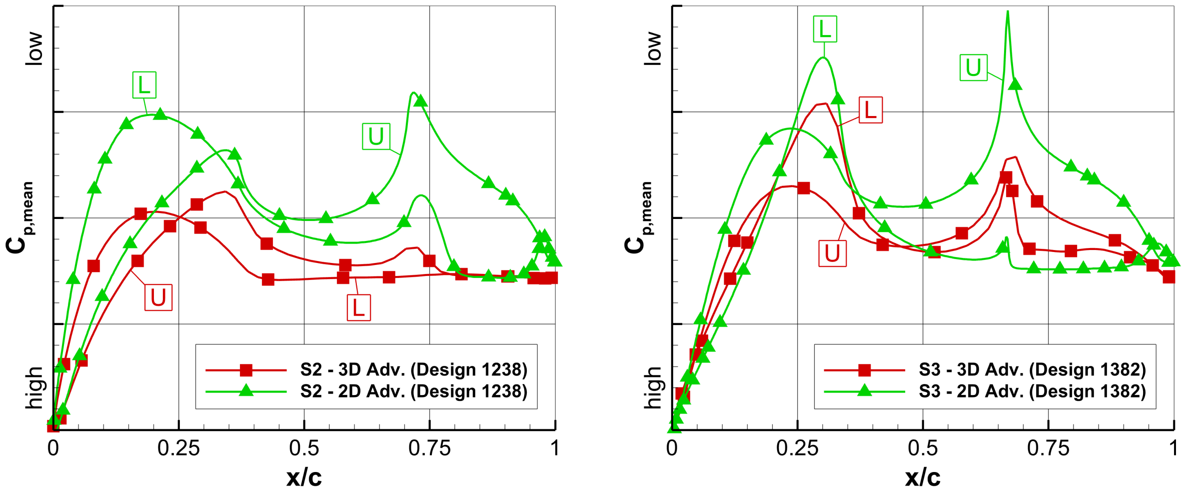

(a) Section S2 with 2D geometry 1238.

(b) Section S3 with 2D geometry 1382.

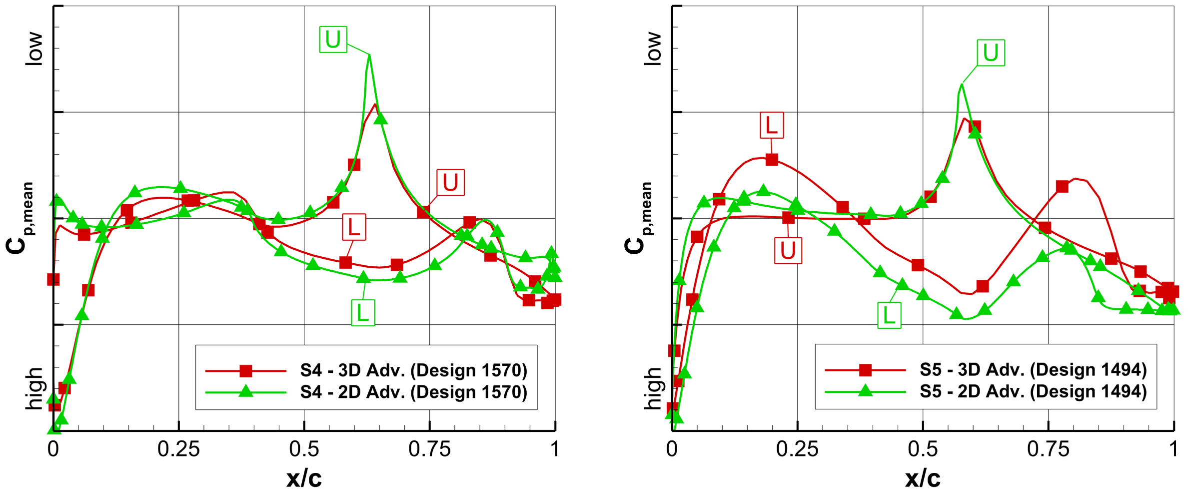

(c) Section S4 with 2D geometry 1570.

(d) Section S5 with 2D geometry 1494.

Figure 5.39: Comparison of the 2D and 3D mean, surface-pressure distributions $C_{p,mean}(x/c)$ at the blade-sleeve sections S2-S5 for the advancing blade case.

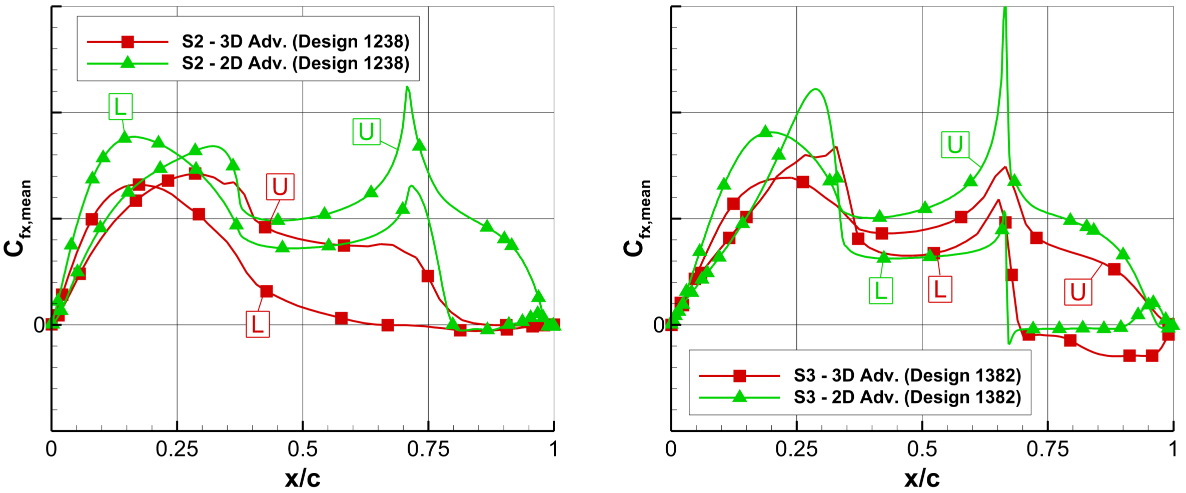

(a) Section S2 with 2D geometry 1238.

(b) Section S3 with 2D geometry 1382.

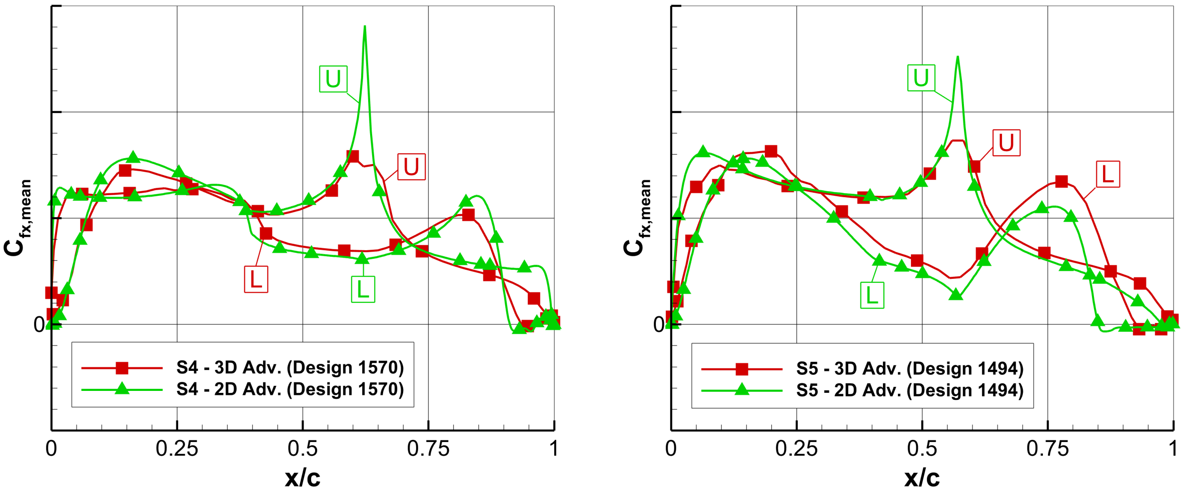

(c) Section S4 with 2D geometry 1570.

(d) Section S5 with 2D geometry 1494.

Figure 5.40: Comparison of the 2D and 3D mean, axial skin-friction distributions $C_{fx,mean}(x/c)$ at the blade-sleeve sections S2-S5 for the advancing blade case.

Regarding the surface-pressure distribution for the most inboard section S2, which is given in Fig. 5.39a, a large discrepancy between the 2D and the 3D solution is observed. This can be related to the flow separation between the blade-sleeve fairing and the full-fairing beanie. The large-scale flow separation is dominating the flow field in this region, see Fig. 5.33. From a global point of view, the 3D solution shows higher pressure levels on both sides of the geometry. Therefore, the pressure difference between the upper and the lower surface is rather small, which causes reduced lift compared to the 2D case. The evaluation of the skin-friction coefficient for the lower surface of the blade-sleeve fairing, which is depicted in Fig. 5.40a, shows flow separation at $x/c \approx 0.65$ for the 3D solution, whereas it is delayed to $x/c \approx 0.80$ for the 2D solution. Furthermore, flow separation on the upper surface of the blade-sleeve fairing is indicated at $x/c \approx 0.85$ for the 3D solution. In contrast, the 2D simulation results for section S2 predict attached flow up to the trailing edge of the fairing.

The surface-pressure distribution for section S3, which is illustrated in Fig. 5.39b, still shows major 3D effects. For example, the suction peaks on the upper and the lower surface of the 2D geometry are significantly reduced by interference effects considering the 3D results. Similar to section S2, there is almost no pressure difference between the upper and the lower surface downstream of $x/c \approx 0.45$, which deteriorates lift. Additionally, better pressure recovery is achieved by the 2D solution. Concerning the flow separation onset at blade-sleeve section S3, similar characteristics are observed for both cases, which can be seen in Fig. 5.40b. On the lower surface, the flow separates at $x/c = 0.7$ and on the upper surface it stays attached up to the trailing edge for both solutions.

The chordwise surface-pressure distributions for section S4 and S5 are depicted in Fig. 5.39c and Fig. 5.39d, respectively. At these outboard sections, comparable pressure distributions regarding the 2D and 3D flow-simulation results are obtained. This leads to the conclusion that the large-scale flow separation in the inboard region has a minor impact and that no other significant 3D effects are present at these radial stations.

5.3 Synthesis

In this chapter, the aerodynamic design optimization of a new blade-sleeve fairing for the RACER compound helicopter has been presented. The fairing has been optimized for a sea-level cruise flight with 220 knots. For this purpose, a fully automated, CFD-based design-optimization toolchain has been developed and applied in the course of this thesis. The design optimization of the blade-sleeve fairing has been performed in two steps. First, a two-dimensional design optimization of selected blade-sleeve sections has been conducted providing a comprehensive database of optimized geometries. Thereafter, these optimized shapes have been used as the basis for the refined, three-dimensional design optimization of the blade-sleeve fairing. For this purpose, a simplified geometry has been created featuring the full-fairing beanie, the blade-sleeve fairing and a truncated rotor blade. Design constraints regarding the minimum and maximum permissible design space have been taken into account and additional aspects, like manufacturing and ease of maintenance have been considered in the final design. A global, multi-objective, genetic optimization algorithm has been employed to optimize lift and drag of the blade-sleeve fairing. Regarding the investigated flow conditions, the advancing ($\Psi = 90°$) and the retreating rotor blade ($\Psi = 270°$) have been studied. Furthermore, the applied angle of attack has been calculated from the flight condition of the helicopter, the proper cyclic blade-pitch angle concerning a trimmed flight as well as the local flow deflection due to the presence of the fuselage. At the end of the design-optimization process, the most promising candidate has been selected from the Pareto front and investigated in more detail.

Moreover, the newly developed fairing has been compared to a reference geometry that was developed by Airbus Helicopters during the preliminary design phase of the RACER demonstrator. Steady-state and transient flow-simulation results have been presented and analyzed in detail. Altogether, the following conclusions can be drawn for the design optimization of the blade-sleeve fairing:

Two-dimensional Design Optimization

- Latin hypercube sampling (LHS) is well suited for the definition of the initial population of designs, especially considering a high number of design variables. This multidimensional parameter-sampling method provides a widespread distribution of candidates covering a large region of the search space. Moreover, the integration of design constraints in the LHS sampling process generates only valid designs for the first population, which offers a good starting point for the design optimization process.
- The parameterization of the blade-sleeve sections by Bézier curves yields a robust method, which is highly flexible in terms of shape generation. Furthermore, the applied definition of the control points ensures a tangential connection between all curves of the geometry. Based on the mathematical description, a smooth curve is always obtained.
- The genetic optimization algorithm is computationally expensive, but it represents a global and robust method, which cannot get caught in a local optimum in case of a multi-modal objective space. Therefore, almost no user interactions are required during the optimization run, which is beneficial in comparison to simple, gradient-based optimization algorithms. The successive improvement of the objective functions can clearly be seen for all optimization runs and a Pareto front is gradually formed up to the final population. A total number of 25 populations provides sufficient convergence for all blade-sleeve sections. In the course of the automated design optimization, a large database of 4281 valid designs is generated considering all blade-sleeve sections (S2-S5). The evaluation of the final population for each of the optimized sections shows an improvement in both objective functions compared to the reference fairing.
- The investigated geometries represent bluff bodies, especially the two inboard sections S2 and S3. Due the high relative thickness t/c, unsteady flow separation is observed for these sections and a vortex street is formed in their wake region. This leads to strong oscillations in the aerodynamic forces. Hence, it is important to perform unsteady flow simulations in order to detect the flow physics properly.

The comparison of steady-state and transient simulation results has shown major discrepancies in the mean aerodynamic forces for the blade-sleeve sections S2 and S3. In contrast, the fourth and the fifth radial blade-sleeve sections (S4 & S5) have a much smaller relative thickness, which leads to a smooth boundary layer separation without vortex shedding. As a result, the steady-state and the transient flow simulations deliver comparable aerodynamic forces.

Three-dimensional Design Optimization

- The applied design parameterization enables an easy shape variation by replacing the four supporting airfoils (S2-S5). Hence, only four design variables are required to define the outer shape of the three-dimensional blade-sleeve fairing. For this purpose, a predefined set of optimized blade-sleeve sections is employed, which consists of low-drag shapes for the advancing and the retreating blade case. Furthermore, designs offering the best compromise between the applied objective functions are included in the pool of candidates. The selected parameterization does not incorporate a relation between the blade-sleeve sections. This could be detrimental for certain design variable combinations, because a bumpy fairing shape could be derived and a violation of the design constraints could occur.

- Based on the experience of the two-dimensional design optimization, the same optimization setup is employed for the current task. The evaluation of the objective space shows that all investigated candidates dominate the reference design, which can be related to the preliminary optimized blade-sleeve sections. The design optimization process is considered as converged after 20 successive populations yielding a total number of 811 investigated blade-sleeve fairing designs. Starting with 150 candidates in the first population, this number is reduced to 62 in the final population.

- During the two-dimensional design optimization, design constraints regarding the permissible design space have been considered, which are all met by the optimized geometries. Therefore, it has been assumed that an unconstrained design optimization can be performed for the three-dimensional blade-sleeve fairing shape. However, the detailed evaluation of selected fairings shows that the design constraints are slightly violated in rare cases. This is caused by the fact that the transition between the blade-sleeve sections is not part of the design parameterization. Therefore, the design constraints cannot be automatically checked in this region during the design optimization process.

- Based on several assessment criteria, design 743 is selected from the final population. The automatically generated design is slightly modified to reduce the waviness of the geometry and to provide a proper transition between the blade-sleeve sections. Therefore, the modified geometry is fully compliant with the applied design constraints and it can be easily mounted on available supporting structures of the RACER rotor head. This could enable an easy integration of the newly developed fairing during flight test. The evaluation of the objective functions for the optimized blade-sleeve fairing predicts a significant performance improvement. According to the transient flow-simulation results, the lift-to-drag ratio for the advancing blade case is increased by 38 % in comparison to the reference geometry. Furthermore, a drag reduction of about 6 % is observed for the retreating blade case. These numbers are based on the total forces of the isolated rotor blade including the contribution of the full-fairing beanie, the blade-sleeve fairing and the rotor-blade stub.

6 Analysis of the Optimized Rotor-Head Fairing

Within this chapter, the newly developed blade-sleeve fairing is put to test on an isolated, five-bladed rotor head. For this purpose, unsteady numerical flow simulations are performed with ANSYS Fluent considering a moving rotor head with cyclic blade-pitch motion. The investigated flight condition represents the steady, sea-level cruise flight with 220 knots. Furthermore, two different full-fairing beanie shapes are analyzed in combination with the optimized blade-sleeve fairing to determine the most promising full-fairing concept in terms of drag reduction. At the beginning, the investigated rotor-head geometry is described and thereafter, the numerical setup is briefly introduced. In order to determine the performance benefit that can be expected by the optimized blade-sleeve fairing, the aerodynamic forces of the isolated rotor head are analyzed in detail. This includes the evaluation of the total forces, the component forces and the frequency spectrum of the aerodynamic loads acting on the isolated rotor head. Furthermore, selected surface and flow-field quantities are presented to illustrate the occurring flow phenomena. Parts of the isolated rotor-head analsyes in this chapter are based on the author's publication in the Aerospace Online Journal [14].

Within a subsequent step, the impact of the optimized full-fairing rotor head on the overall performance of the RACER compound helicopter is analyzed. Here, the focus is on the evaluation of the total helicopter drag. Moreover, the component forces of the core geometry and the rotor head are evaluated. Selected surface and flow-field quantities are presented to complement the analyses of the rotor-head fairing. Regarding the blade-pitch movement of the main rotor, a trimmed cruise-flight condition is investigated. The remaining control surfaces on the wings and the empennage are neglected. Furthermore, the lateral rotors are not considered in the present work, because minor interference effects are expected during cruise flight and the focus lies on the rotor-head flow field. As for the isolated rotor-head investigations, two different full-fairing concepts are examined on the full compound-helicopter configuration. These rotor-head fairings mainly differ in terms of diameter and height.

6.1 Geometry Models

6.1.1 Isolated Rotor Head

The investigated geometry is illustrated in Fig. 6.1 representing a full-scale model of the five-bladed RACER rotor head. The main components of the rotor-head model comprise the full-fairing beanie (FFB), the blade-sleeve fairings (BSFs) and truncated rotor blades (RBs). Furthermore, the lead-lag dampers are included, which are illustrated by the purple components in Fig. 6.1. Additionally, a spherical junction (red) is used between the fairing components, which provides a proper sealing while allowing for the relative movement of the rotor blades. The rotor blades are cut at about one third of the actual rotor radius, which has several reasons. First, the main focus of the present work lies on the evaluation of the rotor-hub forces and therefore, the aerodynamic forces and moments of the rotor blades are of less interest. However, one has to be aware that different aerodynamic interactions between the rotor blades and the rotor-head fairing are obtained in this case. Second, it is common to use truncated rotor blades in wind-tunnel measurements to be able to increase the helicopter model size as much as possible, which enables higher Reynolds numbers, see for example [58, 140]. Moreover, the numerical model with truncated rotor blades enables a direct comparison to experimental wind-tunnel data, if a correctly scaled blade stub is used and the advance ratio is set accordingly. Previous investigations at TUM-AER led to the conclusion that the predicted hub drag of a wind-tunnel model with truncated rotor blades is still representative, see [13, 59, 141].

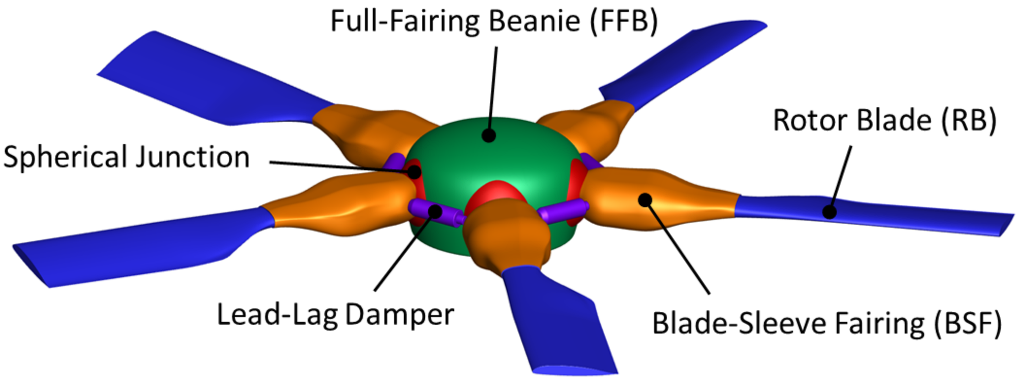

Figure 6.1: Component breakdown of the isolated rotor-head model.

In the frame of the isolated rotor-head investigations, two different full-fairing beanie shapes are analyzed in combination with the optimized and the reference blade-sleeve fairing, respectively. An overview about the investigated rotor-head geometries is given in Fig. 6.2. It can be seen that the full-fairing beanie geometry varies in terms of diameter and height.

The baseline geometry is represented by *Beanie R0H0*, which is illustrated in Fig. 6.2a. Regarding *Beanie R1H1*, the diameter is increased to cover all the rotor-hub components including the lead-lag dampers. Additionally, the height is increased as well to provide a certain relative thickness of the full-fairing beanie.

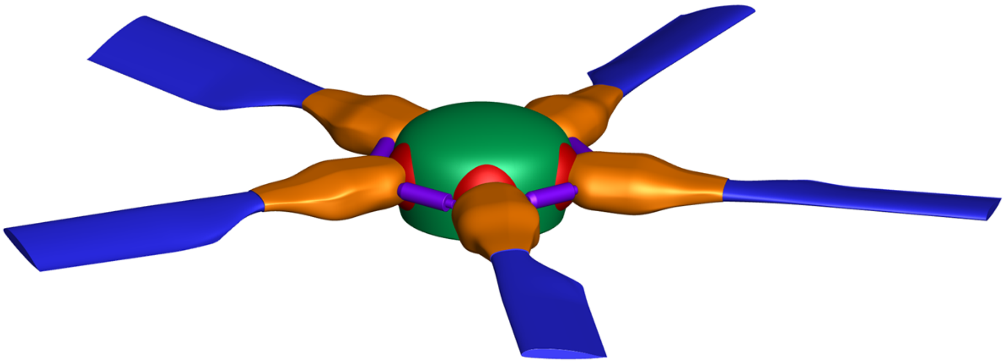

(a) Beanie R0H0.

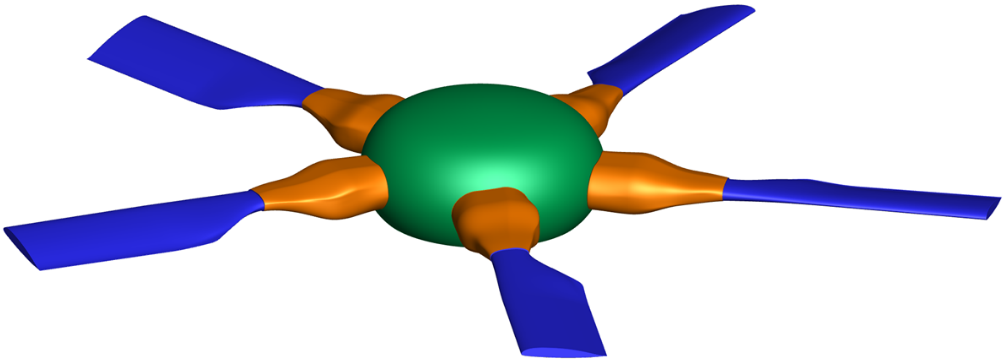

(b) Beanie R1H1.

Figure 6.2: Investigated full-fairing beanie geometries.

6.1.2 RACER Compound Helicopter

Within the final step of the FURADO project, the newly developed blade-sleeve fairing is investigated on the full RACER compound-helicopter configuration to estimate the overall performance benefit that can be expected. Due to the fact that the focus of the present work lies on rotor-head aerodynamics, a simplified core geometry is employed, which is illustrated in Fig. 6.3. It represents a fully watertight geometry with closed air intakes and exhausts. Furthermore, the lateral rotors at the wing tips and the control surfaces on the wings as well as the empennage are neglected. The component breakdown in Fig. 6.3 can be grouped into the rotor-head and the core-geometry components including the cabin, the wings, the tailboom, the horizontal stabilizer, the vertical stabilizers and the pylon fairing. Based on the evaluation of the isolated rotor-head results, two full-fairing concepts are examined in more detail on the full compound helicopter configuration, which can be seen in Fig. 6.4.

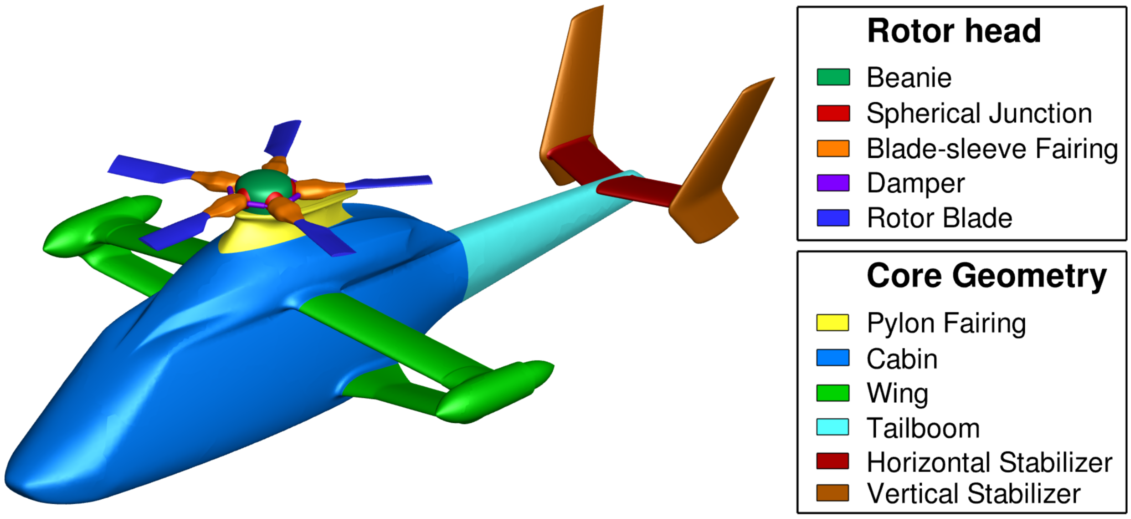

Figure 6.3: Component breakdown of the RACER compound-helicopter model.

Configuration C1 features the baseline full-fairing beanie R0H0 and the original pylon fairing design, which is illustrated by the blue-colored surface in Fig. 6.4a. In contrast, configuration C2 comprises the larger full-fairing beanie R1H1 in combination with an adapted pylon fairing, which can be seen in Fig. 6.4b. The size of the pylon fairing has to be increased in order to fit the larger beanie diameter.

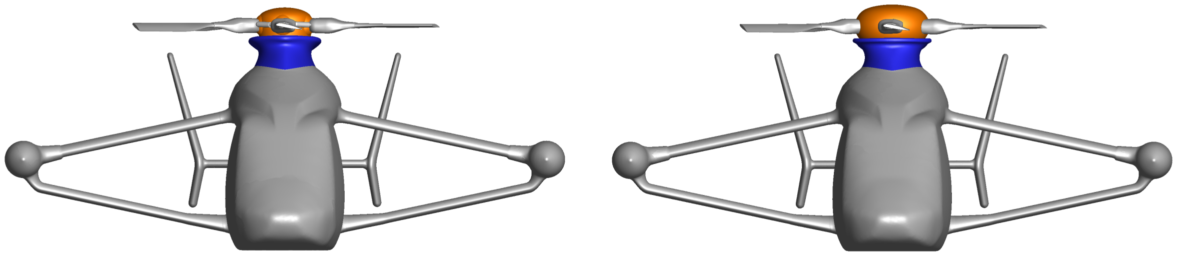

(a) Configuration C1 with the baseline rotor head (Beanie R0H0).

(b) Configuration C2 with the modified rotor head (Beanie R1H1) and an adapted pylon fairing.

Figure 6.4: Comparison of the investigated configurations C1 and C2 featuring different full-fairing beanie shapes and dedicated pylon fairings.

6.2 Computational Grids

The numerical flow simulations consider cyclic blade-pitch motion according to a trimmed, sea-level cruise flight of the RACER demonstrator. In order to realize the rotor-head motion, an overset-mesh approach is used in combination with mesh motion in ANSYS Fluent. The overset-mesh principle is described in Sec. 4.1.2 of the thesis. Within this section, the applied computational grids and preliminary mesh studies are presented.

6.2.1 Isolated Rotor Head

The computational mesh of the isolated rotor-head simulations consists of several subdomains, which are combined by overset-mesh interpolation during the flow simulation process. The rotational symmetry of the rotor head can be exploited, which means that only one fifth of the actual computational mesh must be generated. The remaining four parts of the mesh are then derived as copies. The mesh generation is conducted with ANSYS ICEM CFD providing high-quality, block-structured computational grids with pure hexahedral elements. The blocking of the farfield domain and its extensions are illustrated in Fig. 6.5, where the quantity R represents the rotor radius. It can be seen that the domain is 15 R wide and 30 R long. Furthermore, a detailed view on the background-mesh box of the rotor head is given in Fig. 6.5. This mesh box is located in the middle of the farfield domain at an axial position of $x = 10\,R$. Moreover, the background mesh is connected to the outer free-stream domain by a conformal mesh interface.

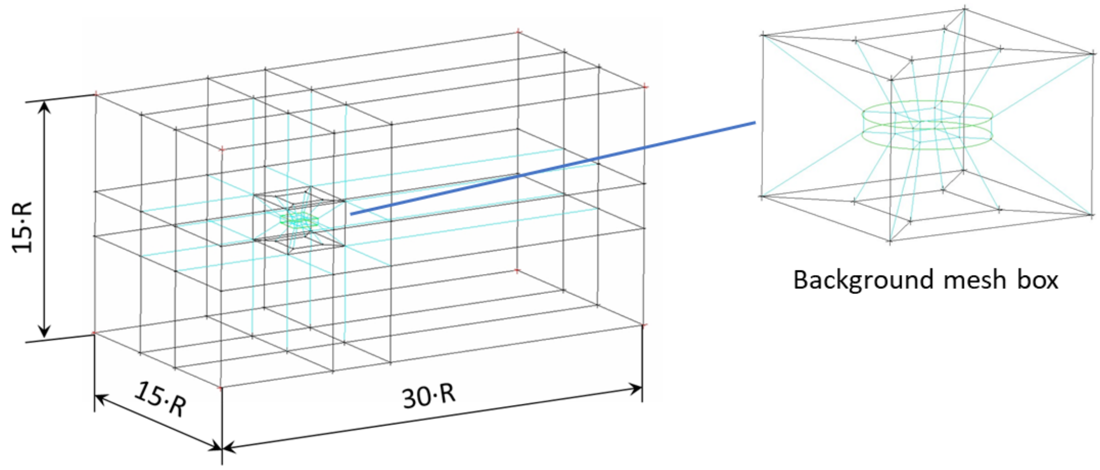

Figure 6.5: Extension of the farfield domain and detailed view on the background-mesh box of the rotor head [14].

The rotor-head mesh is embedded in the background mesh and it consists of 16 component grids. The mesh blocking of the beanie and the rotor blade can be seen in Fig. 6.6. Regarding the rotor-blade mesh, nested O-Grid blocks are used to discretize the rotor blade as well as the blade-sleeve fairing in a single mesh. Furthermore, the beanie mesh features a Y-Grid topology and periodicity is applied to the cell vertices lying on the two symmetry planes, which ensures a proper mesh alignment at the periodic boundaries. All computational grids feature a fully resolved boundary layer and the initial cell height is set according to a dimensionless wall distance of $y^+ \approx 1$. Furthermore, an expansion ratio of 1.1 is used in wall-normal direction. The overset-mesh approach in ANSYS Fluent is not robust in terms of intersecting wall boundaries, which requires special treatment.

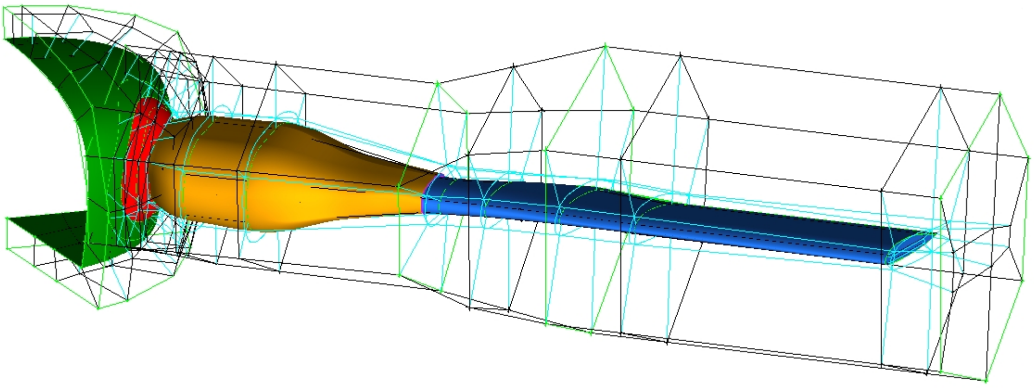

Figure 6.6: Visualization of the periodic mesh blocking for a single rotor blade and the beanie [14].

Regarding the actual flow problem, intersecting wall boundaries are present between the beanie and the spherical junction of the rotor-blade mesh. In order to avoid an excessive amount of orphan cells after the hole-cutting process, and to preserve the boundary-layer mesh in the junction between these two components properly, a so called collar mesh is employed. This collar mesh bridges the gap between the intersecting components and enables reasonable mesh quality in the transition region. The domain of the collar mesh and a detailed view on the surface mesh of the three involved components can be seen in Fig. 6.7. It is very important that the same cell sizes, initial cell heights and expansion ratios are used in the overlapping region to avoid orphan cells in the final mesh.

A grid resolution study is performed to determine the impact of the spatial discretization on the numerical solution. For this purpose, unsteady numerical flow simulations are conducted for a sea-level cruise flight of the RACER demonstrator. Furthermore, cyclic blade-pitch motion is considered in these simulations.

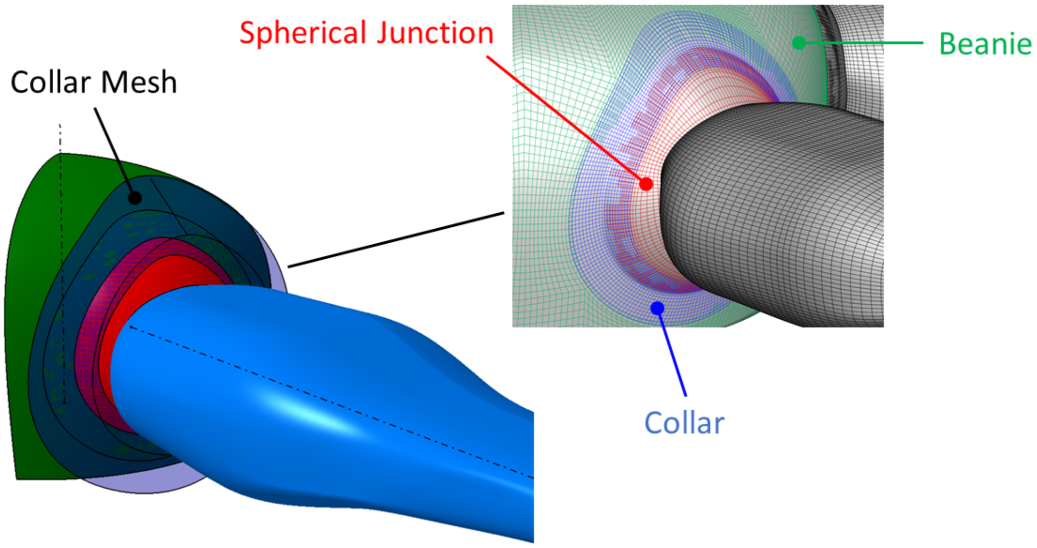

Figure 6.7: Detailed view on the collar mesh providing a valid transition between the beanie and the rotor-blade mesh [14].

The aerodynamic forces and moments are averaged over three rotor revolutions to derive comparable results. In total, three different mesh sizes are examined consisting of 13, 29 and 52 million elements, respectively. The results of the grid resolution study are summarized in Tab. 6.1, where the differences in lift, drag and rotor-head torque are given relative to the solution of the finest mesh. The coarse mesh shows reasonable accuracy regarding lift and torque, but there is a large discrepancy in drag of $\Delta D = +7.8\,\%$ compared to the finest mesh. In contrast, the medium mesh differs by less than 1 % in drag and less than 2 % in lift compared to the reference solution. This represents satisfying accuracy regarding the spatial discretization and therefore, the medium mesh is used for subsequent flow simulations.

Mesh Size	No. of Elements ($x10^6$)	$\Delta Lift$ [%]	$\Delta Drag$ [%]	$\Delta Torque$ [%]
Fine Mesh	52	-	-	-
Medium Mesh	29	+1.9	-0.7	-0.7
Coarse Mesh	13	+1.2	+7.8	+1.3

Table 6.1: Mesh-sensitivity study regarding the spatial discretization of the isolated rotor head.

Figure 6.8 shows a cut through the final computational grid that is used for the isolated rotor-head simulations. Moreover, the overset cell types of the background mesh are illustrated after the hole cutting process. The boundaries of the component meshes can clearly be seen by the colored donor and receiver cells. In the given example, no orphan cells are present.

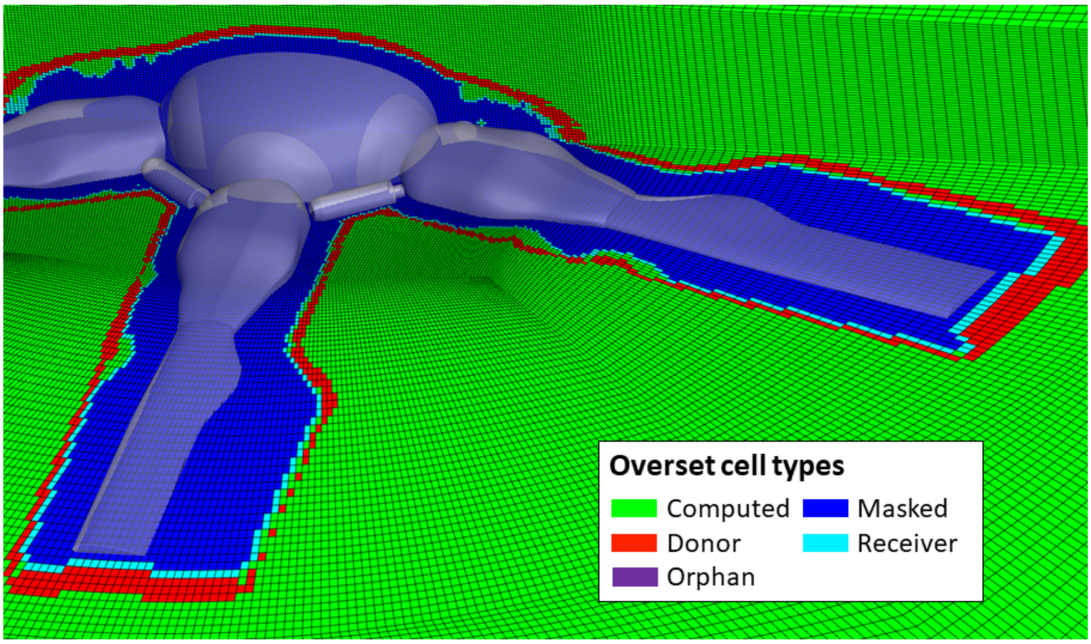

Figure 6.8: Cross-sections in the final rotor-head mesh showing the different overset-mesh cell types [14].

6.2.2 RACER Compound Helicopter

The computational mesh of the full helicopter configuration consists of three major domains, which are given by the free-stream domain, the helicopter domain and the rotor-head domain. Moreover, the rotor-head domain represents the background mesh of the overset mesh and it contains several sub-domains. Figure 6.9 shows the main mesh components and the sizing of the applied computational domain, where the quantity R represents the rotor radius.

Regarding the free-stream and the rotor-head domain, block-structured hexahedral meshes are used and the mesh generation is conducted with ANSYS ICEM CFD. Preliminary tests revealed that the original overset interfaces of the rotor blades, which are used for the isolated rotor-head investigations, lead to excessive intersection times during the flow-simulation process. Based on the author's experience with overset mesh in ANSYS Fluent, it is recommended that the overset interfaces of the component meshes do not excessively overlap the background mesh boundary, which in the present case is also a mesh interface to the helicopter domain. Therefore, the size and shape of the rotor-blade overset interfaces are adapted to fit the rotor-disk background mesh as good as possible. However, the basic blocking of the isolated rotor head can be reused for the present flow problem. The adaptations significantly improve the required mesh intersection time during the overset-mesh generation. The modified overset interfaces can be seen in Fig. 6.9 by the orange colored surfaces. Moreover, the boundary of the background mesh is illustrated by the blue colored surface.

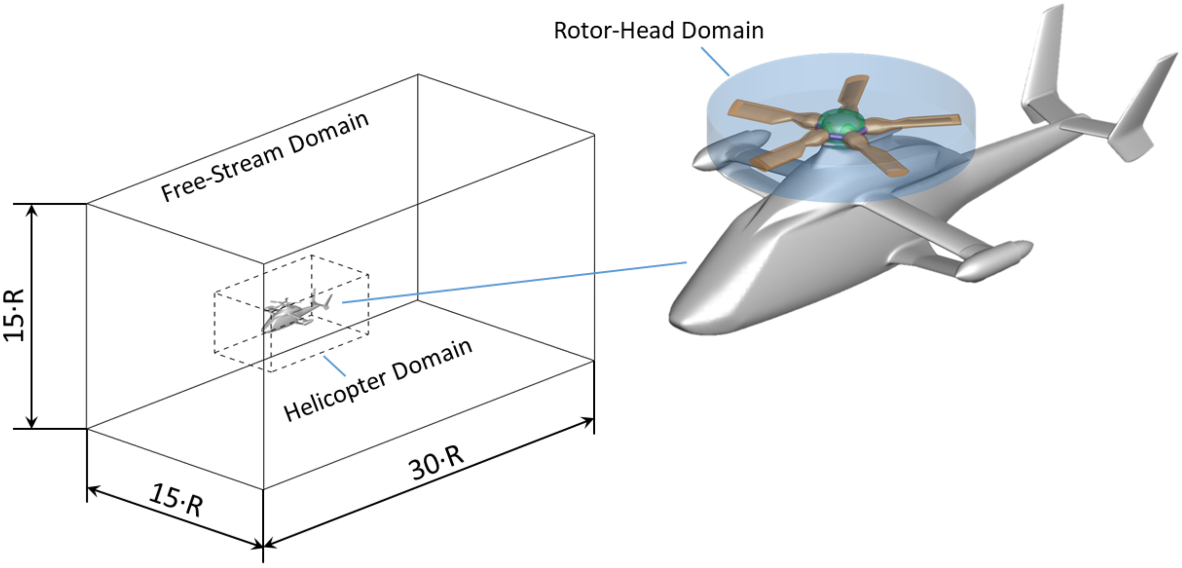

Figure 6.9: Sizing of the computational domain and detailed view on the overset-mesh interfaces.

The helicopter domain comprises a hexcore mesh, which is generated with ANSYS Fluent. The hexcore mesh uses a hybrid meshing scheme with Cartesian cells in the core mesh and tetrahedral cells close to the boundary of the geometry. Therefore, the gap between the boundary-layer mesh and the core mesh is closed by tetrahedral elements. Furthermore, the hexcore mesh follows an octree meshing scheme, which generates a multi-level mesh with discrete cell sizes and hanging nodes between the different refinement levels.

The surface mesh of the investigated helicopter configuration is depicted in Fig. 6.10 with a detailed view on the rotor head, the wings, the empennage and the rear upper deck of the helicopter. It can be seen that the core geometry is discretized by triangular elements, whereas quadrilaterals are used for the surface mesh of the rotor-head components. Moreover, small geometry features and regions of strong curvature are well captured in the surface mesh of the helicopter. The boundary layer of the core mesh is resolved by 35 prism layers and the initial cell height is set according to a dimensionless wall distance of $y^+ \approx 1$. The hexcore elements are well aligned with the main flow direction, which reduces numerical dissipation. Therefore, the hybrid mesh combines the advantages of structured meshes with the convenience of unstructured mesh generation for complex geometries. The three different mesh domains are connected to each other by conformal mesh interfaces. The volume mesh of the investigated helicopter configuration is illustrated in Fig. 6.11 showing selected cross-sections through the computational domain. The wake-region of the rotor head is refined to preserve the vortical flow structures. Moreover, the different refinement levels of the hexcore mesh can clearly be seen. The mesh sizes of the different subdomains are summarized in Tab. 6.2 for configuration C1 and C2, respectively. The final mesh comprises 67.5 million cells for configuration C1 and 70.8 million cells for configuration C2.

	Configuration C1 (Baseline)	Configuration C2
Sub-Domain	No. of Elements	No. of Elements
Free-Stream (Farfield)	518.400	518.400
Helicopter (Core Geometry)	46.028.790	45.943.888
Rotordisk (Background Mesh)	10.750.320	11.031.020
Beanie	2.235.090	3.564.780
Rotor Blade (1-5)	1.310.320 x 5	1.944.088 x 5
Lead-Lag Damper (1-5)	141.097 x 5	-
Collar Grid (1-5)	154.088 x 5	-
Total	**67.560.125**	**70.778.528**

Table 6.2: Summary of the component mesh sizes for the configurations C1 and C2.

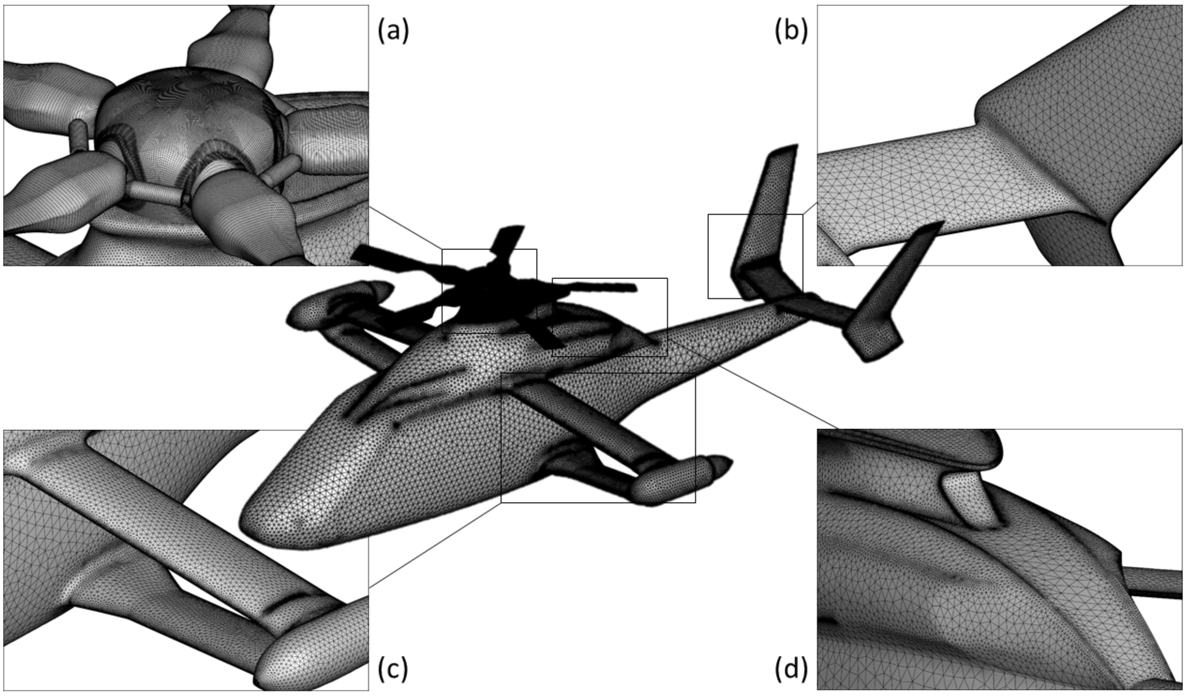

Figure 6.10: Surface mesh of the full helicopter configuration with details of (a) the rotor head, (b) the empennage, (c) the wings and (d) the rear upper deck.

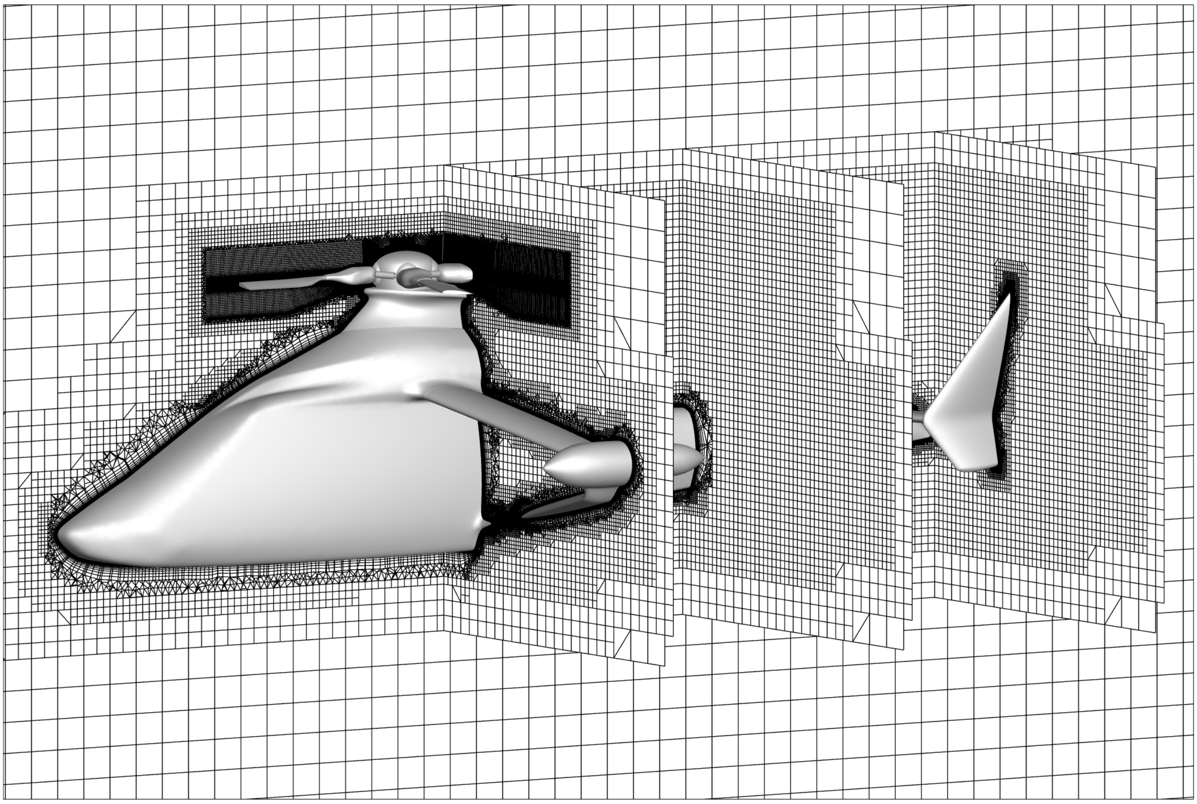

Figure 6.11: Volume mesh of the full helicopter configuration giving a detailed view on the applied mesh refinement.

6.3 Applied Numerical Setup

6.3.1 Blade-Pitch Motion

Within the numerical flow simulations, cyclic blade-pitch movement is implemented according to a trimmed sea-level cruise flight of the RACER demonstrator. Hence, the pitch angle of each rotor blade is continuously adjusted for each time-step depending on the azimuthal rotor position. The RACER features a clockwise rotating rotor and the definition of the azimuthal rotor-blade position is illustrated in Fig. 6.12. $\Psi = 0°$ represents the downwind pointing rotor blade considering the forward flight of the helicopter. The main rotor has two control inputs, which are given by the collective and the cyclic pitch. The definition of the blade-pitch angle depending on the azimuthal rotor position is given by Eq. 6.1. The collective pitch θ_0 changes the pitch angle of all rotor blades simultaneously, which defines the average lift that is generated by the main rotor. The control of the helicopter flight attitude is realized by the cyclic pitch inputs, which are given by the longitudinal cyclic pitch θ_{1s} and the lateral cyclic pitch θ_{1c}. The blade-pitch law that has been implemented in the numerical flow simulations is given by Eq. 6.2. The time-dependent azimuthal rotor position of each rotor blade is derived by the rotational speed ω, the current simulation time t and a certain phase lag depending on the number of rotor blades n. The RACER demonstrator has five rotor blades and therefore, a phase lag of 72° has to be applied. The mesh motion in ANSYS Fluent requires the blade-pitch velocity, which is the time derivative of Eq. 6.2. Hence, the final equation for the user-defined function (UDF) is given by Eq. 6.3. Furthermore, rigid-body motion is assumed in the present investigations and the flapping as well as the lead-lag movement of the rotor blades due to the unsteady aerodynamic loads are neglected.

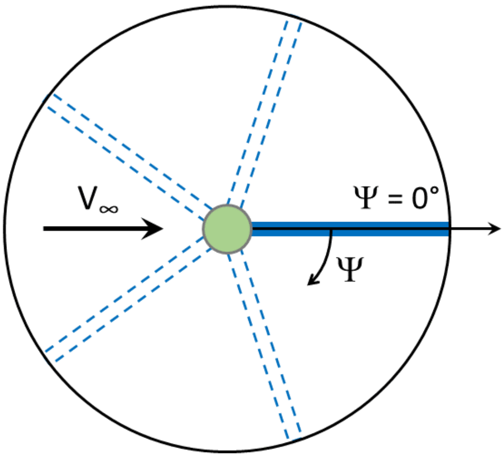

Figure 6.12: Definition of the azimuthal rotor-blade position.

General Blade-Pitch Law:

$$\theta(\Psi) = \theta_0 + \theta_{1s} \cdot sin(\Psi) + \theta_{1c} \cdot cos(\Psi) \tag{6.1}$$

Implemented Blade-Pitch Law:

$$\theta(\omega, t, n) = \theta_0 + \theta_{1s} \cdot sin(\omega t + n\Delta\Psi) + \theta_{1c} \cdot cos(\omega t + n\Delta\Psi) \tag{6.2}$$

$$\dot{\theta}(\omega, t, n) = \frac{d\theta}{dt} = \theta_{1s} \cdot \omega \cdot cos(\omega t + n\Delta\Psi) - \theta_{1c} \cdot \omega \cdot sin(\omega t + n\Delta\Psi) \tag{6.3}$$

for five rotor blades with $n = \{0, 1, 2, 3, 4\}$ and $\Delta\Psi = 72°$

6.3.2 Flow Solver

The numerical flow simulations for the isolated rotor head and the full compound helicopter configuration are performed with ANSYS Fluent using almost the same flow-solver settings for both cases. The investigated flow problem represents the sea-level cruise flight of the RACER demonstrator in ICAO standard atmosphere with a cruise speed of 220 knots. Due to the high flow velocities, compressibility effects must be taken into account and therefore, the compressible, unsteady Reynolds-Averaged Navier-Stokes equations (URANS) are solved using a pressure-based, coupled solver. The standard pressure scheme of Fluent is used to provide pressure interpolation. Furthermore, turbulence modeling is provided by the two-equation k-ω SST model [123]. In general, second-order upwind schemes are used for the spatial discretization, but a bounded central differencing scheme is employed for the momentum equation. Gradient reconstruction is achieved by a least-square cell-based formulation and a bounded second-order implicit scheme is chosen for the temporal discretization.

A pressure far-field boundary condition is set on each side of the far-field domain with a free-stream Mach number of $M_\infty = 0.33$. The ambient conditions are set according to the ICAO standard atmosphere at sea-level leading to an ambient pressure of $p_\infty = 1013.25\, hPa$ and an ambient temperature of $T_\infty = 288.15\, K$. The turbulence at the far-field boundaries is defined by a turbulence intensity of $Tu = 1\,\%$ and a turbulent viscosity ratio of $\mu_t/\mu = 10$. The computational mesh of the isolated rotor head consists of 16 component meshes and one background mesh, which is connected to the far-field domain by a mesh interface. Within the first step of the numerical flow simulations, the correct blade-pitch angles are set for each rotor blade considering one blade pointing upstream to the nose of the helicopter. For this purpose, dynamic mesh is employed and the movement of the blades is defined by a user-defined function (UDF), which contains the blade-pitch law according to Eq. 6.2. The necessary pitch-control inputs for a trimmed cruise flight were provided by the project partner Airbus Helicopters.

Regarding the initialization of the flow simulation, constant values are globally set for pressure, velocity, turbulent kinetic energy, specific dissipation rate and temperature. Thereafter, a steady-state solution is calculated for the non-rotating rotor head, which serves as the input for the transient simulation. During the transient simulations, the cyclic blade-pitch movement is realized by mesh motion. For this purpose, a UDF is prepared for the movement of the beanie and the five rotor blades. The cell zones of the rotor blades, the lead-lag dampers and the collar grids move relative to the beanie domain. The selection of the time-step size is based on several criteria, which comprise the convergence behavior, the accuracy of the rotor-blade positioning and the quality of the overset mesh generation. Due to the fact that the blade-pitch velocity is used to calculate the actual blade-pitch angle, a smaller time-step provides more accuracy. Based on these considerations, a time-step size corresponding to 1° of azimuth angle per time-step is chosen for the isolated rotor head investigations. All scaled residuals are reduced by at least three orders of magnitude. Regarding the flow simulation of the full compound helicopter configuration, the time-step size is reduced to 0.5° of azimuth angle per time step, because better convergence and stability is observed.

6.3.3 Computational Resources

The numerical flow simulations shown within the present thesis were conducted on the high-performance computer SuperMUC-NG of the Leibniz Supercomputing Centre. Regarding the isolated rotor-head simulations, a total number of seven Intel Xeon Platinum 8174 nodes with 336 cores were used, which yields an average load of 86.000 elements per processor. Based on the applied computational resources, a full rotor revolution with 360 time steps was accomplished within 16 hours of simulation time. An average of 30 inner iterations per time step was required to reach convergence. The overset-mesh approach of ANSYS Fluent requires an excessive amount of memory for the present flow problem. The observed peak usage during the isolated rotor-head simulations was 90 GB on a single node, if a total number of seven compute nodes was used.

The flow simulations for the full compound helicopter configuration were performed on SuperMUC-NG using 768 cores on 16 compute nodes, which corresponds to an average load of 88.000 elements per core. Based on the applied time-step size, a full rotor revolution comprises 720 time steps, which were calculated within 22 hours of simulation time. Furthermore, all residuals were reduced by at least three orders of magnitude within approximately 25 inner iterations per time step. Regarding the memory requirements, an average demand of 560 GB was observed and the peak usage on a single node was approximately 47 GB.

6.4 Results and Analysis - Isolated Rotor Head

Within this section, the main results and findings of the isolated rotor-head investigations are presented. In total, four different full-fairing concepts are examined by means of unsteady numerical flow simulations. The analyzed full-fairing geometries are illustrated in Fig. 6.13. The baseline rotor head, which serves as the reference for the evaluation of the other full-fairing variants, is depicted in Fig. 6.13a. It consists of the baseline beanie R0H0 and the reference blade-sleeve fairing. Besides the baseline beanie, a beanie with increased diameter and height, namely beanie R1H1, is evaluated in combination with the reference and the optimized blade-sleeve fairing. This enlarged full-fairing beanie covers the lead-lag dampers and also partly the blade-sleeve fairing.

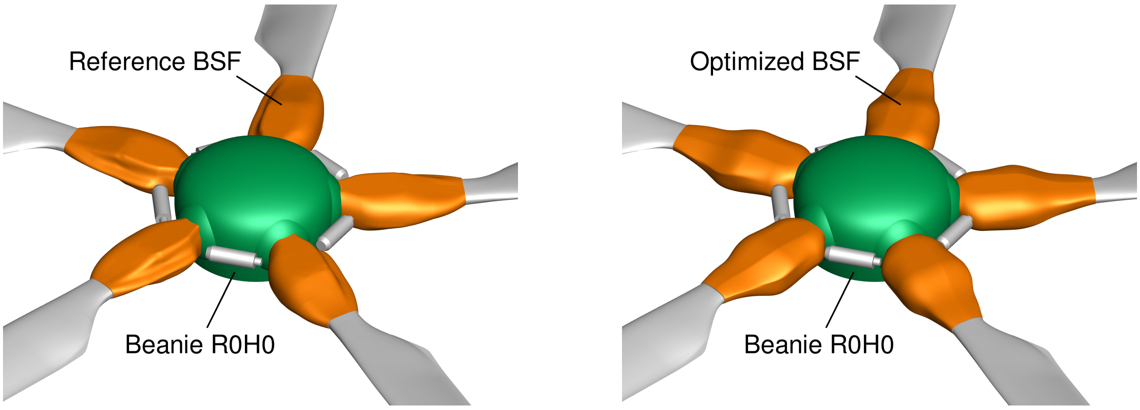

(a) Beanie R0H0 with reference BSF. (b) Beanie R0H0 with optimized BSF.

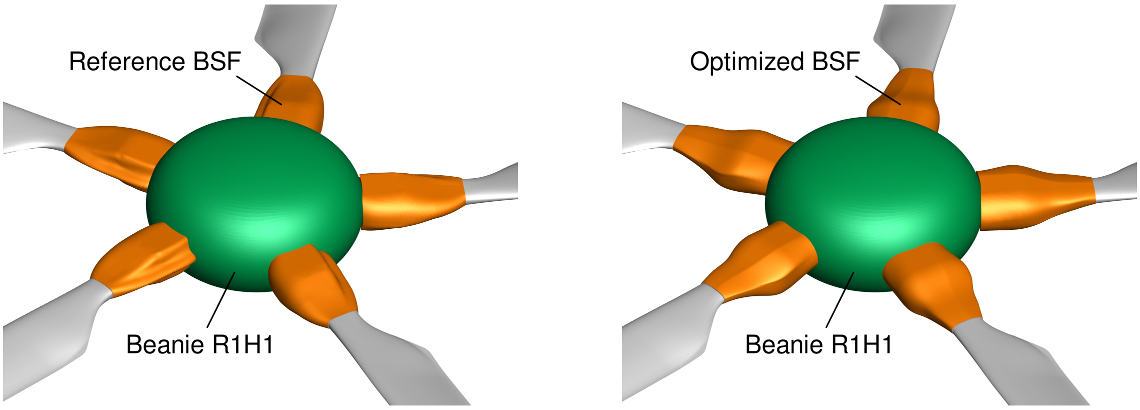

(c) Beanie R1H1 with reference BSF. (d) Beanie R1H1 with optimized BSF.

Figure 6.13: Investigated rotor-head fairing configurations.

6.4.1 Aerodynamic Forces and Moments

In this section, the aerodynamic forces and moments of the isolated rotor head are evaluated to determine the performance differences between the optimized and the reference blade-sleeve fairing. The numerical flow simulations are performed for a steady, sea-level cruise flight of the RACER demonstrator at a constant angle of attack and without angle of sideslip.

The applied coordinate system and the moment reference point (MRP) are illustrated in Fig. 6.14. The MRP is located on the main-rotor axis, at the base of the full-fairing beanie. Furthermore, the x-axis is parallel to the longitudinal axis of the helicopter and the positive x-direction is given from nose to tail. The y-direction is positive from the port wing to the starboard wing and the z-direction is positive from bottom to top. Additionally, positive moments for M_x, M_y and M_z are depicted in Fig. 6.14 following the right-hand rule on each axis. Due to the fact that no angle of sideslip ($\beta = 0°$) is applied in the numerical flow simulations, lift and drag are only depending on the angle of attack α. Hence, lift L and drag D are calculated according to Eq. 6.4 and Eq. 6.5, respectively.

$$L = -F_x \cdot \sin(\alpha) + F_z \cdot \cos(\alpha) \tag{6.4}$$

$$D = \quad F_x \cdot \cos(\alpha) + F_z \cdot \sin(\alpha) \tag{6.5}$$

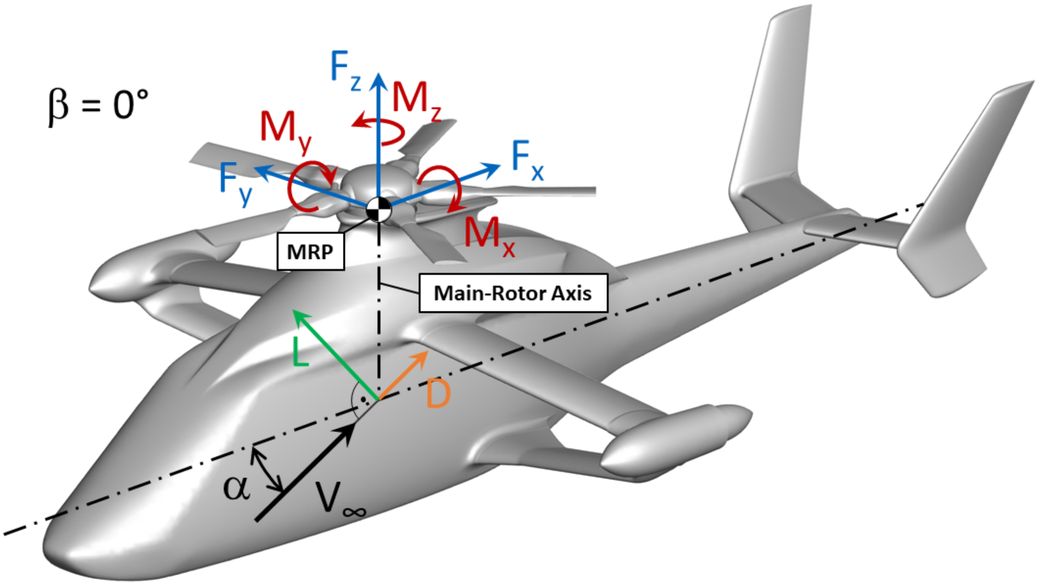

Figure 6.14: Definition of the applied coordinate system and location of the moment reference point (MRP).

In order to evaluate the aerodynamic characteristics of the rotor-head fairings, lift, drag and sideforce of the rotor head are examined. Furthermore, the z-moment of the main rotor, which represents the necessary driving torque, is analyzed. This quantity yields an implicit measure for the circumferential drag of the blade-sleeve fairing and the rotor-blade stub. Regarding the rotor head with the baseline beanie R0H0, a total number of eight rotor revolutions is simulated and the transient results for the final rotor revolution are illustrated in Fig. 6.15. The black curves represent the flow simulation results for the reference rotor head, which comprises the baseline beanie R0H0 and the reference blade-sleeve fairing. The solid lines show the transient solution and the dashed lines yield the averaged solution.

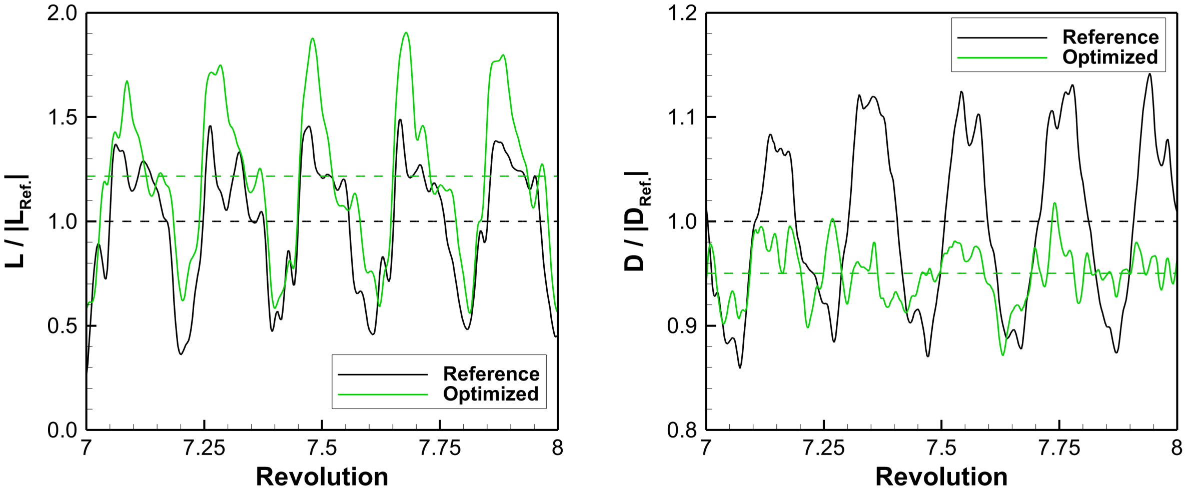

(a) Normalized lift $L \ / \ |L_{Ref.}|$. (b) Normalized drag $D \ / \ |D_{Ref.}|$.

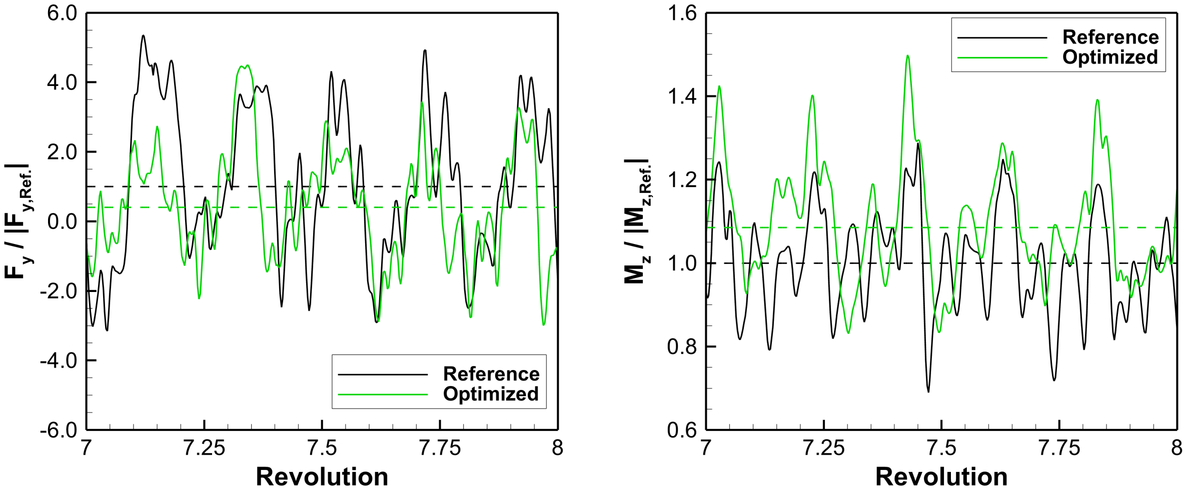

(c) Normalized sideforce $F_y \ / \ |F_{y,Ref.}|$. (d) Normalized moment $M_z \ / \ |M_{z,Ref.}|$.

Figure 6.15: Evaluation of the total aerodynamic forces and the driving torque of the main rotor M_z for a single rotor revolution showing a comparison between the reference and the optimized blade-sleeve fairing in combination with the baseline beanie R0H0. All quantities are normalized by the average values of the AHF reference rotor head.

The mean aerodynamic forces and moments of the reference rotor head are used to normalize all flow simulation results. Based on the selected normalization, the mean values for each quantity of the reference rotor head are +1 or -1 depending on the sign of the actual value. In order to derive the mean values, the flow simulation results are averaged over four rotor revolutions. The flow simulation results for the rotor head with the optimized blade-sleeve fairing are depicted by the green lines in Fig. 6.15. The corresponding mean values are given by the green dashed lines and a direct comparison to the reference rotor head can be conducted. The transient results show five distinct peaks within a single rotor revolution, which is characteristic for the five-bladed rotor head. The rotor head with the optimized blade-sleeve fairing shows a lift increase of $\Delta L = +21.7\,\%$ compared to the reference rotor head.

It can be seen that the previously mentioned peaks in the transient lift curves are much more pronounced for the optimized blade-sleeve fairing and the minimum values are slightly increased, which leads to enhanced lift. Furthermore, a drag reduction of $\Delta D = -5.0\,\%$ is observed for the newly developed blade-sleeve fairing and the force oscillations with the blade-passing frequency are much more damped. The side force F_y of the reference rotor head is almost negligible, because it is in the order of magnitude of two percent of the rotor-head drag. The rotor head with the optimized blade-sleeve fairing further reduces this side force by $\Delta F_y = -59.3\,\%$ compared to the reference rotor head, which means that almost no side force is generated. Regarding the driving torque of the main rotor, which is given by M_z, the rotor head with the optimized blade-sleeve fairing requires about 8.5 % more torque. Nevertheless, the CFD results predict a decent performance benefit that can be expected by the newly developed blade-sleeve fairing in combination with the full-fairing beanie R0H0.

Regarding the aerodynamic forces of the rotor-head components, the focus is on the evaluation of lift and drag for the blade-sleeve fairing (BSF), the full-fairing beanie (FFB) and the truncated rotor blade (RB). All forces are normalized by the magnitudes of the average reference rotor-head forces. The normalized lift for each of the three components is depicted in Fig. 6.16. Concerning the plots on the left-hand side, the normalized lift is shown for three rotor revolutions and on the right-hand side, a detailed view on the final rotor revolution is given. Figure 6.16b shows the normalized lift of the baseline beanie R0H0 depending on the azimuthal rotor position of a single rotor blade. At $\Psi = 0°$ one rotor blade is pointing downstream to the tail of the helicopter and the remaining blades are arranged with an angular offset of $\Delta\Psi = 72°$ between each other. The evaluation of the lift for the baseline beanie R0H0 with the optimized blade-sleeve fairing shows that the maximum lift is reached when the rotor blade is located about 15° after the upstream position ($\Psi = 180°$). Moreover, the beanie generates the lowest lift when the rotor blade is about 28° before the upstream position, which leads to a phase difference of $\Delta\Psi \approx 43°$ between the minimum and maximum lift of the beanie. Furthermore, the difference between the minimum and maximum lift of beanie R0H0 is in the order of magnitude of $\Delta\left(L/|L_{Ref.}|\right) \approx 3.5\text{-}4$ for the reference blade-sleeve fairing and $\Delta\left(L/|L_{Ref.}|\right) \approx 2.75\text{-}3.5$ for the optimized blade-sleeve fairing. In combination with the optimized blade-sleeve fairing, an average lift reduction of 7.5 % is observed for beanie R0H0.

Figure 6.16d shows the normalized lift of the blade-sleeve fairing depending on the azimuthal rotor position. The lift shows significant fluctuations in the azimuthal range of $0° \leq \Psi \leq 60°$, which is related to the interaction with the wake-flow field of the beanie and the preceding rotor blade. At the advancing rotor-blade position ($\Psi = 90°$), the reference blade-sleeve fairing generates about twice as much downforce as the optimized blade-sleeve fairing.

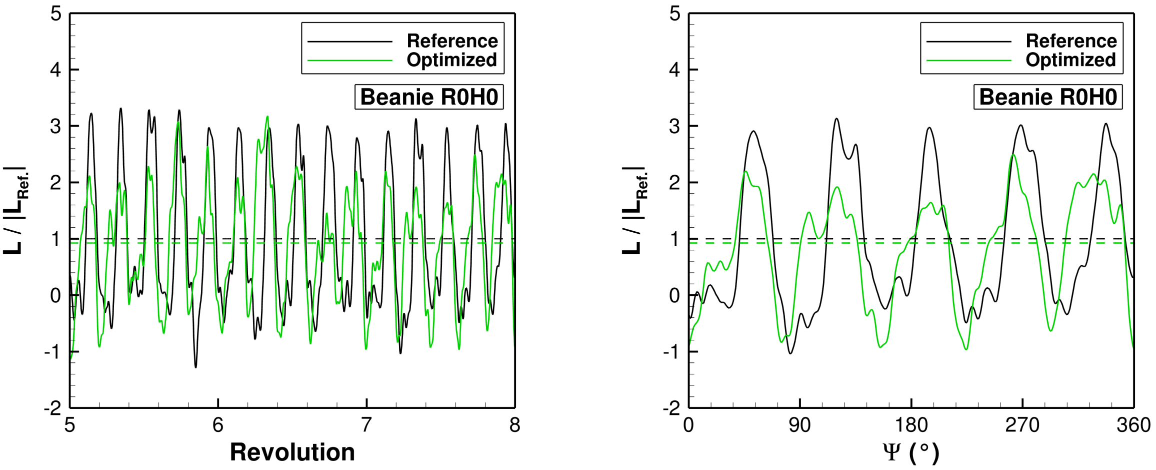

(a) Beanie R0H0 - 3 rotor revolutions.

(b) Beanie R0H0 - Detailed view on the final rotor revolution ($0° \leq \Psi < 360°$).

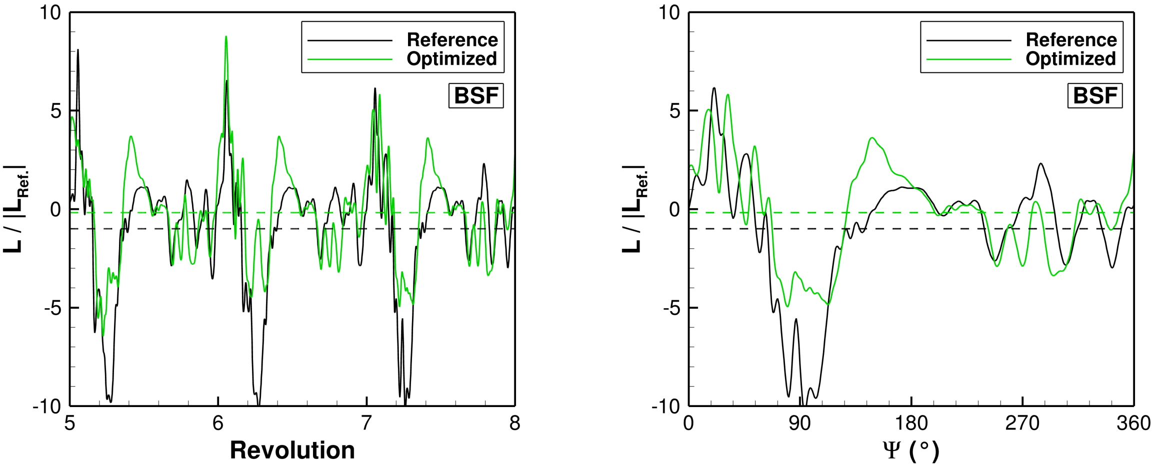

(c) Single BSF - 3 rotor revolutions.

(d) Single BSF - Detailed view on the final rotor revolution ($0° \leq \Psi < 360°$).

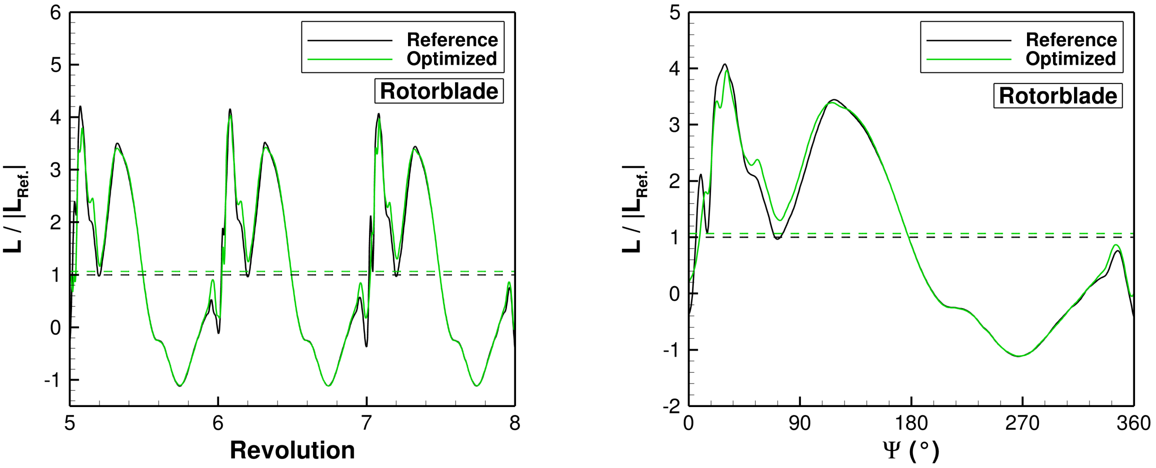

(e) Single Rotorblade - 3 rotor revolutions.

(f) Single Rotorblade - Detailed view on the final rotor revolution ($0° \leq \Psi < 360°$).

Figure 6.16: Evaluation of the normalized lift for the components of the isolated rotor head with beanie R0H0. The lift is normalized by the average value of the respective AHF reference rotor-head component.

Furthermore, the optmized blade-sleeve fairing provides much more lift within the azimuthal range of $126° \leq \Psi \leq 182°$. Regarding the retreating blade sector, comparable lift is obtained by both blade-sleeve fairings within the range $180° \leq \Psi \leq 260°$. In the vicinity of the retreating blade position ($\Psi = 270°$), the optimized blade-sleeve fairing generates less lift than the reference fairing and the force oscillations become stronger beyond this azimuthal position. Regarding the average lift of the blade-sleeve fairings, a downforce is generated by both geometries. However, the optimized blade-sleeve fairing reduces this downforce by 83 % compared to the reference shape. Finally, the azimuthal lift distribution of the truncated rotor blade is evaluated in Fig. 6.16f. It can be seen that there are only minor differences between the two blade-sleeve fairings. These limited differences are observed in the rearward facing sector $-30° \leq \Psi \leq +30°$ and the advancing-blade sector $+45° \leq \Psi \leq +120°$. Regarding the optimized blade-sleeve fairing, the average lift of the rotor blade is increased by $\Delta L = +6.4\,\%$ compared to the rotor blade with the reference blade-sleeve fairing, even though the optimized blade-sleeve fairing has a larger span and covers more of the rotor blade.

The evaluation of the component drag for the rotor head with beanie R0H0 is illustrated in Fig. 6.17. Regarding the rotor head with the optimized blade-sleeve fairing, the drag of the beanie is reduced by five percent compared to the reference rotor head. Moreover, the amplitude of the drag-force oscillation is much more damped in combination with the newly developed fairing shape, which indicates a more favorable interaction between the blade-sleeve fairing and the beanie. The azimuthal drag distribution of the blade-sleeve fairing is depicted in Fig. 6.17d. The maximum drag values are observed at the advancing ($\Psi = 90°$) and the retreating blade position ($\Psi = 270°$), which corresponds to the rotor-blade positions that were addressed during the design optimization of the blade-sleeve fairing. The biggest differences between the two blade-sleeve fairings concerning drag can be seen in the azimuthal region of the advancing blade ($\Psi = 90°$), the upstream pointing blade ($\Psi = 180°$) and the retreating blade($\Psi = 270°$). The differences in terms of drag are rather small, but the optimized blade-sleeve fairing provides slightly less drag within a large portion of the rotor revolution and therefore an average drag reduction of $\Delta D = -5.9\,\%$ is achieved in comparison to the reference blade-sleeve fairing. The comparison of the azimuthal rotor-blade drag is illustrated in Fig. 6.17f and it can be seen that the drag characteristics are almost identical within a wide range. The largest discrepancies are observed in the advancing blade sector between $\Psi = 20°$ and $\Psi = 135°$. There are two local maxima at $\Psi = 54°$ and $\Psi = 111°$, which are smoothed by the optimized blade-sleeve fairing leading to lower drag values in this region. Overall, a drag reduction of $\Delta D = -2.5\,\%$ is obtained for the rotor-blade component with the optimized blade-sleeve fairing.

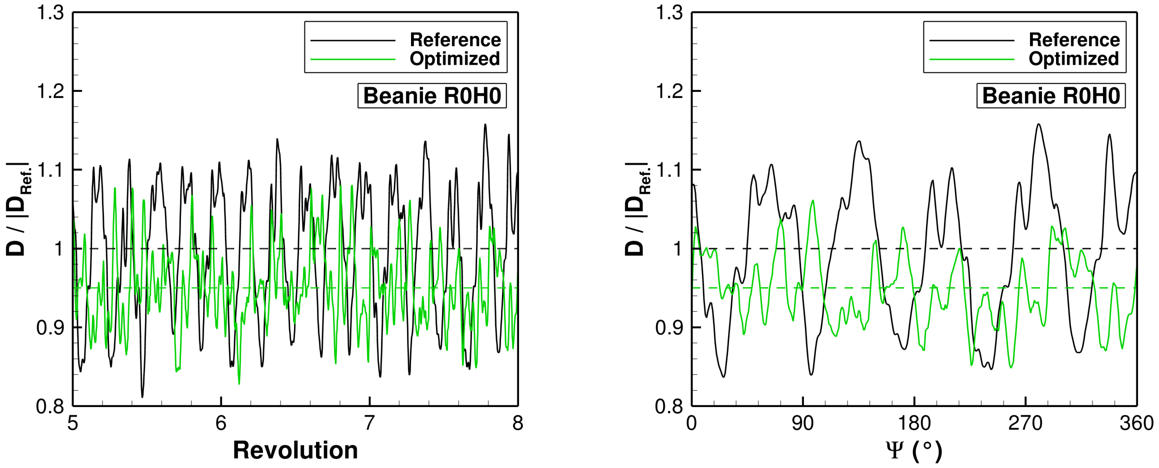

(a) Beanie R0H0 - 3 rotor revolutions.

(b) Beanie R0H0 - Detailed view on the final rotor revolution ($0° \leq \Psi < 360°$).

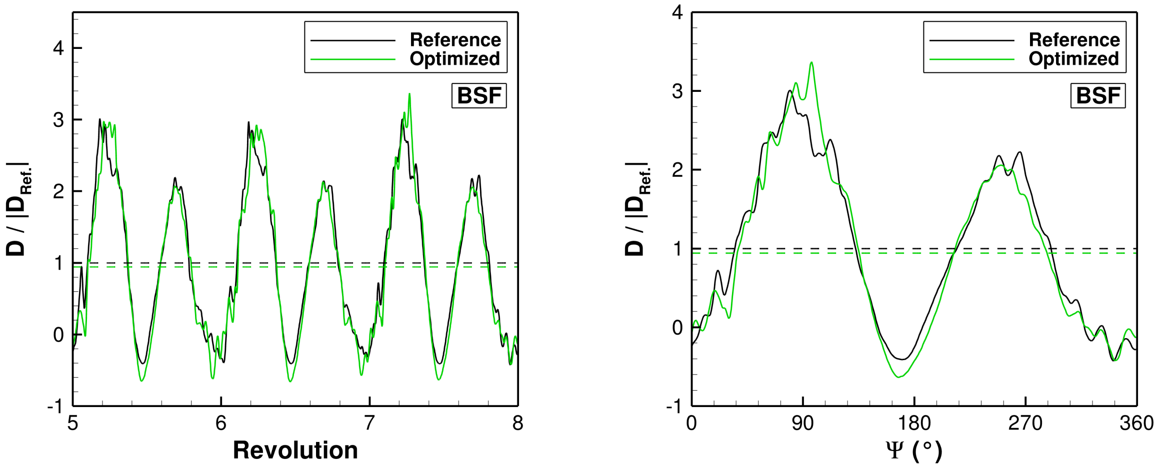

(c) Single BSF - 3 rotor revolutions.

(d) Single BSF - Detailed view on the final rotor revolution ($0° \leq \Psi < 360°$).

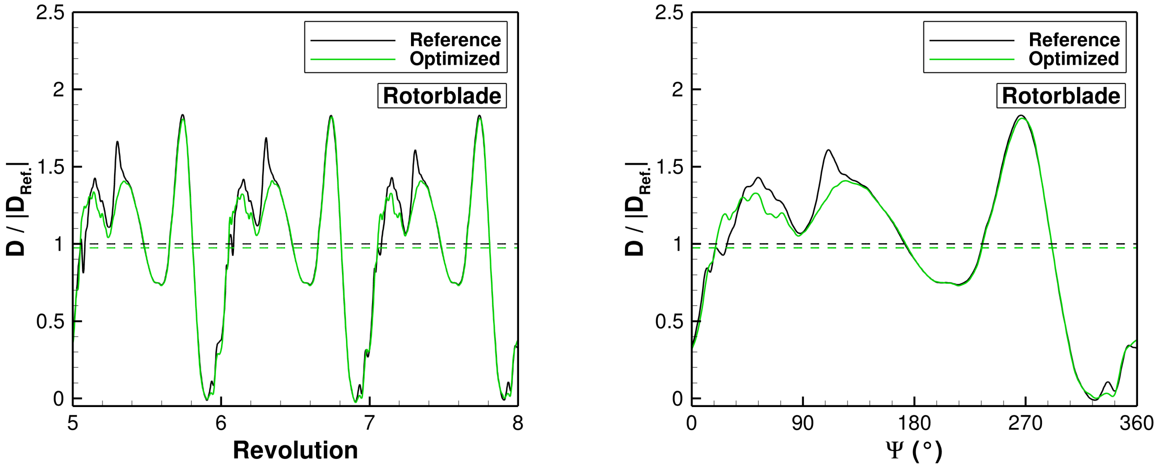

(e) Single Rotorblade - 3 rotor revolutions.

(f) Single Rotorblade - Detailed view on the final rotor revolution ($0° \leq \Psi < 360°$).

Figure 6.17: Evaluation of the normalized drag for the components of the isolated rotor head with beanie R0H0. The drag is normalized by the average value of the respective AHF reference rotor-head component.

The numerical flow simulations for the isolated rotor head with the enlarged beanie R1H1 are performed for both, the optimized and the reference blade-sleeve fairing. The flow simulation results comprise six rotor revolutions and the transient as well as the mean aerodynamic forces are evaluated. The final three rotor revolutions are used to average the aerodynamic forces and moments. The total aerodynamic forces and the driving torque of the main rotor, which is given by M_z, are illustrated in Fig. 6.18 showing the results for the final rotor revolution. As for the baseline rotor head, the black curves correspond to the rotor head with the reference blade-sleeve fairing and the green curves belong to the rotor head with the optimized blade-sleeve fairing. Furthermore, the dashed lines represent the mean values of the respective quantities.

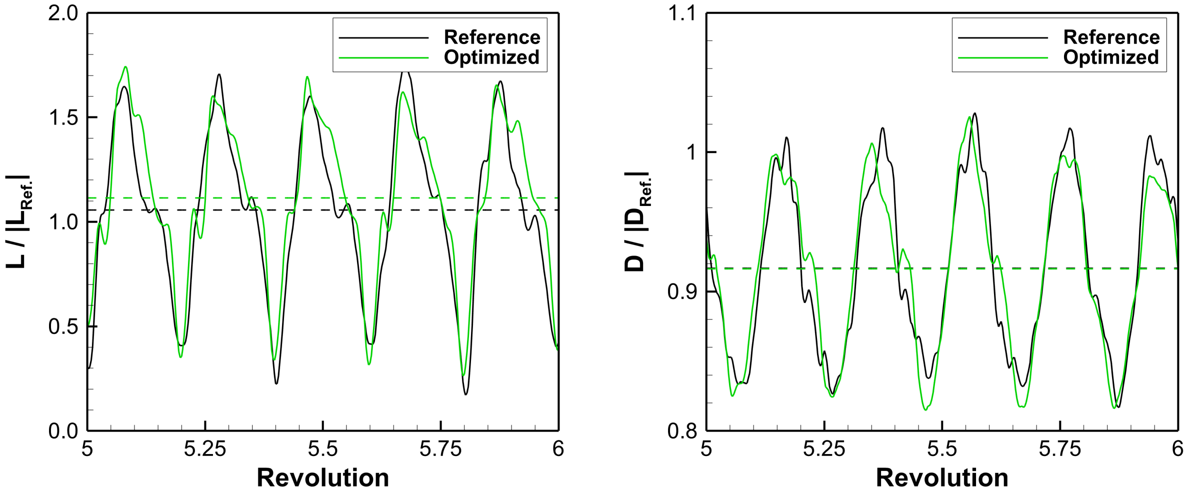

(a) Normalized lift L / $|L_{Ref.}|$. (b) Normalized drag D / $|D_{Ref.}|$.

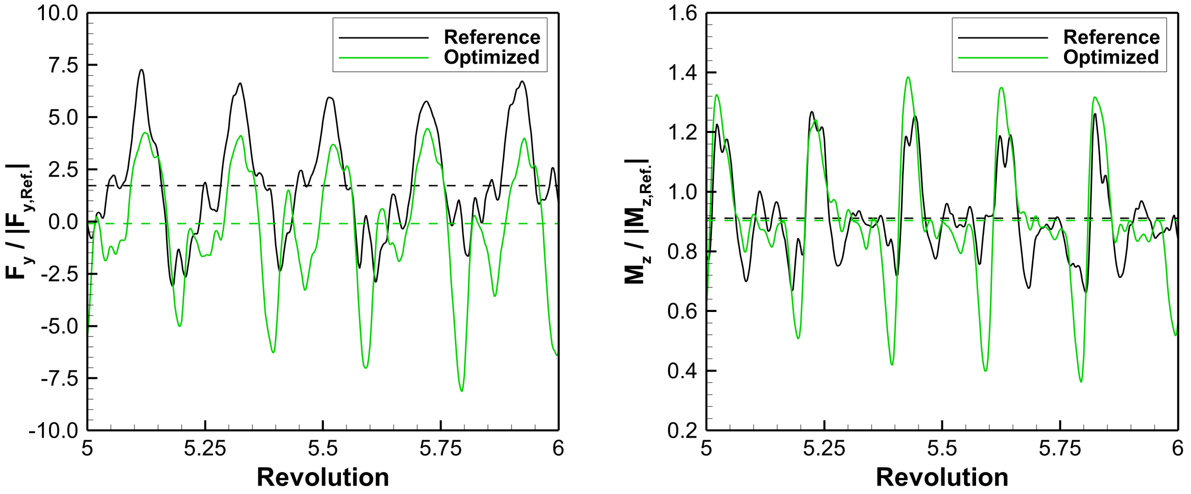

(c) Normalized sideforce F_y / $|F_{y,Ref.}|$. (d) Normalized moment M_z / $|M_{z,Ref.}|$.

Figure 6.18: Evaluation of the total aerodynamic forces and the driving torque of the main rotor M_z for a single rotor revolution showing a comparison between the reference and the optimized blade-sleeve fairing in combination with the enlarged beanie R1H1. All quantities are normalized by the average values of the AHF reference rotor head.

All forces and moments are normalized by the absolute, mean values of the reference rotor head consisting of the baseline beanie R0H0 and the reference blade-sleeve fairing. In contrast to the rotor head with the baseline beanie R0H0, the differences regarding lift and drag are much smaller comparing the two blade-sleeve fairing shapes. The biggest relative difference can be observed for the sideforce, which is illustrated in Fig. 6.18c. Regarding the average value of the sideforce, the optimized blade-sleeve fairing leads to a normalized sideforce of $F_y/F_{y,Ref.} = -0.089$. In contrast, the larger beanie with the reference blade-sleeve fairing causes a normalized sideforce of $F_y/F_{y,Ref.} = 1.72$. Regarding lift and drag, similar characteristics are obtained for both rotor-head fairings and comparable minimum and maximum values are observed, which can be seen in Fig. 6.18a and Fig. 6.18b, respectively. In terms of lift, the rotor head with the optimized blade-sleeve fairing provides a lift-increase of $\Delta L = +11.4\,\%$ in comparison to the reference rotor head. Concerning the combination beanie R1H1 and reference blade-sleeve fairing, a moderate lift-increase of $\Delta L = +5.6\,\%$ is observed. Hence, the newly developed blade-sleeve fairing also provides more lift on the rotor head with the enlarged beanie. The analysis of the rotor-head drag reveals a similar drag-reduction potential for both blade-sleeve fairings with $\Delta D \approx -8.4\,\%$ compared to the reference rotor head. Furthermore, the main-rotor moment M_z is about nine percent lower for the rotor head with the larger beanie. The difference between the two blade-sleeve fairings with respect to the required driving torque of the isolated rotor head is below one percent.

The analysis of the transient and the mean component lift is given in Fig. 6.19 for the enlarged beanie R1H1, the blade-sleeve fairings and the rotor-blade stub. The results are shown for three rotor revolutions and a detailed view on the final revolution is given to be able to determine the azimuthal distribution of the respective quantity. Regarding the lift contribution of beanie R1H1, an increase in lift of $\Delta L = +71.7\,\%$ is derived for the rotor head with the optimized blade-sleeve fairing. Moreover, the lift increase is even higher for the rotor head with the reference blade-sleeve fairing yielding $\Delta L = +118.1\,\%$ in comparison to beanie R0H0 on the reference rotor head. In Fig. 6.19d, it can be seen that both blade-sleeve fairings deliver less lift in combination with the larger beanie. In comparison to the blade-sleeve fairing on the reference rotor head, the optimized blade-sleeve fairing reduces the downforce by $+11.1\,\%$ and the reference blade-sleeve fairing generates more downforce leading to a normalized lift of $L/|L_{Ref.}| = -1.36$. However, the azimuthal lift characteristics of the blade-sleeve fairings are comparable to the rotor head with beanie R0H0. Concerning the lift of the rotor-blade stub, almost the same values are obtained for both blade-sleeve fairings in comparison to the rotor head with beanie R0H0. The difference is in the order of magnitude of 1-2 %. Moreover, the rotor blade reveals similar lift characteristics for both blade-sleeve fairings and the main discrepancies are observed in the advancing blade sector, but they are almost negligible.

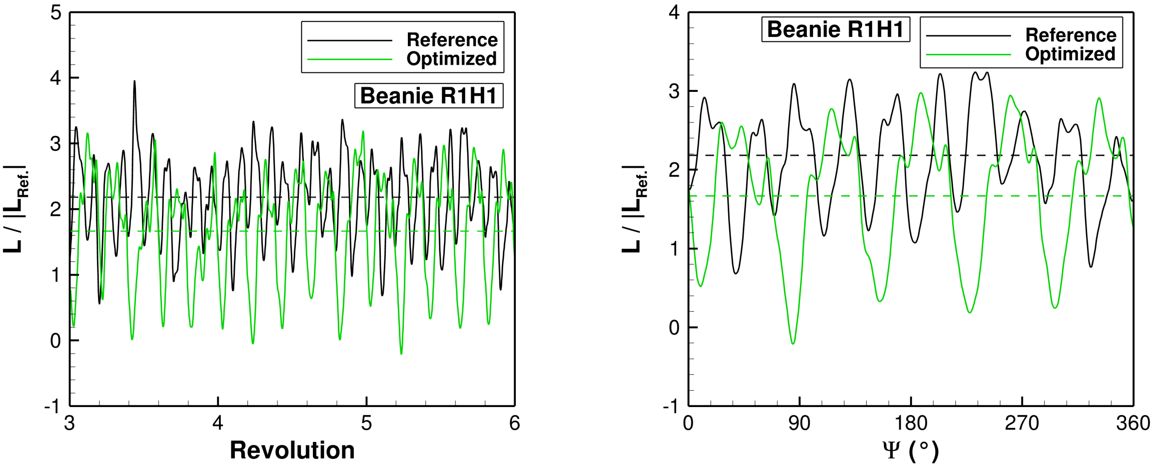

(a) Beanie R1H1 - 3 rotor revolutions.

(b) Beanie R1H1 - Detailed view on the final rotor revolution ($0° \leq \Psi < 360°$).

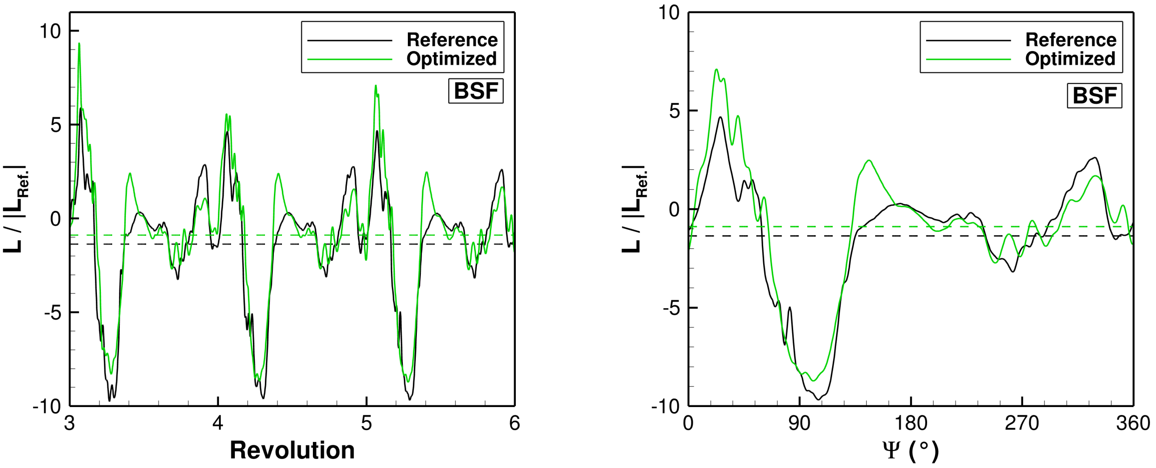

(c) Single BSF - 3 rotor revolutions.

(d) Single BSF - Detailed view on the final rotor revolution ($0° \leq \Psi < 360°$).

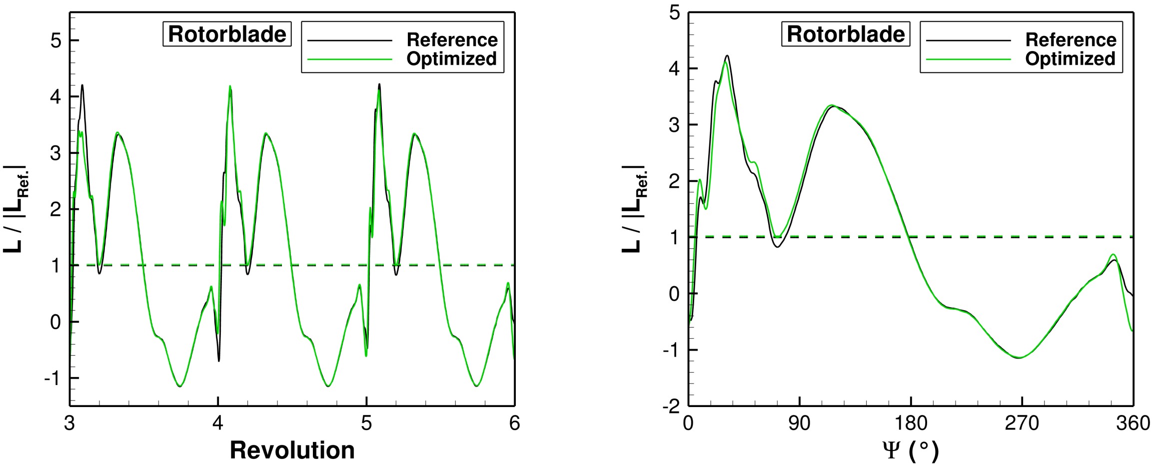

(e) Single Rotorblade - 3 rotor revolutions.

(f) Single Rotorblade - Detailed view on the final rotor revolution ($0° \leq \Psi < 360°$).

Figure 6.19: Evaluation of the normalized lift for the components of the isolated rotor head with the enlarged beanie R1H1. The lift is normalized by the average value of the respective AHF reference rotor-head component.

The evaluation of the normalized drag for the isolated rotor head components with beanie R1H1 is given in Fig. 6.20. In comparison to the baseline beanie R0H0, the enlarged beanie R1H1 causes more drag due to the increased size. In combination with the optimized blade-sleeve fairing, the normalized drag reaches an average value of $D/D_{Ref.} = +1.16$ and with the reference blade-sleeve fairing it is $D/D_{Ref.} = +1.13$. The drag characteristics of the blade-sleeve fairings are almost identical, which can be seen in Fig. 6.20c and more detailed in Fig.6.20d. The mean, normalized drag values are $D/D_{Ref.} = +0.55$ for both blade-sleeve fairings. The largest discrepancy is observed at the azimuthal blade position of $\Psi = 170°$, which is close to the upstream pointing rotor blade. Furthermore, the evaluation of the rotor-blade drag reveals similar characteristics as for the baseline rotor head with beanie R0H0. The main differences regarding the rotor-blade drag are given in the advancing blade sector and the mean values differ by approximately one percent. In comparison to the drag of the rotor blade on the baseline rotor head with beanie R0H0, a drag reduction of $\Delta D = -2.4\,\%$ is obtained with the optimized blade-sleeve fairing.

Finally, a direct comparison between the four investigated full-fairing rotor heads is given in Tab.6.3. The relative differences to the reference rotor head concerning lift L, drag D and the required main-rotor driving torque M_z are summarized. The mean, total aerodynamic forces and moments are evaluated and compared to each other. The baseline beanie R0H0 in combination with the optimized blade-sleeve fairing provides a lift increase of $\Delta L = +21.7\,\%$, a drag reduction of $\Delta D = -5.0\,\%$ and requires slightly more driving torque with $\Delta M_z = +8.5\,\%$. Regarding the larger beanie R1H1, more drag-reduction potential is observed in comparison to the reference rotor head. The drag benefit is $\Delta D = -8.4\,\%$ with the optimized blade-sleeve fairing and $\Delta D = -8.3\,\%$ with the reference blade-sleeve fairing. Therefore, the newly developed blade-sleeve fairing does not provide a significant drag benefit in comparison to the reference blade-sleeve fairing, if the rotor head fairing comprises the larger beanie R1H1. However, a lift increase of $\Delta L = +11.4\,\%$ is obtained for the rotor head with the optimized blade-sleeve fairing, whereas it is only $\Delta L = +5.6\,\%$ with the reference blade-sleeve fairing. Additionally, the rotor head with the larger beanie R1H1 requires less driving torque yielding a reduction of $\Delta M_z = -8.9\,\%$ and $\Delta M_z = -9.7\,\%$, respectively.

Full-Fairing Beanie	**Blade-Sleeve Fairing**	**ΔL** [%]	**ΔD** [%]	$\mathbf{\Delta M_z}$ [%]
R0H0	Reference BSF		Reference	
R0H0	Optimized BSF	+21.7 %	-5.0 %	+8.5 %
R1H1	Reference BSF	+5.6 %	-8.3 %	-8.9 %
R1H1	Optimized BSF	+11.4 %	-8.4 %	-9.7 %

Table 6.3: Comparison of the mean, total aerodynamic forces and the main-rotor moment M_z for the investigated rotor-head fairings.

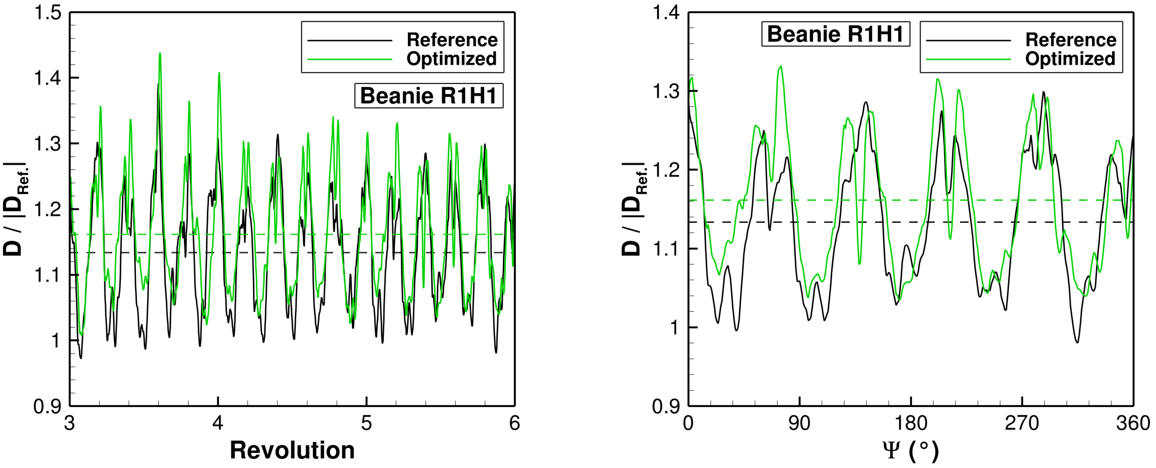

(a) Beanie R1H1 - 3 rotor revolutions.

(b) Beanie R1H1 - Detailed view on the final rotor revolution ($0° \leq \Psi < 360°$).

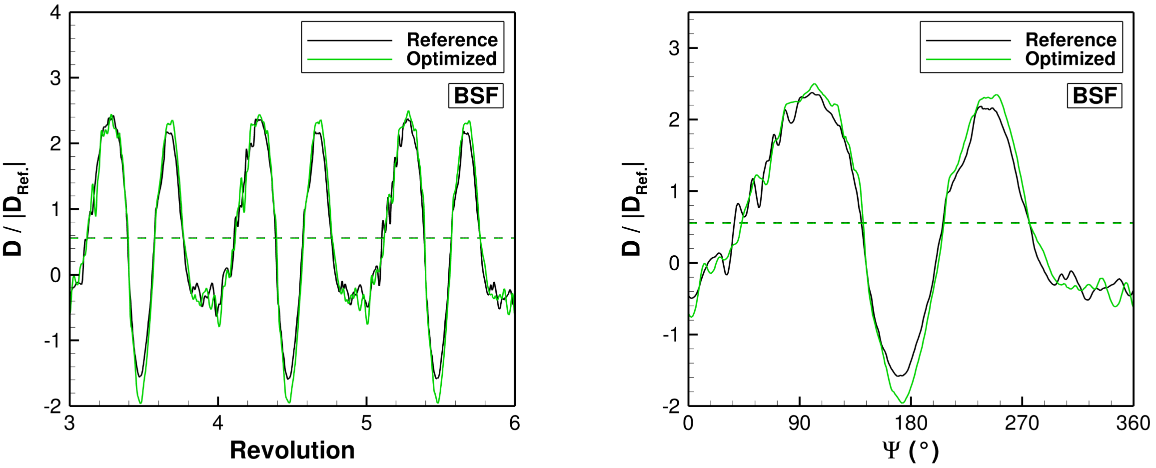

(c) Single BSF - 3 rotor revolutions.

(d) Single BSF - Detailed view on the final rotor revolution ($0° \leq \Psi < 360°$).

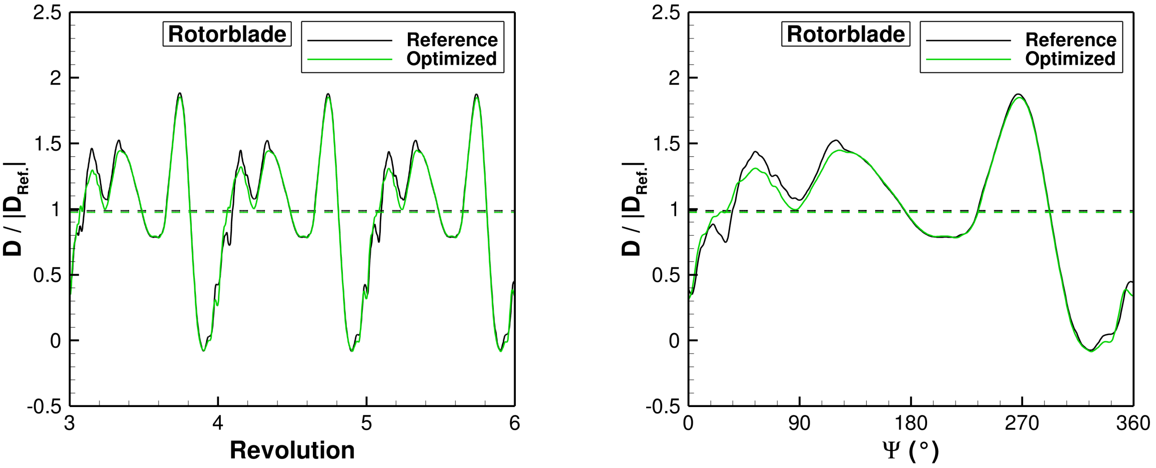

(e) Single Rotorblade - 3 rotor revolutions.

(f) Single Rotorblade - Detailed view on the final rotor revolution ($0° \leq \Psi < 360°$).

Figure 6.20: Evaluation of the normalized drag for the components of the isolated rotor head with the enlarged beanie R1H1. The drag is normalized by the average value of the respective AHF reference rotor-head component.

The evaluation of the transient aerodynamic forces reveals strong oscillations and therefore, a fast Fourier transformation (FFT) is performed to determine the dominant frequencies and the corresponding amplitudes acting on the rotor head with truncated rotor blades. In the present work, the focus is set on the analysis of lift and drag, because these two forces are the most relevant ones for the design optimization of the rotor-head fairing and they also provide the largest amplitudes. Figure 6.21 shows the frequency domain of the normalized lift for the baseline rotor head with full-fairing beanie R0H0 and both blade-sleeve fairing candidates. The forces are normalized by the average values of the reference rotor head and the frequency is given in multiples of the blade-passing frequency (BPF). Regarding the lift spectrum, both rotor heads show relevant amplitudes at the first and the second harmonic of the BPF. The rotor head with the reference blade-sleeve fairing generates an amplitude of $|L(f)|/|L_{Ref.}| = 0.413$ with the BPF and the optimized blade-sleeve fairing slightly increases this amplitude to $|L(f)|/|L_{Ref.}| = 0.456$. Moreover, the amplitude of the second harmonic is $|L(f)|/|L_{Ref.}| = 0.133$ for the reference blade-sleeve fairing and $|L(f)|/|L_{Ref.}| = 0.213$ for the optimized blade-sleeve fairing.

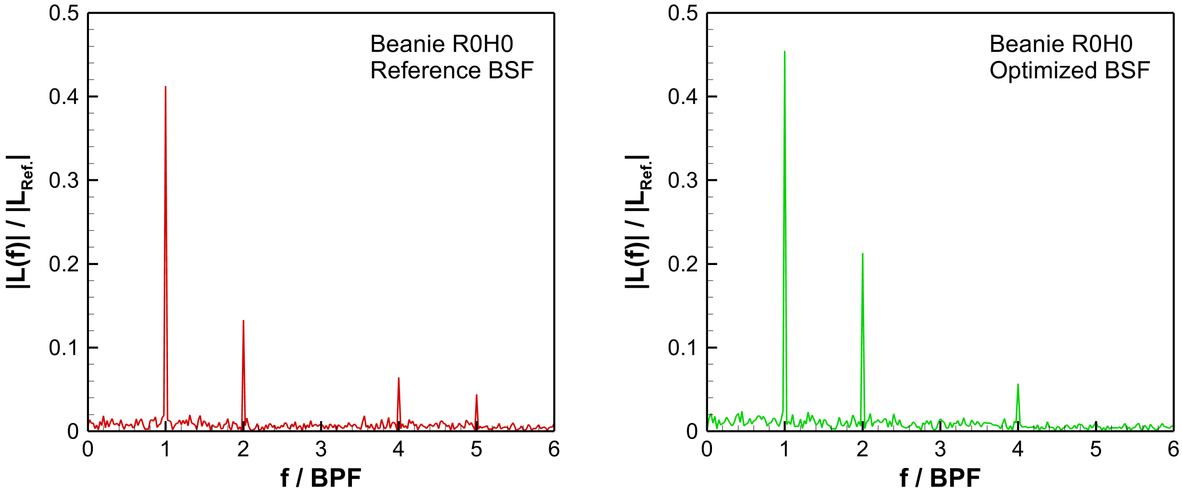

(a) Rotor head with the reference BSF.
(b) Rotor head with the optimized BSF.

Figure 6.21: Spectrum of the rotor-head lift for the baseline beanie R0H0 in combination with the reference and the optimized BSF.

The FFT of the rotor-head drag is depicted in Fig. 6.22. Regarding the results for the reference rotor head, it can be seen that only the first harmonic of the BPF is dominant with an amplitude of $|D(f)|/|D_{Ref.}| = 0.11$. In contrast, the rotor head with the optimized BSF provides a reduced oscillation in drag with an amplitude of $|D(f)|/|D_{Ref.}| = 0.03$ at the BPF and the contributions of higher harmonics are almost negligible. The most relevant results of the FFT analysis for the rotor head with the baseline beanie R0H0 are summarized in Tab. 6.4 showing the normalized lift and drag amplitudes at the first five BPF harmonics.

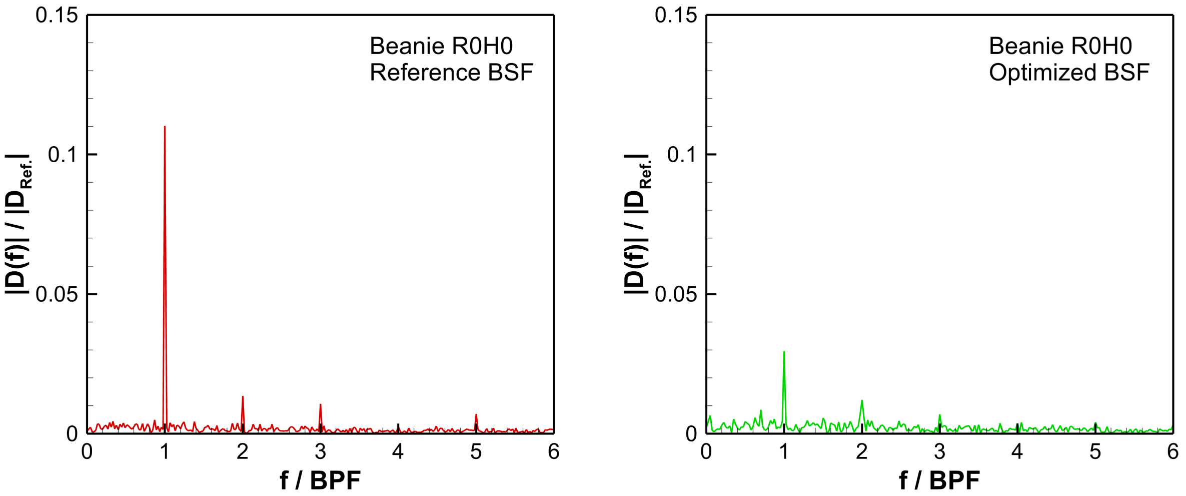

(a) Rotor head with the reference BSF.

(b) Rotor head with the optimized BSF.

Figure 6.22: Spectrum of the rotor-head drag for the baseline beanie R0H0 in combination with the reference and the optimized BSF.

	RH w/ Reference BSF		**RH w/ Optimized BSF**	
f/BPF	$\mathbf{|L(f)| / |L_{Ref.}|}$	$\mathbf{|D(f)| / |D_{Ref.}|}$	$\mathbf{|L(f)| / |L_{Ref.}|}$	$\mathbf{|D(f)| / |D_{Ref.}|}$
1	0.413	0.110	0.456	0.030
2	0.133	0.014	0.213	0.012
3	0.008	0.011	0.015	0.007
4	0.064	0.003	0.057	0.004
5	0.044	0.007	0.011	0.004

Table 6.4: Summary of the FFT analysis regarding lift and drag of the isolated rotor head with the full-fairing beanie R0H0.

Within the next step, the FFT analysis is performed for the rotor head with the larger full-fairing beanie R1H1 in combination with the optimized and the reference blade-sleeve fairing. Figure 6.23a shows the frequency domain of the normalized lift for the reference blade-sleeve fairing. The evaluation of the lift spectrum reveals significant amplitudes at the first and the second harmonic of the BPF reaching $|L(f)|/|L_{Ref.}| = 0.536$ and $|L(f)|/|L_{Ref.}| = 0.212$, respectively. Additionally, a minor oscillation is observed at the third harmonic, but the amplitude is below six percent of the reference lift. The transformed, normalized lift for the rotor head with the optimized blade-sleeve fairing is depicted in Fig. 6.23b. In comparison to the results for the rotor head with the reference blade-sleeve fairing, the amplitudes of the first and the second harmonic are reduced to $|L(f)|/|L_{Ref.}| = 0.443$ and $|L(f)|/|L_{Ref.}| = 0.125$, respectively. Furthermore, the higher harmonics are more pronounced for the optimized blade-sleeve fairing and the fourth harmonic shows a noteworthy amplitude of $|L(f)|/|L_{Ref.}| = 0.113$.

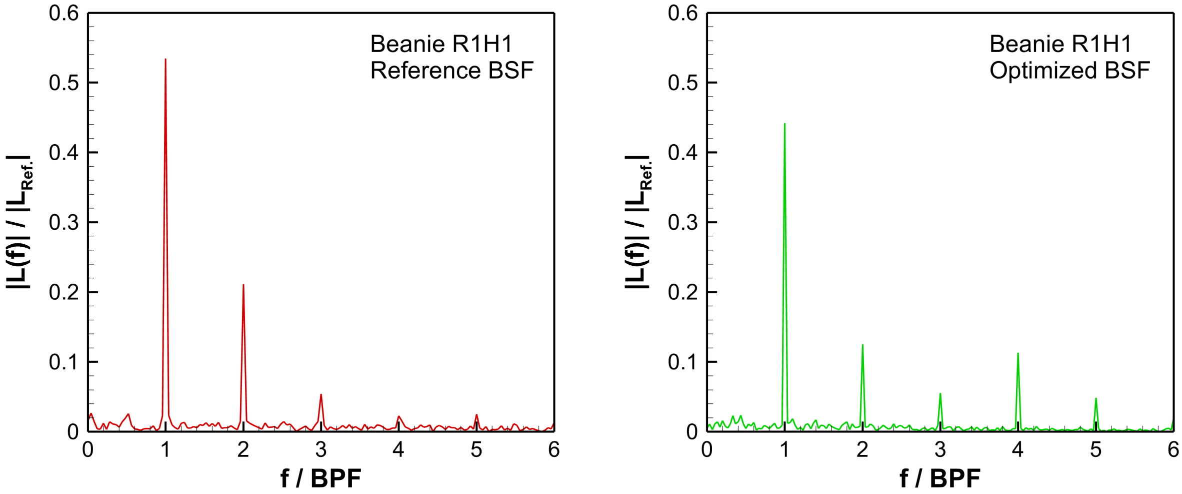

(a) Rotor head with the reference BSF. (b) Rotor head with the optimized BSF.

Figure 6.23: Spectrum of the rotor-head lift for the enlarged beanie R1H1 in combination with the reference and the optimized BSF.

Regarding the spectral analysis of the rotor-head drag, which is shown in Fig. 6.24, the first BPF harmonic shows significant amplitudes for both blade-sleeve fairing designs. Furthermore, the higher harmonics have only a minor contribution to the force oscillation reaching amplitudes below one percent of the reference drag. The rotor head with the reference blade-sleeve fairing exhibits an amplitude of $|D(f)|/|D_{Ref.}| = 0.089$ at the first BPF harmonic. In contrast, the optimized blade-sleeve fairing lowers this amplitude to $|D(f)|/|D_{Ref.}| = 0.082$. A summary about the main results of the FFT analysis for the rotor head with the larger beanie R1H1 is given in Tab. 6.5 showing the normalized lift and drag contributions for the first five BPF harmonics.

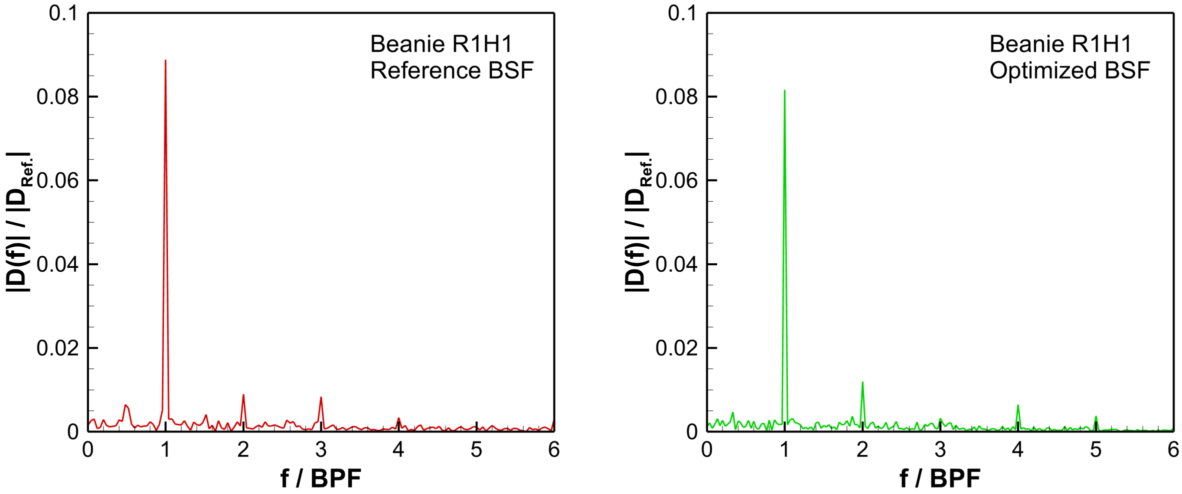

(a) Rotor head with the reference BSF. (b) Rotor head with the optimized BSF.

Figure 6.24: Spectrum of the rotor-head drag for the enlarged beanie R1H1 in combination with the reference and the optimized BSF.

	RH w/ Reference BSF		**RH w/ Optimized BSF**	
f/BPF	$\mathbf{|L(f)| / |L_{Ref.}|}$	$\mathbf{|D(f)| / |D_{Ref.}|}$	$\mathbf{|L(f)| / |L_{Ref.}|}$	$\mathbf{|D(f)| / |D_{Ref.}|}$
1	0.536	0.089	0.443	0.082
2	0.212	0.009	0.125	0.012
3	0.054	0.008	0.056	0.003
4	0.023	0.003	0.113	0.006
5	0.025	0.001	0.049	0.004

Table 6.5: Summary of the FFT analysis regarding lift and drag of the isolated rotor head with the full-fairing beanie R1H1.

6.4.2 Surface Quantities

In this section, the surface-pressure distributions of the investigated rotor-head fairings are compared to each other and the main differences are highlighted. During the design optimization process of the blade-sleeve fairing, the advancing ($\Psi = 90°$) and the retreating ($\Psi = 270°$) blade case were taken into account using the baseline beanie R0H0. Therefore, the surface-pressure distribution is analyzed in more detail for these two cases comparing the reference rotor head and the rotor head with the optimized blade-sleeve fairing. Furthermore, the chordwise surface-pressure distributions of the blade-sleeve sections S2-S5 are evaluated, because these sections were considered during the two-dimensional design optimization of the blade-sleeve fairing.

The surface-pressure distribution for the advancing blade case is illustrated in Fig. 6.25 showing a direct comparison between the reference rotor head and the rotor head with the optimized blade-sleeve fairing. The inflow direction is indicated by the velocity vector V_∞ and the top as well as the bottom side of the rotor head are examined. Moreover, the transient solution is shown at the actual time step for the advancing blade position and the pressure is normalized by a certain reference pressure. Additionally, the color map and the corresponding contour legend allow to identify regions of high and low pressure without disclosing the actual pressure values. Nevertheless, a qualitative comparison between the two rotor-head fairings is possible.

Whereas the surface-pressure distribution on the rotor blades is almost identical, differences can clearly be identified on the blade-sleeve fairings and the full-fairing beanie. Regarding the blade-sleeve fairing on the advancing rotor blade, the main differences are located on the top and the bottom side of the fairing. The low-pressure region on the bottom side is more continuous for the optimized blade-sleeve fairing indicating a smoother contour in this region. Moreover, higher pressure levels are observed on the bottom side of the spherical junction.

Additionally, the low-pressure region on the top-rear surface of the optimized blade-sleeve fairing seems to be more pronounced, whereas it is weaker in the front part of the fairing. Furthermore, higher pressure levels are observed on the leading-edge of the trailing blade-sleeve fairing, which is located at $\Psi = 18°$ for the current time step. This indicates higher dynamic pressure in this region for the optimized fairing. The top surface of the full-fairing beanie shows a region of increased pressure in the rear part for the reference blade-sleeve fairing, which is less pronounced for the rotor head with the optimized blade-sleeve fairing.

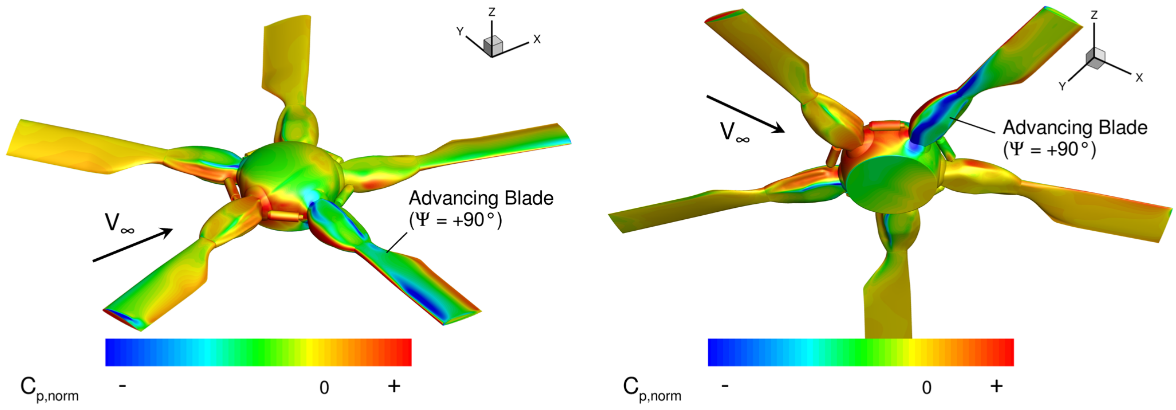

(a) Reference BSF (Top view).

(b) Reference BSF (Bottom view).

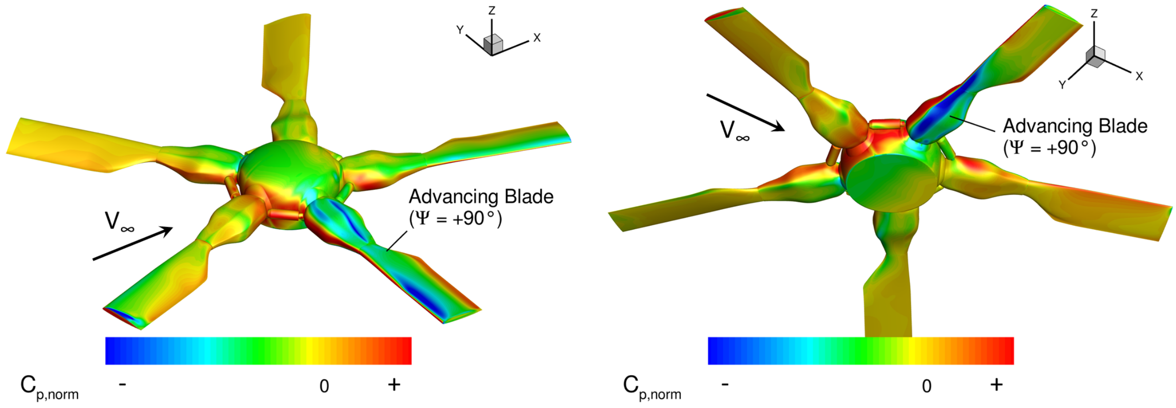

(c) Optimized BSF (Top view).

(d) Optimized BSF (Bottom view).

Figure 6.25: Instantaneous, normalized surface-pressure coefficient $C_{p,norm}$ for the advancing rotor-blade case ($\Psi = 90°$) considering the baseline beanie R0H0 in combination with the reference and the optimized BSF.

In order to identify the main differences in the local surface-pressure distribution of the blade-sleeve fairings, a detailed view is given on the radial blade-sleeve sections S2-S5, which can be seen in Fig. 6.26 for the advancing blade case. The results for the reference blade-sleeve fairing are depicted in Fig. 6.26a and for the optimized blade-sleeve fairing they are given in Fig. 6.26b.

Furthermore, a contour plot of the normalized surface-pressure coefficient is shown and the four chordwise surface-pressure distributions $C_{p,norm}(x/c)$ at the blade-sleeve sections S2-S5 are illustrated. In order to be able to differentiate between the upper and the lower side of the fairing, the curves are marked by "U" and "L", respectively. The evaluation of the chordwise surface-pressure distribution for the reference blade-sleeve fairing shows that the pressure on the upper side is always higher than on the lower side in the front part of the fairing for $x/c < 0.65$, which generates a significant downforce in this region. The sections S2-S4 show a pronounced suction peak on the upper surface of the fairing at $x/c \approx 0.73$, which provides a small amount of lift in this area due to the favorable pressure difference. Furthermore, flow separation is triggered at $x/c = 0.75 - 0.85$ due to a distinct edge in the contour of the reference blade-sleeve fairing. The region of separated flow is indicated by a plateau of constant pressure downstream of $x/c = 0.75$.

Regarding the optimized blade-sleeve fairing, higher pressure levels are observed on the lower side of the fairing, which provides a more favorable pressure difference in terms of lift. As a result, less downforces is generated by the optimized blade-sleeve fairing at this azimuthal blade position. Furthermore, the flow separation onset can be significantly delayed by the new design, especially for the blade-sleeve sections S3 and S4. In terms of pressure recovery, similar values are observed for both blade-sleeve fairings.

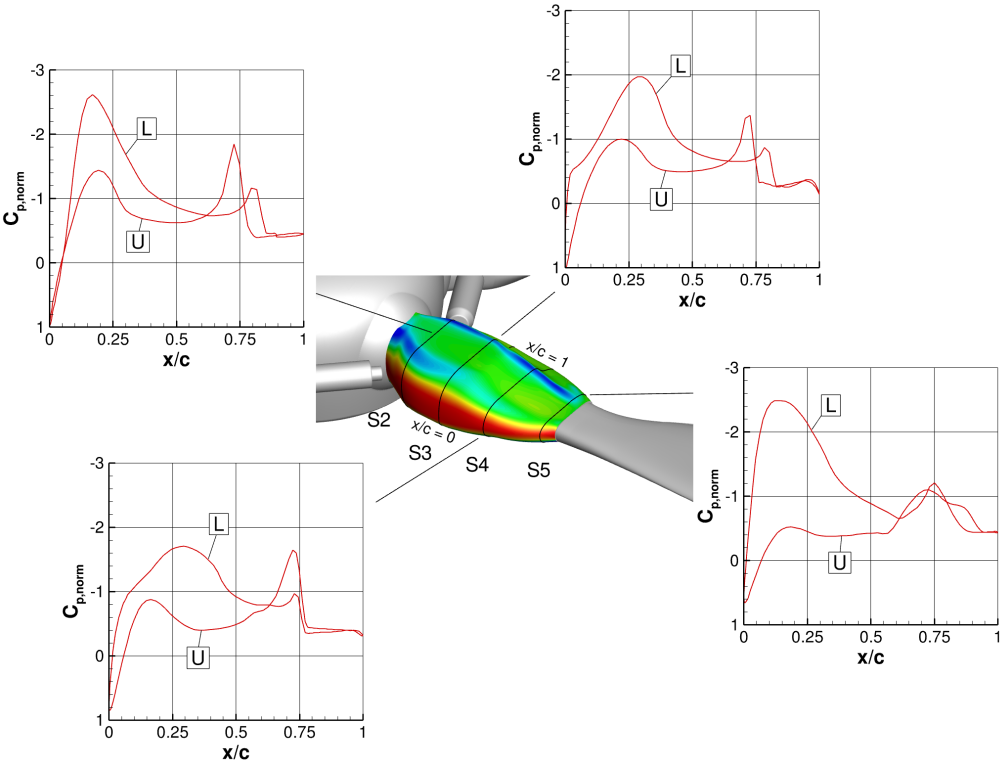

(a) Reference BSF.

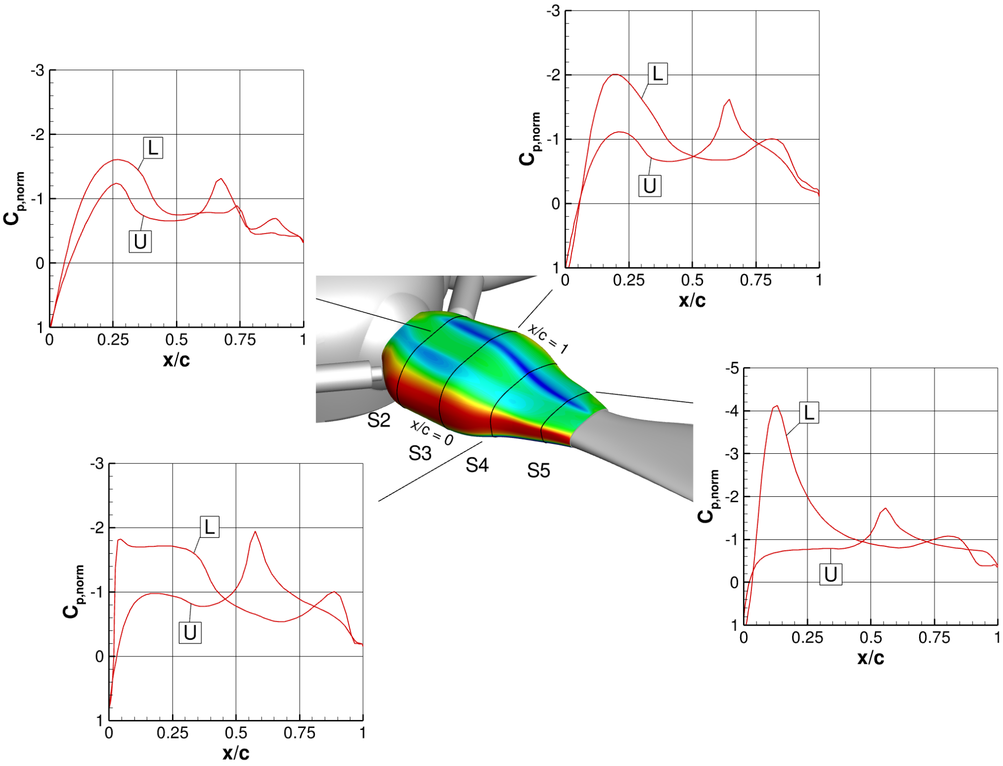

(b) Optimized BSF.

Figure 6.26: Comparison of the instantaneous, normalized surface-pressure distribution $C_{p,norm}$ at the four radial blade-sleeve sections S2-S5 considering the advancing rotor-blade position ($\Psi = 90°$) for the baseline beanie R0H0.

The surface-pressure distribution for the retreating blade case is illustrated in Fig. 6.27. At this azimuthal rotor position, the circumferential speed of the blade-sleeve fairing is much smaller than the cruise speed of the helicopter and therefore, reversed flow occurs in the inboard region. Hence, the dynamic pressure of the incoming flow is reduced on the retreating blade side, which can clearly be seen in the pressure distribution.

Furthermore, the maximum blade-pitch angle is reached at this azimuthal rotor position, which leads to a negative angle of attack for the incoming flow. The reference blade-sleeve fairing shows stronger suction regions in the rear part of the fairing at $x/c \approx 0.75$, which is related to the distinct edges in the contour of the fairing. These low-pressure regions are much weaker on the optimized blade-sleeve fairing. Moreover, the surface pressure distribution on the full-fairing beanie and the spherical junction look very similar for both blade-sleeve fairing designs.

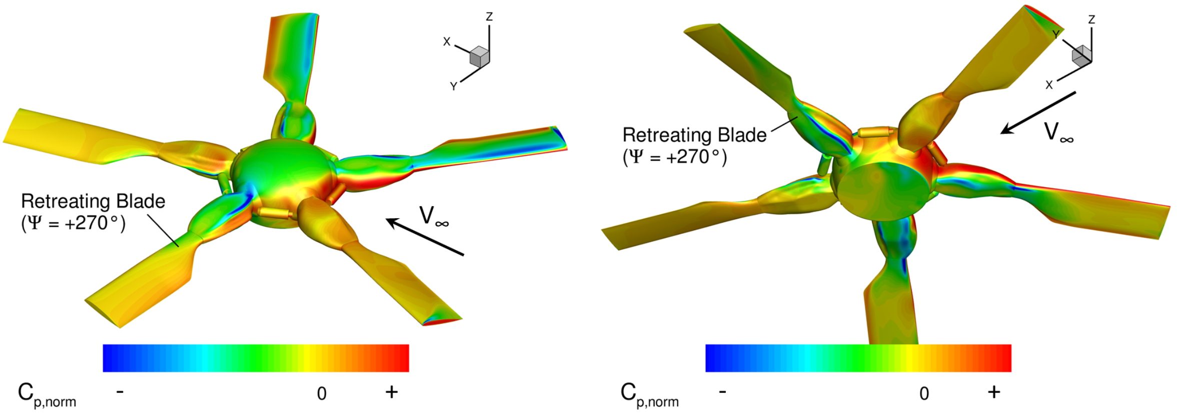

(a) Reference BSF (Top view).

(b) Reference BSF (Bottom view).

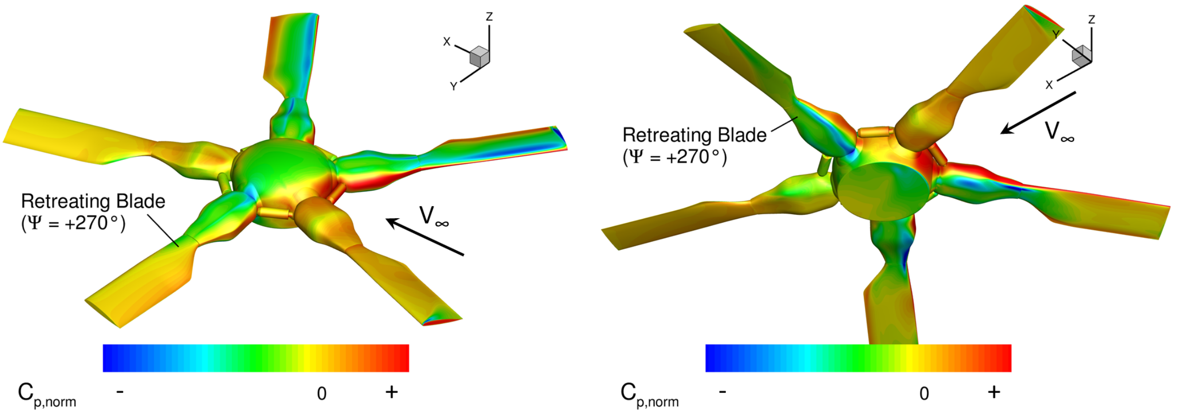

(c) Optimized BSF (Top view).

(d) Optimized BSF (Bottom view).

Figure 6.27: Instantaneous, normalized surface-pressure coefficient $C_{p,norm}$ for the retreating rotor-blade case ($\Psi = 270°$) considering the baseline beanie R0H0 in combination with the reference and the optimized BSF.

The chordwise surface pressure distributions of the blade-sleeve sections S2-S5 are illustrated in Fig. 6.28 for the retreating blade case. Regarding the reference blade-sleeve fairing, the blade-sleeve sections S2 and S3 show two strong suction peaks in the region of $0.75 \leq x/c \leq 0.80$, which are related to the strong curvature of the geometry. The lowest pressure level is observed on the upper surface of section S2 reaching a normalized pressure coefficient of $C_{p,norm} \approx -4.2$. Moreover, a similar minimum pressure is reached on the lower surface of section S3. The weaker suction peak is located on the lower surface for section S2 and on the upper surface for section S3 reaching a similar normalized pressure coefficient of $C_{p,norm} \approx -3.3$.

Regarding blade-sleeve section S4, the minimum pressure is observed on the lower surface at $x/c = 0.7$ with $C_{p,norm} \approx -3.8$. Moreover, the strength of the suction peak on the upper surface of section S4 is significantly reduced in comparison to section S2 and S3. In general, the bottom surface of the blade-sleeve fairing reveals lower pressure levels than the upper surface, which causes a downforce from a global point of view. In contrast to the reference blade-sleeve fairing, the suction peaks in the region $0.65 \leq x/c \leq 0.80$ are much weaker for the optimized blade-sleeve fairing considering the normalized pressure distributions of the blade-sleeve sections S2-S4. As an example, section S2 shows a reduced suction peak on the upper surface at $x/c = 0.75$ with a normalized pressure coefficient of $C_{p,norm} \approx -2.0$, which is about 52 % less than for the reference blade-sleeve fairing. Moreover, both blade-sleeve fairing designs exhibit similar pressure levels at $x/c = 0$ for the sections S4 and S5, which indicates comparable pressure recovery.

Regarding section S2, an improved pressure recovery is predicted by the optimized blade-sleeve fairing showing a normalized pressure difference of $\Delta C_{p,norm} \approx +0.6$. Furthermore, a pressure jump can be observed at $x/c \approx 0$ for section S3 on the optimized blade-sleeve fairing, which is related to a vortical flow structure separating from the fairing and interacting with the surface in this region at the current time step.

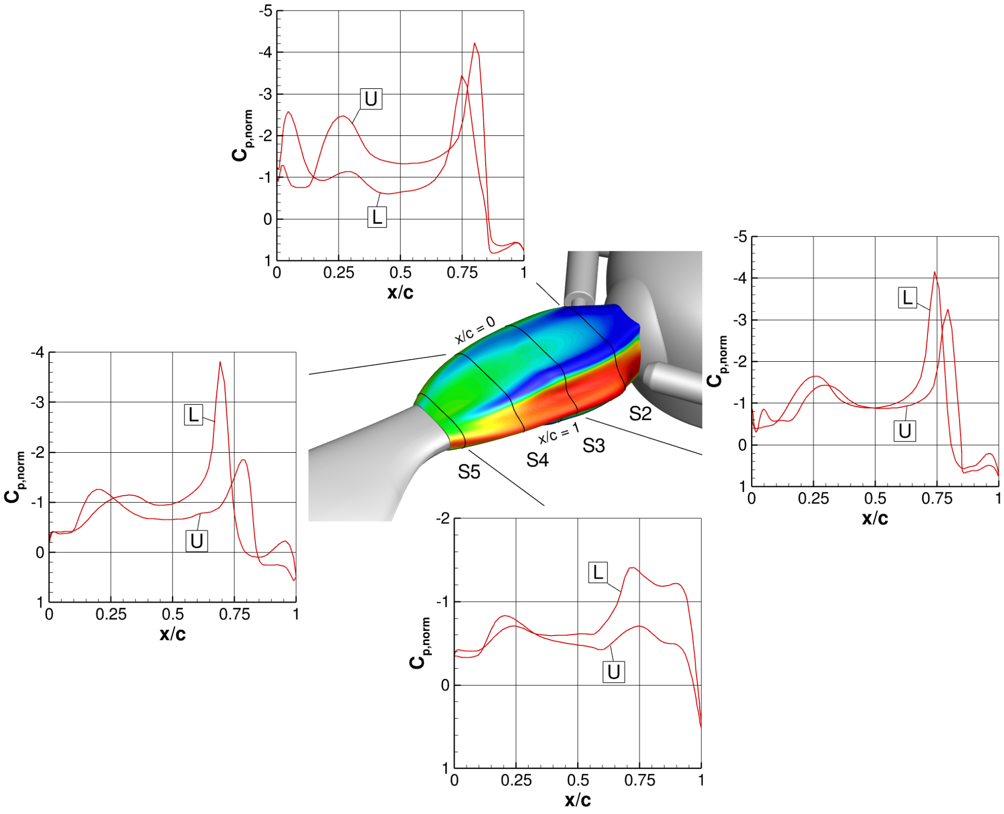

(a) Reference BSF.

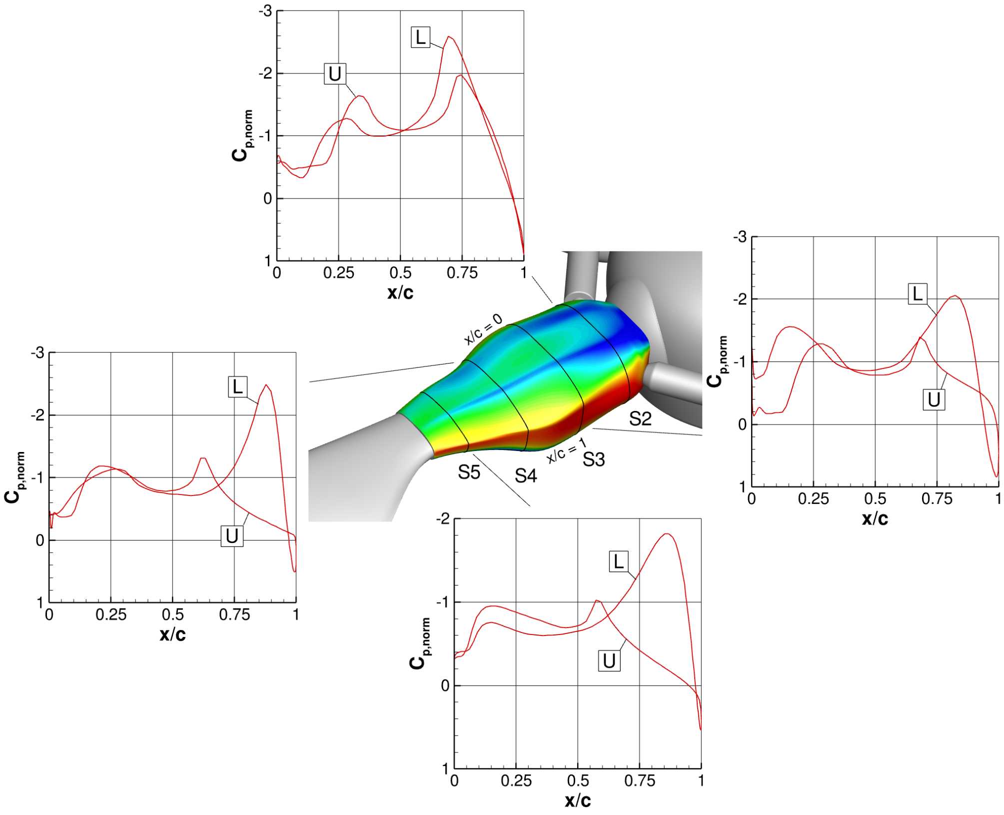

(b) Optimized BSF.

Figure 6.28: Comparison of the instantaneous, normalized surface-pressure distribution $C_{p,norm}$ at the four radial blade-sleeve sections S2-S5 considering the retreating rotor-blade position ($\Psi = 270°$) for the baseline beanie R0H0.

The comparison of the surface-pressure distribution between the baseline rotor head with beanie R0H0 and the rotor head with the enlarged beanie R1H1 is exemplarily shown for an upstream pointing rotor blade, which corresponds to an azimuthal rotor position of $\Psi = 180°$. Figure 6.29 shows the instantaneous, normalized surface-pressure distribution for the baseline beanie R0H0 in combination with the optimized as well as the reference blade-sleeve fairing. Furthermore, the top and the bottom view of the rotor head are given and the inflow direction is marked by the velocity vector V_∞.

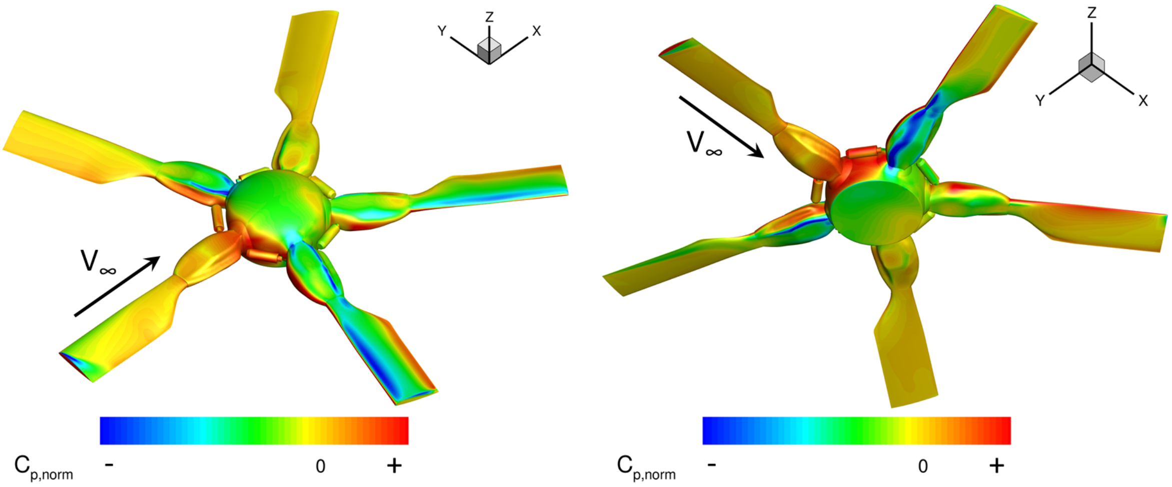

(a) Reference BSF (Top view).

(b) Reference BSF (Bottom view).

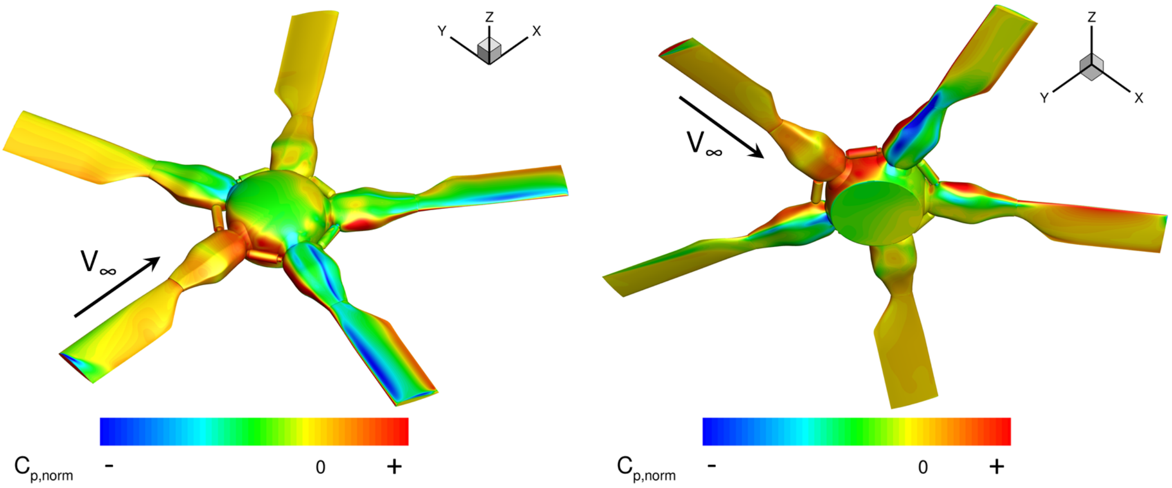

(c) Optimized BSF (Top view).

(d) Optimized BSF (Bottom view).

Figure 6.29: Instantaneous, normalized surface-pressure coefficient $C_{p,norm}$ for an upstream pointing rotor blade ($\Psi = 180°$) considering the baseline beanie R0H0 in combination with the reference and the optimized BSF.

The corresponding pressure distribution for the rotor head with the enlarged beanie R1H1 is given in Fig. 6.30. It can be seen that the blade-sleeve fairings in the front sector of the rotor disk, which is defined by $90° \leq \Psi \leq 270°$, show only minor differences in the pressure distribution compared to the baseline rotor head.

However, the blade-sleeve fairings in the wake region of the full-fairing beanie are clearly impacted by the increased cross section. The blade-sleeve fairing that is located at $\Psi = 36°$ shows lower pressure levels on the leading edge in the inboard region, which can be related to the reduced dynamic pressure in the wake-flow field of the larger full-fairing beanie and the preceding rotor blade. The evaluation of the flow field shows that there is a region of separated and reversed flow, where the blade-sleeve fairing is passing through. Moreover, this effect seems to be bigger for the optimized blade-sleeve fairing, which can be seen in Fig. 6.30c and Fig. 6.30d.

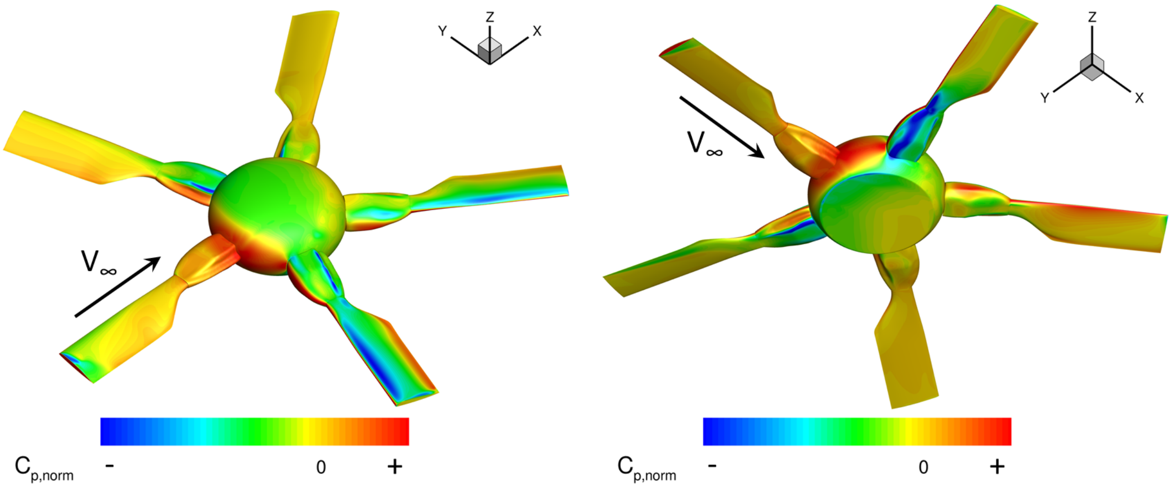

(a) Reference BSF (Top view).

(b) Reference BSF (Bottom view).

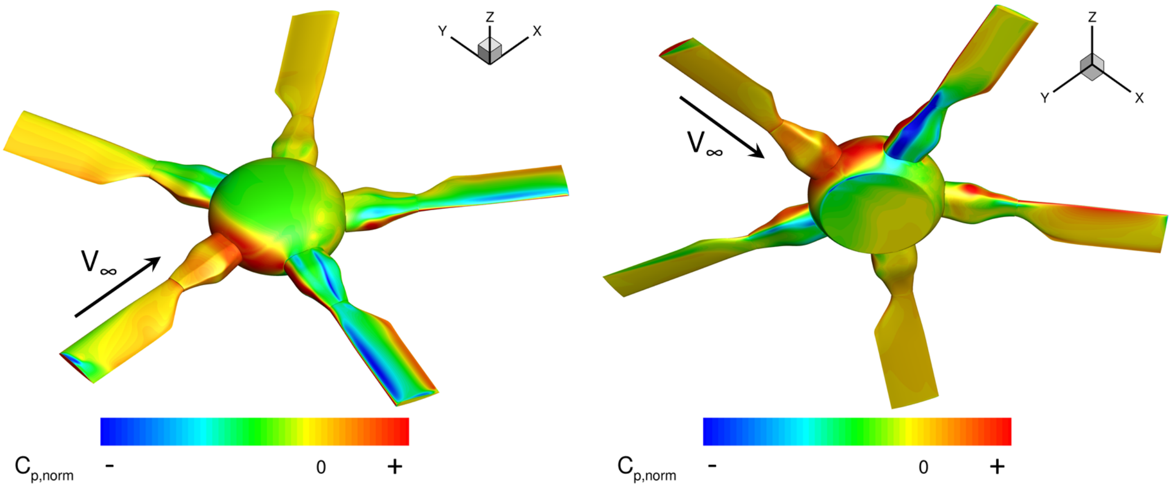

(c) Optimized BSF (Top view).

(d) Optimized BSF (Bottom view).

Figure 6.30: Instantaneous, normalized surface-pressure coefficient $C_{p,norm}$ for an upstream pointing rotor blade ($\Psi = 180°$) considering the enlarged beanie R1H1 in combination with the reference and the optimized BSF.

6.4.3 Flow-field Quantities

Within this section, selected flow-field quantities are presented to give an impression of the prevailing flow field in the vicinity of the isolated rotor head. For this purpose, the flow simulation results of the rotor head with the optimized blade-sleeve fairing are directly compared to the ones obtained for the reference blade-sleeve fairing. Figure 6.31 illustrates the instantaneous, normalized axial flow velocity u/V_∞ in equally spaced cross sections that are located in the wake-flow field of the isolated rotor head. In order to limit the visualization of the axial flow velocity to a relevant range, all values above $0.99 \cdot u/V_\infty$ are cut off. Hence, the velocity deficit that is introduced by the isolated rotor head can directly be seen. Furthermore, the flow field of the baseline rotor head (Beanie R0H0) is depicted in Fig. 6.31a for the reference blade-sleeve fairing and in Fig. 6.31b for the optimized blade-sleeve fairing. Additionally, the corresponding flow simulation results for the larger beanie R1H1 are illustrated in Fig. 6.31c and Fig. 6.31d, respectively. Regions of stagnated or even reversed flow can be identified by dark blue areas in the cross sections. It can be seen that flow separation occurs on the aft-port side of the beanie and close to the blade-sleeve fairing of the advancing rotor blade.

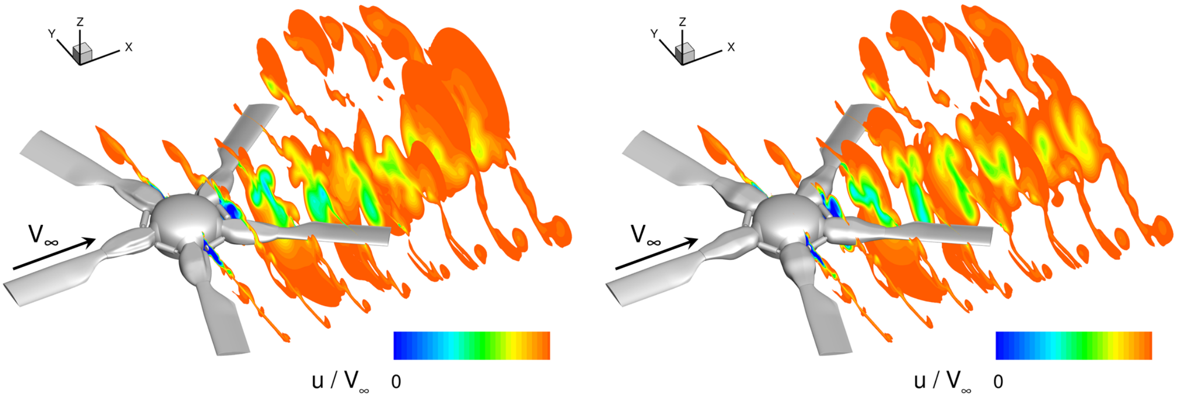

(a) Beanie R0H0 with the reference BSF. (b) Beanie R0H0 with the optimized BSF.

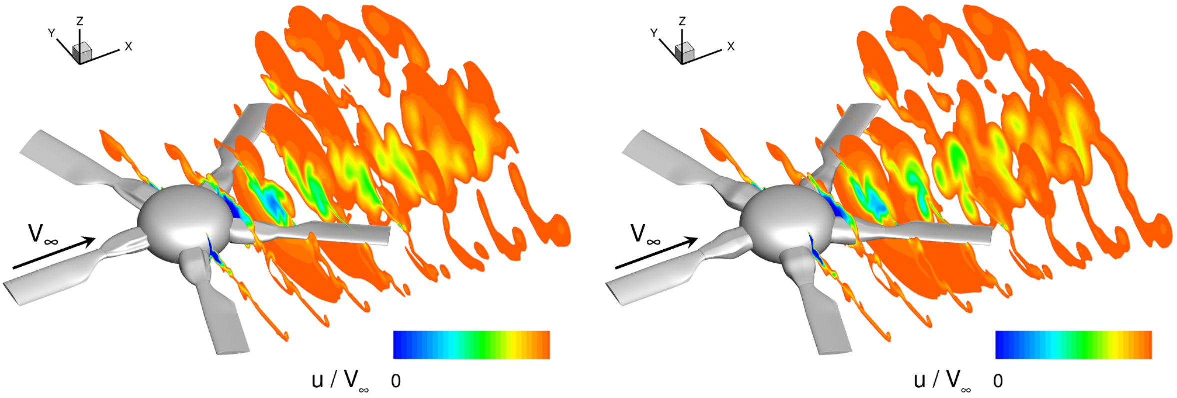

(c) Beanie R1H1 with the reference BSF. (d) Beanie R1H1 with the optimized BSF.

Figure 6.31: Instantaneous, normalized axial flow velocity u/V_∞ shown in equally spaced cross-sections in the wake region of the rotor head. Flow-velocities above $0.99 \cdot u/V_\infty$ are cut off.

Moreover, due to the increased size of beanie R1H1, a more pronounced velocity deficit is observed in the third cross section in comparison to the rotor head with the baseline beanie R0H0. The shape of the blade-sleeve fairing seems to have less impact on the axial flow-velocity recovery.

Figure 6.32 illustrates the instantaneous, normalized axial vorticity $\omega_x \cdot R/V_\infty$ for all investigated full-fairing combinations in equally spaced cross sections along the flow direction. A large number of vortical flow structures and discrete vortices can be seen in the wake region of the full-fairing beanie. Furthermore, the blade tip vortices of the advancing and the upstream pointing rotor blade can clearly be observed. Based on the azimuthal rotor position, the blade-tip vortex of the preceding rotor blade is interacting differently with the rotor blade in the advancing blade region, which locally changes the surface pressure distribution. Therefore, the blade-vortex interaction in the advancing blade region is depending on the rotor-blade length considering the same cruise speed of the helicopter and the same rotational speed of the main rotor. Regarding the vortical flow structures in the wake region of the full-fairing beanie, strong interactions can be observed and the axial vorticity is rapidly decreasing in downstream direction.

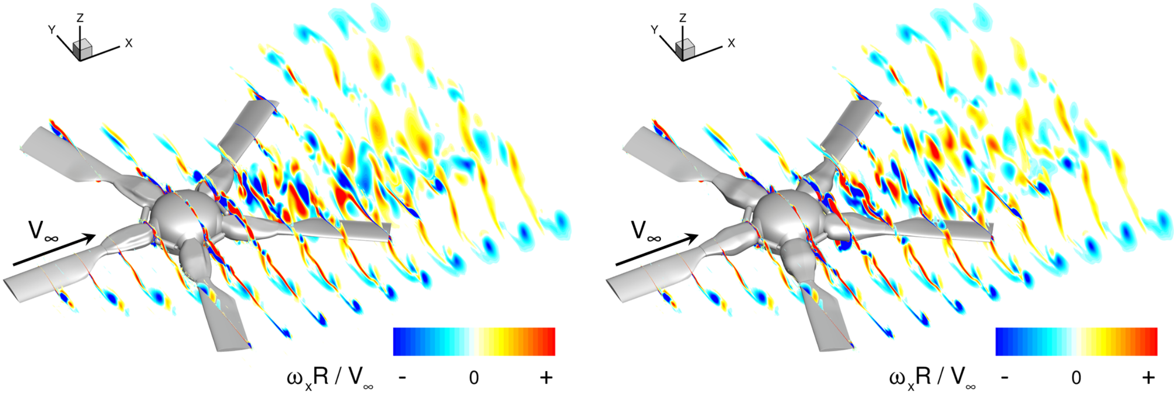

(a) Beanie R0H0 with the reference BSF. (b) Beanie R0H0 with the optimized BSF.

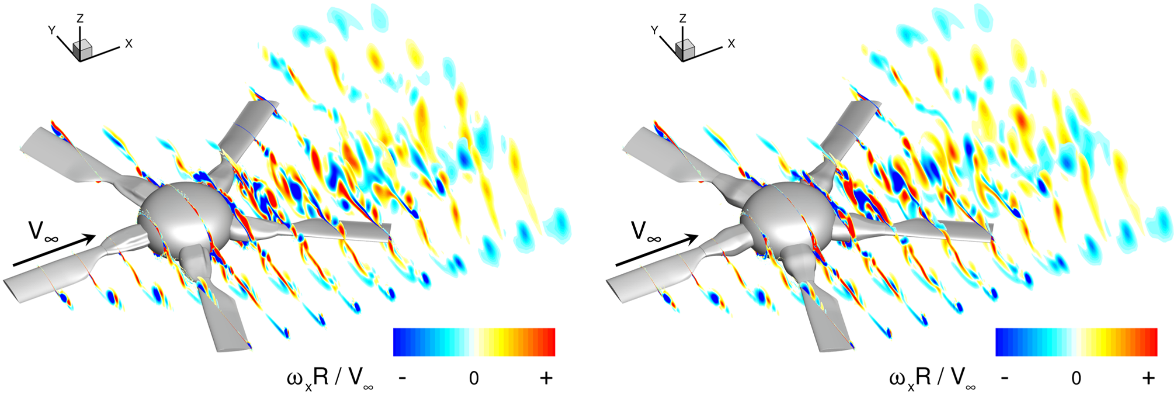

(c) Beanie R1H1 with the reference BSF. (d) Beanie R1H1 with the optimized BSF.

Figure 6.32: Instantaneous, normalized axial vorticity $\omega_x \cdot R/V_\infty$ shown in equally spaced cross-sections along the flow direction.

In order to complement the flow-field analysis, the Q-criterion is used to visualize vortical flow structures. This vortex identification criterion allows to better understand the dynamics of the flow field and it enables the identification of coherent flow structures. For the present flow problem, an iso-surface of the Q-criterion with an iso-value of $Q = 2000\,s^{-2}$ is used and the iso-surface is colored by the normalized axial flow velocity u/V_∞, which can be seen in Fig. 6.33 for all investigated rotor-head fairing variants. The Q-criterion allows to demonstrate the complexity of the highly turbulent rotor-head wake-flow field. Furthermore, the flow separation on the aft-port side of the beanie can clearly be identified. Regions with high axial flow velocity are indicated by the red-colored iso-surfaces and stagnated or reversed flow is characterized by blue-colored regions. Moreover, the blade-tip vortices of the advancing and the upstream facing rotor blade are well captured by the Q-criterion. The evaluation of the flow field for the rotor head with the larger beanie R1H1 and the optimized blade-sleeve fairing, which is depicted in Fig. 6.33d, shows that the flow separation in the transition region between the advancing blade-sleeve fairing and the beanie generates bigger coherent flow structures in comparison to the remaining full-fairing candidates.

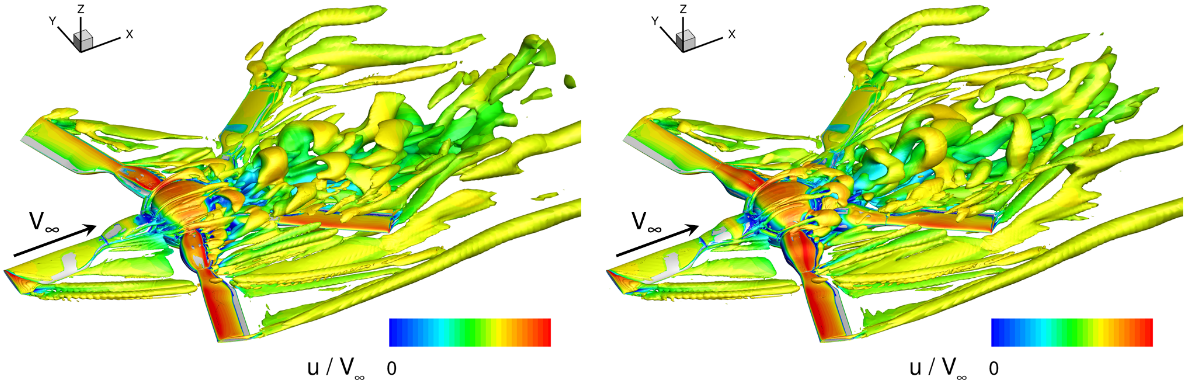

(a) Beanie R0H0 with the reference BSF. (b) Beanie R0H0 with the optimized BSF.

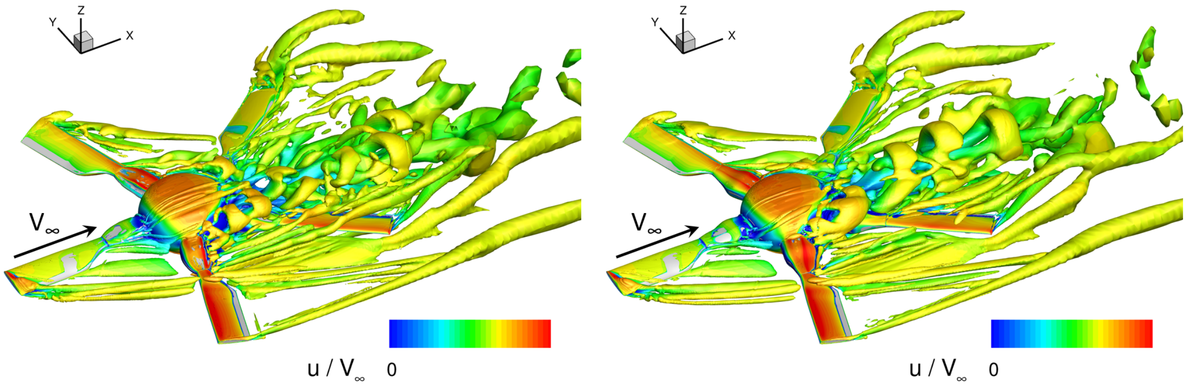

(c) Beanie R1H1 with the reference BSF. (d) Beanie R1H1 with the optimized BSF.

Figure 6.33: Iso-surface of the Q-criterion ($Q = 2000\,s^{-2}$), which is colored by the normalized axial flow velocity u/V_∞.

6.5 Results and Analysis - RACER Compound Helicopter

The isolated rotor-head investigations of the optimized fairing reveal promising results in terms of aerodynamic performance improvement. In order to determine the actual performance benefit that can be expected by the newly developed rotor-head fairing on the RACER demonstrator, unsteady numerical flow simulations are conducted for the full compound helicopter configuration. The investigated flight condition represents a steady, sea-level cruise flight with 220 knots. Furthermore, a moving rotor head is considered and the cyclic blade-pitch motion is set according to a trimmed flight condition. Overall, three different configurations of the RACER demonstrator are examined. The reference configuration comprises the baseline beanie R0H0 in combination with the reference blade-sleeve fairing. The two remaining full-fairing configurations feature the optimized blade-sleeve fairing together with the baseline beanie R0H0 and the larger beanie R1H1, respectively. In the present work, the full-fairing rotor head with the optimized blade-sleeve fairing and the baseline beanie R0H0 is referred to as configuration C1. Moreover, configuration C2 features the larger beanie R1H1 and the optimized blade-sleeve fairing. The integration of beanie R1H1 requires an adaptation of the pylon fairing in terms of shape and size, which has also been performed in the course of the present thesis.

Regarding the analyses of the flow simulation results, the focus is set on the evaluation of the aerodynamic forces and moments. For this purpose, the transient and the mean quantities are examined and compared to each other. Furthermore, a Fourier analysis is performed to determine the dominant frequencies and amplitudes acting on the main-rotor head. Additionally, the surface-pressure distributions of the investigated configurations are compared to each other and the main differences are highlighted. Finally, selected flow-field quantities are presented to demonstrate the main flow features and to illustrate the impact of the full-fairing rotor head geometry on the wake-flow field of the helicopter.

6.5.1 Aerodynamic Forces and Moments

Regarding the present analysis, lift and drag are taken into account to characterize the cruise flight performance of the RACER demonstrator. Moreover, the main-rotor driving torque is evaluated as an additional implicit measure for the rotor-head drag. However, the driving torque of the main rotor is reduced by one order of magnitude in comparison to the isolated rotor-head investigations, which makes this quantity less meaningful for the evaluation of the rotor head performance. Due to the low absolute values of the main-rotor driving torque, larger relative differences between the investigated configurations are observed, which are not significant for the overall performance of the rotor-head fairing. The rolling moment M_x, the pitching moment M_y and the yawing moment M_z of the core geometry are not considered in the present investigations, because the actual design center of gravity is not known to the author. In order to ensure a converged solution for each of the investigated configurations, a total number of six rotor revolutions is simulated. Furthermore, the flow simulation results are averaged over the final three rotor revolutions to provide mean values that can be compared to each other. The core geometry of the RACER demonstrator comprises all components except the main rotor and the lateral rotors. The applied moment reference point is located on the main-rotor axis and it is illustrated in Fig. 6.14. Regarding the evaluation of the rotor-head moments, the pitching and the rolling moment are less important for the present work and they are not representative due to the truncated rotor blades. Therefore, the main-rotor driving torque is the only moment that is evaluated for the aerodynamic characterization of the rotor-head fairings.

The transient aerodynamic forces and the main-rotor driving torque are illustrated in Fig. 6.34 for the final rotor revolution. In addition, a direct comparison between the three investigated configurations is given. The solid lines show the 5/rev-periodic force history and the dashed lines of the same color show the respective mean values. All quantities are normalized by the average values of the reference configuration. The normalized lift $L/|L_{Ref.}|$ is depicted in Fig. 6.34a. It can be seen that configuration C1 provides a lift increase of $\Delta L = +1.29\,\%$ compared to the reference configuration. Regarding configuration C2, the lift is only slightly increased by $\Delta L = +0.23\,\%$. In terms of drag, the biggest improvement is obtained for configuration C2 yielding a drag reduction of $\Delta D = -4.07\,\%$ in comparison to the reference configuration. Moreover, configuration C1 reveals a drag reduction of $\Delta D = -1.37\,\%$ in combination with increased lift. Hence, even lower drag values can be expected for configuration C1 considering the same level of lift for all configurations. Regarding the side force F_y, the main contributors are given by the vertical stabilizers, the cabin and the pylon fairing. The vertical stabilizers of the RACER demonstrator are designed to counteract a large portion of the main-rotor driving torque during cruise flight, which means that a significant negative side force is generated for the clockwise rotating rotor head in the given coordinate system.

Figure 6.34c shows the normalized side force $F_y/|F_{y,Ref.}|$ for the investigated full-fairing configurations. The differences in the side force are mainly related to interference effects with the core geometry, because the changes in the direct contribution of the rotor-head are less significant. Regarding configuration C1, the negative side force is reduced by $\Delta F_y = 19.14\,\%$ and configuration C2 reveals an increased normalized side force of $F_y/|F_{y,Ref.}| = -1.26$. Furthermore, the comparison of the normalized main-rotor moment $M_z/|M_{z,Ref.}|$ is illustrated in Fig. 6.34d. Due to the low reference value, high amplitudes are observed in the transient solution for all configurations. Regarding the mean values, configuration C1 shows an increased main-rotor moment of $M_z/|M_{z,Ref.}| = 1.50$ and configuration C2 reaches $M_z/|M_{z,Ref.}| = 1.57$. However, the changes in the absolute values are negligible compared to the magnitude of lift and drag.

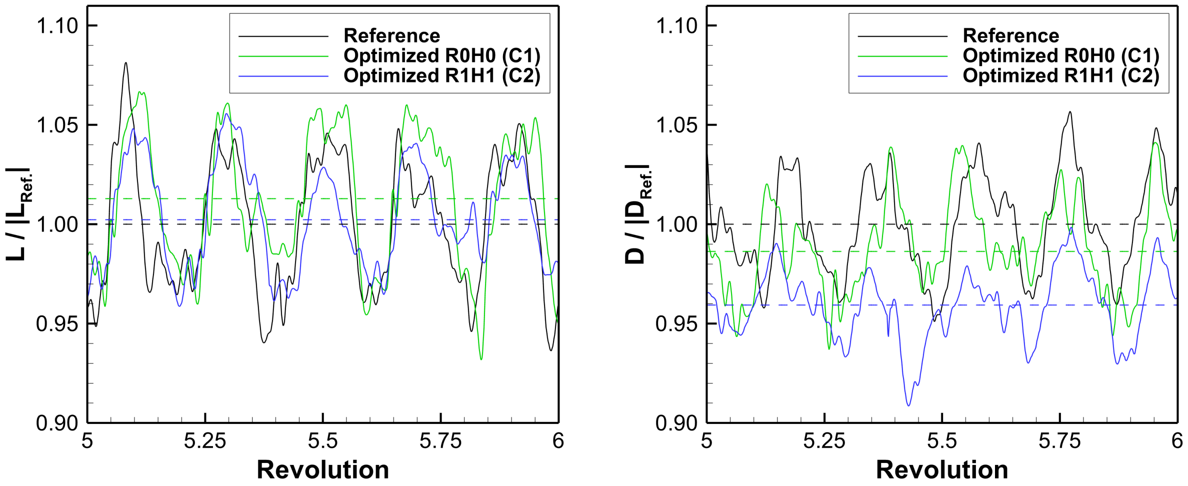

(a) Normalized Lift L / $|L_{Ref.}|$. (b) Normalized Drag D / $|D_{Ref.}|$.

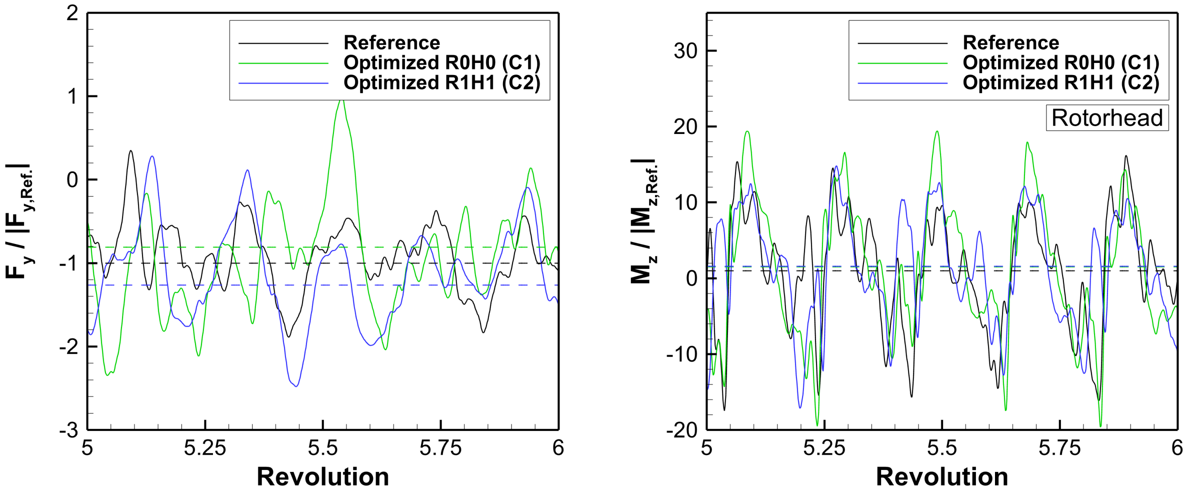

(c) Normalized Sideforce F_y / $|F_{y,Ref.}|$. (d) Normalized Moment M_z / $|M_{z,Ref.}|$.

Figure 6.34: Evaluation of the total aerodynamic forces and the main-rotor moment M_z for a single rotor revolution showing a direct comparison between the configurations C1, C2 and the reference configuration. All quantities are normalized by the average values of the reference configuration.

The evaluation of the aerodynamic forces and the main-rotor moment is summarized in Tab. 6.6 showing the relative differences to the reference configuration. Regarding the side force, the differences are given as a percentage of the magnitude. Hence, configuration C1 generates a lower and configuration C2 a higher negative side force.

Configuration	**ΔL** [%]	**ΔD** [%]	$\|\mathbf{\Delta F_y}\|$ [%]	$\mathbf{\Delta M_z}$ [%]
Ref. (Beanie R0H0 & Reference BSF)		Reference		
C1 (Beanie R0H0 & Optimized BSF)	+1.29 %	-1.37 %	-19.14 %	+50.36 %
C2 (Beanie R1H1 & Optimized BSF)	+0.23 %	-4.07 %	+26.23 %	+56.94 %

Table 6.6: Comparison of the mean, total aerodynamic forces and the main-rotor moment M_z for the investigated rotor-head fairings.

Within the next step, the aerodynamic forces of the core geometry and the rotor head are evaluated independently of each other. Therefore, the contribution of the rotor head and its impact on the core geometry can be determined. The transient forces and the corresponding mean values are illustrated in Fig. 6.35 showing the final rotor revolution. The forces are normalized by the average value of the respective reference component. The normalized lift of the core geometry is depicted in Fig. 6.35a and it can be seen that the impact of the rotor-head fairing on the core geometry is quite limited. Regarding configuration C1, a slight reduction of lift of $\Delta L = -0.52\,\%$ is obtained and configuration C2 shows a minor lift increase of $\Delta L = +0.31\,\%$. The evaluation of the rotor-head lift shows a significant lift-increase of $\Delta L = +16.73\,\%$ for configuration C1, which is illustrated in Fig. 6.35b. Furthermore, the larger full-fairing beanie R1H1 on configuration C2 reduces the rotor-head lift by $\Delta L = -0.42\,\%$.

The normalized drag is given in Fig. 6.35c and Fig. 6.35d, respectively. Concerning the core geometry, a drag reduction of $\Delta D = -1.25\,\%$ is obtained for configuration C1 and a drag increase of $\Delta D = +1.60\,\%$ is observed for configuration C2, which is mainly caused by the larger pylon fairing. However, the analysis of the rotor-head drag shows that configuration C2 achieves a normalized drag value of $D/|D_{Ref.}| = 0.804$, whereas configuration C1 reaches only a minor drag reduction with $D/|D_{Ref.}| = 0.983$. Furthermore, the normalized side force $F_y/|F_{y,Ref.}|$ is illustrated in Fig. 6.35e and Fig. 6.35f, respectively. Regarding the core geometry, configuration C1 reduces the side force by 12.5 % and configuration C2 increases the side force by 24.6 % percent. In contrast, both configurations with the optimized blade-sleeve fairing (C1 & C2) reveal a similar side force for the rotor-head, which is approximately 17.3 % higher than for the reference rotor head.

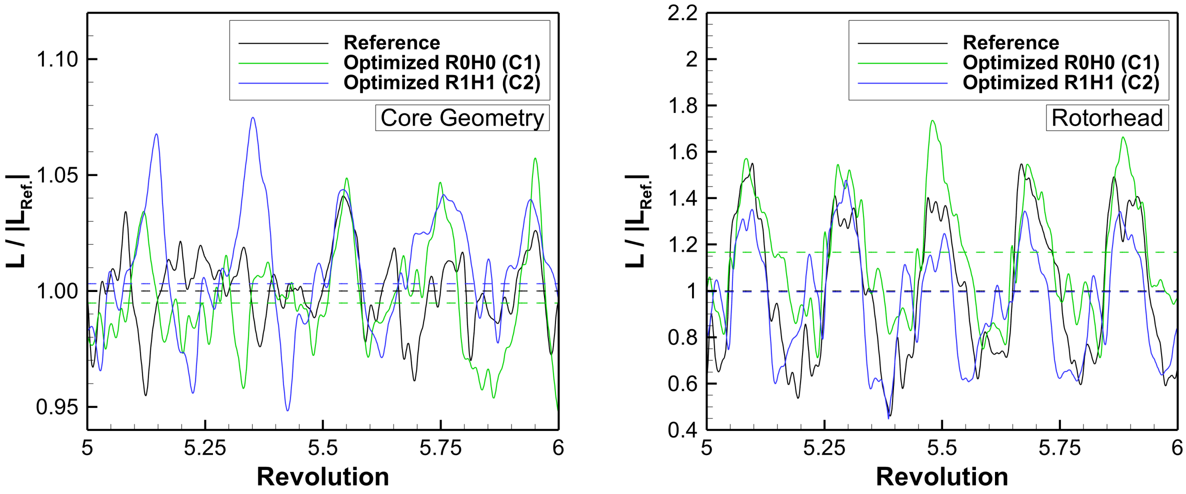

(a) Normalized Lift - Core Geometry. (b) Normalized Lift - Rotor Head.

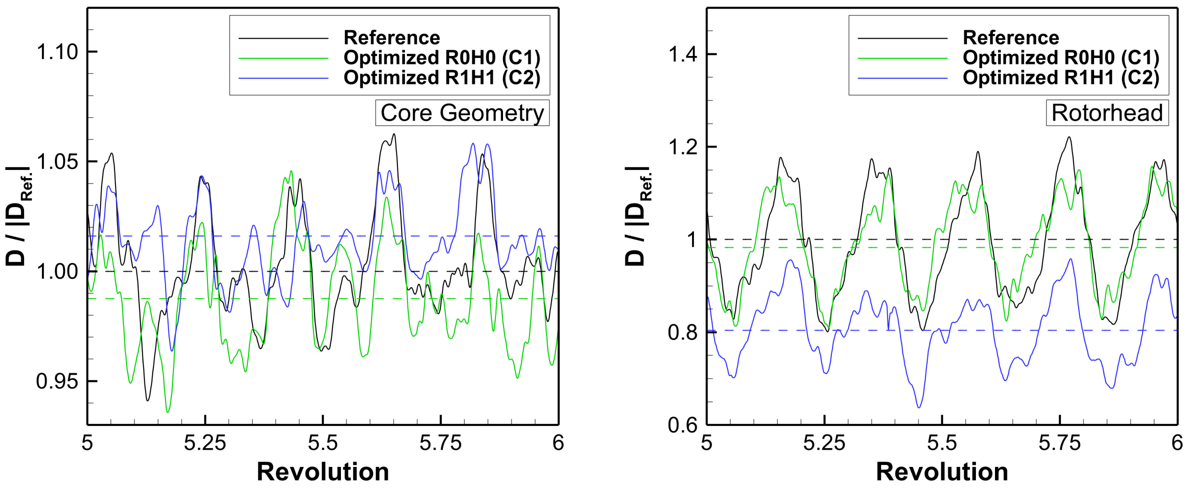

(c) Normalized Drag - Core Geometry. (d) Normalized Drag - Rotor Head.

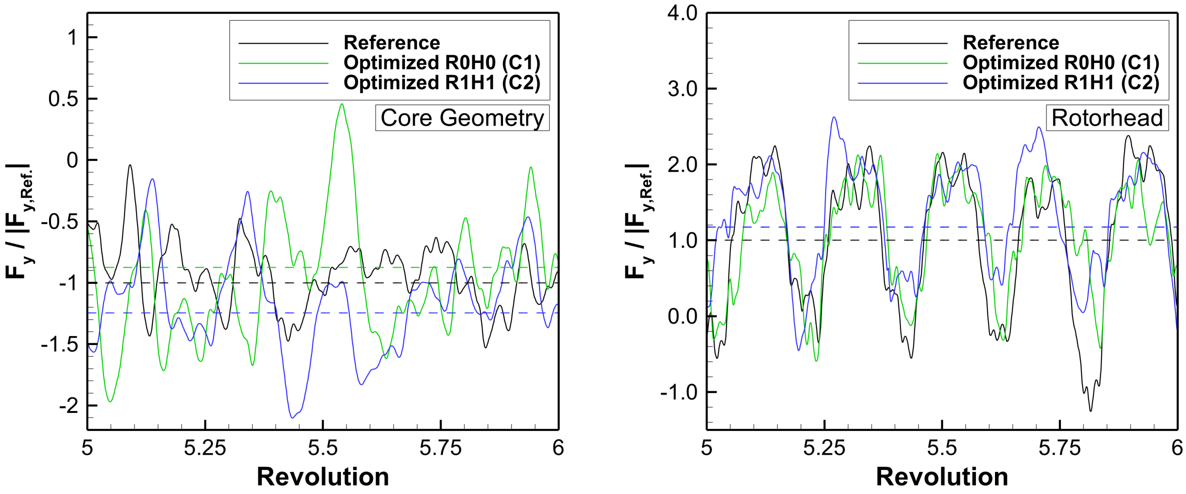

(e) Normalized Sideforce - Core Geometry. (f) Normalized Sideforce - Rotor Head.

Figure 6.35: Evaluation of the component forces for the core geometry and the rotor head showing the transient results for a single rotor revolution. A comparison between the configurations C1, C2 and the reference configuration is given. All quantities are normalized by the average values of the respective component forces of the reference configuration.

In order to determine the impact of the rotor-head fairing on the unsteady aerodynamic loads, a fast Fourier transformation (FFT) is performed for lift and drag of the investigated rotor heads. The spectra of the selected rotor-head forces are illustrated in Fig. 6.36. The amplitudes are normalized by the average values of the reference rotor head and the frequency is given in multiples of the blade-passing frequency (BPF). The frequency domains for the reference configuration are depicted in Fig. 6.36a and Fig. 6.36b, respectively. Regarding lift, the reference rotor head shows relevant amplitudes within the frequency range of $1 \leq f/BPF \leq 4$. At the first BPF, the reference rotor head reaches a normalized lift of $|L(f)|/|L_{Ref.}| = 0.410$. Furthermore, the amplitudes of the second, third and fourth harmonic lie within a range of $0.056 \leq |L(f)|/|L_{Ref.}| \leq 0.081$. In terms of drag, the first harmonic of the BPF is the main contributor to the unsteady aerodynamic loads reaching an amplitude of $|D(f)|/|D_{Ref.}| = 0.160$. Moreover, higher harmonics reveal normalized drag values below $2\,\%$ of the reference drag.

The frequency domain for the rotor-head lift of configuration C1 is illustrated in Fig. 6.36c. In comparison to the reference rotor head, the amplitude at the first BPF is reduced to $|L(f)|/|L_{Ref.}| = 0.336$. However, the second harmonic shows a slightly increased amplitude of $|L(f)|/|L_{Ref.}| = 0.107$, which is about $62\,\%$ higher than for the reference rotor head. Moreover, the amplitudes of the third and fourth harmonic lie within the range of $0.039 \leq |L(f)|/|L_{Ref.}| \leq 0.060$. The FFT of the rotor-head drag for configuration C1 is shown in Fig. 6.36d and it can be seen that the amplitude of the first BPF harmonic is reduced to $|D(f)|/|D_{Ref.}| = 0.129$. Furthermore, no relevant contribution of higher harmonics can be observed for configuration C1.

Regarding the normalized lift of configuration C2, the first, the second and the fourth BPF harmonic show noticeable amplitudes, which can be seen in Fig. 6.36e. The normalized lift at $f/BPF = 1$ reaches an amplitude of $|L(f)|/|L_{Ref.}| = 0.326$, which is about $19\,\%$ lower than for the reference rotor head. The second and the fourth harmonic reveal amplitudes of $|L(f)|/|L_{Ref.}| = 0.090$ and $|L(f)|/|L_{Ref.}| = 0.067$, respectively. Additionally, the spectrum of the rotor-head drag is illustrated in Fig. 6.36f. Similar to the other configurations, the first harmonic of the BPF is the only frequency causing a relevant amplitude. The normalized drag value reaches an amplitude of $|D(f)|/|D_{Ref.}| = 0.083$ at $f/BPF = 1$, which is about $48\,\%$ lower than for the reference configuration. Hence, the rotor-head fairing of configuration C2 even further reduces the unsteady loads in comparison to configuration C1. Moreover, the higher harmonics do not show noticeable contributions in terms of drag oscillations.

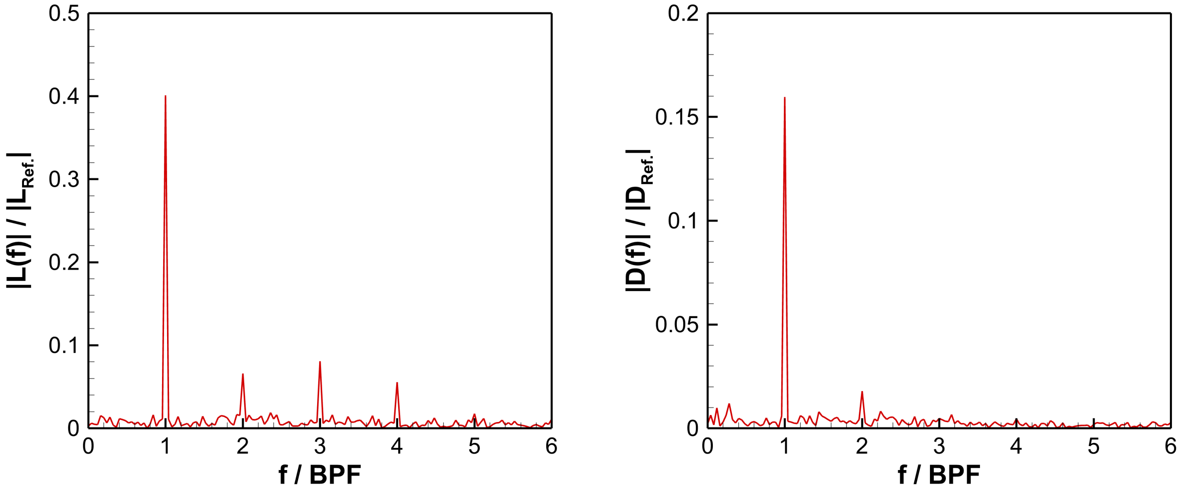

(a) Reference Configuration - RH Lift.

(b) Reference Configuration - RH Drag.

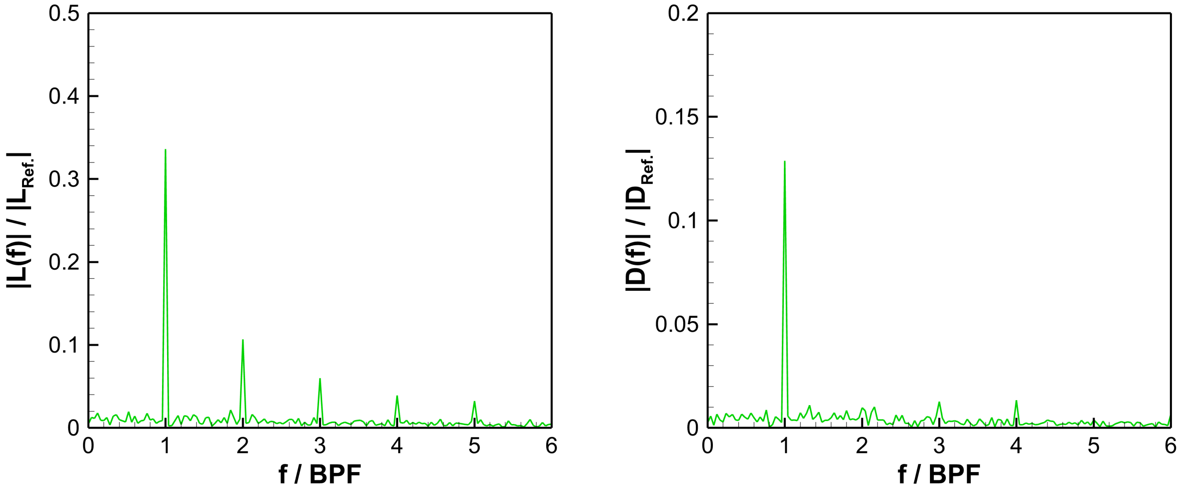

(c) Configuration C1 - RH Lift.

(d) Configuration C1 - RH Drag.

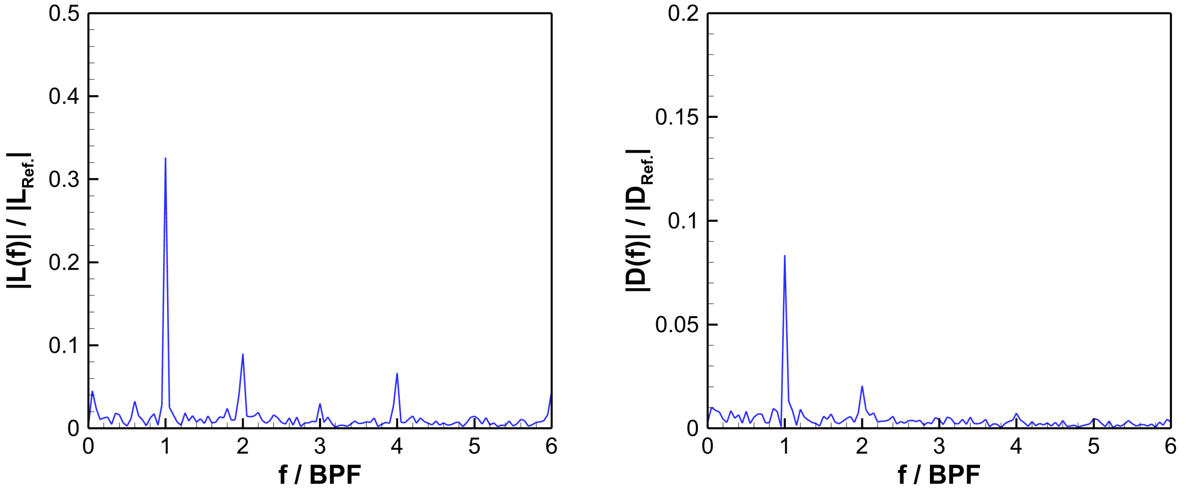

(e) Configuration C2 - RH Lift.

(f) Configuration C2 - RH Drag.

Figure 6.36: Analysis of the rotor-head (RH) lift and drag spectrum showing a comparison between the reference configuration, configuration C1 and configuration C2.

A summary about the main results of the FFT analysis is given in Tab. 6.7. The normalized lift and drag contributions are shown for the first five BPF harmonics allowing for a direct comparison between the investigated configurations. It can be seen that the amplitudes of the force oscillations at $f/BPF = 1$ are significantly reduced by the optimized blade-sleeve fairing. Furthermore, configuration C2 introduces less vibrations than configuration C1 at the first BPF harmonic, especially in terms of drag. The amplitudes of the force oscillations are reduced with increasing frequency and the contribution of higher harmonics above $f/BPF = 2$ is in the order of magnitude of $0 < |L(f)|/|L_{Ref.}| \leq 0.067$ for lift and $0 < |D(f)|/|D_{Ref.}| \leq 0.013$ for drag.

	$\mathbf{|L(f)| / |L_{Ref.}|}$			$\mathbf{|D(f)| / |D_{Ref.}|}$		
f/BPF	Reference	Config. C1	Config. C2	Reference	Config. C1	Config. C2
1	0.401	0.336	0.326	0.160	0.129	0.083
2	0.066	0.107	0.090	0.018	0.010	0.021
3	0.081	0.060	0.030	0.005	0.013	0.004
4	0.056	0.039	0.067	0.005	0.013	0.007
5	0.018	0.032	0.015	0.002	0.004	0.005

Table 6.7: Summary of the FFT analysis regarding lift and drag of the rotor head comparing the configurations C1 and C2 to the reference configuration.

6.5.2 Surface Quantities

In this section, the surface-pressure distributions of the investigated compound helicopter configurations are evaluated and compared to each other to complement the analyses of the aerodynamic forces and moments. The results are exemplarily shown for a single rotor-blade position corresponding to the upstream pointing rotor blade ($\Psi = 180°$). Hence, the variation of the instantaneous, local surface-pressure distribution in dependency of the azimuthal rotor position is not discussed within the present thesis. Nevertheless, for the selected rotor blade position, the main differences between the three configurations are elaborated and the impact of the rotor-head fairing on the surface-pressure distribution is demonstrated.

The comparison of the instantaneous surface-pressure distribution for the three investigated configurations is depicted in Fig. 6.37 showing the front view of the helicopter. Besides the global view on the entire helicopter, a detailed view on the rotor head is given. Moreover, the surface-pressure coefficient is normalized by a certain reference value leading to $C_{p,norm}$. The color map of the contour plot allows to determine regions of negative and positive pressure coefficients without disclosing actual pressure values. The comparison of the surface-pressure distribution between the reference configuration and configuration C1 reveals almost no differences on the core geometry. However, minor discrepancies can be determined in the rear part of the pylon fairing.

Furthermore, the biggest differences are observed on the full-fairing beanie and the blade-sleeve fairings. Regarding configuration C1, the advancing blade-sleeve fairing, which is located at $\Psi = 108°$ in Fig. 6.37b, shows partially lower pressure values on the upper surface of the fairing. Additionally, higher pressure levels are observed on the leading edge of the trailing blade-sleeve fairing ($\Psi = 36°$), which is passing through the wake of the full-fairing beanie and the preceding rotor blade. The upstream pointing rotor blade shows an almost identical pressure distribution on the rotor-blade stub and minor differences on the blade-sleeve fairing. Regarding the retreating blade-sleeve fairing at $\Psi = 252°$, a more pronounced low-pressure area is present in the inboard region on the upper surface of the fairing for configuration C1. In contrast, this low-pressure region is more pronounced in radial direction for the reference configuration.

Regarding configuration C2, the increased size of the full-fairing beanie and the adapted pylon fairing significantly alter the local surface-pressure distribution, see Fig. 6.37c. The different inclination of the pylon fairing in the front part causes a higher pressure level in this region. Moreover, the pylon fairing of configuration C2 is wider, which leads to a stronger flow displacement. Therefore, an increased flow velocity is indicated by the strong suction region on the side wall of the pylon fairing, where the maximum thickness is located. Additionally, the area of high surface pressure in the front part of the full-fairing beanie is more pronounced on configuration C2, which also impacts the pressure distribution on the upstream pointing blade-sleeve fairing. The remaining blade-sleeve fairings reveal similar surface-pressure characteristics as observed for configuration C1.

The optimized blade-sleeve fairing could be introduced as a retrofit measure during the flight-test phase of the RACER demonstrator. Therefore, a detailed comparison between configuration C1 and the reference configuration is given. In contrast to configuration C1, the analysis of configuration C2 only represents a feasibility study for the larger full-fairing beanie, because the introduction of this fairing would require significant modifications on the upper deck and the pylon fairing of the RACER demonstrator, which is not feasible at the current stage of the demonstrator program. In order to give an impression on the average pressure forces that are acting on the helicopter and the rotor-head fairings, the mean, normalized surfaces-pressure coefficient is analyzed, see Fig. 6.38. A direct comparison between the reference configuration and configuration C1 is given showing the front view of the helicopter and a detailed view on the rotor head. The flow simulation results are averaged over three rotor revolutions and therefore, all rotor blades reveal the same pressure distribution independent of the azimuthal blade position. The main differences between the two configurations can be observed on the blade-sleeve fairing and the full-fairing beanie. The pylon fairing and the core geometry show almost no differences between both configurations.

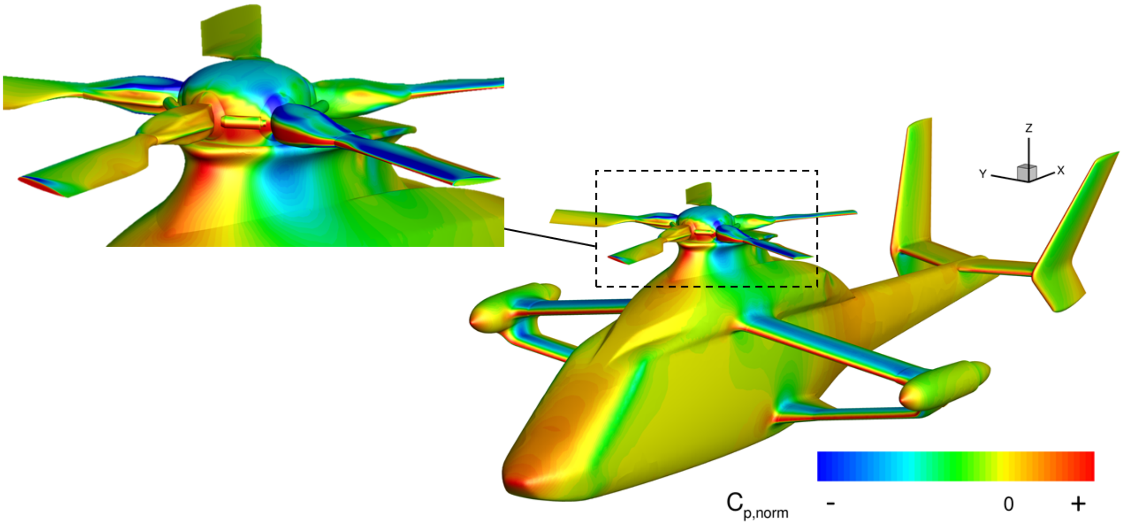

(a) Reference Configuration (Baseline Beanie R0H0 & Reference BSF).

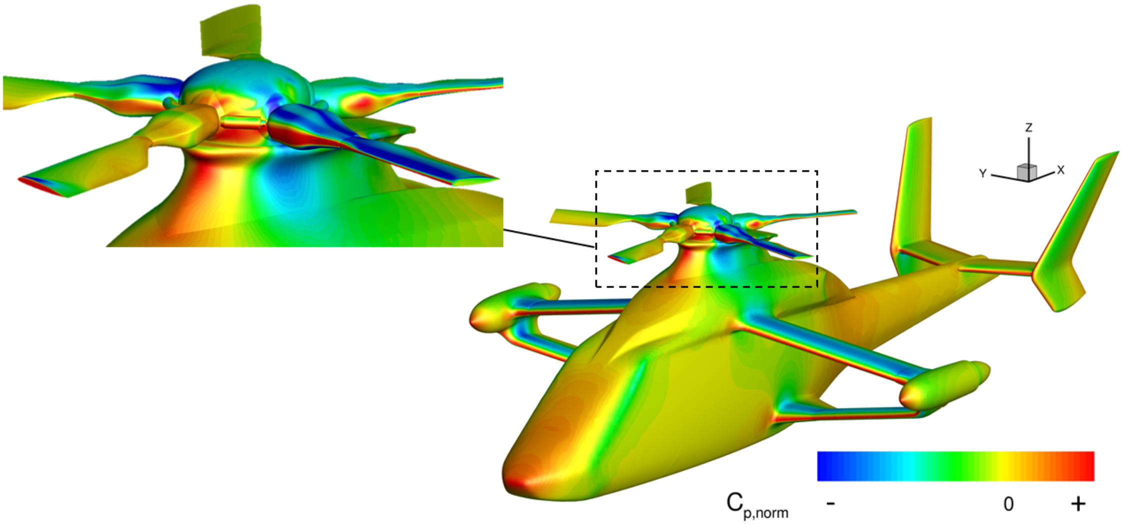

(b) Configuration C1 (Baseline Beanie R0H0 & Optimized BSF).

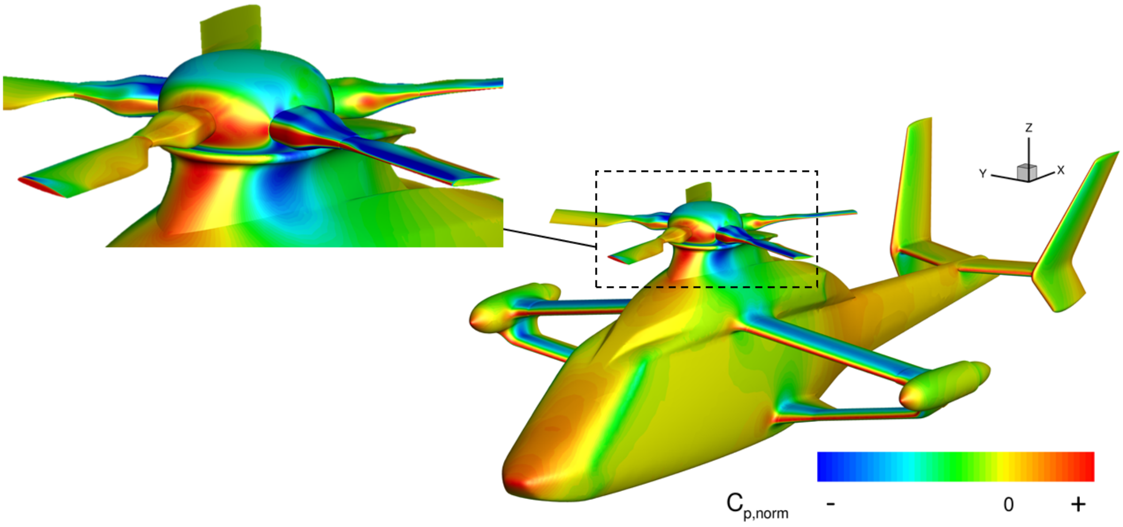

(c) Configuration C2 (Enlarged Beanie R1H1 & Optimized BSF).

Figure 6.37: Comparison of the instantaneous, normalized surface-pressure coefficient $C_{p,norm}$ for an upstream pointing rotor blade ($\Psi = 180°$) showing the front view of the helicopter.

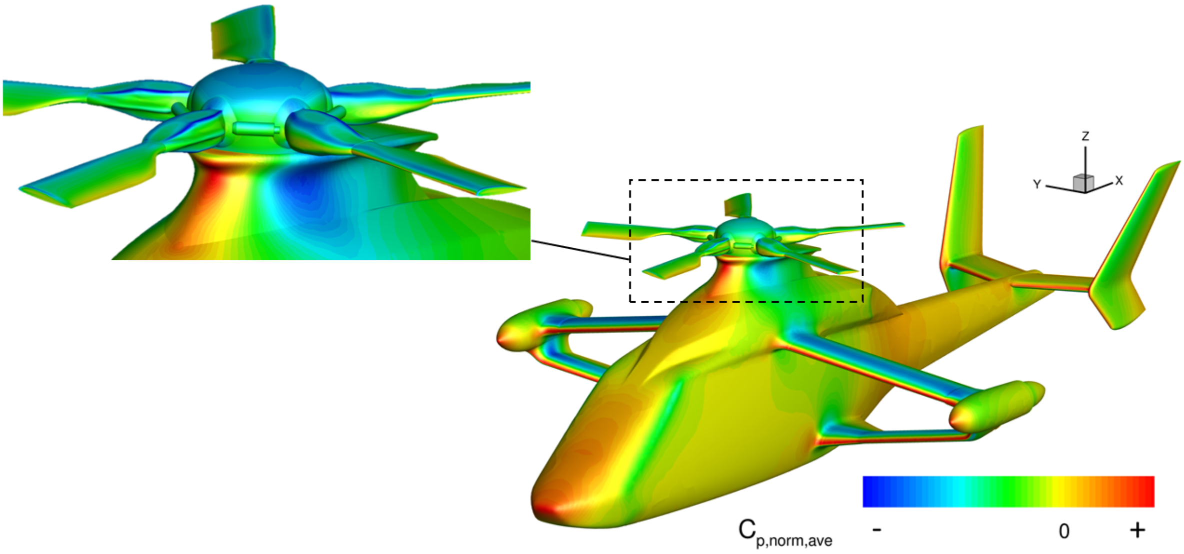

(a) Reference Configuration.

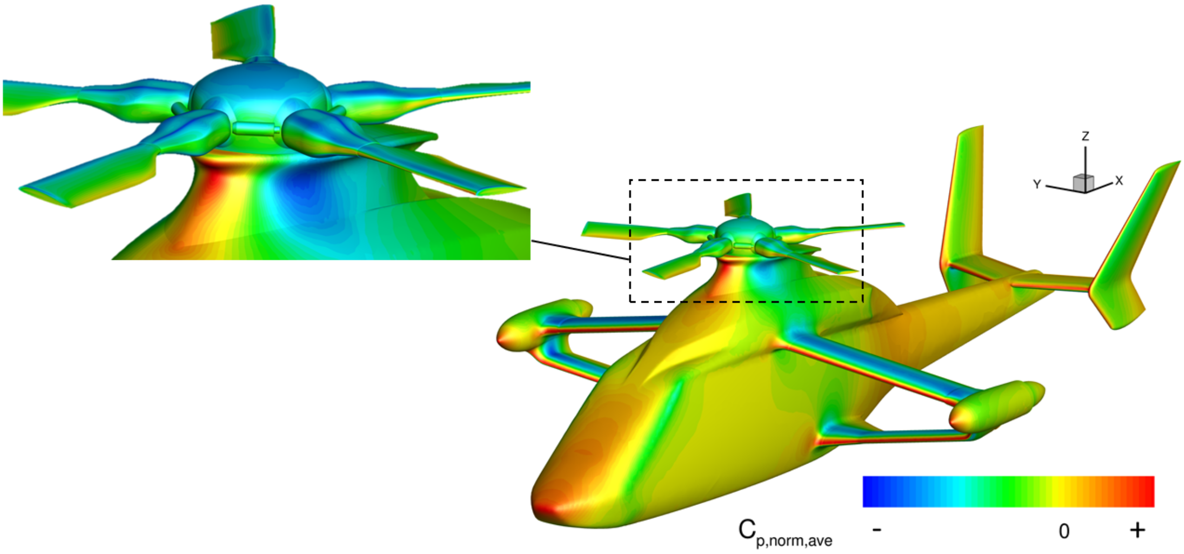

(b) Configuration C1 with the optimized blade-sleeve fairing.

Figure 6.38: Comparison of the mean, normalized surface-pressure coefficient $C_{p,norm,ave}$ for an upstream pointing rotor blade ($\Psi = 180°$) showing the front view of the helicopter.

Regarding the reference blade-sleeve fairing, the effect of the kink in the rear part of the fairing becomes clearly visible by the strong suction region. In comparison, the suction regions on the upper side of the optimized blade-sleeve fairing are generally less pronounced due to the reduced curvature of the geometry. Furthermore, the strength of the low-pressure region on the top of the full-fairing beanie is comparable between the two configurations showing only minor local differences. In addition, the rear view of the helicopter and the rotor head is illustrated in Fig. 6.39 to complement the present analysis. As previously mentioned, the main differences in the surface-pressure distribution are located on the rotor-head fairing. The upper deck, the tailboom and the empennage show almost identical pressure distributions.

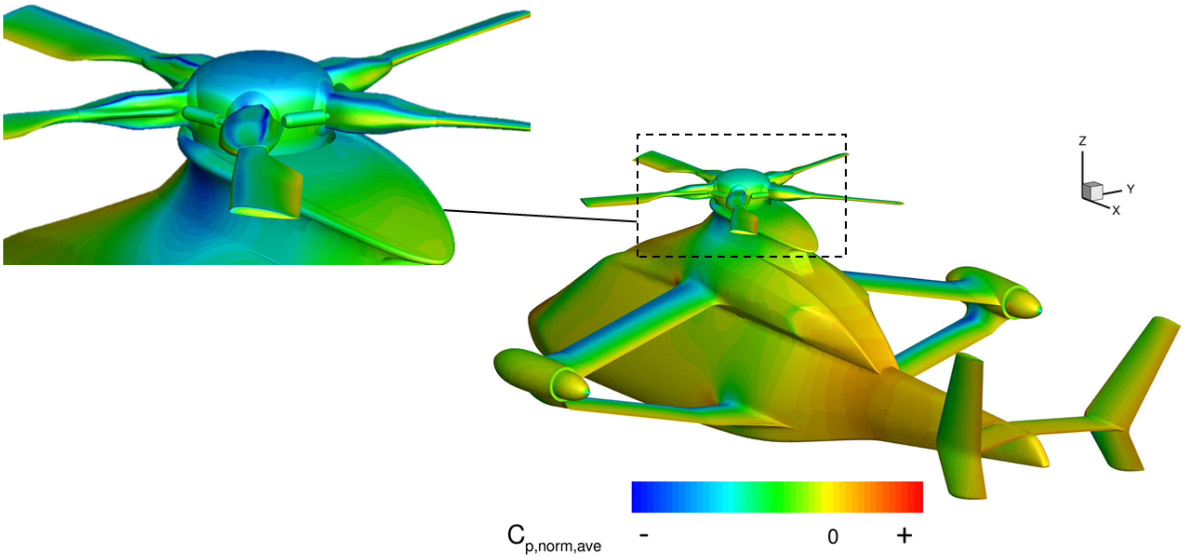

(a) Reference Configuration.

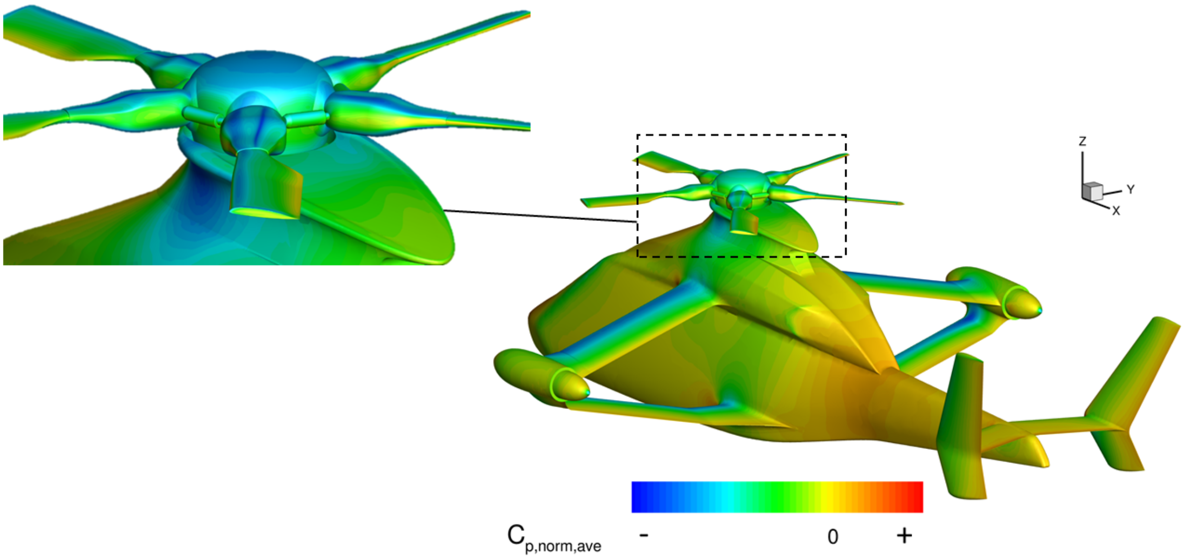

(b) Configuration C1 with the optimized blade-sleeve fairing.

Figure 6.39: Comparison of the mean, normalized surface-pressure coefficient $C_{p,norm,ave}$ for an upstream pointing rotor blade ($\Psi = 180°$) showing the rear view of the helicopter.

6.5.3 Flow-field Quantities

In this section, selected flow-field quantities are used to illustrate the flow field in the wake region of the rotor head and to demonstrate the main flow features. At first, the instantaneous, normalized axial flow velocity u/V_∞ is evaluated, which can be seen in Fig. 6.40. The normalized axial flow velocity is illustrated in equally spaced cross sections for all investigated configurations. In order to limit the visualization of the axial flow velocity to a relevant range, all values above $0.99 \cdot u/V_\infty$ are cut off. Hence, the velocity deficit that is introduced by each configuration can directly be seen.

In general, flow separation can be observed on the pylon fairing behind the full-fairing beanie for all configurations, which is indicated by the dark blue regions. Within these dark blue regions, stagnated or even reversed flow occurs. The comparison of the velocity field for configuration C1 and the reference configuration shows marginal differences regarding the flow separation on the pylon fairing. Hence, the introduced velocity deficit is comparable and a similar recovery of the axial flow velocity is observed in downstream direction. Regarding configuration C2, the velocity deficit in the vicinity of the full-fairing beanie is slightly more pronounced due to the increased size, which can be seen in Fig. 6.40c. However, the more downstream located cross sections show a velocity deficit that is comparable to configuration C1 and the reference configuration. Furthermore, the H-type architecture of the empennage seems to be beneficial in terms of stability and control, because the fluid flow with reduced dynamic pressure is passing between the two fins.

A more detailed view on the flow separation in the wake of the full-fairing beanie is given in Fig. 6.41 comparing the reference configuration and configuration C1. Moreover, an iso-surface of the normalized, axial flow velocity is shown with an iso-value of $u/V_\infty = 0$. The instantaneous solution for an upstream pointing rotor blade is given on the left-hand side of Fig. 6.41 and the corresponding averaged solution is depicted on the right-hand side. The evaluation of the mean flow field shows that the size and the position of the separation bubble are almost identical for both rotor head fairings.

Figure 6.42 shows the instantaneous, normalized axial vorticity $\omega_x \cdot R/V_\infty$ in equally spaced cross sections along the flow direction for the three investigated configurations. It can be seen that there is a large number of vortical flow structures with different orientation in the wake region of the rotor head. Moreover, discrete vortices can clearly be identified and the most prominent ones are given by the wing-tip vortices and the blade-tip vortices of the advancing as well as the upstream pointing rotor blade. The advancing rotor blade is impacted by the blade-tip vortex of the preceding rotor blade. The blade-tip vortex induces a flow velocity that is altering the surface-pressure distribution of the advancing rotor blade depending on its azimuthal position. Regarding the present flow problem, the blade-vortex interaction in the advancing blade region is only depending on the rotor blade length. Therefore, the interaction is not correctly predicted by the simplified rotor-head model in the given test case. Nevertheless, a relative comparison between the different rotor-head fairings is still reasonable. Additionally, there are strong interactions of the turbulent flow structures in the wake of the full-fairing beanie, which leads to a rapid decrease of the axial vorticity in downstream direction. From a global point of view, no significant differences between the three investigated configurations can be identified in terms of the axial vorticity.

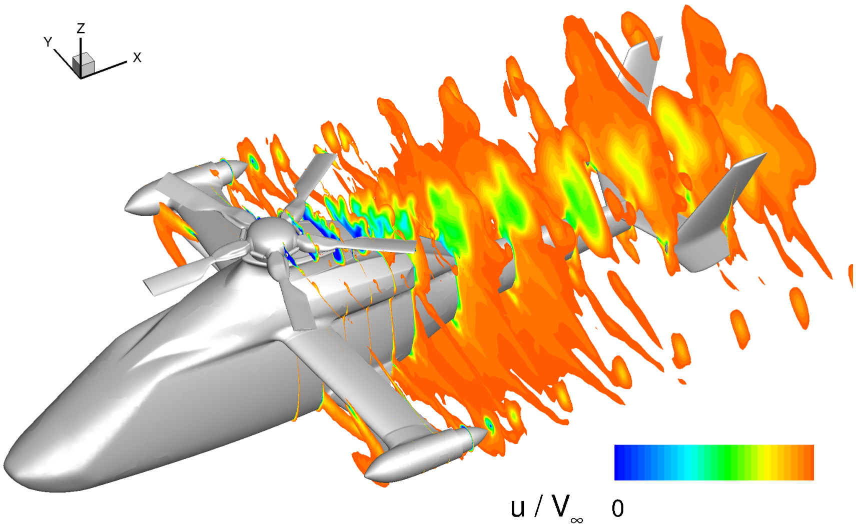

(a) Reference Configuration (Baseline Beanie R0H0 & Reference BSF).

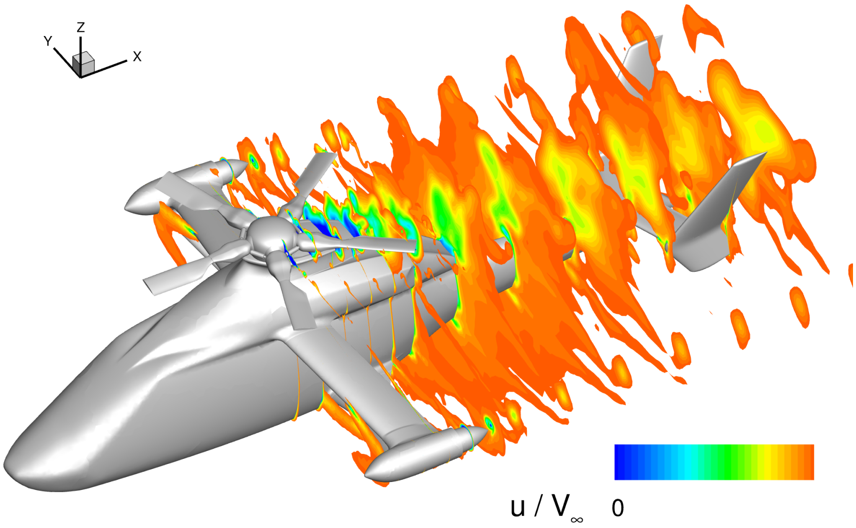

(b) Configuration C1 (Baseline Beanie R0H0 & Optimized BSF).

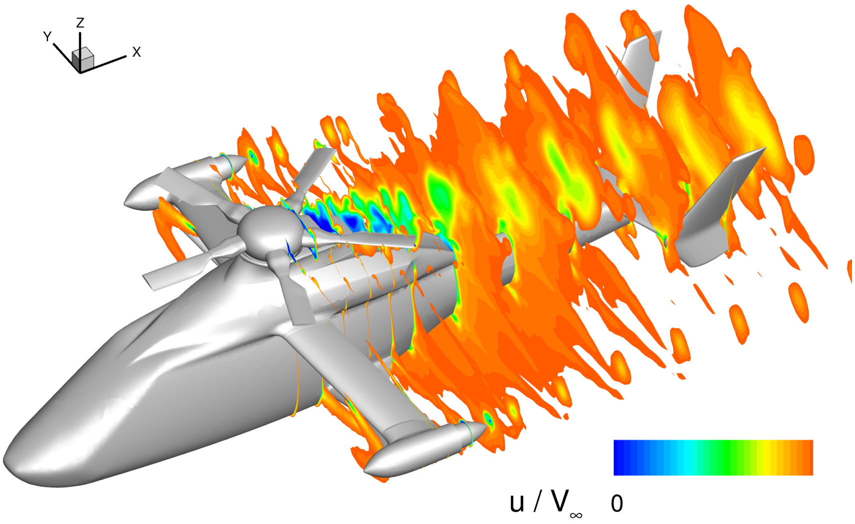

(c) Configuration C2 (Enlarged Beanie R1H1 & Optimized BSF).

Figure 6.40: Instantaneous, normalized axial flow velocity u/V_∞ shown in selected cross-sections in the wake region of the rotor head. Flow velocities above $0.99 \cdot u/V_\infty$ are cut off.

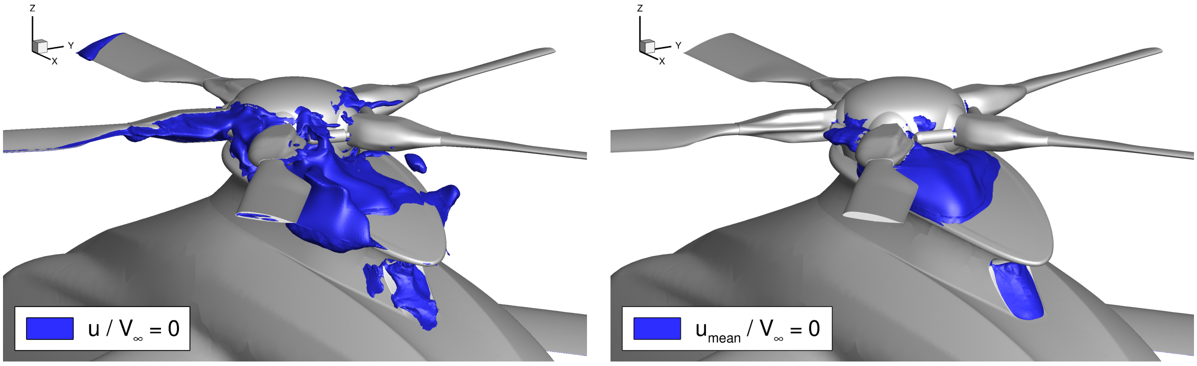

(a) Reference Configuration (Baseline Beanie R0H0 & Reference BSF).

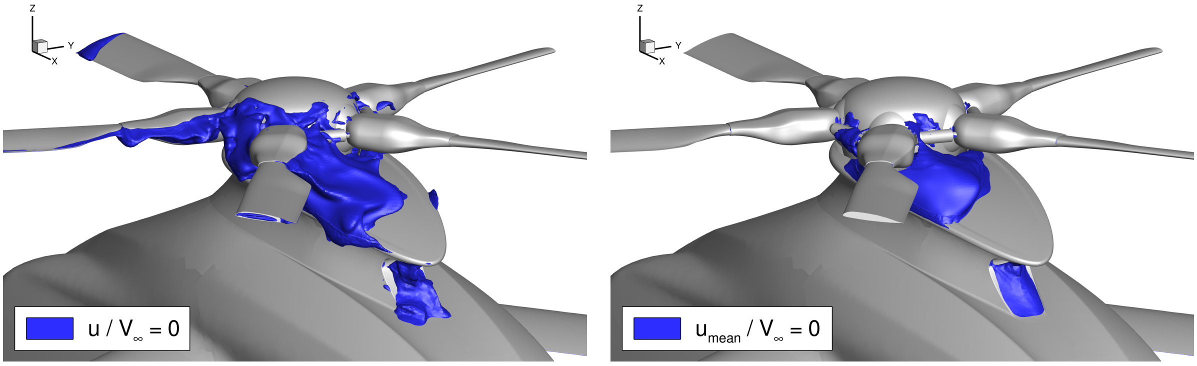

(b) Configuration C1 (Baseline Beanie R0H0 & Optimized BSF).

Figure 6.41: Iso-surface of the normalized, axial flow velocity with an iso-value of $u/V_\infty = 0$ illustrating the region of separated flow behind the full-fairing beanie for configuration C1 and the reference configuration.

The flow-field analysis is complemented by the evaluation of the Q-criterion, which represents a prominent vortex identification criterion. The Q-criterion is mainly used to visualize coherent vortical flow structures. Regarding the present flow problem, an iso-surface of the Q-criterion with an iso-value of $Q = 2000\,s^{-2}$ is used. Moreover, the iso-surface is colored by the normalized axial flow velocity u/V_∞. The comparison of the vortical flow field for the three investigated configurations is given in Fig. 6.43. The complexity of the highly turbulent rotor-head wake flow becomes clearly visible. The red-colored surfaces represent regions of high axial flow velocity and the blue-colored surfaces indicate regions of stagnated or even reversed flow. Hence, high flow velocities are observed on the wings, the full-fairing beanie, the advancing rotor blade and the inboard region of the retreating blade-sleeve fairing. Moreover, a reversed flow region is present in the wake of the full-fairing beanie for all configurations. The evaluation of the vortical flow field for configuration C2 reveals a more pronounced flow separation in the transition between the full-fairing beanie and the advancing rotor blade, which also generates bigger coherent vortical flow structures. The comparison between the reference configuration and configuration C1 shows no major discrepancies in the wake-flow field of the rotor head. The size and appearance of the vortical flow structures is very similar and no big impact of the blade-sleeve fairing geometry can be identified.

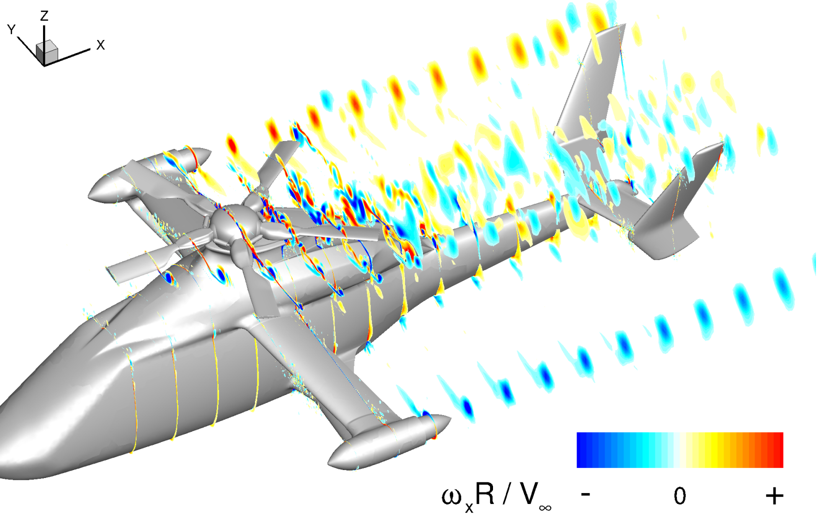

(a) Reference Configuration (Baseline Beanie R0H0 & Reference BSF).

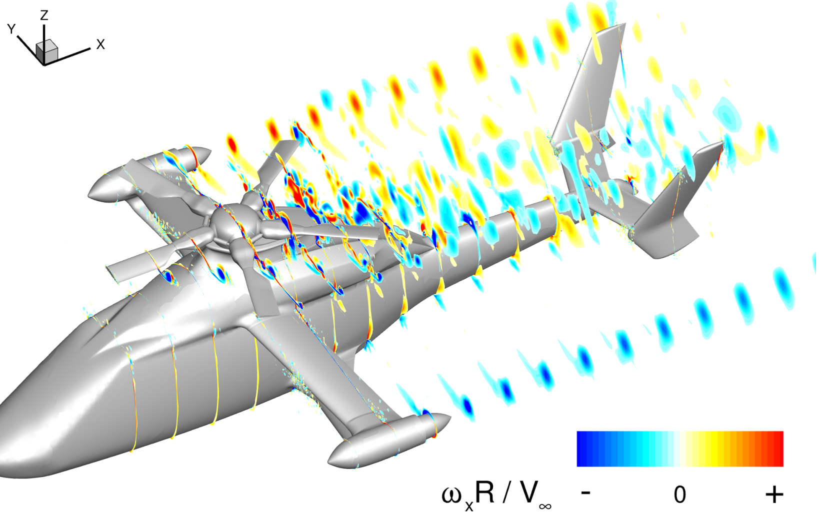

(b) Configuration C1 (Baseline Beanie R0H0 & Optimized BSF).

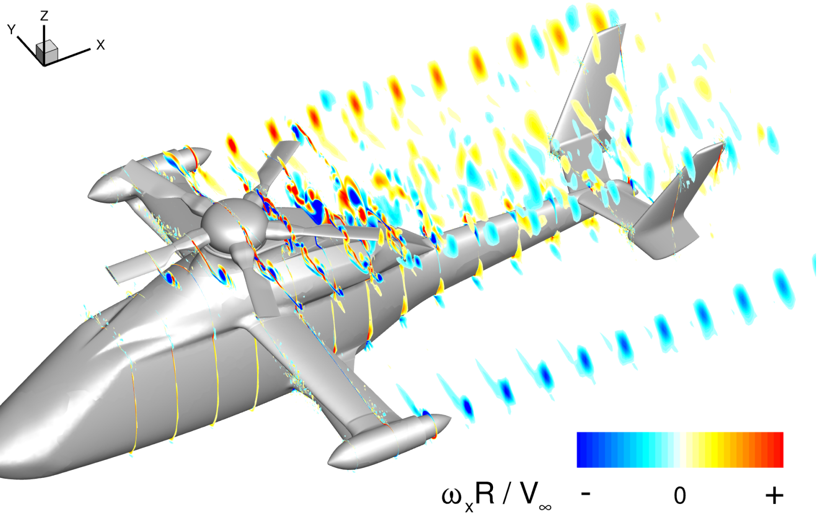

(c) Configuration C2 (Enlarged Beanie R1H1 & Optimized BSF).

Figure 6.42: Instantaneous, normalized axial vorticity $\omega_x \cdot R/V_\infty$ shown in selected cross-sections in the wake region of the rotor head.

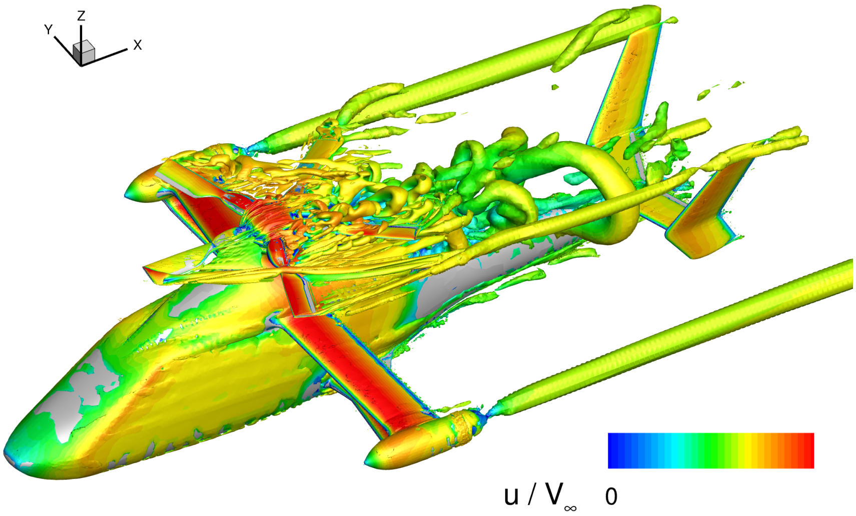

(a) Reference Configuration (Baseline Beanie R0H0 & Reference BSF).

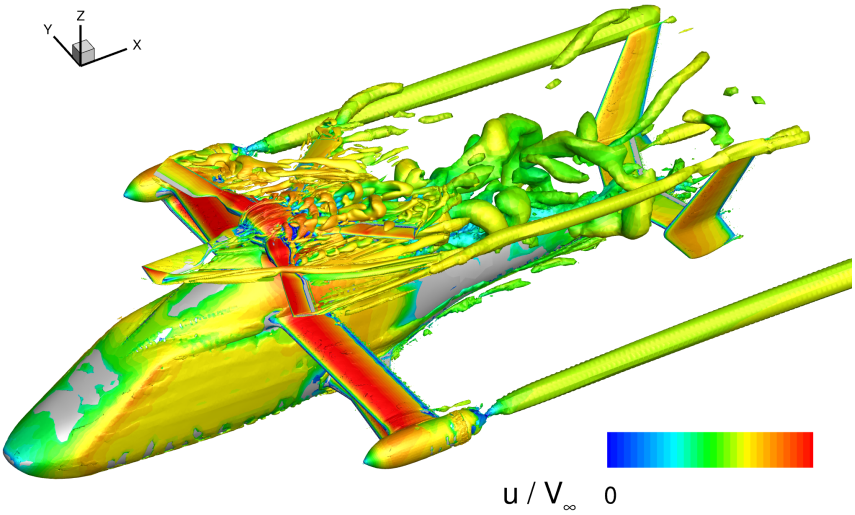

(b) Configuration C1 (Baseline Beanie R0H0 & Optimized BSF).

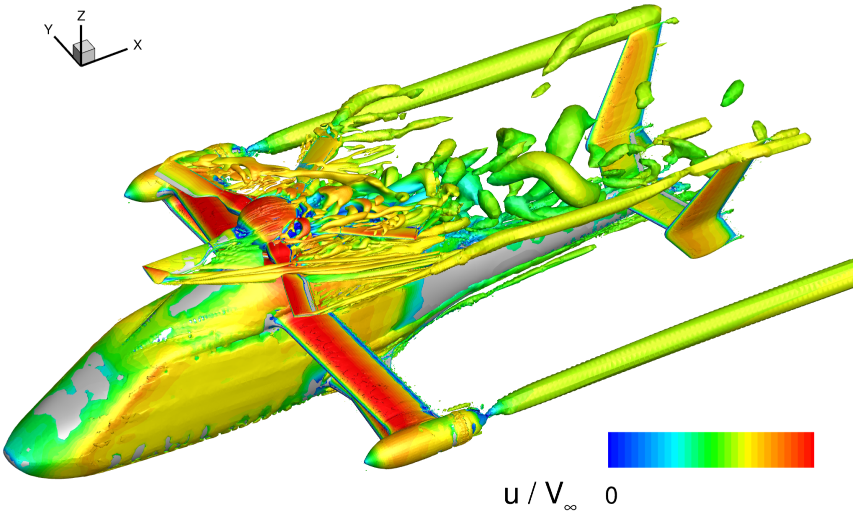

(c) Configuration C2 (Enlarged Beanie R1H1 & Optimized BSF).

Figure 6.43: Iso-surface of the Q-criterion ($Q = 2000\,s^{-2}$), which is colored by the normalized axial flow velocity u/V_∞.

6.6 Synthesis

In this chapter, the aerodynamically optimized blade-sleeve fairing has been put to test on the five-bladed RACER rotor head with truncated rotor blades. For this purpose, unsteady, high-fidelity numerical flow simulations have been performed considering a sea-level cruise flight of the RACER demonstrator with 220 knots. The main focus has been set on the evaluation of the compound helicopter performance to determine possible improvements that can be expected by the newly developed blade-sleeve fairing. Furthermore, the unsteady aerodynamic loads of the rotor head have been evaluated to determine possible vibrations that are introduced by the rotor-head fairing. The performance assessment has been conducted in two steps. First, the new rotor-head fairing has been investigated on an isolated, five-bladed rotor head without the core geometry of the helicopter to suspend any interference effects. Within the second step, the optimized rotor-head fairing has been evaluated on the full compound-helicopter configuration to determine the overall performance improvement. Regarding the numerical flow simulations, a spinning rotor head has been considered and the cyclic blade-pitch motion has been set according to a trimmed, sea-level cruise-flight. The remaining control surfaces on the wings and the empennage have not been used for trimming. Additionally, the lateral rotors have been neglected in the present work. The optimized blade-sleeve fairing has been compared to a reference geometry, which had been developed by Airbus Helicopters during the preliminary design phase of the RACER demonstrator. Moreover, two full-fairing beanie shapes with varying diameter and height have been analyzed in combination with the optimized blade-sleeve fairing to determine the most promising full-fairing concept.

Altogether, the following conclusions can be drawn for the design evaluation of the optimized rotor-head fairing:

Isolated Rotor-Head Analysis:

- It is common to use rotor-blade stubs on a helicopter wind-tunnel model in order to be able to increase the size of the model as much as possible, which leads to higher Reynolds numbers. Hence, the application of truncated rotor blades in the numerical simulations provides better comparability to wind-tunnel data considering the same advance ratio. However, one has to be aware that the aerodynamic interactions between the rotor blades and the rotor-head fairing are different than for the full-size rotor. Hence, it is recommended to check the performance of the new rotor-head fairing by numerical flow simulations using the full rotor blade length in future simulations.

- The overset-mesh approach in combination with mesh motion is well suited to realize the rotor-head movement in ANSYS Fluent. The rotational symmetry of the rotor head can be exploited allowing to generate only one fifth of the actual rotor head mesh. Block-structured, hexahedral meshes have been used for all components, which enables detailed grid adaptations in critical regions. However, the selected mesh topology requires a significant amount of time to generate the mesh, which must be taken into account in the overall simulation strategy. In order to avoid an excessive amount of orphan cells in the transition region between the rotor blades and the full-fairing beanie, the application of a collar grid is necessary. The present flow simulations have shown that the overset mesh is very sensitive to intersecting wall boundaries and discrepancies in the cell sizing of the overlapping mesh components.

- Regarding the rotor head with the baseline beanie R0H0, the optimized blade-sleeve fairing reveals a drag reduction of 5 % and a lift-increase of about 22 % in comparison to the reference rotor head. Furthermore, the FFT analysis of the aerodynamic forces shows a comparable lift spectrum and reduced oscillations in drag regarding the first and the second harmonic of the blade-passing frequency (BPF). The oscillations in lift show an amplitude of about 41-46 % of the average rotor-head lift regarding the first BPF harmonic. In terms of drag, the unsteady aerodynamic loads due to the first BPF harmonic are comparably low with approximately 3-11 % of the average drag value. No relevant amplitudes are observed for frequencies above the second BPF harmonic.

- In contrast to the rotor head with the baseline beanie R0H0, the differences between the optimized and the reference blade-sleeve fairing in terms of lift and drag are much smaller in combination with the larger full-fairing beanie R1H1. Regarding lift, the rotor head with the optimized blade-sleeve fairing provides a lift-increase of 5.5 % in comparison to the reference blade-sleeve fairing with beanie R1H1. Moreover, a similar drag reduction potential of 8.4 % is obtained for both blade-sleeve fairing shapes compared to the reference rotor head. The FFT analysis of the rotor head with the larger full-fairing beanie shows increased amplitudes for the first BPF harmonic. Regarding lift, an amplitude within the range of 44-54 % of the average lift is observed. Concerning the unsteady drag, an amplitude of 8-9 % of the average drag is noticed.

Full Compound-Helicopter Analysis:

- The overset mesh approach in ANSYS Fluent is very sensitive regarding overset interfaces that are overlapping the background-mesh boundary. Preliminary tests have revealed excessive intersection times during the flow simulation process for such cases. This could partly be related to the fact that the background-mesh boundaries are also used as a mesh interface to the helicopter domain in the present flow problem. However, the root cause for the disproportional intersection time could not be clearly identified in the present work. The required mesh-intersection time could be limited to a reasonable frame by reducing the size of the overset interfaces as much as possible. Therefore, it is recommended to keep the component meshes inside the background-mesh domain. Additionally, the size of the background mesh has an impact on the required intersection time, which leads to the conclusion that the smaller the background mesh, the lower the time required for the overset-mesh generation during the flow-simulation process.

- The applied meshing strategy allows to combine different mesh topologies for the component meshes in the final computational grid. The mesh components are connected by dedicated mesh interfaces. Here, conformal as well as non-conformal mesh interfaces are supported. This allows to adapt the mesh generation process to the complexity of the investigated geometry. In the present work, the versatility of the applied computational meshes has been demonstrated by combining independently generated meshes for the rotor head, the core geometry of the helicopter and the farfield domain.

- In comparison to the reference rotor-head fairing, the optimized blade-sleeve fairing on configuration C1 achieves a drag reduction of 1.4 % considering the total drag of the full compound helicopter configuration. Moreover, this comes along with a lift-increase of 1.3 % providing even more drag reduction potential considering an iso-lift condition. The evaluation of the aerodynamic forces for configuration C2, which features the larger full-fairing beanie R1H1 and the optimized blade-sleeve fairing, reveals a drag reduction of 4.1 % in comparison to the reference rotor-head fairing. Furthermore, a minor lift-increase of 0.23 % is observed for configuration C2. Therefore, the highest drag-reduction potential could be identified for configuration C2, but the introduction of this rotor-head fairing would require a redesign of the pylon fairing to fit the larger full-fairing beanie.

- The spectral analyses of the unsteady rotor-head forces on the full compound-helicopter configuration reveal different amplitudes than for the isolated rotor-head investigations due to interference effects. Regarding the reference configuration, the amplitude of lift at the first BPF harmonic is almost the same as for the isolated rotor head with 40.1 % of the respective average lift.

However, the drag amplitude of the first BPF harmonic is about 5 % higher than for the isolated rotor-head case. At the second BPF, the lift amplitude is reduced by 6.7 % and the drag amplitude is almost the same in comparison to the isolated rotor-head. The evaluation of configuration C1 shows that the lift amplitude at the first BPF harmonic is about 12 % lower than on the isolated rotor head. Furthermore, the corresponding drag amplitude is increased by 9.9 % reaching 12.9 % of the average rotor-head drag. Regarding the second BPF harmonic of the rotor-head lift for configuration C1, the amplitude is reduced to 10.7 % of the average lift. In terms of drag, the same amplitudes are observed for configuration C1 at this frequency.

7 Conclusion and Outlook

The expansion of the helicopter flight envelope towards higher cruising speeds is one of the main challenges the helicopter industry is dealing with nowadays. Based on the fact that the maximum cruise speed of a conventional helicopter is naturally limited by rotor aerodynamics and drag, new concepts are required to be able to unlock the high-speed domain. Within the framework of the European Clean Sky 2 research initiative, the Rapid And Cost-Effective Rotorcraft (RACER) is developed. It represents an innovative compound-helicopter configuration providing the key technologies to tackle the speed limitation. Due to the high cruise speed of the RACER demonstrator, drag reduction is an important topic. In this regard, the rotor head represents one of the main drag sources and previous studies have shown that the implementation of rotor-head fairings can be an effective drag-reduction measure.

The present work is part of the European Clean Sky 2 project FURADO, which is mainly focusing on the aerodynamic design optimization and flow analysis of a full-fairing rotor head for the RACER compound helicopter. For this purpose, a sophisticated optimization tool chain has been developed allowing for automated aerodynamic design optimization by means of CFD simulation. The tool chain is based on a Python framework and it comprises state-of-the-art software packages for optimization, mesh generation and flow simulation. Moreover, it is designed in a modular manner allowing for an easy replacement of software packages and the extension of its capabilities. Additionally, it enables the parallel evaluation of multiple designs using the high-performance computer SuperMUC of the Leibniz Supercomputing Centre. Regarding the optimization software, the Design Analysis Kit for Optimization and Terascale Applications (DAKOTA) has been used. DAKOTA contains state-of-the-art optimization algorithms ranging from local, gradient-based to global, evolutionary algorithms.

The rotor-head fairing of the RACER demonstrator consists of two main components, which are given by the blade-sleeve fairing and the full-fairing beanie. In the present thesis, the main focus is on the aerodynamic design optimization of the blade-sleeve fairing. Nevertheless, different full-fairing beanie shapes are analyzed as well in combination with the optimized blade-sleeve fairing to identify the most promising full-fairing concept. The following paragraphs summarize the design optimization process and the subsequent performance evaluation of the newly-developed blade-sleeve fairing. Moreover, the optimization strategy is explained and key results as well as major findings are highlighted.

Blade-Sleeve Fairing Design Optimization

The design optimization of the blade-sleeve fairing has been performed for a sea-level cruise flight of the RACER demonstrator with 220 knots, which is considered as the most relevant flight condition in terms of drag reduction. A step-wise optimization strategy has been used comprising a preliminary and a refined design optimization of the blade-sleeve fairing. Moreover, design constraints regarding the minimum and maximum permissible design space have been incorporated. In order to realize the design optimization of the blade-sleeve fairing within a reasonable time frame, a simplified model of a single, stationary rotor blade has been investigated. Furthermore, the advancing and the retreating rotor-blade position reveal the highest drag values in the azimuthal drag distribution. Therefore, these two rotor-blade positions have been selected for the design optimization purpose and two different objective functions have been employed. Regarding the advancing blade case, the maximization of the lift-to-drag ratio has been considered and for the retreating blade case, the minimization of drag has been pursued. A global, multi-objective, genetic optimization algorithm has been used, which does not require a weighting of the objective functions and delivers a Pareto front of non-dominated designs.

During the preliminary design optimization, four radial blade-sleeve sections have been aerodynamically optimized for cruise flight. The geometry parameterization has been realized by Bézier curves offering a robust and highly flexible method for shape generation. For this purpose, 14 design variables have been used to define the control points of the Bézier curves. The applied flow conditions are based on the flight condition of the helicopter, the rotational speed of the main rotor, the radial position of the respective blade-sleeve section, the proper cyclic blade-pitch angle and the local flow deflection due to the presence of the helicopter geometry. The optimization runs have been finalized after 25 successive populations for each of the blade-sleeve sections. As a result, a large database of 4281 optimized geometries has been generated. The optimized shapes have been compared to the sectional shapes of a reference blade-sleeve fairing, which was developed by Airbus Helicopters during the preliminary design phase of the RACER demonstrator.

The present work has shown that Latin Hypercube Sampling (LHS) is very useful for the definition of the initial population, because it covers a wide region of the search space and it avoids clustering of geometries in certain design-variable ranges. Hence, it provides a reasonable starting point for the design optimization purpose, especially considering a large number of design variables. The evaluation of the objective space shows significant improvements in both objective functions for the two inboard sections S2 and S3. These two sections feature a high relative thickness, which leads to unsteady flow separation and the formation of a vortex street in the wake region. This flow phenomenon causes strong oscillations in the aerodynamic forces and requires transient flow simulations to properly capture the flow physics.

In contrast, the outboard sections S4 and S5 have a comparably low relative thickness leading to smooth boundary layer separation without vortex shedding. Regarding the advancing blade case, the sections S4 and S5 reveal a major increase in the aerodynamic efficiency. Moreover, the evaluation of the retreating blade case shows a minor drag reduction. This is caused by the fact that the reference geometries already feature a low relative thickness at these radial stations, which limits the drag reduction potential. The designs offering the best compromise between the applied objective functions are investigated in more detail, because they represent the basis for the initial, three-dimensional blade-sleeve fairing shape. The evaluation of angle-of-attack (AoA) polars shows that the optimized blade-sleeve sections are quite robust regarding the inflow direction within a wide AoA range. However, the newly developed shapes are specifically optimized for a single AoA and therefore, they are less robust than the reference shapes. A detailed view on the surface-pressure distribution of the optimized blade-sleeve sections reveals the main reasons for the performance improvement. Additionally, the axial skin-friction coefficient is used to determine the flow-separation onset for each of the blade-sleeve sections.

Subsequent to the preliminary design optimization of the blade-sleeve sections, a refined design optimization of the three-dimensional blade-sleeve fairing shape has been performed. The parameterization of the geometry has been realized by four discrete design variables representing a predefined set of optimized shapes for the blade-sleeve sections S2-S5. Moreover, twelve optimized geometries have been selected from the Pareto front for each of the four blade-sleeve sections. This yields a total number of 48 specific geometries and 20.736 possible shape combinations. The same genetic optimization algorithm as for the preliminary design optimization has been used with comparable settings. An unconstrained design optimization has been performed, because the optimized supporting airfoils already satisfy the design constraints. Based on the limited changes in the objective functions of the final populations, the design optimization has been considered as converged after 20 successive populations. This yields a total number of 811 investigated blade-sleeve fairing shapes. The initial population consists of 150 randomly selected candidates and in the final population this number is reduced to 62.

The evaluation of the objective space shows that all designs from the final population are dominating the reference blade-sleeve fairing. Design 743 has been selected from the Pareto front for further analyses, because it offers the best compromise between the applied objective functions and it satisfies all design constraints. Furthermore, the shape of design 743 has been slightly modified to reduce the waviness of the geometry and to provide a proper transition between the blade-sleeve sections. The final assessment of the optimized blade-sleeve fairing predicts a significant performance improvement in comparison to the reference geometry. Regarding the advancing-blade case of the stationary, single rotor blade, the lift-to-drag ratio is increased by 38 %. Additionally, a drag reduction of about 6 % is observed for the retreating blade case.

Analysis of the Optimized Rotor-Head Fairing

The performance assessment of the newly developed blade-sleeve fairing has been conducted in two steps. First, numerical flow simulations have been performed for the isolated, five-bladed rotor head without the core geometry of the helicopter to suspend any interference effects. Thereafter, the full compound-helicopter configuration has been investigated by high-fidelity numerical flow simulations to determine the overall performance benefit of the newly developed blade-sleeve fairing. The cyclic blade-pitch movement has been realized by an overset-mesh approach in combination with mesh motion. Moreover, the cyclic blade-pitch input has been set according to a trimmed sea-level cruise flight of the RACER demonstrator with 220 knots. A rigid-body motion has been assumed and the lead-lag movement as well as the flapping of the rotor blades have been neglected. The numerical flow simulations have shown that the overset-mesh approach of the applied ANSYS Fluent version is very sensitive to intersecting wall boundaries and discrepancies in the cell sizing of overlapping mesh components. In order to avoid an excessive amount of orphan cells in the transition region between the blade-sleeve fairing and the full-fairing beanie, a collar grid has been used to improve the quality of the overset interface.

Regarding the isolated rotor-head simulations, four different rotor-head fairings have been compared to each other. The reference rotor head consists of the baseline beanie R0H0 and the reference blade-sleeve fairing. Moreover, a full-fairing beanie with increased diameter and height, namely beanie R1H1, has been analyzed in combination with the optimized and the reference blade-sleeve fairing, respectively. Regarding the rotor head with the baseline beanie R0H0 and the optimized blade-sleeve fairing, the evaluation of the mean aerodynamic forces reveals a drag reduction of 5 % and a lift-increase of about 22 %. The impact of the newly developed blade-sleeve fairing on the unsteady aerodynamic forces has been investigated by means of FFT analyses. The comparison between the reference and the optimized blade-sleeve fairing shows a similar lift spectrum and reduced drag oscillations concerning the first and the second harmonic of the blade-passing frequency for the optimized shape. Regarding the rotor head with the larger full-fairing beanie R1H1, the differences in the mean aerodynamic forces of the reference and the optimized blade-sleeve fairing are much smaller. The biggest discrepancy between the two blade-sleeve fairings is observed for lift, which is about 5.5 % higher for the optimized blade-sleeve fairing. In terms of drag, both blade-sleeve fairings achieve a drag reduction of about 8.4 % compared to the reference rotor head with the smaller beanie R0H0.

The applied simulation setup allows to combine different mesh topologies in the computational grid of the full helicopter configuration. The mesh components are connected to each other by dedicated mesh interfaces. Therefore, the block-structured rotor-head mesh from the isolated rotor-head simulations can be reused and combined with the hybrid, unstructured mesh of the core geometry.

The aerodynamic characteristics of three different rotor-head fairings are compared to each other by unsteady, numerical flow simulations of the full compound-helicopter configuration. The reference configuration features the baseline beanie R0H0 and the reference blade-sleeve fairing. Furthermore, the two remaining configurations comprise the optimized blade-sleeve fairing together with the baseline beanie R0H0 (Configuration C1) and the enlarged beanie R1H1 (Configuration C2). The pylon fairing of the RACER demonstrator has been adapted within the present work to fit the larger full-fairing beanie. Regarding the total drag of the compound-helicopter configuration, a drag reduction of 1.4 % is achieved by configuration C1. Additionally, a lift increase of 1.3 % is obtained, which provides even more drag-reduction potential considering an iso-lift condition. Configuration C2, with the larger full-fairing beanie R1H1, predicts a drag reduction of 4.1 % together with a minor lift increase of 0.23 %. The spectral analyses of the unsteady rotor-head forces reveals different amplitudes than for the isolated rotor-head simulations, which can be related to interference effects between the rotor head and the core geometry of the helicopter.

The evaluation of the surface-pressure distributions and the comparison of selected flow-field quantities show minor differences between configuration C1 and the reference configuration. In contrast, more significant changes in the surface-pressure distribution and the wake-flow field of the helicopter are identified for configuration C2, which is related to the increased size of the full-fairing beanie and the adapted pylon fairing. The analysis of configuration C2 only represents a feasibility study for the larger full-fairing beanie, because the introduction of this fairing would require significant modifications on the upper deck and the pylon fairing of the RACER demonstrator. At the end of the FURADO project, a supporting structure has been designed for the new blade-sleeve fairing to be able to integrate it on the RACER demonstrator during the flight-test campaign.

Outlook

In the present thesis, the blade-sleeve fairing has been aerodynamically optimized for the sea-level cruise flight with 220 knots. This represents a single spot point of the RACER flight envelope and the investigation of additional flight conditions would help to determine the robustness of the new blade-sleeve fairing. Relevant flight conditions include hover, climb and descent as well as cruise flight at different speeds and altitudes. Furthermore, wind-tunnel measurements would complement the present analysis and the experimental data could be used to validate the numerical results. The applied rotor-head fairing fully seals the hub region of the main rotor, which reduces the cooling of the mechanical and elastomeric components inside the fairing. The increased thermal stress requires a risk assessment to determine the thermal situation inside the upper deck and the rotor-head fairing.

Based on this assessment, necessary cooling requirements could be derived and the corresponding solutions could be implemented on the RACER demonstrator. Starting from the optimized blade-sleeve fairing shape, the design could be further improved by using a gradient-based optimization algorithm in combination with an updated parameterization of the geometry. Finally, the introduction of the optimized blade-sleeve fairing in the RACER flight-test campaign would conclude the present work and reveal the actual performance benefit in comparison to the reference blade-sleeve fairing.

Bibliography

[1] International Air Transport Association (IATA). **World Air Transport Statistics 2019**, 2019.

[2] T.W. Sheehy. **A General Review of Helicopter Rotor Hub Drag Data**. *Journal of the American Helicopter Society*, 22(2):2–10, 1977.

[3] D. Desvigne and D. Alfano. **Rotor-head/Fuselage Interactional Effects on Helicopter Drag: Influences of the Complexification of the Rotor-head Geometry**. In *39th European Rotorcraft Forum, Moscow, Russia*, 2013.

[4] Airbus Helicopters. **Press release: Airbus Helicopters reveals RACER high-speed demonstrator configuration**. `https://www.airbus.com/newsroom/press-releases/en/2017/06/Airbus-Helicopters-reveals-Racer-high-speed-demonstrator-configuration.html`, 2017. [Online; accessed 2020-09-15].

[5] Airbus Helicopters. **H160 Photo Gallery**. `https://www.airbus.com/helicopters/civil-helicopters/medium/h160.html`, 2020. [Online; accessed 2020-11-20].

[6] FOX 52. **Line drawing of a Eurocopter EC 155 CCBY3.0**. `https://commons.wikimedia.org/wiki/File:Eurocopter_EC155_orthographical_image.svg`, 2014. [Online; accessed 2020-11-20].

[7] Airbus Helicopters. **Magazine about the H175 Helicopter**. `http://ah.mg/uploads/3b119a5f329700afd373c7621f3e34f3.pdf`, 2016. [Online; accessed 2020-11-20].

[8] J.G. Leishman. ***Principles of Helicopter Aerodynamics, Second Edition***. Cambridge University Press, New York, USA, 2006.

[9] B.G. Van der Wall. ***Grundlagen der Hubschrauber-Aerodynamik***. Springer-Verlag Berlin Heidelberg, Heidelberg, Germany, 2015.

[10] J.R.R.A. Martins and A. Ning. ***Engineering Design Optimization***. First electronic edition, January 2020, Michigan, USA, 2021.

[11] P. Pölzlbauer, D. Desvigne, and C. Breitsamter. **Aerodynamic Design Optimization of a Helicopter Rotor Blade-Sleeve Fairing**. *CEAS Aeronautical Journal*, 10(3):665–685, 2019.

[12] A. Olsson, G. Sandberg, and O. Dahlblom. **On Latin hypercube sampling for structural reliability analysis**. *Structural Safety*, 25(1):47–68, 2003.

[13] M. Stuhlpfarrer, A. Kümmel, and C. Breitsamter. **Investigations of Helicopter Wake Flow Including Rotor-Head Motion**. *Journal of Aircraft*, 55(5):2114–2126, 2018.

[14] P. Pölzlbauer, A. Kümmel, D. Desvigne, and C. Breitsamter. **Numerical Investigation of an Optimized Rotor Head Fairing for the RACER Compound Helicopter in Cruise Flight**. *Aerospace*, 8(3), 2021.

[15] J.F. Wendt, J.D. Anderson, J. Degroote, G. Degrez, E. Dick, R. Grundmann, and J. Vierendeels. ***Computational Fluid Dynamics - An Introduction***. Springer-Verlag Berlin Heidelberg, Heidelberg, Germany, 2009.

[16] B. Zohuri and N. Fathi. ***Thermal-Hydraulic Analysis of Nuclear Reactors***. Springer International Publishing, Springer International Publishing Switzerland, 2015.

[17] S. Cakmakcioglu. **SU2 Tutorial: Transitional Flat Plate**. `https://su2code.github.io/tutorials`, 2021. [Online; accessed 2021-08-18].

[18] H. Schlichting and K. Gersten. ***Grenzschicht-Theorie***. Springer-Verlag Berlin Heidelberg, Heidelberg, Germany, 2006.

[19] M.S. Thordal, J.C. Bennetsen, and H.H. Koss. **Review for practical application of CFD for the determination of wind load on high-rise buildings**. *Journal of Wind Engineering and Industrial Aerodynamics*, 186:155–168, 2019.

[20] J. Hart. **Comparison of Turbulence Modeling Approaches to the Simulation of a Dimpled Sphere**. *Procedia Engineering*, 147:68–73, 2016.

[21] S.B. Pope. ***Turbulent Flows***. Cambridge University Press, Cambridge, United Kingdom, 2000.

[22] ANSYS Inc. ***ANSYS Fluent Theory Guide***. ANSYS, Inc., Canonsburg, Pennsylvania, USA, 2019.

[23] A. Schwöppe and B. Diskin. **Accuracy of the Cell-Centered Grid Metric in the DLR TAU-Code**. In *New Results in Numerical and Experimental Fluid Mechanics VIII: Contributions to the 17th STAB/DGLR Symposium Berlin, Germany 2010*, 2013.

[24] HI Helicopter Investor. **Insight on the Helicopter Investor homepage**. `https://www.helicopterinvestor.com/insight/98935/nhv-group-logs-70000-flying-hours-with-the-h175-175`, 2022. [Online; accessed 2024-07-14].

[25] R.D. Blevins. ***Flow-induced Vibration***. Van Nostrand Reinhold, 1990.

[26] European Commission. **Horizon 2020**. `https://ec.europa.eu/programmes/horizon2020`, 2020. [Online; accessed 2020-04-29].

[27] European Commission. **Flightpath 2050 Europe's Vision for Aviation**. Technical report, European Union, 2011.

[28] W. Johnson. ***Helicopter Theory, Dover Books on Aeronautical Engineering Series***. Dover Publications, Inc., Mineola, New York, 1994.

[29] S. Ransom. **The British Experimental Rotor Programme IV (BERP IV) - Technology Demonstration Programme**. In *34th European Rotorcraft Forum, Liverpool, United Kingdom*, 2008.

[30] R.K. Burgess. **Development of the ABC Rotor**. In *27th Annual Forum of the American Helicopter Society, Washington D.C., USA*, 1971.

[31] A. Bagai. **Aerodynamic Design of the X2 Technology Demonstrator Main Rotor Blade**. In *64th Annual Forum of the American Helicopter Society, Montreal, Canada*, 2008.

[32] C. Da Silva. **The Revolution has begun X^3**. *Rotor Journal*, 88:14–19, 2011.

[33] G. Byham. **30th Anniversary of G-LYNX Flight - The Absolute World Helicopter Speed Record Held for 30 Years and Counting**. `https://vtol.org/news/30th-anniversary-of-g-lynx-flight`, 2016. [Online; accessed 2020-09-15].

[34] Lockheed Martin. **Future Vertical Lift - X2 Technology**. `https://www.lockheedmartin.com/en-us/products/x2-helicopter-technology-demonstrator.html`, 2010. [Online; accessed 2020-09-15].

[35] Airbus Helicopters. **Press release: X3 - Celebrating 10 years of the high-speed demonstrator**. `https://www.airbus.com/newsroom/events/X3.html`, 2020. [Online; accessed 2020-09-15].

[36] P. Gronemann. **V22-Osprey**. `https://commons.wikimedia.org/w/index.php?curid=21346760`, 2012. [Online; accessed 2020-09-15].

[37] Boeing. **Defense V-22 Osprey**. `https://www.boeing.com/defense/v-22-osprey`, 2020. [Online; accessed 2020-04-29].

[38] European Commission. **Clean Sky 2 Joint Technical Programme**. Technical report, European Union, 2015.

[39] M. Grawunder, R. Reß, C. Breitsamter, and N.A. Adams. **Flow characteristics of a helicopter fuselage configuration including a rotating rotor head**. In *28th Congress of the International Council of the Aeronautical Sciences, Brisbane, Australia*, 2012.

[40] S. Wagner. **Problems of estimating the drag of a helicopter**. In *AGARD Conference Proceedings No. 124 on Aerodynamic Drag, AGARD-CP-124, Izmir, Turkey*, 1973.

[41] M. Wentrup, W. Khier, and Q. Zhang. **Drag reduction of a transport helicopter by application of an adjoint-based fuselage optimization chain and modification of the rotor head**. In *Greener Aviation: Clean Sky breakthroughs and worldwide status, Brussels, Belgium*, 2014.

[42] C. Keys and R. Wiesner. **Guidelines for Reducing Helicopter Parasite Drag**. *Journal of the American Helicopter Society*, 20(1):31–40, 1975.

[43] D.R. Graham, D.Y. Sung, L.A. Young, A.W. Louie, and R.H. Stroub. **Helicopter Hub Fairing and Pylon Interference Drag**. Technical report, NASA Technical Memorandum 101052, Ames Research Center, Moffett Field, California, USA, 1989.

[44] P. Pölzlbauer. **FURADO project homepage**. `www.furado.tum.de`, 2016. [Online; accessed 2020-09-15].

[45] P. Pölzlbauer, D. Desvigne, and C. Breitsamter. **Performance Improvement of a Compound Helicopter Rotor Head by Aerodynamic Design Optimization of a Blade-Sleeve Fairing**. *The Aeronautical Journal*, 123(1268):1456–1475, 2019.

[46] R.D. Harrington. **Reduction of Helicopter Parasite Drag**. Technical report, NACA Technical Note 3234, Langley Aeronautical Laboratory, Langley Field, Virginia, USA, 1954.

[47] G.B. Churchill and R.D. Harrington. **Parasite-Drag Measurements of Five Helicopter Rotor Hubs**. Technical report, NASA Technical Memorandum 1-31-59L, Langley Research Center, Langley Field, Virginia, USA, 1959.

[48] G.E. Sweet and J.L. Jenkins. **Wind-Tunnel Investigation of the Drag and Static Stability Characteristics of Four Helicopter Fuselage Models**. Technical report, NASA Technical Note D-1363, Langley Research Center, Langley Station, Hampton, Virginia, USA, 1962.

[49] J.L. Jenkins, M.M. Winston, and G.E. Sweet. **A Wind-Tunnel Investigation of the Longitudinal Aerodynamic Characteristics of two Full-Scale Helicopter Fuselage Models with Appendages**. Technical report, NASA Technical Note D-1364, Langley Research Center, Langley Station, Hampton, Virginia, USA, 1962.

[50] E.L. Brown and J.M. Drees. **Increasing Helicopter Speeds**. In *16th Annual Forum of the American Helicopter Society, May 11-14, 1960, Washington, D.C., USA*, 1960.

[51] J.M. Duhon. **Cost Benefit Evaluation of Helicopter Parasite Drag Reductions**. In *American Helicopter Society Symposium on Helicopter Aerodynamic Efficiency, March 6-7, 1975, Hartford, Connecticut, USA*, 1975.

[52] J.P. Rabbott and R.H. Stroub. **Wasted Fuel - Another Reason for Drag Reduction**. In *American Helicopter Society Symposium on Helicopter Aerodynamic Efficiency, March 6-7, 1975, Hartford, Connecticut, USA*, 1975.

[53] R.M. Williams and P.S. Montana. **A Comphrehensive Plan for Helicopter Drag Reduction**. In *American Helicopter Society Symposium on Helicopter Aerodynamic Efficiency, March 6-7, 1975, Hartford, Connecticut, USA*, 1975.

[54] J. Seddon. **Aerodynamics of the Helicopter Rear Fuselage Upsweep**. In *8th European Rotorcraft Forum, Aix-En-Provence, France*, 1982.

[55] M. Grawunder, R. Reß, and C. Breitsamter. **Optimized Skid-Landing-Gears for Twin-Engine-Light Utility Helicopter**. In *39th European Rotorcraft Forum, Moscow, Russia*, 2013.

[56] C. Breitsamter, M. Grawunder, and R. Reß. **Aerodynamic Design Optimisation for a Helicopter Configuration including a rotating Rotor Head**. In *29th Congress of the International Council of the Aeronautical Sciences, St. Petersburg, Russia*, 2014.

[57] M. Grawunder, R. Reß, and C. Breitsamter. **Helicopter Aft-Body Drag Reduction by Passive Flow Control**. In *40th European Rotorcraft Forum, Southampton, Great Britain*, 2014.

[58] R. Reß, M. Grawunder, and C. Breitsamter. **Parasite Drag Reduction of a Twin Engine Lightweight Helicopter Configuration**. In *63th German Aerospace Congress, Augsburg, Germany*, 2014.

[59] M. Grawunder. ***Aerodynamic Design Optimisation for Utility Helicopter Drag Reduction***. Dissertation, Technical University of Munich, 2017.

[60] K.G. Pahlke. **The GOAHEAD Project**. In *33rd European Rotorcraft Forum, Kazan, Russia*, 2007.

[61] O.J. Boelens, G. Barakos, M. Biava, A. Brocklehurst, M. Costes, A. D'Alascio, M. Dietz, D. Drikakis, J. Ekaterinaris, I. Humby, W. Khier, B. Knutzen, J. Kok, F. Le Chuiton, K. Pahlke, T. Renaud, T. Schwarz, R. Steijl, L. Sudre, H. Van der Ven, L. Vigevano, and B. Zhong. **The blind-test activity of the GOAHEAD project**. In *33rd European Rotorcraft Forum, Kazan, Russia*, 2007.

[62] O.J. Boelens, H. Van der Ven, J.C. Kok, G. Barakos, M. Biava, A. Brocklehurst, M. Costes, A. D'Alascio, M. Dietz, D. Drikakis, J. Ekaterinaris, I. Humby, W. Khier, B. Knutzen, F. LeChuiton, K. Pahlke, T. Renaud, T. Schwarz, R. Steijl, L. Sudre, L. Vigevano, and B. Zhong. **Aerodynamic simulation of a complete helicopter configuration - The blind test activity of the GOAHEAD project**. Technical report, Technical Report NLR-TP-2007-604 of the National Aerospace Laboratory (NLR), Amsterdam, Netherlands, 2007.

[63] Q. Zhang, J.-D. Lee, and J.-H. Wendisch. **An adjoint-based optimization method for helicopter fuselage backdoor geometry**. In *36th European Rotorcraft Forum, Paris, France*, 2010.

[64] Q. Zhang. **An automatic Optimization Chain for the Reduction of Helicopter Fuselage Drag**. In *Heli Japan 2010, Sitama, Japan*, 2010.

[65] T. Schwarz and K. Pahlke. **The GOAHEAD project - overview and selected results**. In *36th European Rotorcraft Forum, Paris, France*, 2010.

[66] A. D'Alascio, K. Pahlke, and F. Le Chuiton. **Application of a structured and an unstructured CFD-Method to the Fuselage Aerodynamics of the EC145 Helicopter. Prediction of the time averaged Influence of the Main Rotor**. In *4th European Congress on Computional Methods in Applied Sciences and Engineering, Jyväskylä, Finland*, 2004.

[67] M. Dietz, D. Schimke, and M. Embacher. **Advanced Industrial Application of CFD for Helicopter Development**. In *36th European Rotorcraft Forum, Paris, France*, 2010.

[68] L. Sudre, S. Borie, P. Alliot, and S. Finck. **Industrial Applications of Computational Fluid Dynamics to Helicopter Development**. In *36th European Rotorcraft Forum, Paris, France*, 2010.

[69] Y. Tanabe, S. Saito, and I. Otani. **Validation of Computational Results of Rotor/Fuselage Interaction Analysis using rFlow3D Code**. Technical report, Research and Development Report JAXA-RR-10-001E of the Japan Aerospace Exploration Agency (JAXA), Tokyo, Japan, 2010.

[70] S. Schneider, S. Mores, M. Edelmann, A. D'Alascio, and D. Schimke. **Drag Analysis for an Economic Helicopter**. In *37th European Rotorcraft Forum, Cascina Costa, Italy*, 2011.

[71] M. Biava, W. Khier, and L. Vigevano. **CFD prediction of air flow past a full helicopter configuration**. *Aerospace Science and Technology*, 19(1):3–18, 2011.

[72] Q. Zhang, A. Garavello, A. D'Alascio, and D. Schimke. **Advanced CFD-based Optimization Methods Applied to the Industrial Design Process of Airframe Components at Airbus Helicopters**. In *70th Annual Forum of the American Helicopter Society, Montreal, Canada*, 2014.

[73] J.-C. Boniface. **A Computational Framework for Helicopter Fuselage Drag Reduction Using Vortex Generators**. *Journal of the American Helicopter Society*, 61(3):1–13, 2016.

[74] P.B. Martin, C. Tung, A.A. Hassan, D. Cerchie, and J. Roth. **Active Flow Control Measurements and CFD on a Transport Helicopter Fuselage**. In *61st Annual Forum of the American Helicopter Society, Grapevine, Texas, USA*, 2005.

[75] N.W. Schaeffler, B.G. Allan, C. Lienard, and A. Le Pape. **Progress Towards Fuselage Drag Reduction via Active Flow Control: A Combined CFD and Experimental Effort**. In *36th European Rotorcraft Forum, Paris, France*, 2010.

[76] B.G. Allan and N.W. Schaeffler. **Numerical Investigation of Rotorcraft Fuselage Drag Reduction using Active Flow Control**. In *67th Annual Forum of the American Helicopter Society, Virginia Beach, Virginia, USA*, 2011.

[77] C. Lienard, A. Le Pape, and C. Verbeke. **Numerical and Experimental Investigation of Helicopter Fuselage Drag Reduction Using Active Flow Control**. In *68th Annual Forum of the American Helicopter Society, Fort Worth, Texas, USA*, 2012.

[78] F. De Gregorio. **Helicopter Fuselage Model Drag Reduction by Active Flow Control Systems**. In *43rd European Rotorcraft Forum, Milan, Italy*, 2017.

[79] A. Le Pape, C. Lienard, C. Verbeke, M. Pruvost, and J.-L. De Coninck. **Helicopter Fuselage Drag Reduction Using Active Flow Control: A Comprehensive Experimental Investigation**. *Journal of the American Helicopter Society*, 60(3):1–12, 2015.

[80] T.W. Sheehy. **A Method for Predicting Helicopter Hub Drag**. Technical report, Final Report AD-A021 201, United Technologies Corporation, Sikorsky Aircraft Division, Stratford, Connecticut, USA, 1976.

[81] P.S. Montana. **Experimental Investigation of three Rotor Hub Fairing Shapes**. Technical report, Technical Report ASED 333, Naval Ship Research and Development Center, Bethesda, Maryland, USA, 1975.

[82] P.S. Montana. **Experimental Investigation of analytically shaped Helicopter Rotor Hub-Pylon Configurations using the Hub Pylon Evaluation Rig**. Technical report, Technical Report ASED 355, David W. Taylor Naval Ship Research and Development Center, Bethesda, Maryland, USA, 1976.

[83] L.A. Young and D.R. Graham. **Experimental Investigation of Rotorcraft Hub and Shaft Fairing Drag Reduction**. In *4th Applied Aerodynamics Conference*, 1986.

[84] L.A. Young, D.R. Graham, and R.H. Stroub. **Reduction of Hub- and Pylon-Fairing Drag**. In *43rd Annual Forum and Technology Display of the American Helicopter Society, St. Louis, Missouri, USA*, 1987.

[85] L.A. Young, D.R. Graham, and R.H. Stroub. **Experimental Investigation of Rotorcraft Hub and Shaft Fairing Drag Reduction**. *Journal of Aircraft*, 24(12):861–867, 1987.

[86] R.H. Stroub, L.A. Young, and D.R. Graham. **Investigation of Generic Hub Fairing and Pylon Shapes to Reduce Hub Drag**. Technical report, NASA Technical Memorandum 100008, Ames Research Center, Moffett Field, California, USA, 1987.

[87] D.Y. Sung, M.B. Lance, L.A. Young, and R.H. Stroub. **An Experimental Investigation of Helicopter Rotor Hub Fairing Drag Characteristics**. Technical report, NASA Technical Memorandum 102182, Ames Research Center, Moffett Field, California, USA, 1989.

[88] D. Reich, R. Shenoy, M. Smith, and S. Schmitz. **A Review of 60 Years of Rotor Hub Drag and Wake Physics: 1954-2014**. *Journal of the American Helicopter Society*, 61(2):1–17, 2016.

[89] D. Desvigne and D. Alfano. **Helicopter Drag Mitigation during the CARD Project: Numerical Investigation of Rotor-And-Pylon Fairings**. In *42nd European Rotorcraft Forum, Lille, France*, 2016.

[90] A. Fink and M. Blacha. **Der Hochgeschwindigkeitshubschrauber RACER**. In *68th German Aerospace Congress, Darmstadt, Germany*, 2019.

[91] AHS International. **Airbus Helicopters H175 main rotor head**. `https://gallery.vtol.org/image/EtSD`, 2015. [Online; accessed 2020-11-20].

[92] R.E. Froude. **On the Part Played in Propulsion by Difference in Pressure**. *Transaction of the Institute of Naval Architects*, 30(1):390–405, 1889.

[93] N.E. Joukowsky. **Vortex theory of the screw propeller IV.** *Trudy Avia Raschetno-Ispytatelnogo Byuro (in Russian). French translation in: Théorie tourbillonnaire de l'hélice propulsive (Gauthier-Villars, Paris, 1929)*, 17(3):1–97, 1918.

[94] R.W. Prouty. ***Helicopter Performance, Stability, and Control***. PWS Engineering, Boston, Massachusetts, USA, 1986.

[95] J.M. Seddon and S. Newman. ***Basic Helicopter Aerodynamics***. Aerospace Series. Wiley, 2011.

[96] F. Rothlauf. ***Design of Modern Heuristics***. Springer-Verlag Berlin Heidelberg, Heidelberg, Germany, 2011.

[97] Y. Nesterov. ***Intoductory Lectures on Convex Optimization***. Springer Science+Business Media New York, New York, USA, 2004.

[98] B. Adams, M. Ebeida, M. Eldred, J. Jakeman, K. Maupin, J. Monschke, L. Swiler, D. Stephens, D. Vigil, W. Wildey, W. Bohnhoff, K. Dalbey, J. Eddy, R. Hooper, K. Hu, P. Hough, E. Ridgway, and A. Rushdi. ***Dakota, A Multilevel Parallel Object Oriented Framework for Design Optimization, Parameter Estimation, Uncertainty Quantification, and Sensitivity Analysis: Version 6.4 User Manual***. Sandia National Laboratories, Albuquerque, New Mexico, USA, 2016.

[99] A. Migdalas, P. Pardalos, and P. Värbrand. ***From Local to Global Optimization***. Springer Science+Business Media Dordrecht, Springer US, 2001.

[100] M.J. Kochenderfer and T.A. Wheeler. ***Algorithms for Optimization***. The MIT Press, Cambridge, Massachusetts, USA, 2019.

[101] S.N. Sivanandam and S.N. Deepa. ***Introduction to Genetic Algorithms***. Springer-Verlag Berlin Heidelberg, Heidelberg, Germany, 2008.

[102] D.E. Goldberg. ***Genetic Algorithms in Search, Optimization, and Machine Learning***. Addison-Wesley Publishing Company, Inc., Boston, Massachusetts, USA, 1989.

[103] A. Winkler. ***Ein automatisiertes Verfahren zur aerodynamischen Formentwicklung***. Dissertation, Technical University of Munich, 2011.

[104] Leibniz Supercomputing Centre. **SuperMUC-NG System Description**. `https://doku.lrz.de/display/PUBLIC/SuperMUC-NG`, 2020. [Online; accessed 2020-02-15].

[105] ANSYS Inc. ***ANSYS ICEM CFD User's Manual***. ANSYS, Inc., Canonsburg, Pennsylvania, USA, 2019.

[106] CentaurSoft. **CENTAUR Software**. `https://www.centaursoft.com`, 2021. [Online; accessed 2021-03-16].

[107] ANSYS Inc. ***ANSYS Fluent User's Manual***. ANSYS, Inc., Canonsburg, Pennsylvania, USA, 2019.

[108] T. Gerhold. **Overview of the Hybrid RANS Code TAU**. In N. Kroll and J.K. Fassbender, editors, *MEGAFLOW - Numerical Flow Simulation for Aircraft Design*, pages 81–92, Berlin, Heidelberg, 2005. Springer Berlin Heidelberg.

[109] D. Schwamborn, T. Gerhold, and R. Heinrich. **The DLR TAU-Code: Recent Applications in Reseach and Industry**. In *Proceedings of the* 4^{th} *European Conference on Computational Fluid Dynamics, ECCOMAS ECFD 2006. Egmond aan Zee, Netherlands*, 2006.

[110] K. Deb. ***Multi-Objective Optimization using Evolutionary Algorithms***. John Wiley and Sons Inc., Hoboken, New Jersey, USA, 2001.

[111] D.E. Goldberg and J.J. Richardson. **Genetic algorithms with sharing for multi-modal function optimization**. In *Genetic Algorithms and Their Applications: Proceedings of the* 2^{nd} *ICGA, Lawrence Erlbaum Associates, Hillsdale, New Jersey, USA*, 1987.

[112] J. Horn, N. Nafpliotis, and D.E. Goldberg. **A niched Pareto genetic algorithm for multiobjective optimization**. In *Proceedings of the* 1^{st} *IEEE Conference on Evolutionary Computation. IEEE World Congress on Computational Intelligence, Orlando, Florida, USA*, 1994.

[113] M.D. McKay, R. Beckman, and W. Conover. **A Comparison of Three Methods for Selecting Values of Input Variables in the Analysis of Output from a Computer Code**. *Technometrics*, 21(2):239–245, 1979.

[114] R.L. Iman and W.J. Conover. **A distribution-free approach to inducing rank correlation among input variables**. *Communications in Statistics - Simulation and Computation*, 11(3):311–334, 1982.

[115] A.B. Owen. **Controlling Correlations in Latin Hypercube Samples**. *Journal of the American Statistical Association*, 89(428):1517–1522, 1994.

[116] J.A. Benek, J.L. Steger, and F.C. Dougherty. **A Flexible Grid Embedding Technique with Application to the Euler Equations**. In *Proceedings of the* 6^{th} *AIAA Computational Fluid Dynamics Conference, Danvers, Massachusetts, USA*, 1983.

[117] J.A. Benek, J.L. Steger, F.C. Dougherty, and P.G. Buning. **Chimera: A Grid-Embedding Technique**. Technical report, Final Technical Report AEDC-TR-85-64, Arnold Engineering Development Center, Air Force Systems Command Arnold Air Force Station, Tennessee, USA, 1986.

[118] C.K. Lombard and E. Venkatapathy. **Implicit boundary treatment for joined and disjoint patched mesh systems**. In *Proceedings of the 7^{th} AIAA Computational Physics Conference, Cincinnati, Ohio, USA*, 1985.

[119] J.H. Ferziger and M. Peric. ***Numerische Strömungsmechanik***. Springer-Verlag Berlin Heidelberg, Heidelberg, Germany, 2008.

[120] P. Wesseling. ***Principles of Compuational Fluid Dynamics***. Springer-Verlag Berlin Heidelberg, Heidelberg, Germany, 2001.

[121] J. Boussinesq. ***Théorie de l'écoulement tourbillonnant et tumultueux des liquides dans les lits rectilignes à grande section***. Gauthier-Villars et Fils, Imprimeurs-Libraires, Paris, France, 1897.

[122] G. Alfonsi. **Reynolds-Averaged Navier-Stokes Equations for Turbulence Modeling**. *Applied Mechanics Reviews*, 62(4), 2009.

[123] F.R. Menter. **Two-Equation Eddy-Viscosity Turbulence Models for Engineering Applications**. *AIAA Journal*, 32:1598–1605, 1994.

[124] A.J. Chorin. **Numerical Solution of the Navier-Stokes Equations**. *Mathematics of Computation*, 22(104):745–762, 1968.

[125] A. Meister. ***Numerik linearer Gleichungssysteme***. Springer Spektrum, Wiesbaden, 2015.

[126] J. Xu and L. Zikatanov. **Algebraic Multigrid Methods**. *Acta Numerica*, 26:591–721, 2017.

[127] D. Schwamborn, T. Gerhold, and R. Kessler. **DLR-TAU Code - an Overview**. In *1st ONERA/DLR Aerospace Symposium, Paris, 21.-24. Juni 1999*, pages S4–2–S4–10, 1999. LIDO-Berichtsjahr=1999,.

[128] Institute of Aerodynamics and Flow Technology, German Aerospace Center (DLR), Braunschweig/Göttingen, Germany. ***Technical Documentation of the DLR TAU-Code Release 2019.1.2, Technical Report***, 2019.

[129] Bram van Leer. **Towards the ultimate conservative difference scheme. V. A second-order sequel to Godunov's method**. *Journal of Computational Physics*, 32(1):101–136, 1979.

[130] N. Kroll and R. Radepsiel. **An Improved Flux Vector Split Discretization Scheme for Viscous Flows**. Technical report, Technical Report DLR-36187 of the German Aerospace Center (DLR), Cologne, Germany, 1994.

[131] Y. Wada and M. Liou. ***A flux splitting scheme with high-resolution and robustness for discontinuities***.

[132] P.L. Roe. **Approximate Riemann solvers, parameter vectors, and difference schemes**. *Journal of Computational Physics*, 43(2):357–372, 1981.

[133] R. Courant, K. Friedrichs, and H. Lewy. **On the Partial Difference Equations of Mathematical Physics**. *IBM Journal of Research and Development*, 11(2):215–237, 1967.

[134] R. Heinrich. **Dual-Time Stepping Method**. volume Volume 71, pages 112–117. Vieweg Verlag Braunschweig, 1999. LIDO-Berichtsjahr=1999,.

[135] Airbus Helicopters. **Product website of the Airbus Helicopters H175**. `https://www.airbus.com/helicopters/civil-helicopters/Super-medium/h175.html`, 2021. [Online; accessed 2021-10-03].

[136] Wolfgang Böhm, Gerald Farin, and Jürgen Kahmann. **A survey of curve and surface methods in CAGD**. *Computer Aided Geometric Design*, 1(1):1–60, 1984.

[137] D. Salomon. ***Curves and Surfaces for Computer Graphics***. Springer-Verlage New York, 2006.

[138] E. Achenbach and E. Heinecke. **On vortex shedding from smooth and rough cylinders in the range of Reynolds numbers** 6×10^3 **to** 5×10^6. *Journal of Fluid Mechanics*, 109:239–251, 1981.

[139] Sunil Lakshmipathy and Vamshi Togiti. ***Assessment of alternative formulations for the specific-dissipation rate in RANS and variable-resolution turbulence models***.

[140] G. Gibertini, A. Zanotti, G. Droandi, D. Grassi, G. Campanardi, F. Auteri, A. Aceti, and A. Le Pape. **Wind-tunnel tests of a heavy-class helicopter optimised for drag reduction**. *The Aeronautical Journal*, 120(1231):1446–1467, 2016.

[141] R. Reß, M. Grawunder, and Ch. Breitsamter. **Aerodynamic analysis of a helicopter fuselage with rotating rotor head**. In *EUCASS Proceedings Series – Advances in AeroSpace Sciences*, volume 7, pages 99–110, 2015.

List of Publications

Peer-Reviewed Publications

- **P. Pölzlbauer**, D. Desvigne, C. Breitsamter, "Aerodynamic Design Optimization of a Helicopter Rotor Blade-Sleeve Fairing", *CEAS Aeronautical Journal*, Vol. 10(3), pp. 665-685, 2019. DOI: `10.1007/s13272-018-0341-0`

- **P. Pölzlbauer**, D. Desvigne, C. Breitsamter, "Performance Improvement of a Compound Helicopter Rotor Head by Aerodynamic Design Optimization of a Blade-Sleeve Fairing", *The Aeronautical Journal*, Vol. 123(1268), pp. 1456-1475, 2019. DOI: `10.1017/aer.2018.172`

- **P. Pölzlbauer**, A. Kümmel, D. Desvigne, C. Breitsamter, "Numerical Investigation of an Optimized Rotor Head Fairing for the RACER Compound Helicopter in Cruise Flight", *Aerospace 2021*, Vol. 8(3):66. DOI: `10.3390/aerospace8030066`

- A. Kümmel, M. Stuhlpfarrer, **P. Pölzlbauer**, C. Breitsamter, "Propeller Blade Shape Optimization with a Hybrid BEMT/CFD Approach", *Notes on Numerical Fluid Mechanics and Multidisciplinary Design*, Vol. 142, 2019.
DOI: `10.1007/978-3-030-25253-3_35`

Conference Contributions w/o Peer-Review Process

- **P. Pölzlbauer**, D. Desvigne, C. Breitsamter, "Aerodynamic Design Optimization of a Helicopter Rotor Blade-Sleeve Fairing", *66th German Aerospace Congress* (DLRK), Munich, Germany, 2017.

- **P. Pölzlbauer**, D. Desvigne, C. Breitsamter, "Performance Improvement of a Compound Helicopter Rotor Head by Aerodynamic Shape Optimization", *31st Congress of the International Council of the Aeronautical Sciences* (ICAS), Belo Horizonte, Brazil, 2018.

Conference Presentations w/o Publication

- **P. Pölzlbauer**, D. Desvigne, C. Breitsamter, "CFD-Based Aerodynamic Design Optimization of a Helicopter Rotor Blade-Sleeve Fairing", *18th STAB-Workshop*, Göttingen, Germany, 2017.

- **P. Pölzlbauer**, "CFD-basierte aerodynamische Formoptimierung einer Rotorblattanschlussverkleidung", *36th CADFEM ANSYS Simulaton Conference*, Leipzig, Germany, 2018.

- **P. Pölzlbauer**, “Numerical Investigations of a Shape Optimized Compound Helicopter Rotor Head”, *37th CADFEM ANSYS Simulaton Conference*, Kassel, Germany, 2019.